ALUMINUM (ELECTRO)COAGULATION AND MEMBRANE FILTRATION FOR PURIFICATION OF IMPAIRED WATERS: APPLICATIONS TO SURFACE WATER, HYDRAULIC FRACTURING WASTEWATER, AND WATER REUSE

A Dissertation

by

MUTIARA AYU R. RAHARDIAN SARI

Submitted to the Office of Graduate and Professional Studies of
Texas A&M University
in partial fulfillment of the requirements for the degree of

DOCTOR OF PHILOSOPHY

Chair of Committee,	Shankar Chellam
Committee Members,	Scott Socolofsky
	Yossef Elabd
	Mustafa Akbulut
Head of Department,	Robin Autenrieth

May 2017

Major Subject: Civil Engineering

ABSTRACT

This research investigates the utilization of aluminum coagulation (electrocoagulation (EC) and conventional chemical coagulation) and membrane-based separation processes (microfiltration (MF), ultrafiltration (UF), nanofiltration (NF), and reverse osmosis (RO)) for treatment of various impaired water sources. The first and major part of this research emphasizes the evaluation and optimization of aluminum (electro)coagulation combined with MF as pretreatment to NF and RO for surface water purification and water reclamation. The second part of this work focuses on mechanisms of boron removal by aluminum EC during hydraulic fracturing wastewater treatment. The overall hypothesis of the research is that aluminum EC, which generates $Al(OH)_3$ precipitates *in situ* partially removes dissolved, macromolecular, and colloidal contaminants including natural organic matter (NOM), boron, and turbidity, which can significantly improve water quality and reduce fouling in downstream membrane-based water treatment operations.

In the first part of this research, coupling of electrocoagulation/electroflotation (EC/EF) with MF was shown to provide multiple barriers against contaminants such as NOM, microorganisms, and inorganics (e.g. silica) while reducing MF fouling. Furthermore, coupled EC-MF was also shown to control NF fouling during non-saline and brackish surface water treatment. This was attributed to fractional removal of both hydrophobic and hydrophilic NOM fractions along with “nanocolloids” which consequently reduced pressure requirement for NF. Since NF fouling mechanisms depend on membrane solute rejection characteristics, this study also demonstrated the need to balance product water quality with the need to minimize NF membrane fouling through appropriate membrane selection. Potential mechanisms and

effectiveness of pretreatment were evaluated by conducting forensic post-analysis of NF/RO membrane surfaces via various surface characterization techniques (e.g. Fourier transform infrared spectroscopy, X-ray photoelectron spectroscopy, scanning electron microscopy-energy dispersive X-ray spectroscopy, and atomic force microscopy). The effect of added chemicals (i.e. coagulant and anti-scalant) during operation of real-world pilot-scale RO plant for wastewater reclamation was also investigated by extensive membrane autopsy.

Investigations on the feasibility of aluminum EC for treatment of hydraulic fracturing wastewater (particularly for boron removal) was also conducted. This work emphasized mechanistic understandings of the boron uptake by freshly precipitated amorphous $Al(OH)_3$ generated during EC. The hypothesized ligand-exchange mechanism governing boron uptake by $Al(OH)_3$ precipitates was confirmed via extensive surface characterization.

DEDICATION

Untuk Mamah dan Papah,

yang pergi dari dunia ini terlalu cepat…

Doaku selalu untuk kalian berdua

To my Mother and Father,

who left this world far too soon…

You both are always in my prayers

ACKNOWLEDGEMENTS

First and foremost, I would like to express my sincerest gratitude to my advisor, Dr. Shankar Chellam. Without your tremendous patience, motivation, support, and guidance throughout my journey as a Ph.D. student, my research work and dissertation would not have been completed. I cannot thank you enough for relentlessly pushing me to expand the limits of my skills and intellectual curiosity, while still giving me a space and opportunities to grow. Your profound knowledge, strong work ethic, curiosity to science, and creativity has inspired me to strive for the best as a scientist and engineer every day.

I would also like to thank my Ph.D. committee members, Dr. Scott Socolofsky, Dr. Yossef Elabd, and Dr. Mustafa Akbulut, for spending their precious time to help me in my scientific endeavors. A special vote of thanks also goes out to Dr. Boris Makarenko from University of Houston for equipment tranining and many hours of consultation. I would also like to acknowledge the original member of my committee, Dr. Christodoulos Floudas, who sadly passed away several months before my defense. His many extraordinary accomplishments and great kindness will be remembered forever.

I was very lucky to have a chance to work with the most wonderful, talented, highly motivated, and hardworking students in Dr. Chellam's group. Special thanks to Dr. Charan Tanneru, Dr. Neranga Gamage, Dr. Nick Spada, and Dr. Ayse Bozlaker, who were my source of inspiration, motivation, intellectual discussions, and moral support. I can thank you enough for your extra efforts in helping me get through my research. I would also like to thank the previous students in Dr. Chellam's group, Dr. Ramesh Sharma, Dr. Appalaraju Badireddy, Dr. Yongki Shim, Dr. Pranav Kulkarni, Dr. Wendong Xu, and Ashima Bagga, for their transfer of

knowledge and very useful advices. To the new members of the group, Darpan Chorghe, Kyungho Kim, Sourav Das, Kunal Gupta, Bilal Abada, Katie McNeal, and Sammy Wilson, I wish you all the best in your endeavors.

I would also like to thank the faculty and staff of Texas A&M Civil Engineering Department. To Laura Byrd, Maria Bunch, Chris Grunkemeyer, Sherry Hoffman, Pamela Spangle, Mimi Bowman, Joyce Green, Larry John, and Béla Hahn, thank you very much for your patience and kind assistance.

I would have never chosen this path in life if it was not because of my brother, Dr. Anditya Rahardianto. He is not only my brother but he is also my best friend, my teacher, my mentor, my endless source of information, and my shoulder to cry on. There is nobody in this world who gets me so well, with all of my quirkiness, but you. You are truly the most inspirational person in my life. I would have not also survived this long and tiring journey without the help and moral support from my other brother, Rizky Rahardiansyah, and his family (his wife, Putu Dewanti and my niece, Ganesha Rahardiansyah). They are my source of joy and happiness during hard times. Also to my big family, including my grandmother, my uncles and aunts, and my cousins, thank you for your endless love and support for me.

I would also like to thank all of my friends in Houston. To Aris Pramudito, Andini Haryani, and Anindita Suhardono, I cannot imagine my life in Houston without you all. You have been the most helpful and loving friends I have ever had in life. Thank you for always letting me crash in your house whenever I was in town. To my Cougar best friends, Sophia Thang and Ally Luo, I really value our life-long friendship. You both are the best listener ever.

Lastly, very special thanks go to my boyfriend, Rifky Brahmanthya, for his tremendous love and patience. I know I could be extremely difficult to deal with sometimes, but you have never left my side even once. Thank you for being you.

.

CONTRIBUTORS AND FUNDING SOURCES

Contributors

This work was supervised by a dissertation committee consisting of Professor Shankar Chellam (advisor) and Professor Scott Socolofsky of the Department of Civil Engineering and Professor Yossef Elabd and Professor Mustafa Akbulut of the Department of Chemical Engineering.

All work for the dissertation was completed independently by the student.

Funding Sources

This work was made possible in part by United States Bureau of Reclamation (Grant Number 05FC811172, R14AP00152, and R16AP00006) and Texas Hazardous Waste Research Center. Its contents are solely the responsibility of the authors and do not necessarily represent the official views of the sponsors.

TABLE OF CONTENTS

Page

LIST OF FIGURES

Page

LIST OF TABLES

Page

CHAPTER I

INTRODUCTION

Introduction

Factors such as climate change, drought, and anthropogenic influences concomitant with rapid growth in population and industrial activities have resulted in prolonged shortages in fresh water supply. It is projected that almost half of the world's population will be living in areas of high water stress by 2030 [1]. Groundwater has served as the main source of water especially in regions where water scarcity is almost endemic [2]. However, the sustainability of intensive groundwater use has been long debated since excessive extraction causes land subsidence which affects the aboveground infrastructure [3, 4]. The diminishing groundwater supplies, along with deteriorating quality of other water sources due to rapid evaporation and wastewater discharge, have increased the need to explore new water sources and advanced water treatment technologies to satisfy the rising demand for water.

Surface water has been increasingly utilized to replace groundwater. However, its purification is challenging due to the presence of higher concentrations of microorganisms, colloids, and organics [5], increase in salinity in some instances [6], and occurrence of contaminants of emerging concern [7, 8]. As a consequence, conventional drinking water treatment processes are becoming ineffective, necessitating the use of advanced treatment processes [9]. Nanofiltration (NF) and reverse osmosis (RO) are becoming increasingly relevant to remove dissolved solids and micropollutants from surface water [5, 10, 11]. However, effective applications of NF/RO to treat surface waters is a challenging proposition due to membrane fouling [12, 13]. Membrane fouling, which is caused by the accumulation of

materials on membranes can lead to reduction in water productivity, increased energy and operating costs, and eventually membrane damage [14, 15]. Membrane fouling by natural organic matter (NOM) and colloids are especially challenging due to their high concentrations in many surface water resources [5, 16, 17]. Minimization of organic passage into NF/RO product water is also very important due to their potential health concerns, such as the formation of disinfection byproducts [18, 19].

In order to mitigate NF/RO membrane fouling by NOM and colloids present in surface water, microfiltration (MF) or ultrafiltration (UF) can be integrated for feed water pretreatment [12, 20, 21]. Nonetheless, for highly fouling waters, MF/UF fouling can also be a major operational challenge [22]. Moreover, MF/UF, which removes contaminants primarily by size exclusion, only removes particles and some colloidal portion of NOM. As a consequence, downstream NF/RO fouling by "nanocolloids" and dissolved organics can still be a major issue even after MF pretreatment. Coagulation pretreatment to MF/UF is commonly employed to reduce organic fouling and simultaneously improve filtered water quality [23-27]. Colloidal and particulate agglomeration by coagulation aids in reducing internal pore fouling and formation of more permeable cake layer which consequently reduces MF fouling [24, 28]. In this regard, incorporation of coagulation process as an additional pretreatment is a promising approach to enhance both MF and NF/RO operational performance by simultaneously reducing organic and colloidal fouling.

There is an increasing interest in electrolytic addition of coagulant (i.e., electrocoagulation or electroflotation) as an alternative to conventional chemical coagulation, especially in smaller communities. In electrocoagulation and electroflotation, a coagulant is dissolved *in situ* by electrolytic oxidation of an elemental anode [29]. Hydrogen gas evolution

(and oxygen, in some cases) at the cathode facilitates floc-flotation [30, 31]. Co-production of gases is utilized in electroflotation to enhance separation of solids from water in order to reduce colloidal loading onto subsequent downstream treatment processes (i.e., MF-NF/RO). Electrocoagulation/electroflotation has several advantages over chemical coagulation due to its (1) portability and modularity, (2) reduced handling of corrosive chemicals, (3) lower alkalinity consumption, (4) negligible effect on bulk pH, (5) less sludge production, and (6) easier implementation for automated process control [32-35]. Moreover, the use of electrocoagulation/electroflotation is more suitable in treating high saline water compared to chemical coagulation because the unit can be operated at higher current density with low internal cell resistance.

While previous investigations have evaluated electrocoagulation pretreatment for low pressure membrane systems (MF/UF) [23, 24, 31, 36, 37], very little work has been devoted to determining the ultimate impact on NF/RO performance, including membrane fouling and product water quality. Several studies focusing on chemical coagulation as pretreatment to integrated membrane systems (i.e. MF/UF-NF/RO) have been established [38-40], whereas the knowledge of the impact of electrocoagulation/electroflotation pretreatment to similar systems is still lacking. It should be noted that there are inherent differences between chemical coagulation and electrolytic coagulation processes (e.g. hydrogen gas formation and potential for chlorine formation [41]). Studies of chemical coagulation, while useful, do not provide sufficient information for understanding the impact of electrocoagulation on NF/RO performance. For example, one of the major issues in the use of chemical coagulation is the carryover of excess coagulants into RO feed, which exacerbates fouling [42, 43]. The extent and chemical characteristics of potential coagulant carryover to NF/RO remains unclear when

electrolytic coagulation is employed. Lastly, it should be noted that membrane selection is important for NF especially for treating high salinity waters. NF concentration polarization is strongly influenced by rejection of individual solutes/ions, which in turn affects the fouling mechanisms. This interplay between product water quality and fouling needs more thorough investigation.

An unconventional water source that has been gaining more recent attention is hydraulic fracturing wastewater. The increasing desire to reuse these waters have resulted in growing technological interest in their treatability. One of the more challenging contaminants to remove from flowback and produced water is boron, which often occurs at elevated levels because it is used as a cross-linking agent during fracking. Reverse osmosis is an effective method for boron removal, although the process can only withstand a low concentration level of boron in the feed water despite employing a multistage system [44-46]. Moreover, produced water is highly saline and laden with dispersed and soluble oil, organic compounds, naturally occurring radioactive materials, heavy metals, and other chemicals. These factors alone contribute to the difficulty of using RO without extensive pretreatment. Electrocoagulation is considered to be a potentially promising technology for on-site treatment of such high-strength wastewaters due to its small size and portability which is amenable for rapid field deployment. Moreover, electrocoagulation of most hydraulic fracturing wastewaters can be performed at elevated current densities in an energy efficient manner due to their high electrical conductivity [47]. To date, boron removal by electrocoagulation has been predominantly evaluated using low salinity synthetic wastewaters to empirically determine the role of operating parameters [47-49] although limited data with actual wastewater is becoming available [50-52]. In any case, the nature of specific interactions leading to a mechanistic understanding of boron uptake

during electrochemical treatment remains elusive even though bulk measurements suggest that chemisorption of boron to aluminum precipitates is endothermic [51].

The above literature review demonstrated that further fundamental studies on (electro)coagulation for treatment of various water sources are still needed. This research mainly focused on developing and demonstrating aluminum (electro)coagulation as an effective and robust pretreatment process to membrane separation systems for surface water treatment and wastewater reclamation. Another part of the research work is the elucidation of boron removal mechanisms by aluminum electrocoagulation during treatment of hydraulic fracturing wastewater. To our knowledge, this is amongst the first rigorous and systematic investigations of (electro)coagulation for purification of such impaired water sources.

Research goal and objectives

The main goal of my research is to understand the basic principles for optimizing aluminum (electro)coagulation processes in conjunction with membrane separation systems (MF-NF/RO) or as a stand-alone system for treating various water sources (surface water, municipal and hydraulic fracturing wastewater). The overall hypothesis of the research is that aluminum EC, which generates $Al(OH)_3$ precipitates *in situ* partially removes dissolved, macromolecular, and colloidal contaminants including natural organic matter (NOM), boron, and turbidity, which can significantly improve water quality and reduce fouling in downstream membrane-based water treatment operations. In order to achieve this goal, the following specific objectives were formulated:

a. Review the literature on integrated aluminum electrocoagulation and MF processes for surface water treatment.

b. Compare and assess the effectiveness of various coagulation methods in improving NF performance during non-saline surface water treatment.

c. Optimize NF during brackish surface water desalination by appropriate membrane selection and integration of EC-MF as pretreatment for fouling control.

d. Extensively characterize fouled NF/RO membranes in order to identify major foulants and elucidate possible fouling mechanisms.

e. Elucidate boron removal mechanisms during aluminum electrocoagulation of hydraulic fracturing wastewater.

Dissertation organization

The main components of this dissertation are six manuscripts (chapter II – VII), five of which have already been published and a sixth one that was recently submitted for peer-review before possible publication. The format of each of these chapters is the same as the published articles; each beginning with an introduction, followed by the material and methods, results and discussion, and finally the concluding remarks. The final chapter in the dissertation summarizes the important aspects of all the chapters and recommends future research directions.

Chapter II summarizes the current knowledge on MF pretreatment by aluminum electrocoagulation particularly focusing on mechanisms of (1) electrocoagulant dosing, (2) (bio)colloid destabilization, (3) fouling reductions, and (4) enhanced removal of viruses, natural organic matter (NOM), and DBP precursors. This work was published in: S. Chellam and M.A. Sari, Aluminum electrocoagulation as pretreatment during microfiltration of surface

water containing NOM: A review of fouling, NOM, DBP, and virus control, *Journal of Hazardous Materials,* **304** (2016) 490-501 [35].

Chapter III discusses the bench-scale evaluation of NF for treating non-saline surface water following different pretreatments (MF-only, EC-MF, EF-MF, and conventional chemical coagulation-MF) and extensive surface characterization for foulant identification. These findings can be found in M.A. Sari and S. Chellam, Surface water nanofiltration incorporating (electro) coagulation–microfiltration pretreatment: Fouling control and membrane characterization, *Journal of Membrane Science,* **437** (2013) 249-256 [53].

The performance of NF for treating brackish surface water treatment was evaluated in Chapter IV and V. Chapter IV highlights the strong dependency of NF fouling mechanisms on the membrane solute rejection characteristics during brackish surface water treatment. Hence, optimal membrane selection needs to balance total dissolved solids concentration of the product water with the need to minimize fouling These findings can be found in M.A. Sari and S. Chellam, Relative contributions of organic and inorganic fouling during nanofiltration of inland brackish surface water, *Journal of Membrane Science,* **523** (2017) 68-76 [54]. Following membrane selection discussed in Chapter IV, Chapter V discusses the integration and optimization of EC-MF pretreatment for fouling control during brackish surface water NF. This work was recently accepted for publication in *Desalination*.

Chapter VI shows that forensic post-analysis of RO membranes for fouling identification via surface characterization methods from real-world pilot-scale RO water reuse plant can reveal: (1) the potential fouling mechanisms, (2) the effectiveness of RO feed pretreatment, (3) the contribution of added chemicals (i.e. coagulant, antiscalant) to fouling, and (4) the cleaning requirements for effective membrane regeneration. This work has already

been published in M.A. Sari and S. Chellam, Reverse osmosis fouling during pilot-scale municipal water reuse: Evidence for aluminum coagulant carryover, *Journal of Membrane Science*, **520** (2016) 231-239 [55].

Chapter VII focuses on aluminum electrocoagulation as a stand-alone system for treating hydraulic fracturing wastewater. Boron uptake mechanisms by $Al(OH)_3$ precipitates generated during electrocoagulation of hydraulic fracturing wastewater were elucidated using several surface characterization methods. Experiments were conducted using actual hydraulic fracturing wastewater and synthetic solution. These findings are available in M.A. Sari and S. Chellam, Mechanisms of boron removal from hydraulic fracturing wastewater by aluminum electrocoagulation, *Journal of Colloid and Interface Science*, **458** (2015) 103-111 [56].

CHAPTER II

ALUMINUM ELECTROCOAGULATION AS PRETREATMENT DURING MICROFILTRATION OF SURFACE WATER CONTAINING NOM: A REVIEW OF FOULING, NOM, DBP, AND VIRUS CONTROL *

Introduction

The United Nations estimates that 1.2 billion people currently live in areas of physical water scarcity, a number which is projected to increase to 1.8 billion by the year 2025 [1]. The deteriorating quality of existing "freshwater" sources, uncertainties in precipitation associated with climate change, and unsustainable water usage, necessitate advanced treatment technologies to quench the thirst of a growing population. It is prudent to meet the growing demand using surface water since excessive groundwater extraction causes land subsidence damaging the built-infrastructure and wetlands and increasing the frequency and intensity of flooding [57]. However, surface water purification requires advanced water treatment technologies since it is typically laden with high concentrations of particles (i.e. turbidity), pathogenic microorganisms, and precursors to potentially carcinogenic, teratogenic, and mutagenic disinfection by-products (DBPs), i.e. natural organic matter (NOM) [58].

Microfiltration (MF) and ultrafiltration (UF) are low-pressure liquid-solid membrane separation technologies that have found widespread use in purifying drinking water and wastewater largely because they directly remove *Giardia*, *Cryptosporidium*, bacteria, and turbidity [59]. Physical removal of difficult-to-inactivate parasites significantly reduces the

* Reprinted with permission from "Aluminum electrocoagulation as pretreatment during microfiltration of surface water containing NOM: A review of fouling, NOM, DBP, and virus control", S. Chellam, M.A. Sari, 2016, Journal of Hazardous Materials, 304, 490-501, Copyright 2016 by Elsevier.

requisite chemical disinfectant concentrations to meet primary microbiological drinking water standards when MF and UF are implemented for water treatment. In turn, lower disinfectant concentrations decrease DBP formation. Hence, MF and UF directly reduce microbial risks and indirectly reduce chemical risks in the water we drink. However, waterborne viruses [60-62] and natural organic matter (NOM) largely pass unimpeded across MF and UF membranes [63-65]. Importantly, micro- and ultrafilters are subject to fouling, which refers to reducing permeate flux (at constant pressure) or increasing transmembrane pressure (at constant flux) [59]. Fouling decreases productivity, which can be partially counteracted by pretreating the feed water thereby facilitating MF and UF implementation.

One common membrane pretreatment method is coagulation where traditionally aluminum or iron salts are added externally to the feed water ahead of MF or UF [62, 66-68]. Recent advances in electrochemical technologies have generated much interest in evaluating them as alternatives to conventional coagulants [29, 69]. During electrocoagulation (EC), current is passed through a sacrificial anode to dissolve coagulant precursor ions *in situ*, which hydrolyze rapidly to form dissolved hydroxyl complexes and insoluble hydroxide precipitates. Gas exsolution during electrolysis sometimes leads to floc-flotation, which is sometimes termed electroflotation (EF) when the floating layer is skimmed and only the remaining non-floating colloids present in the water column are sent downstream for additional liquid-solid separation [31, 70, 71]. The burgeoning interest in applying electrolytic technologies can be attributed to their (i) suitability for use in predesigned portable packaged plants, (ii) reduced use of corrosive chemicals, (iii) availability of optimized module configurations, and (iv) effectiveness over a wide range of water chemistries (e.g. varying pH and alkalinity) [34, 72]. Most previous investigations and reviews of EC have focused on its capabilities as a stand-

alone process to remove physicochemical contaminants including arsenic, copper, zinc, fluoride, turbidity, NOM, etc. [73-83]. However, electrochemical processes are beginning to be integrated with low-pressure membranes e.g. [23, 24, 31, 84-90] necessitating their optimization in close conjunction with MF/UF, which is our focus. The principal objectives of this work are to summarize the state-of-the-art of integrated electrochemical and MF/UF systems for drinking water treatment emphasizing (i) aluminum electrodissolution reactions, (ii) membrane fouling mechanisms, and (iii) control of NOM, DBP precursors, and viruses. Only limited information on iron EC is presented herein and the reader is referred elsewhere for detailed information about this process [23, 29, 34, 91, 92]. It is emphasized that we focus largely on results generated in our laboratories and NOM and DBP precursor control results presented herein are previously unpublished information.

Experiments

The majority of data that this review is based on was obtained from our earlier publications [23, 24, 31, 36, 41, 53, 93, 94]. However, new experiments were also performed to generate data on DBP control since this topic is central to surface water treatment and as yet, such information is not available in the literature for integrated EC/MF. Membrane fouling control and removal of viruses, NOM, and DBP precursors was studied using Lake Houston as a representative surface water whose important characteristics are summarized in Table II-1. As seen, this lake can be characterized as being moderately turbid, low in dissolved salts, hardness, and buffering capacity, and moderately high in NOM content.

Table II-1. Summary of Lake Houston water quality parameters.

Parameter	Unit	Concentration or value
pH	-	7.9 ± 0.16
Turbidity	NTU	18.8 ± 1.0
Dissolved organic carbon	mg/L	6.9 ± 0.3
UV_{254}	cm^{-1}	0.170 ± 0.009
Conductivity	µS/cm	394.4 ± 14.9
Chloride	mg/L	22.1 ± 3.2
Total hardness	mg/L as $CaCO_3$	67 ± 3.3
Calcium hardness	mg/L as $CaCO_3$	56.1 ± 2.1
Alkalinity	mg/L as $CaCO_3$	85.7 ± 3.2
Dissolved silica	mg/L as SiO_2	9.36 ± 3.84

Dissolved organic carbon (DOC) was measured using the combustion infrared method (Shimadzu 5050TOC, Columbia, MD) after acidification and N_2 purging. Ultraviolet absorbance at 254 nm was measured using a DR/4000 spectrometer (Hach Company, Loveland, CO) with a 1-cm path length quartz cell. Water samples were prefiltered using a 0.45 µm syringe filter to avoid interferences from suspended particles for both DOC and UV_{254}. DBP precursor removal was measured at simulated distribution system (SDS) conditions (24 hour contact time, 20 °C temperature, pH 8.3, and 1 mg/L free Cl_2 residual). Water samples were first collected in demand free amber colored bottles, buffered with borate, and dosed with the appropriate amount of chlorine solution to have a residual of 1 ± 0.2 mg/L after 24 hours. Four THMs ($CHCl_3$, $CHCl_2Br$, $CHClBr_2$, $CHBr_3$) were analyzed by EPA Method 551.1; i.e. liquid/liquid extraction with tertiary-butyl methyl ether and by gas chromatography with electron capture detection. Six haloacetic acids containing chlorine and bromine (monochloroacetic acid, dichloroacetic acid, trichloroacetic acid, monobromoacetic acid,

dibromoacetic acid, and bromochloroacetic acid) were analyzed by EPA Method 552.2 (i.e. liquid/liquid extraction, derivatization with acidic methanol, and gas chromatography with electron capture detection.

Electrocoagulation was conducted at pH 6.3 (near the pH of minimum Al solubility) and a current density of 20 mA/cm^2 that necessitated a voltage of nearly 10 V. The anode was a Puratronic grade aluminum (99.9965% as Al, Alfa Aesar) rod fitted inside a perforated hollow 316-stainless steel cathode with 2 mm spacing constituting an annular geometry. The anode was mechanically scrubbed and gently washed with weak acid to present a polished surface for each experiment. Total aluminum was measured by atomic absorption spectroscopy (Flame AA-AAnalyst 300, Perkin-Elmer) after acidifying samples to < 2 using HCl according to Standard Method 3111. More details on the source water and the electrocoagulation apparatus can be obtained from our previous publications [23, 24, 31, 36, 41, 53, 90, 94]. After select EC experiments, flocs were harvested, vacuum dried, and examined using powder X-ray photoelectron spectroscopy (XPS). Both survey scans (0–1400 eV) and high-resolution spectra were obtained for photoelectrons with a 1.1 mm spot diameter.

Unstirred MF was performed at constant pressure (2–24 psig) using a 4.1 cm^2 disc PVDF membrane with pores rated at 0.22 µm. First, 100 mL of ultrapure water was passed through the system first to measure the clean membrane resistance. Then, a minimum of 150 mL of the electrocoagulated suspension was filtered during which time the instantaneous pressure and cumulative filtered water volume were monitored at a variable frequency between 0.1 – 1 Hz using a computerized data acquisition system and a program written in LabVIEW [24, 31, 90, 95, 96]. To probe fouling mechanisms, the instantaneous flux $\frac{d(V/A_m)}{dt}$ was first obtained by numerically differentiating the cumulative volume filtered (V) per unit membrane

area (A_m) after exponential smoothing and analyzing it using blocking laws [95-97]:

$$\frac{dt}{d(V/A_m)} = \frac{1}{J_o} e^{k_i (V/A_m)} \qquad \text{(intermediate blocking)} \qquad (1)$$

$$\frac{dt}{d(V/A_m)} = k_c \left(\frac{V}{A_m} \right) + \frac{1}{J_o} \qquad \text{(cake filtration)} \qquad (2)$$

where J_o is the initial permeate flux and k_i and k_c are parameters describing intermediate blocking and cake filtration respectively [59].

Coagulant electrodissolution

We have reported short-term coagulant electrodissolution into Lake Houston to quantitatively obey Faraday's law (Equation 3), where m is the total mass of iron or aluminum (g), AW is the atomic weight of the elemental coagulant precursor (i.e. 55.85 g/mol for Fe and 26.98 g/mol for Al), I is the electric current (A), t is time (s), z is number of electrons transferred, and F is the Faraday's constant (96,486 C/eq) [23, 24, 31, 36].

$$\mathrm{m} = \frac{\mathrm{AW\ I\ t}}{\mathrm{z\ F}} \qquad (3)$$

Applying Equation 3 to laboratory measurements during surface water EC has provided evidence for a 3- and 2-electron transfer for aluminum and iron EC respectively [23, 24, 31, 36]. Electrodissolved coagulant concentrations increased linearly with the amount of electrical charge passed as predicted by Faraday's law. Hence, chemical dissolution, which has been reported to augment electrocoagulant dosing to super-Faradaic levels at high chloride ion concentrations [32, 41, 70] does not appear to be significant under our experimental conditions for low salinity surface water. Accurate Faraday's law predictions also arise from vigorously cleaning the anode prior to each experiment [32, 91, 98]. Additionally, since Lake Houston water is NOM-laden and low in salinity and chloride ion concentration, chemical dissolution,

pitting corrosion, and chlorine generation did not accompany electrolysis [32, 70]. Hence, all electrons appear to have participated in anodic aluminum dissolution and similar to another recent report [98], oxygen was not released. Since this behavior can potentially change in the presence of other electrochemically active species and at higher applied voltages, electrocoagulant dosing needs to be evaluated on a case-by-case basis.

These results suggest the following electrochemical reactions for low-salinity, high NOM content surface waters at typical pH values [29, 34, 69, 91, 99-101]:

Anode $Fe(0)_{(s)} \rightarrow Fe(II) + 2e^-$ or $Al(0)_{(s)} \rightarrow Al(III) + 3e^-$

Cathode $2H_2O + 2e^- \rightarrow H_{2(g)} + 2OH^-$

Electrodissolved iron and aluminum undergo hydrolysis to form various mono, di, and polynuclear complexes, which behave as Brønsted acids, consume buffering capacity and tend to reduce pH [80, 102-104]. Hydroxyl ions released at the cathode tend to neutralize the Brønsted acidity of hydrolysis products even causing a temporary upward drift in pH for typical initial pH values depending on the buffering capacity of the feed water, current density, and electrolysis duration [24, 32, 98]. Limited change in pH has been reported for high alkalinity waters or when electrolysis is performed for short-durations [23, 85, 105]. Electrodissolution of highly soluble Fe(II) has been confirmed by direct aqueous phase measurements [36, 91, 99] and can be problematic since it does not directly induce sweep coagulation. Consequently, Fe(III) is preferred over Fe(II) as a coagulant for water purification applications. However, in the absence of significant NOM concentrations, Fe(II) can be potentially oxidized to precipitate $Fe(OH)_{3(s)}$ in oxygenated waters by raising the pH (kinetics is first order in dissolved oxygen concentration and inverse second order in pH) to induce sweep coagulation and enmeshment [73, 106-109]:

$4Fe(II) + O_2 + 2H_2O + 8OH^- \rightarrow 4Fe(OH)_{3(s)}$

Importantly, complexation of electrodissolved Fe(II) inhibits oxidation, limiting the coagulation ability of iron during electrochemical pretreatment if NOM or other chelating agents are present [23, 36, 99, 110]. Along with anodic dissolution, hydrogen gas is released from the cathode due to water splitting explaining the observed bubble formation. These bubbles adhere to flocs, which can cause them to float to the top of the water column, which is sometimes referred to as EF [31, 71, 85, 107, 111-113]. When the entire electrolyzed suspension is directly filtered (without intermediate liquid-solid separation), the process is referred to as EC [24, 29, 86, 87, 90]. It is emphasized that these definitions, although very useful, are not yet universally accepted in the literature.

A multitude of solid phases have been reported following iron and aluminum EC including predominantly magnetite and maghemite with traces of lepidocrocite and akaganeite in sea water [84], green rust, magnetite, and lepidocrocite in highly colored natural water as well as traces of bayerite and boehmite but predominantly amorphous $Al(OH)_3$ in surface water of moderate NOM content [31, 104, 113]. Raman spectroscopy has provided evidence that operating conditions influence iron polymorphs with dissolved oxygen concentrations being an important parameter [98]. Conditions favoring low dissolved oxygen form green rust, but lepidocrocite is crystallized in oxygen-rich environments, and magnetite is precipitated at intermediate dissolved oxygen values. However, under conditions typical of drinking water treatment, iron oxyhydroxide morphology appears to remain relatively invariant to electrolysis conditions [114]. XPS survey scans of EC flocs from Lake Houston at a 10 mg/L dosage showed a 1:3 Al:O stoichiometric ratio suggesting formation of insoluble $Al(OH)_{3(s)}$ in natural surface water [90]. High resolution spectra of photoelectrons emitted from Al 2p measured the

peak location to be 74.55 eV [31] corresponding to the value reported for pure $Al(OH)_3$ [115]. Hence, oxides and oxy-hydroxides formed by EC in natural water appear to be dominated by amorphous $Al(OH)_{3(s)}$, separately verified by the lack of crystal habit in electron micrographs [24]. Broad shallow peaks corresponding to boehmite nanocrystals (γ-AlO(OH)) have been observed only in X-ray diffractograms of electrochemically generated solids in buffered nanopure water [24]. In contrast, the weak boehmite signals do not appear in diffractograms following electrolysis of surface water. Hence, NOM disrupts precipitation of crystalline Al precipitates during EC similar to reports for chemical precipitation with $AlCl_3$ [116]. These results demonstrate the strong influence of the source water matrix on the morphology of the *in situ* precipitated coagulant during EC.

Membrane fouling control by electrochemical pretreatment

Pretreating seawater by iron EC has been reported to be effective for UF fouling control [84, 85] but not for MF during surface water treatment [23]. This apparent discrepancy could arise from the generated pin-point flocs penetrating the larger pores of the more porous MF polymer matrix compared to the denser UF skin layer or due to the lower NOM content of seawater [84, 85]. Iron EC is effective in the absence of NOM [73, 87], but NOM complexes Fe(II) [106, 110], which has been reported to prevent effective sweep coagulation [23, 36]. This is in contrast to conventional iron pre-coagulation, which can efficiently control MF/UF fouling [23, 25, 117]. It is emphasized that conventional iron coagulation during water and wastewater treatment is accomplished using Fe(III) salts such as $FeCl_3$ or $Fe_2(SO_4)_3$ [103]. Therefore, *in situ* Fe(II) oxidation and hydrolysis appears to be significantly less effective than

direct hydrolysis of externally added Fe(III) during MF pretreatment of NOM-laden surface water [23].

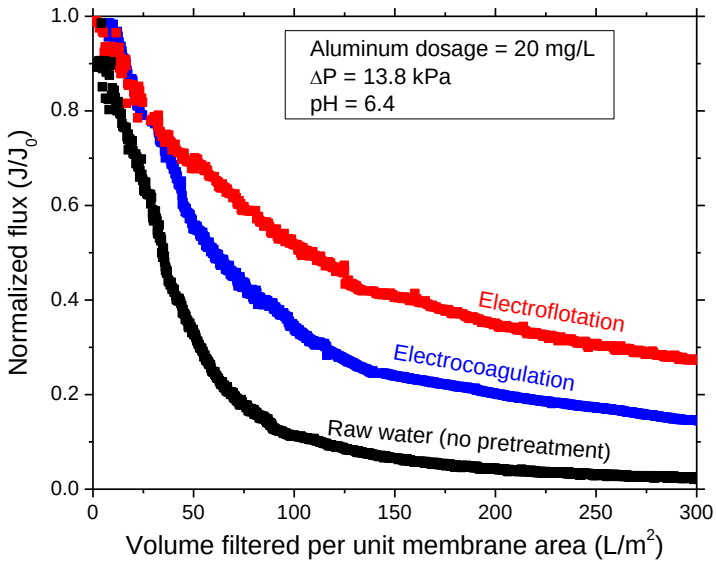

Figure II-1. Fouling control during surface water MF by aluminum EC and EF. Note that raw water was obtained from Lake Houston, which contains ~ 7 mg/L of NOM measured as dissolved organic carbon (DOC). EF enhances flux over EC primarily by reducing the total mass loading of foulants onto the membrane (data adapted from [24, 31, 90]).

In contrast to iron, aluminum EC has been reported to significantly reduce colloidal fouling during forward MF of NOM-containing surface waters. Figure II-1 compares normalized flux during constant pressure dead-end MF for untreated Lake Houston water containing approximately 7 mg/L DOC and after electrochemical pretreatment. As seen, the flux decreased severely reaching only 2% of its initial value in the absence of pretreatment at the conclusion of the experiment. EC pretreatment increased the final flux to 15% of the initial value and even better results were obtained for EF pretreatment, which enhanced flux to 27% of the initial value. Aluminum hydrolysis products destabilize foulants by reducing the zeta potential ($\rightarrow$ 0 mV) [24]. Enmeshment into $Al(OH)_{3(s)}$ precipitates also forms large flocs

reducing penetration into membrane pores and increases cake permeability compared to MF of untreated water [24, 31, 90]. In other words, EC reduces both internal pore fouling and external cake resistance.

Hydrogen bubbles released at the cathode undergo hydrophobic interactions with NOM sorbed on flocs inducing floc-flotation especially over relatively longer electrolysis durations, which can be used to reduce mass loading onto downstream filters by skimming off the floating flocs [31, 70, 85, 113]. This explains significantly better MF flux obtained when only the portion of the solids that do not float during electrolysis is microfiltered (i.e. EF over EC pretreatment) as shown in Figure II-1. Empirically, floc-flotation has not been reported to be substantial at low aluminum dosages (< ~5 mg/L) presumably because bubble number and attachment efficiency is low due to reduced hydrophobic interactions [31]. MF flux is substantially improved when significant flotation occurs during EC, because the solids loading on the membrane i.e. the total foulant mass is reduced. This reduces the cumulative cake resistance of deposited $Al(OH)_3$ flocs even though the specific resistance is higher because smaller particles are preferentially suspended in the water column and sent to the microfilter [31].

Aluminum electrochemical treatment has been shown to best control fouling at (i) pH of lowest solubility (i.e. near 6.3), (ii) an intermediate dosage due to counteracting effects of increasing floc size (that decreases specific resistance) and mass loading (that increases cumulative resistance) as more and more coagulant is added, and (iii) lower transmembrane pressures that compress cakes to a lower extent [24, 31, 86]. Bench-scale testing has revealed an optimum dosage for fouling control to be in the range 10 – 15 mg Al/L for Lake Houston [24, 31, 90].

Flux decline mechanisms

During the early stages of MF of untreated surface water, i.e. with no pretreatment, the inverse instantaneous permeate flux typically exhibits a concave-upward profile with respect to cumulative volume quantitatively obeying Equation 1. This is shown in Figure II-2 by the exponential fit to the early portion of the curve (from 0 – ~200 L/m^2) in green color and labeled "intermediate blocking." As filtration of the untreated water progresses and more and more particles are deposited on the surface of the membrane, the inverse instantaneous flux profile transitions to a straight line relationship corresponding to cake filtration as quantitated by Equation 2. This is shown in Figure II-2 by the straight line fit to the latter portion of the curve (from ~200 – 350 L/m^2) in blue color and labeled "cake filtration" [23, 24, 59]. These data were generated during MF of Lake Houston water at a relatively low pressure of 2 psig and at an optimal Al dosage of 10 mg/L.

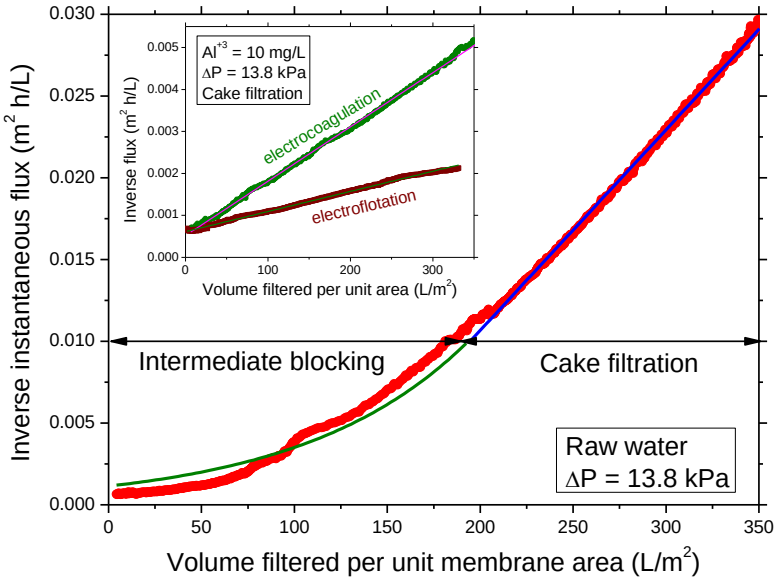

Figure II-2. Deducing MF fouling mechanisms from experimental flux profiles. Note a strong concave-upward shape during MF of untreated or raw water, which later transitioned to a straight-line. In contrast, the entire filtration cycle for pretreated waters closely fit a straight-line as shown in the inset (adapted from [23, 24, 31]).

Blocking law modeling suggests that early on, natural colloids have a similar propensity to deposit on previously deposited foulants or on the free microfilter surface to block pores that are open to water permeation as given by the intermediate blocking law (Equation 1). As filtration progresses, viscous resistance to water flow increases as a surficial deposit grows in thickness causing the flux to decline according to cake filtration theory (Equation 2). The initial blocking stage is eclipsed at higher pressures for raw water MF suggesting that the increased rate of foulant deposition at high initial fluxes quickly leads to cake filtration [96, 97].

In contrast to raw water, the complete flux profile obeys the cake filtration model for electrochemically pretreated suspensions (entire straight-line behavior in Figure II-2 inset). This demonstrates that adding electrocoagulant and increasing the mass concentration of solids in the MF feed water increases the rate of cake layer build-up to a point where a distinct pore blocking phase cannot be observed [23, 24, 31]. An additional concern is that fouling typically worsens with increasing pressure for dead-end MF of electrocoagulated and electrofloated waters due to cake compression:

$$\alpha^{*} = \alpha_{0}^{*}\Delta P^{n} \qquad (4)$$

where α^* and α_0^* denote the specific resistance at pressure ΔP and for an unstressed cake ($\Delta P = 0$) respectively [24, 118, 119]. It should be noted that the absolute water flux across the membrane increases with pressure according to Darcy's law and the resistance in series approach to modeling MF flux decline [120]. However, MF experiments performed in a range of pressures has shown that cake compression decreases the relative flux (instantaneous flux normalized by initial flux) at a faster rate at higher pressures even without any pretreatment [119, 121, 122]. When electrocoagulation pretreatment is employed, flocs formed are typically

highly open and porous, characterized by low mass fractal dimensions [31, 72, 93, 123]. Cake compression is important in EC/MF systems as well in the range 2-24 psig of transmembrane pressure and aluminum dosages of 2 – 30 mg/L [23, 24, 31, 93]. These data suggest that inelastic mechanisms such as floc breakage or cake collapse (at the extreme) dominate cake compression [118, 124].

Chemical aspects of fouling control by electrochemical pretreatment

Recently, there is much interest in utilizing spectroscopic techniques including XPS, Fourier transform infra-red (FTIR), nuclear magnetic resonance (NMR), liquid chromatography, and fluorescence excitation emission matrix to diagnose foulants and MF fouling mechanisms for raw and coagulated waters [31, 66, 90, 125, 126]. XPS has shown that in addition to reducing fouling by changing physical parameters such as increasing foulant effective size by aggregation, the inclusion of hydrogen bubbles in electrocoagulated flocs induces a larger uptake of hydrophobic compounds than during conventional chemical coagulation [93]. This was deduced by measuring higher peak areas indicative of hydrophobic bonds (i.e. C-C/C-H) in electrocoagulated flocs in comparison with similar measurements of alum-coagulated flocs.

Electrochemically generated flocs at a concentration of 10 mg Al/L were analyzed by XPS survey scans, which showed strong C, N, and O signals and high O/Al ratios in the range 5 – 6 (i.e. > 3 from $Al(OH)_{3(s)}$), and have been attributed to sorbed NOM and bacteria [31]. The location and intensity of deconvoluted C, O, and N peaks in high resolution XPS scans can be used to infer NOM sorption during EC [31, 93]. For example, Figure II-3 shows representative high resolution X-ray spectra of O 1s and C 1s photoelectrons from flocs formed by electrocoagulating Lake Houston water at 10 mg Al/L [93]. Uptake of aromatic and

aliphatic hydrocarbon backbones (-C-C-/-C-H at 284.95 eV), alcohols, phenols, and proteins (-C-O-/-C-N- at 286.76 eV), aldehydes, ketones, amides, and (hemi)acetals (-C=O/-O-C-O- at 288.58 eV), and humic acids, fulvic acids, and esters (C(=O)OH/C(=O)OR at 289.25 eV) can be inferred from C1s core level spectra [31, 90, 115, 127, 128]. Similarly, sorption of carboxylates/carboxyl (C(=O)OH/C(=O)O^-), esters (C(=O)OR), and amides (C(=O)N), hydroxides and (hemi)acetals (O-(C, H)), and singly bonded oxygen in carboxyls (C(=O)OH) and esters (C(=O)OR) has been measured by decomposing the O1s core level peak at 531.68 eV, 532.65 eV, and 533.72 eV respectively as shown in Figure II-3 [93, 115, 129]. Greater uptake of hydrophobic compounds during EC has been verified by gross NOM characteristics, e.g. lower UV_{254} absorbance values in EC/MF permeates compared with conventional alum coagulation pretreatment to MF [93].

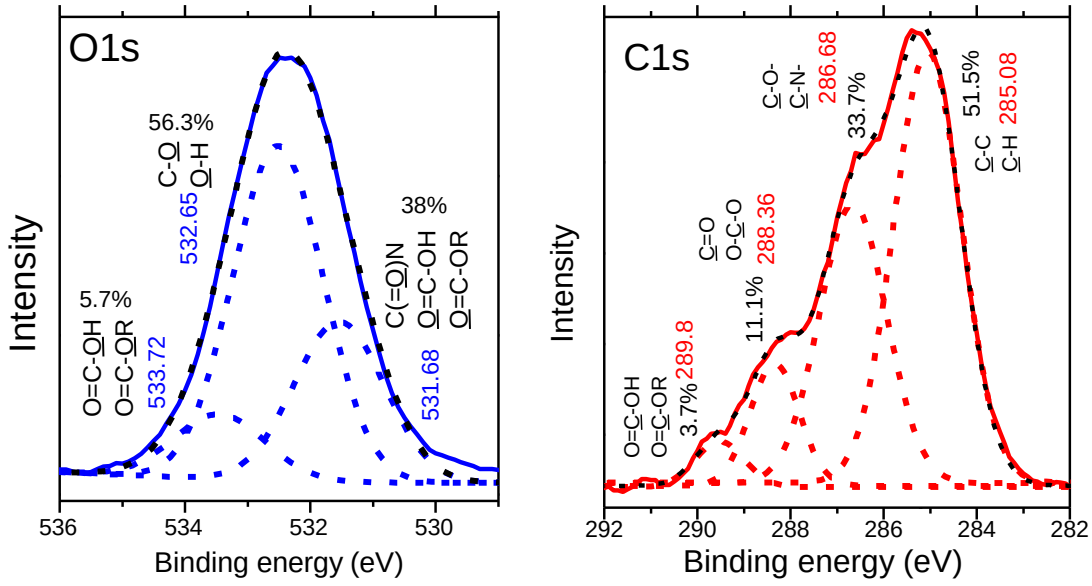

Figure II-3. Examples of curve fitted high resolution XPS spectra before and after pretreatment. O1s core level peaks of raw (untreated) colloids in surface water are shown on the left. Deconvoluted C1s spectrum following electrochemical treatment is shown on the right. Adapted from [93].

During raw water MF, it has been proposed that fouling is initiated by sorption of hydrophobic humic-like molecules present in the influent, which is then followed by more hydrophilic moieties causing the flux to decrease [90, 125]. Any added electrocoagulant partitions a portion of the hydrophobic NOM reducing direct interactions of these molecules with the polymeric matrix of the membrane thereby controlling flux decline [31, 90]. Although aluminum coagulation reduces fouling, $Al(OH)_{3(s)}$ accumulates on the membrane over long durations and can intensify complexation of hydrophilic molecules such as biopolymers on MF and UF membranes [66, 90, 126]. These results indicate that maximizing bubble surface area (e.g. by increasing bubble number and decreasing their size for the same $H_{2(g)}$ volume released) would be optimal MF pretreatment to increase hydrophobic interactions and NOM uptake onto flocs.

Water quality improvements

In aluminum EC/MF systems, membrane fouling is alleviated only up to a point where the electrocoagulant dosage is optimal, after which point fouling worsens if more coagulant is added [24, 31]. Unlike fouling control, which is best controlled at an intermediate electrocoagulant dose, contaminant removal by the integrated system typically increases progressively as more and more electrocoagulant is added. It is emphasized that integral micro- and ultrafilters directly remove protozoa and bacteria even without any pretreatment because membrane pore sizes are about one order of magnitude smaller than these microorganisms [59, 130]. Consequently, in this paper we focus only on NOM, DBP precursor, and virus control, which are not well-removed by MF/UF alone during drinking water treatment. The reader is referred elsewhere for the removal of other contaminants (e.g. trace metals and metalloids) by

EC [29, 33, 73].

NOM and DBP precursor control

Both aluminum and iron are effective electrocoagulants in enhancing NOM removal [23, 89, 90, 105, 131, 132]. Iron polymorphs show significant differences in NOM removal with green rust outperforming lepidocrocite and magnetite [98]. In addition to monitoring DOC, it is also useful to evaluate specific UV absorbance (SUVA, defined as the ratio of UV_{254} in m^{-1} and DOC concentration in mg/L) since SUVA is an indicator of NOM chemical composition and reactivity [133].

NOM removal and DBP precursor control results

DOC concentrations and UV_{254} values in MF permeate for a range of electrochemical aluminum dosages (0 – 30 mg/L) added to surface water are shown in Figure II-4 at two pH values of 6.4 and 7.5. DOC concentrations (Figure II-4a) and UV_{254} absorbance values (Figure II-4b) in the EC/MF water can be seen to decrease progressively as more and more aluminum is added. Additionally, as depicted in Figure II-4a, NOM removal is higher at pH 6.4. This is attributed to more effective charge neutralization (charge density → 0) by the dominant hydrolysis product $Al(OH)_2^+$ compared with $Al(OH)_4^-$ at pH 7.5, which formed more insoluble complexes and made NOM more adsorbable [134]. Since pH 6.4 approximately corresponds to minimum aluminum solubility [103, 135], NOM is also probably better enmeshed onto $Al(OH)_3$ precipitates at 6.4. Also, UV-absorbing compounds are typically removed to a greater extent than DOC during coagulation [136]. Results summarized in Figure II-4 are consistent with previous investigations of conventional chemical coagulation [136, 137] wherein aromatic, higher molecular weight, and hydrophobic humic components are also preferentially removed by EC [105, 138]

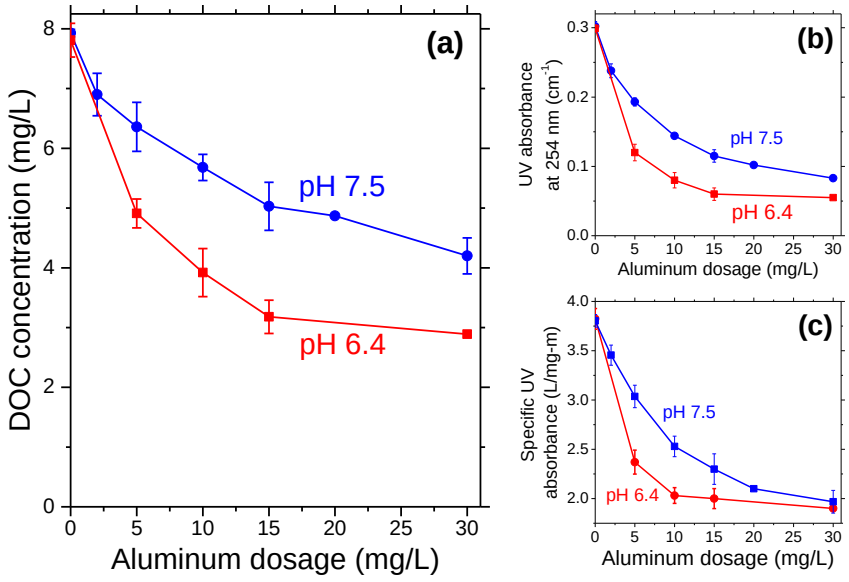

Figure II-4. Improvements in NOM removal measured as dissolved organic carbon (a) and UV_{254} (b) as well as decreasing specific UV absorbance (c) through aluminum electrocoagulation pretreatment of Lake Houston water at pH 7.5 and 6.4.

SUVA, an indicator of NOM's reactivity towards chlorine [133], was also reduced by EC/MF as shown in Figure II-4c. lower SUVA coupled with decreasing NOM molecular weight following EC/MF suggests that DBPs are controlled by reducing the absolute concentration of organic precursors as well as their reactivity. To our knowledge, earlier EC work has focused only on NOM removal e.g. [23, 89, 98, 105, 131] and DBP formation has not yet been directly measured. Previously unpublished data presented in Figure II-4 demonstrate that for example at 10 mg/L aluminum dosage, EC/MF removed ~40% DOC (from 6 mg/L to 3.58 mg/L) and 52% UV_{254} removal (from 0.117 cm^{-1} to 0.056 cm^{-1}) from Lake Houston. This resulted in 52% removal of total SDS-THMs and 60% removal of SDS-HAA6. SUVA reduction by EC shown in Figure II-4c correspondingly decreased SDS-THM and SDS-HAA specific yield (μM of DBPs produced per mM of DOC) by 20% and 34% respectively. As discussed earlier, this can be attributed to the preferential removal of the

hydrophobic and higher molecular weight fractions of NOM, which are generally accepted to be more reactive in forming DBPs coupled with a reduction in chlorine demand. Therefore, DBP control by EC appears to be achieved by removing precursors measured as DOC and UV_{254} and simultaneous reduction in reactivity of NOM with chlorine.

THM and HAA speciation during chlorination depends on the individual ratios of NOM present, Cl_2 dosed, and Br^- concentration [136, 139]. Electro- and alum coagulation changes Br^-/NOM and Cl_2/NOM ratios compared with the raw water since they preferentially remove NOM and not Br^-. Therefore, EC cannot be expected to control individual THM and HAA species to the same extent. As expected, EC induced a slight shift towards brominated THM and HAA6 species, which can be visualized by analyzing mole fractions (Figure II-5). As seen, mole fractions of brominated THMs, $CHBrCl_2$, $CHBr_2Cl$ and $CHBr_3$ increased after EC/MF and similar results were obtained for HAAs. In this case, the Br^-/DOC ratio was increasing from 0.028 to 0.045 µM/µM and simultaneously chlorine consumption was decreased by 42%. This corresponds to a decrease in bromide utilization for both THMs and HAAs because excess Br^- could not react once all available reactive sites on NOM were occupied, similar to changes in DBP speciation following nanofiltration discussed earlier [19]. On the other hand, EC significantly increased the bromine incorporation factor for THMs and HAAs attributed to initial formation of brominated DBPs since HOBr is a stronger halogenating agent than HOCl.

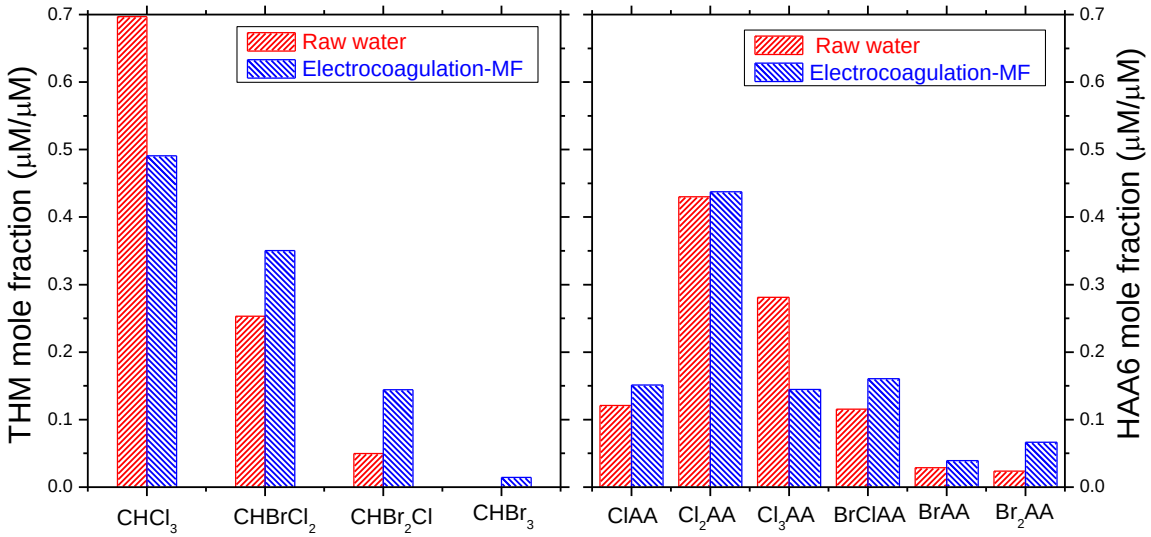

Figure II-5. Changes in THM and HAA speciation following electrocoagulation – MF of Lake Houston water. Note the general shift towards brominated THM and HAA species after treatment.

Behavior of microorganisms in electrochemical systems

Electrodisinfection has been demonstrated using carbon, mixed metal oxides, boron doped diamond, and other dimensionally stable anodes largely using model waters not containing NOM [101, 140-143]. The primary advantage of purely electrochemical inactivation is that *in situ* disinfectant generation reduces the risk associated with transport and on-site storage of large amounts of highly toxic chemicals [144]. Inactivation in such systems occurs through generation of oxidants (e.g. chlorine) and free radical intermediates (e.g. reactive oxygen species) [140, 141, 145]. In contrast, as discussed earlier in this manuscript, EC is performed using sacrificial (not dimensionally stable) anodes and real-world surface waters contain NOM. It is emphasized that intact MF membranes alone have been shown to remove > 99.9999% (6-logs) of bacteria and protozoa simply due to size exclusion but they allow nearly unhindered virus passage [36, 61, 94, 146]. Additionally, EC alone is highly effective for bacteria and algae control [70, 112, 143]. Hence, this review is focused largely

towards microorganisms that are smaller than MF membrane pores (i.e. viruses).

Iron EC/MF was initially shown to be more effective than conventional coagulation for virus removal from synthetic water devoid of NOM achieving > 4 log removal (as required by the United States Environmental Protection Agency) at 10 mgFe/L dosage compared with only 2 log removal at an equivalent ferric chloride dosage [37]. However, we recently demonstrated that this trend is reversed for surface water containing 5 mg-C/L NOM where EC/MF only removed 1.5 log of MS2 viruses at 13 mgFe/L whereas 6.5 log removal was measured from synthetic water at a similar iron dosage [36]. Presence of 5 mg-C/L of Suwannee River Humic Acid (SRHA) decreased virus removal by approximately 4-log at pH 6.4 and approximately 2-log at pH 7.5 by EC/MF compared to $FeSO_4$ coagulation/MF [36]. Hence, it was hypothesized that NOM worsened virus removal by complexing electrodissolved Fe(II), inhibiting its oxidation to insoluble Fe(III) [110], and consequently reducing coagulant precipitation and sweep flocculation [36]. In contrast, it has been recently reported that 3 mg-C/L of Suwannee River Fulvic Acid (SRFA) did not significantly influence *Escherichia coli* attenuation from synthetic groundwater [142]. Hence, the concentration and composition of NOM appears to play important roles in affecting microorganism removal/inactivation in surface- and groundwaters. Additionally, viruses are inactivated by Fe(II) and Fe(0) (when no NOM is present) but the underlying mechanisms have not yet been undisputedly identified [147] although current evidence points to oxidative stress [142, 148]. It is emphasized that the early favorable results on virus removal by iron EC/MF were obtained using synthetic waters with no NOM [37]. Apparently conflicting reports on NOM effects during iron EC for bacteria and viruses and between surface- and groundwater [36, 142] demonstrates the need for more

research to systematically evaluate the role of NOM on the performance of iron EC/MF for treating NOM-laden surface waters.

All infective viruses taken up by flocs generated by conventional alum coagulation and aluminum EC of surface water has been recovered by dissolving them at high pH using beef extract (but not for polyaluminum chloride) [63, 94, 149, 150]. Hence, unlike iron, aluminum electrolysis does not inactivate viruses under low-salinity conditions typical of natural water. Nevertheless, aluminum is more effective than iron in removing viruses from NOM-containing surface waters (see Figure II-6a) due to successful $Al(OH)_{3(s)}$ precipitation and enmeshment whereas iron did not significantly precipitate following electrolysis under these conditions [36, 94].

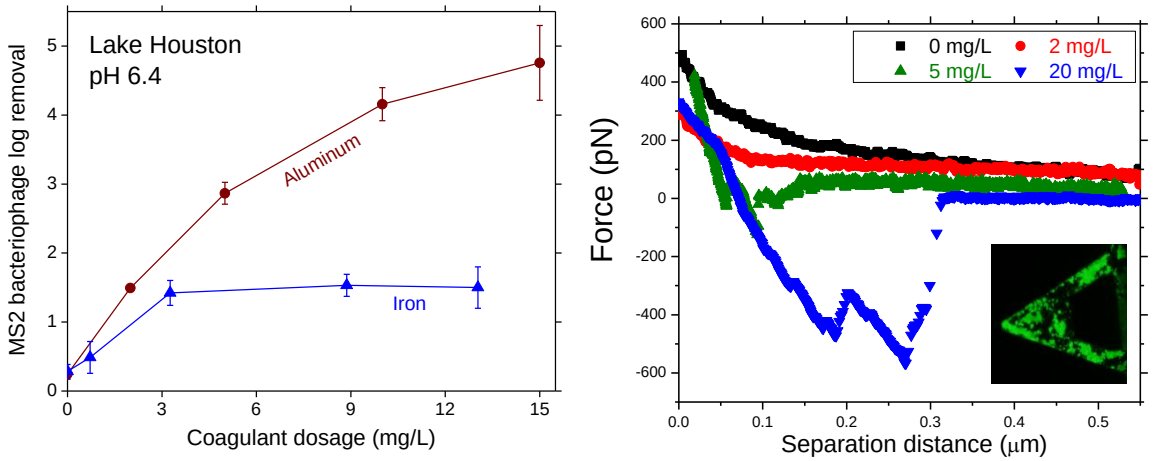

Figure II-6. Aluminum electrocoagulation removes viruses from surface water to a greater extent than iron (left). AFM pull-off curves during for the retraction of virus-coated tips from the surfaces of Al(OH)3 flocs formed during electrocoagulation of lake Houston water. Fluorescent image of viruses bonded on Si3N4 tips using 3-aminopropyl-triethoxysilane (APTES) is shown in the inset on the right. Adapted from [36, 94].

Insights into virus-floc interactions have been obtained via atomic force microscopy using tips with covalently immobilized viruses (see inset in Figure II-6b) [94]. Unbinding force

calculated from pull-off curves corresponding to the vertical retraction of virus-coated tips from the floc interface in a liquid cell are shown in Figure II-6b for 0, 2, 5, and 20 mgAl/L dosages. For the raw water and the lowest dose studied (2 mg/L), there was negligible interactions between the tip and the flocs leading to poor removals by EC. Higher dosages caused viruses to adhere strongly and multiple peaks were observed as the tip was retracted from the floc surface in the contact mode. Multiple pull-off events correspond to interactions of capsid proteins of viruses on the tip with NOM, viruses, and $Al(OH)_3$ precipitates (including polyvalent cations bridges) as well as formation and breakage of intra-protein bonds as the virus is pulled [151]. Fluorescence microscopy also has provided visual evidence for virus enmeshment during EC [94]. EF of cyanobacteria by taking advantage of its positive buoyancy (with no inactivation) has also been to be successful for algae removal [112].

An issue specific to integrated EC/MF treatment is the potential effect of a foulant layer on further removal of viruses. Previously deposited colloids do indeed serve as a secondary filter to increase observed (not intrinsic) rejection [36, 94, 152, 153] but the magnitude depends on the nature of viruses and coagulation conditions. For example, by precoating a MF membrane with precipitates produced by polyaluminum chloride coagulant, improvements in virus log-removal has been measured in the order MS2 > Qβ > recombinant norovirus virus-like particles [152]. This effect is more prominent at higher dosages for both iron and aluminum EC [36, 94]. Reanalyzing recently published data from our research group [94] demonstrates a strong positive correlation with cake mass at different dosages as shown in Figure II-7. Hence, it appears that thick cake layers can function as dynamic membranes [154] to remove viruses by an additional 1-log compared with the identical coagulant dosage without cake formation. It should be noted that pore blocking can also contribute to secondary virus removal

both in raw and precoagulated waters; i.e. both reversible and irreversible fouling contribute to measured enhancements in microorganism removal [155].

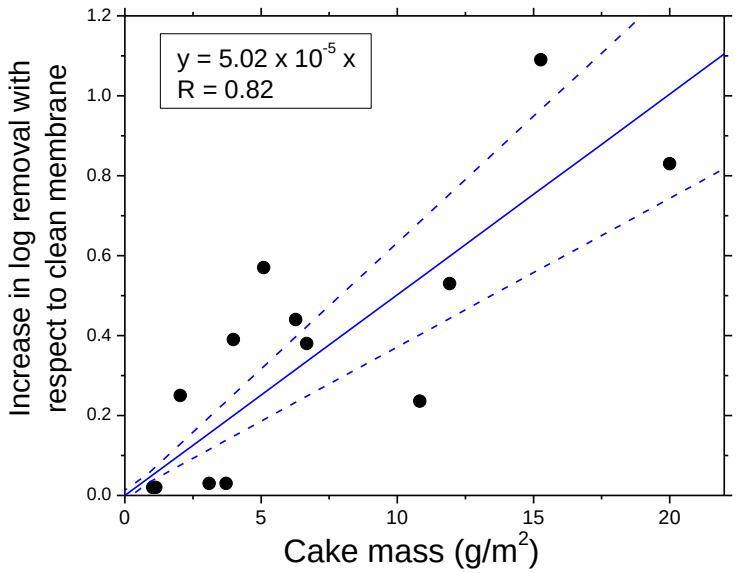

Figure II-7. Additional removal of the MS2 bacteriophage due to cake formation during aluminum EC/MF (adapted from [94]).

Figure II-8 depicts a reanalysis of our recently published data during EC/MF of Lake Houston water (10 mg/L and pH 6.4) over a period of 5 hours [94]. The brown and blue symbols correspond to Fe and Al respectively, which demonstrate statistically similar concentrations of infective viruses. Relatively constant virus concentrations measured by the plaque assay demonstrates no inactivation in the presence of NOM as discussed earlier. However, unlike surface waters with low-salinity, EC of brackish waters can oxidize chloride ions at the anode to free chlorine [70, 143], which is a strong oxidant/disinfectant capable of inactivating microorganisms:

$$2Cl^- \rightarrow Cl_2 + 2e^-;\ Cl_2 + H_2O \leftrightarrow HOCl + H^+ + Cl^-;\ HOCl \leftrightarrow H^+ + OCl^-$$

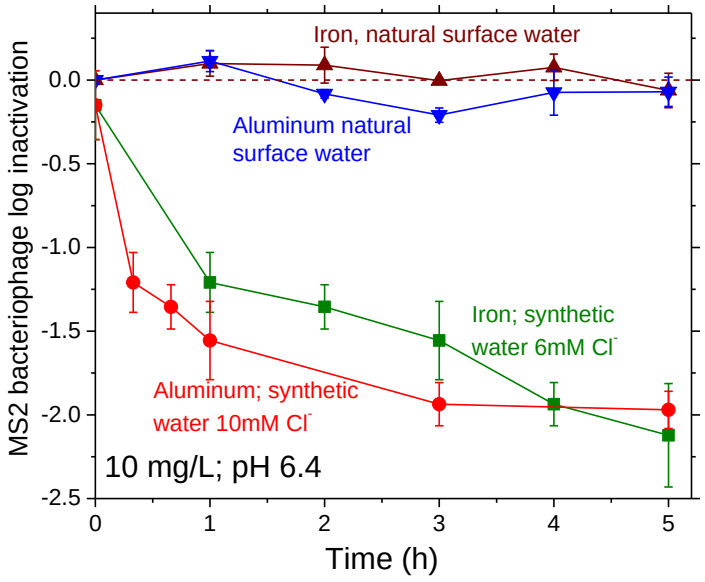

Figure II-8. Viruses are not inactivated during electrocoagulation of NOM-laden surface water. The MS2 bacteriophage loses infectivity during electrolysis of chloride-rich synthetic waters that do not contain NOM. Adapted from [36, 41].

Algae and virus control is enhanced at high chloride ion concentrations due to chlorine-induced inactivation on top of physical removal by coagulation [41, 70]. This is also depicted in Figure II-8, which shows decreasing infectivity of the MS2 virus during electrolysis of synthetic water containing high chloride ion concentrations but lacking NOM (green and red curves). Under these conditions approximately 0.02 mg Cl_2/L was measured resulting in 1 – 1.5 log inactivation during the first hour. However, shielding and aggregation within flocs significantly slows down disinfection kinetics reaching only 2 log inactivation after 5 hours. Hence, physical removal dominates inactivation for overall microorganism control corresponding to residence times typical of electrochemical treatment [41]. Chlorine is also expected to react with any NOM that may be present in natural water. Hence, artificially extended flocculation/contact times would be necessary to achieve significant inactivation during iron/aluminum EC of surface water.

In addition to being disinfectant precursors, chloride ions also attack the passivation layer on sacrificial electrodes enhancing coagulant chemical dissolution due to pitting corrosion. This can result in super-Faradaic coagulant dissolution, in excess of Equation 2 predictions [100, 111, 156]. In contrast, accumulation of precipitates and other contaminants on electrode surfaces can result in sub-Faradaic coagulant dissolution lower than Equation 3 predictions [84]. Reversing the polarity (by using sacrificial anodes and cathodes) and increasing tangential shear (similar to crossflow filtration) can potentially reduce such problems related to unpredictable or changing coagulant dosing over time [32, 84].

Concluding remarks

In this manuscript, we mainly reviewed data generated in our research group regarding the integration of aluminum EC and MF for drinking water treatment while including limited information on iron EC/MF. It is shown that aluminum EC significantly reduces MF fouling by inducing the formation of a cake comprised of particles larger than in the raw water. However, aluminum flocs can compact or compress and relatively worsen MF fouling at higher pressures. New results are also included showing significant improvements in microfiltered water quality by EC pretreatment. $Al(OH)_3$ flocs sorb NOM and DBP precursors, which are then retained on the MF membrane surface. EC/MF induces a slight shift towards brominated THMs and HAAs by increasing the Br^-/DOC ratio compared to the raw water. It is also shown that viruses are effectively sweep coagulated by EC and removed subsequently by MF. A thick cake layer of $Al(OH)_3$ flocs further improved virus removal by acting as a dynamic membrane. In summary, results presented herein suggest that EC/MF systems are promising alternatives for small-scale decentralized facilities because they inherently provide multiple barriers

against contaminants of health concern and minimize membrane fouling while requiring limited operator attention [157].

Although the concept of employing electrical current to dissolve coagulants and generate oxidants *in situ* has a long history, EC has not yet obtained a firm foothold in water/wastewater treatment. Recently, much progress has been made to elucidate various performance aspects including pH profiles between electrodes, precipitated solid phases, electrode passivation, and other factors influencing EC performance. However, much more work needs to be done since a universal understanding of the nature and composition of precipitated phases based on water chemistry and electrolysis conditions continues to remain elusive. Additionally, preliminary cost estimates suggest that EC is competitive to conventional coagulation especially for smaller installations [85]. Importantly, electrochemical treatment does not consume buffering capacity unlike hydrolyzing metal salt coagulants that behave as Brønsted acids. Hence, EC may be suitable for a wide range of water chemistries and eliminates the need to add base to maintain pH during coagulation (leading to reduced chemical handling and increased process simplicity). Improved designs incorporating multiple electrode configurations have also been proposed [29, 33, 104]. These indicate the growing interest in electrochemical and MF technologies especially for small, portable systems for localized treatment [157].

However, electrode passivation [100] and inconsistent coagulant dosing over long periods of operation [158] continues to impede EC, in the same sense that fouling still limits MF application. Research is being actively conducted to identify solid phases and dissolved hydrolysis products in electrochemical cells [98, 102, 113] since this intimately impacts contaminant removal and subsequent MF performance. However, more work remains to be

done in order to predict the precipitate morphology and composition based on background water chemistry and EC operating conditions. Such knowledge would benefit our understanding of contaminant removal and fouling control by EC and future design of hybrid EC/MF systems. It is hypothesized that compressibility indices would depend on the nature of the solid phase, which in turn would strongly influence MF flux and fouling. It is emphasized that more work is necessary to carefully delineate electrocoagulant species which may be different than in chemical coagulation because of inherent disparities in the microenvironment at the anode-water interface compared with alum addition (although work is being done for the case of iron e.g. [159, 160]). Specific interactions of hydrolysis products with polymeric MF membranes also need to be measured to estimate (ir)reversible fouling. Further, long-term pilot-scale on-site evaluations for individual applications are necessary to build an empirical database for integrated EC/MF treatment in parallel to developing a more detailed understanding of underlying mechanisms and best design practices.

CHAPTER III

SURFACE WATER NANOFILTRATION INCORPORATING (ELECTRO)COAGULATION – MICROFILTRATION PRETREATMENT: FOULING CONTROL AND MEMBRANE CHARACTERIZATION *

Introduction

Nanofiltration (NF) can be implemented for removing divalent ions such as calcium and magnesium (hardness), macromolecules such as natural organic matter (NOM) and disinfection by-product precursors, as well as aggregate and trace contaminants such as color, pesticides, and pharmaceuticals and personal care products from surface waters and shallow groundwaters [161-163]. However, in contrast to groundwater, these feed waters rapidly foul nanofilters necessitating advanced pretreatment such as microfiltration (MF) [12, 20, 21]. Since MF alone does not remove significant amounts of NOM, it primarily only reduces colloidal fouling of downstream NF membranes in these applications. Therefore, we hypothesize that incorporating additional MF pretreatment capable of NOM removal (e.g. coagulation) will enhance NF specific fluxes in integrated membrane systems by simultaneously reducing both organic and colloidal fouling. Note that coagulation pretreatment to MF will provide the supplementary benefit of reducing MF fouling as well [68]. There is increasing interest in electrochemical coagulation due to its portability, reduced handling of corrosive chemicals, and its improved performance e.g. [29, 164]. For this reason, we evaluate both conventional chemical coagulation and electrocoagulation methods in this manuscript.

*Reprinted with permission from "Surface water nanofiltration incorporating (electro) coagulation–microfiltration pretreatment: Fouling control and membrane characterization", M.A. Sari and S. Chellam, 2013, Journal of Membrane Science, 437, 249-256, Copyright 2013 by Elsevier.

Detailed reports of NF foulants in dual membrane systems are available for wastewater reclamation and surface water treatment [165-168]. It is emphasized that due to the inherent heterogeneity of water supplies, additional information from geographically diverse sources would aid in the better design and implementation of integrated surface water NF systems. Our interests in this topic arise from the mandate for the greater Houston area to completely convert to surface water by the year 2030 to combat ground subsidence while meeting the demands associated with the projected 45% growth in population over the same timeframe.

The principal objective of this research is to empirically demonstrate improved permeate fluxes during constant pressure NF of surface water following coagulation – MF pretreatment. We comparatively evaluate conventional alum coagulation with electrolytic aluminum addition as MF pretreatment alternatives (see Figure III-1 for a schematic of various pretreatment processes evaluated). To our knowledge, this is the first systematic and rigorous investigation of these integrated membrane systems. Virgin and fouled NF membranes were extensively characterized in terms of hydrophobicity, surface morphology (scanning electron microscopy (SEM) and atomic force microscopy (AFM)), organic functionalities and elemental composition (Fourier Transform Infrared (FTIR) spectroscopy and X-ray Photoelectron Spectroscopy (XPS) respectively) to identify dominant foulants and fouling mechanisms. Alcian Blue staining was also performed to detect acidic polysaccharides, which may represent transparent exopolymers of biological origin. Lake Houston was used as a representative surface water source.

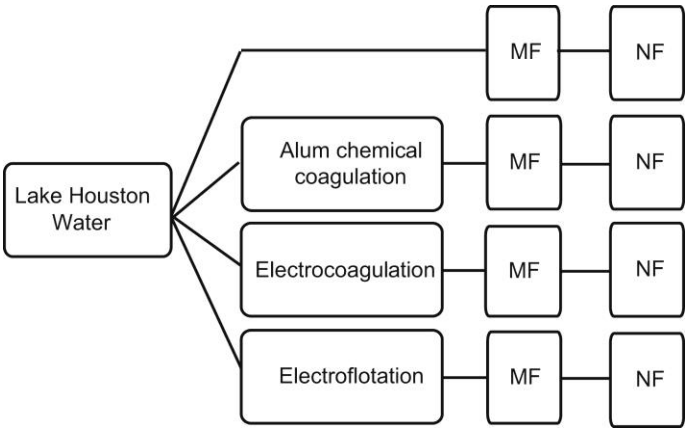

Figure III-1. Schematic representation of NF pretreatment alternatives and integrated membrane systems evaluated in this study.

Experimental work

Source water

A 25-gallon sample was collected from the Lake Houston canal at the East Water Purification Plant in January 2012 and stored in the dark at 4 °C over the course of experimentation. The water was slightly alkaline (pH 7.9 ± 0.16), moderately turbid (18.8 ± 1.0 NTU), had medium concentrations of natural organic matter (dissolved organic carbon (DOC) 6.92 ± 0.33 mg/L and UV_{254} 0.170 ± 0.009 cm^{-1}), low in conductivity (394.4 ± 14.9 μS/cm), soft (total hardness 67 ± 3.3 and calcium hardness 56.13 ± 2.05 mg/L as $CaCO_3$) and low in buffering capacity (alkalinity 85.7 ± 3.2 mg/L as $CaCO_3$). Over the entire duration of this study, the coefficient of variation for all monitored water quality parameters was ≤ 5% allowing the comparison of results from various experiments performed using this sample.

Electrocoagulation, electroflotation, and conventional chemical coagulation

Electrocoagulation was conducted in a custom made Perspex cell fitted with an annular electrode geometry comprised of a 15 cm aluminum anode (Puratronic grade, 99.9965% as Al, Alfa Aesar) and a porous cylindrical 316-stainless steel cathode. The electrodes were

mechanically cleaned before each experiment and the desired coagulant concentration was achieved via constant current operation in accordance with Faraday's law [24]:

$$m_{Al} = \frac{26.98It}{zF}$$

where m_{Al} is the mass of Al generated, z is the number of electrons transferred per Al atom (= 3), I is the current, t is time, and F is Faraday's constant (96,486 C eq^{-1}). Using a current density of 20 mA/cm^2 necessitated 193 seconds of electrolysis to produce 10 mg/L Al in batch mode, which was independently verified using atomic absorption spectroscopy. An aluminum dose of 10 mg/L at pH of 6.4 was employed for (electro)chemical coagulation since we have found this to be optimal for Lake Houston water [24]. Under these experimental conditions, the majority of the flocs floated to the top of the electrolysis cell due to the hydrogen gas released at the cathode. For electrocoagulation, the entire contents of the cell were gently mixed and microfiltered. In electroflotation, the suspension was withdrawn from the bottom of the cell through a valve to prevent the transfer of the floating flocs to MF.

Conventional alum coagulation was performed using a programmable jar tester (Model PB-900, Phipps & Bird) with 1-minute rapid mixing (at 300 rpm) and 30 minutes flocculation at a velocity gradient of 30 s^{-1}. Similar to electrochemical experiments, a pH 6.4 and 10 mg/L Al was employed. Due to the relatively low buffering capacity of Lake Houston water, NaOH was added to maintain the pH. The coagulated/flocculated water was then transferred for MF.

Microfiltration

Constant pressure, unstirred dead-end filtration experiments were conducted using a 300 mL stainless steel cell and Nylon membranes rated at 0.45 μm with 17.3 cm^2 effective area (HNWP04700, Millipore). Approximately 8 L of permeate was collected for each type of pretreatment (electrocoagulation, electroflotation, chemical coagulation) for subsequent NF.

Lake Houston water was also simply microfiltered (without any type of coagulation) to serve as a negative control for NF fouling comparisons.

Nanofiltration

Bench-scale crossflow NF experiments were performed using a stainless steel cell (SEPA-CF, Osmonics) fitted with a 19 cm x 14 cm flat sheet (155 cm^2 effective area) of a commercially available thin-film composite membrane (DL, GE Osmonics) including feed and permeate spacers. This membrane consists of four layers including a ~ 0.2 mm thick polyester reinforcing fabric, ~ 0.05 mm thick microporous polysulfone support, ~ 0.2 µm thick polyamide active layer, and a proprietary ultrathin skin. We have measured the molecular weight cut-off (MWCO) of this membrane to be 268 g/mol corresponding to an approximate mean pore size of 1.46 nm [169].

The feed water was delivered by a positive displacement gear pump (head model 73004-02 and drive model 75211-10, Cole-Parmer). The recovery was accurately controlled at 80% with a flow meter (1450NIA/7506, Fischer & Porter) and a high precision needle valve (316 JWS, Swagelok) in the concentrate stream. The system was operated in batch recycle mode by continuously returning permeate and concentrate flows to the feed tank (except during sampling) [170]. Pressures and temperature were monitored using analog transducers (PX603 and TJ120 CPSS 116G respectively, Omega). Additionally, permeate and concentrate flows were measured with digital balances (Ohaus Navigator N1H110, Fisher Scientific) connected via LabView (v. 8.5, National Instruments) to a personal computer. Membrane setting was achieved by passing 5 mM NaCl solution for 24 h at 470 kPa. Pretreated surface water was then filtered at constant pressure of 470 kPa corresponding to an initial clean membrane flux of 29.9 ± 2.9 L/m^2-h, and a Darcy resistance of 5.83 x 10^{13} ± 5.68 x 10^{12} m^{-1}. Experiments

were conducted at room temperature (24 °C) for a minimum of 170 hours at 80% recovery. Due to flux decline, adjustments were periodically made to the back pressure valve to maintain constant pressure and recovery.

Two-sided, two sample t-tests revealed no differences (at the 0.05 significance level) between experimentally measured and theoretically predicted retentate DOC concentrations, UV absorbance at 254 nm, and conductivity at steady-state. Additionally, very similar instantaneous NF fluxes were measured when the entire electroflotation – MF – NF experiment was repeated. These observations coupled to the consistency of the raw water quality demonstrate the accuracy of our experimental protocols and instrumental analyses.

Spectroscopy

ATR-FTIR spectra of virgin and fouled membranes were collected using a Nicolet iS10 spectrometer equipped with a Ever-Glo MIR source, DTGS detector, KBr beam splitter and Omnic 8.5 Software. Membrane samples were placed on the transmissive Ge window. Spectra reported herein are averages of measurements from six different locations of the membrane, each averaged from 128 co-added scans collected from 650 to 4000 cm^{-1} at 4 cm^{-1} resolution and a zero filling factor of 1 using a Happ-Genzel apodization and Mertz phase correction. The overlapping peaks in the amide I region (1700-1600 cm^{-1}) was deconvoluted by enhancing spectral resolution by taking the second derivative of the original spectra after nine-point Savitzky-Golay smoothing [171]. Maximum absorption intensity, band frequency, and bandwidth, obtained from the second derivative spectra, were used to perform curve-fitting on the original spectra by assuming a Gaussian-Lorentzian shape for the amide I band and for each peak. This procedure gave insights into protein secondary structures comprising the foulant layer.

The surface elemental composition of fouled and clean nanofilters were measured with a PHI 5700 X-ray photoelectron spectrometer equipped with a monochromatic Al Kα X-ray source ($h\nu$ = 1486.7 eV) incident at 90° relative to the axis of a hemispherical energy analyzer. The neutralizer was turned on to reduce problems with charging arising from membranes that were non-conducting. Survey spectra were obtained over the entire range (0-1400 eV) and high-resolution spectra were obtained only for photoelectrons emitted from C1s to verify functionalities inferred from FTIR spectroscopy. Electron binding energies were calibrated with respect to the C1s line at 284.8 eV. Peak areas were obtained after deconvoluting C1s peaks following integrated baseline background subtraction (Shirley routine), assuming mixed Gaussian-Lorentzian shapes, and correcting for sensitivity factors. We report the average of measurements made from six different locations on each membrane.

Contact angle and zeta potential

Approx. 3µL of ultrapure water was gently placed on dried virgin and fouled membrane surfaces and contact angle was recorded using a goniometer (Dataphysics OCA 15EC) fitted with a camera. The sessile drop technique applied to the entrance and exit regions (3 replicates each) of the specimens gave very similar contact angles. Therefore, average of the equilibrium right and left angles (total of 12 measurements) from different locations allowing for ~ 15 seconds droplet spreading is reported.

Microscopy

Scanning electron micrographs of clean and fouled membranes were obtained (LEO 1525, Carl Zeiss) after sputter coating the samples with a 10 nm layer of gold (data not shown). Surface topography was also measured via AFM (Asylum Research) in tapping mode using a TESP silicon probe (PPP-NCH, Nanosensors). The TESP probe has a spring constant range of

10-130 N/m, frequency range of 204-497 kHz, tip radius of 8 ± 2 nm, and cantilever length of 125 µm. The measured root mean square (RMS) roughness values for virgin and fouled membranes were obtained along with the images at multiple locations.

Staining for acidic polysaccharides

Membrane samples were cut into 1 cm squares and stained with ~ 2 mL of 1% Alcian Blue 8 GX in 3% acetic acid buffer solution at pH 2.5 (Fluka, Sigma Aldrich). After a contact time of 5 minutes, the excess stain was removed by rinsing with ultrapure water, and the membrane was viewed under an optical microscope with 20x magnification (Olympus BX51). The entire procedure was completed rapidly (< 15 minutes) to avoid potential degradation of the active layer of the nanofilter at low pH.

Results and discussion

Effect of pretreatment type on nanofilter fouling

DOC concentrations in the NF feed and permeate waters along with steady-state specific flux values are summarized in Table III-1. Instantaneous NF fouling profiles with varying pretreatment types are compared in Figure III-2.

Table III-1. Comparison of DOC concentrations and steady-state NF fluxes for various pretreatments.

Pretreatment	Feed water (mg/L)	Permeate water (mg/L)	Steady state normalized specific flux (%)
MF only	5.99 ± 0.60	0.66 ± 0.04	51
Electrocoagulation-MF	3.58 ± 0.36	0.77 ± 0.09	72
Chemical coagulation-MF	3.82 ± 0.53	0.54 ± 0.07	77
Electroflotation-MF	3.55 ± 0.46	0.67 ± 0.07	88

As expected, the highest feed water DOC concentration (6 mg/L) and lowest steady-state NF flux (49% decline) was measured following pretreatment with MF only. Similar to other reports, the flux rapidly declined initially before reaching steady-state e.g. [167]. As seen in Figure III-2, any type of coagulation – MF pretreatment improved steady-state NF fluxes compared with pretreatment with MF alone, which is attributed to correspondingly lower DOC concentrations in the NF feed water (see Table III-1). Importantly, even though NF feed water DOC concentrations following any coagulation-MF pretreatment were similar (average 3.65 mg/L), a consistent trend was observed over all times where fouling was best controlled by electroflotation-MF, followed by alum coagulation-MF, and electrocoagulation-MF (and MF only gave lowest fluxes). This demonstrates the inadequacy of DOC concentration alone as a measure of fouling potential as reported by others e.g. [172, 173]. Hence, the surfaces of fouled membranes and deposited foulants were characterized extensively to obtain insights into foulants that caused different flux decline profiles based on pretreatment.

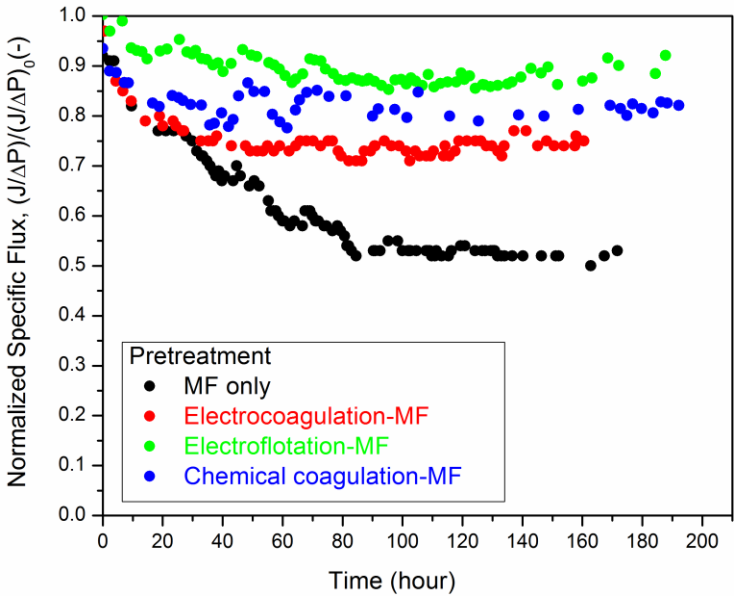

Figure III-2. Comparison of NF flux decline profiles following various pretreatments.

Characterization by ATR-FTIR

ATR-FTIR spectra of the virgin and fouled NF membranes are compared in Figure III-3 and peak assignments are summarized in Table III-2. The virgin membrane exhibited bands typical of modified semi-aromatic polyamide nanofilters [174, 175]. Only the Amide I band (1640 cm^{-1}) was observed for the virgin DL membrane and amide II (1541 cm^{-1}) and aromatic amide bands (1609 cm^{-1}) were absent [175]. Aryl-O-aryl stretching (1243 cm^{-1}), symmetric SO_2 stretching (1151 cm^{-1}), and asymmetric SO_2 stretching (1323 cm^{-1}) peaks are attributed to the polysulfone support layer arising from penetration of the incident beam below the active layers of the DL membrane. Attenuation of these peak intensities in fouled membranes provides additional evidence that they are associated with the support layer.

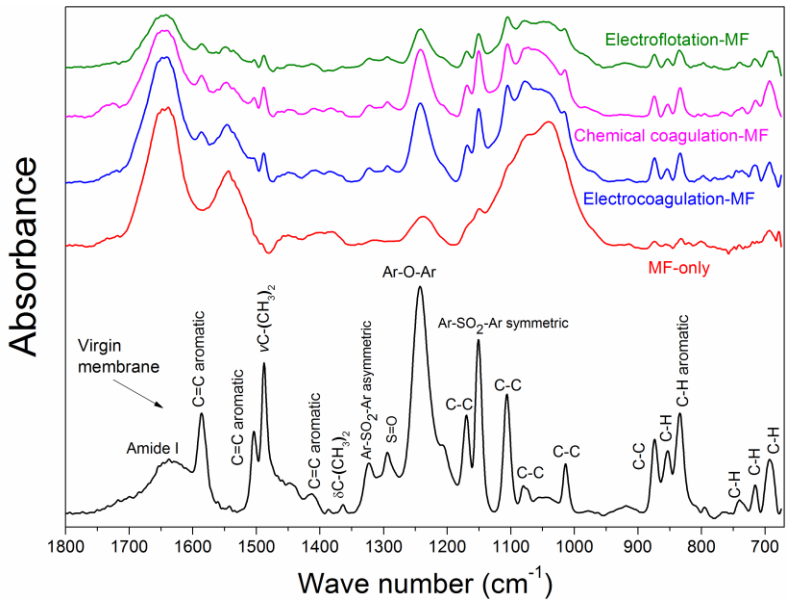

Figure III-3. ATR-FTIR spectra of virgin and fouled NF membranes.

For fouled nanofilters, bands in the region 950 – 1110 cm^{-1} were assigned to C-O-C and C-O-P vibrations, demonstrating that polysaccharides were important foulants. The peak

at 1040 cm^{-1} signifies proteins or N-acetyl amino sugars from bacterial cell walls suggesting that these polysaccharides potentially originated from bacterial extracellular polymeric substances [173]. Weak peaks in the bacterial fingerprint region 650 – 900 cm^{-1} for all the fouled membranes (possibly arising from aromatic ring vibrations of various nucleotides) also suggest the biological origin of NF foulants in our study [176]. Similar to other surface- and wastewaters, protein foulants were also identified by the presence of amide I (1700-1600 cm^{-1}), II (1543-1548 cm^{-1}), and III (1240-1310 cm^{-1}) bands in fouled membranes e.g. [17, 165, 166, 177]. The amide I band is mainly associated with C=O stretching of peptide linkages with contributions from C-N stretching and CCN deformation. Amide II is largely the result of in plane N-H bending and C-N stretching with small contributions from C=O stretching. Amide III is due to complex mixture of coordinate displacements [178] and *v*C-N stretching [171]. In fouled membranes, amide I peak intensities were higher than the virgin membrane and amide II peaks appeared (but were completely absent in the virgin membrane). Also, the amide II band was absent in ATR-FTIR spectra of potential NF foulants removed by MF-alone pretreatment (data not shown). Therefore, its appearance on fouled surfaces suggest that peptides with predominantly C-N and N-H stretching either were not significantly removed during pretreatment or were generated by biological activity over the duration of nanofilter operation.

In all cases, highest peak intensities were measured following MF-only pretreatment indicating increased NF foulant removal of polysaccharides and proteins during pretreatment by electro- and chemical-coagulation. For example, the broad polysaccharide peak (950 – 1200 cm^{-1}) attenuated individual C-C and Ar-SO_2-Ar stretches in the virgin membrane. However, these peaks were recovered (but with lower intensities) following (electro)coagulation – MF

signifying partial polysaccharide removal during pretreatment. Analogously, NF foulant peaks were weakest following electroflotation-MF pretreatment suggesting that this process was most efficient in foulant removal.

Table III-2. Peak assignments for FTIR spectral features of virgin and fouled membranes [173, 175, 176, 179].

	Peak (cm^{-1})	**Possible Peak Assignments**
Polysulfone support	834	In-phase out-of-plane hydrogen deformation of para-substituted phenyl groups
	875-1110	*v*C-C (C-C stretching vibrations)
	1151	Ar-SO_2-Ar stretching vibrations from polysulfone support
	1243	Ar-O-Ar stretching vibrations
	1323	Asymmetric SO_2 stretching vibration
	1365-1385	C-H symmetric deformation vibration of $>C(CH_3)_2$
	1586, 1504, 1488	Aromatic in-plane ring bend stretching vibration
Active/skin layer	1640	Amide I for virgin DL membrane
Foulant layer	650-900	*v*C-H (C-H rocking), bacterial fingerprint region, ring "breathing"
	1040	Proteins or N-acetyl amino sugar present in bacterial wall
	900-1200	*v*C-O-C, C-O dominated by the ring vibrations of polysaccharides C-O-P, P-O-P
	1240-1310	Amide III band from protein
	1543-1548	δNH bending and vC-N stretching associated with polypeptide chains in protein (Amide II bend)
	~1640	*v*C=O stretching associated with protein (Amide I band)

Protein secondary structures

Detailed information on the secondary structures of protein foulants was obtained by analyzing amide I band (1700-1600 cm^{-1}) to compare pretreatment effects on foulant conformation (Figure III-4). Table III-3 summarizes the secondary structures detected on the surfaces of fouled nanofilters obtained based on spectral analysis of model peptides and proteins of known structures [171, 176, 180]. All fouled NF membranes contained predominantly α helices and β structures in nearly equal parts suggesting similar contributions

from animal or plant tissues and bacteria [171, 176]. The decrease in intramolecular β structures from MF only to electroflotation-MF pretreatment and turns and bends and corresponding increase in random coils (left to right in Table III-3) indicates loss of proteins' 3-dimensional structural stability and adoption of unordered structures. Progressively increasing fraction of random coils from MF-only to electroflotation-MF pretreatment suggests coagulation-induced denaturation of protein foulants. Coagulation also decreased α helices and increased 3_{10}–helix indicating a possible shift from carbonyl oxygen-to-amide hydrogen bonds between residues i and i+4 (α helices) to residues i and i+3 (3_{10}–helix) [181].

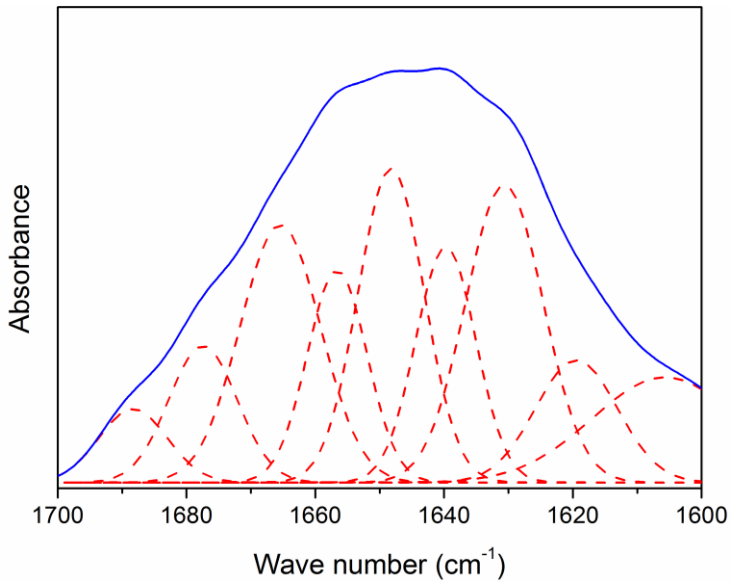

Figure III-4. Representative second derivative spectrum of the NF membrane surface with chemical coagulation pretreatment. The curve fitted amide I peak is also shown.

Table III-3. Secondary structure peak assignments for amide I band and the percentage area of each peak for NF foulants with different pretreatments.

Wave number (cm^{-1})	Secondary Structures	MF only (%)	Electrocoagulation-MF (%)	Chemical coagulation-MF (%)	Electroflotation-MF (%)
1600-1610	Amino acid side chain	4.9	6.8	8.5	10.1
1610-1625	Intermolecular β structure	7.9	7.7	7.9	13.4
1630-1640	Intramolecular β structure (β sheet)	22.3	17.8	11.2	5.8
1640-1650	Unordered structure/random coil	5.6	8.2	16.4	17.4
1650-1660	α helices	27.4	20.1	10.0	11.3
1659-1666	3_{10} – helix	0.0	18.5	16.4	11.8
1660-1680	Higher frequency of β structure	3.7	4.1	7.4	17.4
1663, 1680-1690	Turns and bends	28.2	16.9	22.2	12.9

Foulant characterization by XPS

Survey and high resolution scans of virgin and fouled membranes are summarized in. Table III-4. O/C and N/C ratios generally increased with any kind of coagulation pretreatment compared with MF-alone consistent with greater DOC removal (as shown earlier in Table III-1). High resolution scans were obtained to analyze amide functionalities and polysaccharides and compare with FTIR spectra. The C1s peak was resolved into four components (Figure III-5): (1) a peak at 284.8 eV due to C-(C,H) from lipids or amino acid side chains, (2) a peak at 286 eV attributed to C-(O,N, OH) associated with alcohol, ether, or amine, (3) a peak at 287.8 eV from C=O, or N-C=O as in carboxylate, carbonyl, amide, acetal, or hemiacetal, and (4) a weak peak at 288.9 eV arising from O=C-OH and O=C-OR, commonly found in carboxyl or ester groups. In all cases, higher percentages of the 286, 287.8, and 288.9 eV C1s peak were measured for fouled membranes compared with the virgin membrane consistent with the presence of protein and acidic polysaccharides in the foulant layer as reported earlier via FTIR. Partial removal of protein and carbohydrates by any type of coagulation is manifested as lower percentages of the same peaks (and correspondingly higher 284.8 eV peak) compared with MF-only pretreatment. Substantial contributions from C-(O,N), C=O, and HO-C=O in Table III-4 is consistent with FTIR finding that polysaccharides and amide I and amide II conformations of proteins contributed to NF fouling.

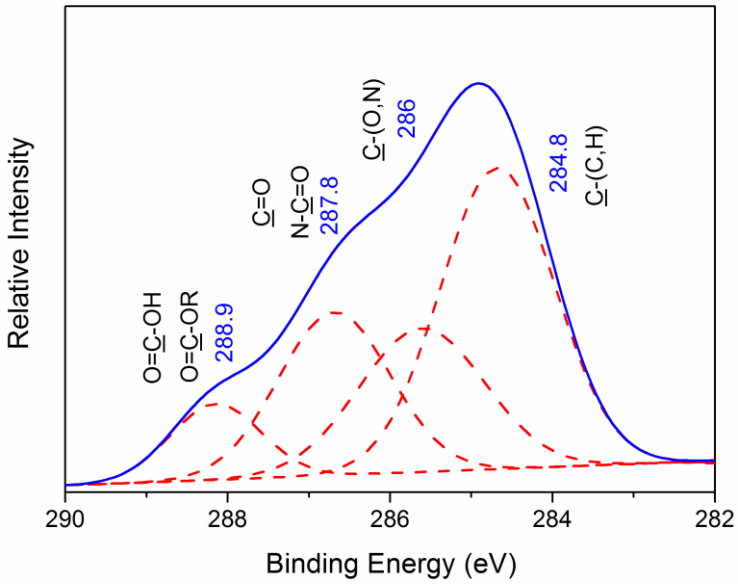

Figure III-5. Representative high resolution scan of C1s region of a fouled NF membrane following pretreatment by chemical coagulation – MF.

Table III-4. XPS survey and high resolution scans for virgin and fouled NF membranes.

NF pretreatment	Survey scans		High resolution scans of the C1s peak			
	O/C	N/C	284.8 eV C-(C,H) (%)	286 eV C-(O,N) (%)	287.8 eV (C=O, N-C=O) (%)	288.9 eV (O=C-OH, O=C-OR) (%)
Virgin (no pretreatment)	0.28	0.16	56.1	18.4	18.0	7.5
MF only	0.37	0.07	31.5	32.6	25.6	10.4
Electrocoagulation-MF	0.39	0.07	39.0	28.6	24.2	8.2
Chemical coagulation-MF	0.37	0.09	44.2	23.5	24.1	8.2
Electroflotation-MF	0.41	0.08	54.8	19.9	17.4	7.9

Alcian blue staining to detect the presence of acidic polysaccharides

Further evidence for polysaccharide fouling was obtained by colorimetry. Apparent bright blue to green spots or islands were observed in all fouled membranes following Alcian Blue staining indicating that acidic polysaccharides contributed to fouling. It was observed that the polysaccharides generally accumulated near the vertices of the feed spacer (dead zone). One potential source of these foulants are transparent exopolymeric particles of biological

origin especially since MF alone is not effective in their removal [182, 183]. Positive stains in all pretreated nanofilters also indicate the ineffectiveness of coagulation to remove these foulants.

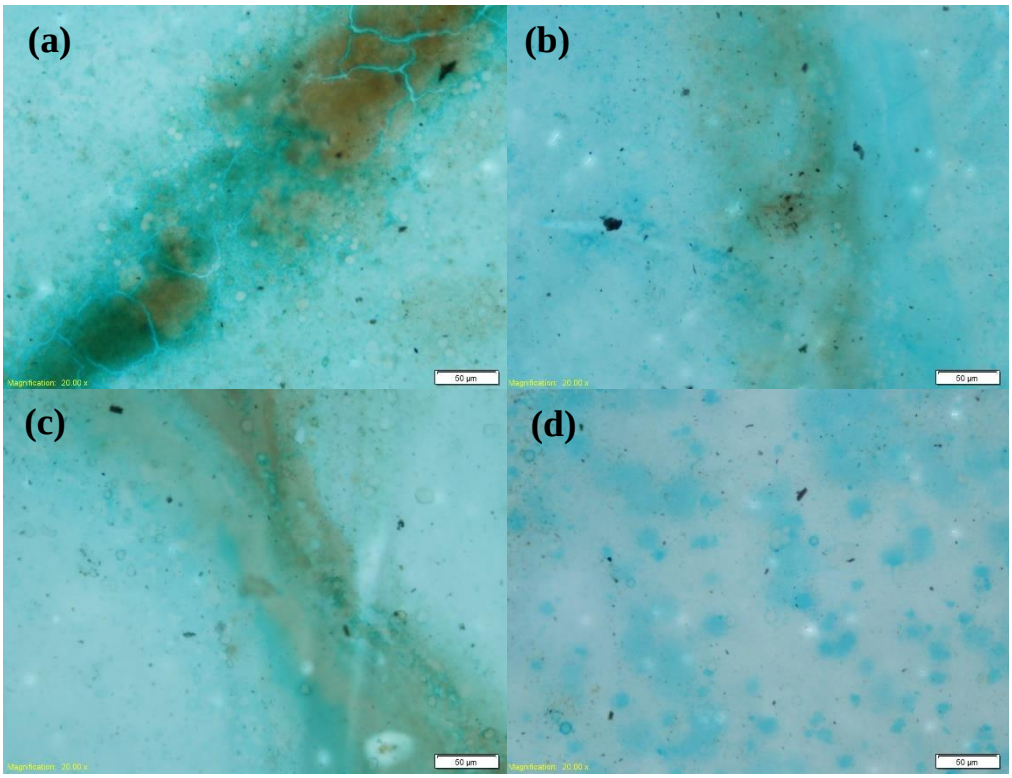

Figure III-6. Images of NF membrane surfaces after Alcian Blue staining following various pretreatment processes showing the presence of transparent exopolymeric particles. Top left (MF-alone), top right (electrocoagulation-MF), bottom left (alum coagulation-MF), and bottom right (electroflotation-MF).

Hydrophobicity

Contact angles of fouled NF membranes (62 ± 3.7°) were very similar to each other and the virgin membrane (61 ± 1.1°) as depicted in Figure III-7. Hence, fouling and pretreatment type did not have significant effects on nanofilter wettability. Similar results have been reported for other nano- and ultrafilters with virgin membrane contact angles in the range 40 – 60 degrees fouled by hydrophilic components of NOM [173, 177]. Therefore, it appears

that predominant foulants in our experiments were also hydrophilic neutrals such as polysaccharides and amides identified earlier by spectroscopy (§3.2 and 3.3). This is consistent with preferential removal of high molecular weight hydrophobic components by coagulation pretreatment. Additionally, the contact angle of the raw water colloids removed by MF alone as a cake layer was measured to be significantly higher (73 ± 0.9°) indicating preferential removal of hydrophobic NOM by MF-alone. Hence, the pretreatment alternatives evaluated appear to have removed more of the hydrophobic components in the raw water thereby relatively enhancing the hydrophilic fraction of NOM in the NF feed water.

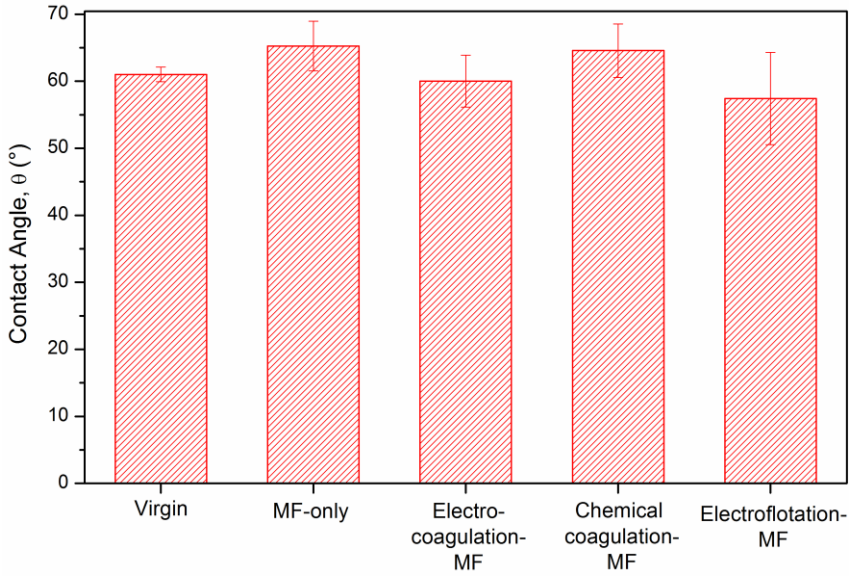

Figure III-7. Contact angles for the virgin and fouled NF membranes.

Surface topography by AFM

3-D AFM images of virgin and a representative fouled membrane (after chemical coagulation – MF pretreatment) and corresponding roughness values are given in Figure III-8 and Table III-5 respectively. The DL membrane exhibited the typical "peak and valley"

network characteristic of all polyamide membranes and the roughness was 49 nm similar to previously reported values [184]. Foulant deposition changed the surface morphology (see Figure III-8) and only slightly increased the RMS roughness for all pretreatments. This is attributed to the relatively low divalent cation concentrations (total hardness of 67 mg/L as $CaCO_3$) in the feed water which lowered NOM complexation resulting in thinner and sparser foulant deposition [185, 186]. The efficient removal of larger molecular weight (more bulky) hydrophobic compounds by all pretreatments evaluated resulted in statistically similar surface roughness values (at 95% confidence) for all fouled nanofilters.

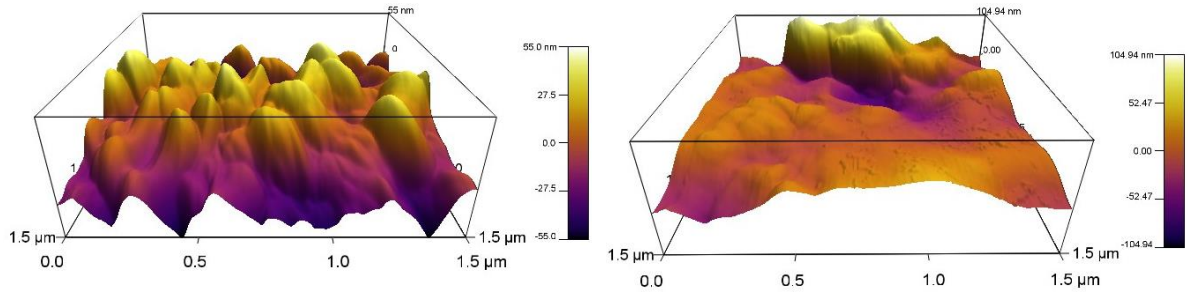

Figure III-8. Surface topography of NF membranes. The virgin membrane is shown on the left and fouled membrane after chemical coagulation – MF pretreatment is shown on the right.

Table III-5. Root mean square (RMS) roughness values for virgin and fouled NF membranes.

NF pretreatment	RMS (nm)
Virgin (no filtration)	49 ± 1.11
MF only	77 ± 11.51
Electrocoagulation-MF	76 ± 8.30
Chemical coagulation-MF	61 ± 1.55
Electroflotation-MF	60 ± 7.99

Conclusions

Electroflotation – MF was empirically shown to more effectively control NF fouling

compared with electrocoagulation – MF, alum coagulation – MF, or MF-alone in integrated membrane systems during surface water NF. ATR-FTIR and XPS spectral analyses revealed that polysaccharides and proteins are the predominant NF foulants following advanced pretreatment of Lake Houston water. Importantly, the hydrophilic fraction of NOM was poorly removed by (electro)chemical coagulation – MF making it the major NF foulant. Additional evidence for this was provided by Alcian Blue staining, which revealed the presence of acidic polysaccharides (e.g. transparent exopolymeric particles) on nanofilter surfaces. Negligible changes in the contact angle between virgin and fouled membranes also suggest the major role of hydrophilic NOM components in causing decline in nanofilter productivity under our experimental conditions. Low divalent cation concentrations in feed water coupled with removal of hydrophobic components during pretreatment resulted in only small increases in surface roughness upon fouling.

NF fouling in dual membrane systems is a complex combination of NOM and small particles (sometimes termed “nanocolloids”) that penetrate pretreatment processes [165, 187, 188]. The small colloidal foulants not removed by MF pretreatment are more likely to reside in the “valleys” of the DL membrane surface (observed by AFM) which subsequently decreased the flux [184]. Even though DOC concentrations in the feed water were similar for all (electro)coagulated waters, weaker FTIR peaks suggest improved foulant removal by EF-MF. Therefore, better NF fouling control by electroflotation – MF pretreatment is attributed to its ability to better remove colloids and some of the hydrophilic components of NOM [24].

CHAPTER IV

RELATIVE CONTRIBUTIONS OF ORGANIC AND INORGANIC FOULING DURING NANOFILTRATION OF INLAND BRACKISH SURFACE WATER *

Introduction

Persistent drought conditions, deteriorating quality of water supplies, and diminishing groundwater resources have accentuated our reliance on low quality surface waters [189]. Climate change and population growth further deplete our "freshwater" sources, necessitating the exploitation of impaired (e.g. high salinity) surface waters to meet our drinking water demands [6, 190]. Inland brackish water from rivers and lakes is already being desalinated by reverse osmosis (RO) [191-194]. However, energy costs can be reduced while continuing to meet drinking water standards by implementing nanofiltration (NF) instead of RO when divalent ions are dominant. Extended drought conditions has increased the total dissolved solids (TDS) concentration of many inland lakes in West-Central United States largely by sulfate and calcium [195, 196] suggesting the applicability of NF for cost-effective and facile desalination. However, to our knowledge, only very few reports of NF of high TDS inland surface waters are available to date and consequently our knowledge of nanofilter fouling during such applications is incomplete.

Natural organic matter (NOM) by itself has been shown to be an important foulant during NF of low-salinity surface water [5, 17, 177]. Using synthetic salt solutions, gypsum scaling has also been shown to determine RO flux decline in the absence of NOM [10, 197].

*Reprinted with permission from "Relative contributions of organic and inorganic fouling during nanofiltration of inland brackish surface water", M.A. Sari and S. Chellam, 2017, Journal of Membrane Science, 523, 68-76, Copyright 2017 by Elsevier.

Moreover, it has been recently reported that gypsum precipitation is enhanced in the presence of organic matter [198, 199] or a preformed biofilm [200, 201] thereby exacerbating fouling. Similar observations have also been reported during forward osmosis where precipitation of sparingly soluble salts and organic matter synergistically combine to worsen fouling compared to experiments with individual foulants [202]. It is emphasized that most of these previous investigations of combined NOM and gypsum fouling of desalination membranes have been performed using model/synthetic waters [10, 197-199, 202]. Therefore, more efforts are needed to identify the relative importance of NOM and mineral scaling during NF of natural brackish surface water.

A closely related issue is that RO flux decline during surface water desalination is typically caused by a combination of organic fouling and inorganic scaling since both ions and NOM are both very highly rejected by RO [192-194, 203]. In contrast, all NF membranes remove NOM and divalent ions to a very high extent but they reject monovalent ions to varying degrees [204, 205]. Hence, concentration polarization and relative importance of organic fouling versus mineral scaling can be strongly membrane-dependent as determined by ion rejection characteristics of individual nanofilters. This interplay between product water quality (ion passage) and fouling also needs to be investigated more thoroughly.

The principal objective of this research is to assess the relative contributions of mineral scaling and NOM fouling during NF of saline lake water. Experiments were performed with two commercially available nanofilters to investigate whether gypsum precipitation or organic fouling would be the dominant fouling mechanism based on differences in mono- and divalent ion rejection. Foss Reservoir, a brackish source in West-Central Oklahoma with sulfate and calcium as the major ions was chosen as a model inland surface water. Control experiments

were also performed with synthetic water formulated to match the ionic composition of Foss Reservoir but with no added NOM. Surfaces of fouled and virgin membranes were extensively characterized with X-ray photoelectron spectroscopy (XPS) and Fourier transform infra-red (FTIR) spectroscopy to evaluate specific inorganic and organic foulants.

Materials and methods

Source water

A water sample was taken from the Foss Reservoir in West-Central Oklahoma in September 2014 and stored at 4 °C as soon as it was brought to the laboratory. Several water quality parameters were monitored after bringing samples to room temperature and pre-filtration using a 0.45 μm syringe filter over the duration of experimentation. The pH and conductivity were measured using probes; alkalinity and calcium and total hardness were measured by titration; TDS was measured gravimetrically after complete evaporation at 60 °C. Dissolved organic carbon (DOC) and UV_{254} were quantified instrumentally (Shimadzu 5050 and HACH DR4000 respectively). Major cations (Ca, Mg, K, Na, Al, Fe) were measured by inductively coupled plasma – mass spectrometry (ICP-MS). Ion chromatography showed that sulfate, chloride, and bicarbonate were the major anions and phosphate, nitrate, ammonia, fluoride, and bromide were < 0.01 mg/L. Turbidity was measured using a ratio turbidimeter (HACH 2100N).

As shown in Table IV-1, the source water was slightly alkaline, hard (high in calcium), well-buffered, and high in conductivity and TDS. Sulfate was the major anion accounting for 60% of TDS. Although the turbidity was low, it had moderate amounts of NOM. Its low specific UV absorbance (SUVA, the ratio of UV_{254} in m^{-1} and DOC concentration in mg/L)

value of 1.12 ± 0.023 m·L/mg indicated that non-humic, highly hydrophilic, and low molecular weight compounds were dominant [133, 206]. Fractionation using Supelite DAX-8 resin (Sigma Aldrich) showed that the NOM was 76% hydrophilic and 24% hydrophobic, consistent with its low SUVA value. The charge balance discrepancy was only 1.9% demonstrating the accuracy of our ion measurements.

Table IV-1. Composition of Foss Reservoir water.

Parameter	Unit	Value
pH	-	7.86 ± 0.13
Turbidity	NTU	9.24 ± 1.88
DOC	mg/L	8.02 ± 0.32
UV_{254}	cm^{-1}	0.101 ± 0.008
Conductivity	µS/cm	2852 ± 192
TDS	mg/L	2911 ± 33.5
Alkalinity	mg/L as $CaCO_3$	93.9 ± 7.63
Ca Hardness	mg/L as $CaCO_3$	697 ± 57
Total Hardness	mg/L as $CaCO_3$	1671 ± 124
Silicon	mg/L	14.0 ± 0.2
Chloride	mg/L	90.2 ± 0.28
Sulfate	mg/L	1,757 ± 1.4
Bicarbonate*	mg/L	114.5 ± 9.3
Sodium	mg/L	180.5 ± 3.7
Calcium	mg/L	281.5 ± 6
Magnesium	mg/L	238.1 ± 9.8
Potassium	mg/L	12.8 ± 0.5
Strontium	mg/L	6.4 ± 0.1
Aluminum	mg/L	0.2 ± 0.002
Iron	mg/L	0.7 ± 0.006
Gypsum saturation index	-	*0.51*
Langlier saturation index	-	*0.44*

*Bicarbonate concentration is calculated based on the alkalinity, i.e. mg/L alkalinity as HCO_3 = 1.22 x mg/L total alkalinity as $CaCO_3$, assuming most of the alkalinity is due to bicarbonate.

Model solution

In order to operationally separate inorganic and organic fouling, baseline NF experiments were performed with a synthetic solution having similar ionic composition and pH to the Foss Reservoir water except it had no organic matter (Table IV-2).

Table IV-2. Composition of model scaling solution.

Salt	Concentration (mg/L)
Na_2SO_4	439.4
$MgSO_4$	1213.1
$CaCO_3$	180.0
$CaSO_4$	698.5
NaCl	43.5
HCl	65.6

Microfiltration

Foss Reservoir water was treated by constant pressure, unstirred dead-end microfiltration (MF) using 0.22 μm modified PVDF membranes (GVWP04700, Millipore) prior to NF. MF was performed using a 300 mL stainless steel cell (SEPA ST, Osmonics) with 16.9 cm^2 effective filtration area. The system was pressurized by compressed air and the feed pressure was maintained at 20 psig using a precision regulator (PRG101-60, Omega). Approximately 8 L of MF permeate (i.e. pretreated Foss Reservoir water) was collected to perform NF.

Nanofiltration

Two membranes, NF270 and NF90 were selected based on manufacturer (Dow Chemical) recommendations and literature data. As summarized in Table IV-3, NF90 is less permeable to both water and monovalent salts compared with NF270. Measurements with

natural water from Foss Reservoir showed that both membranes highly rejected sulfate (>99.5%) attributed to anion repulsion since both membranes are negatively charged at the operating pH of 7.8 [207, 208]. NF90 better removed mono- and divalent cations compared with NF270; with observed rejections of 99.8% and 91.8% for calcium, 99.9% and 94.2% for magnesium, and 97.4% and 60.0% for sodium, respectively from Foss Reservoir water. Also, the surface of the NF90 membrane is more hydrophobic, more negatively charged, and rougher than NF270.

NF was performed using a stainless steel cell (SEPA-CF, Osmonics) fitted with feed and permeate spacers and a 139 cm^2 flat membrane sheet. The channel width, length, and height were 9.5 cm, 14.6 cm, and 0.086 cm, respectively with spacer-filled effective cross sectional area of 0.70 cm^2. A cooling water recirculator (RTE-111 Neslab) maintained the feed water temperature at 23 ± 0.4 °C during the entire course of filtration. The feed water was delivered by a positive displacement gear pump (head model GB series P.23 and drive model DP-415A.A Micropump) at 480 mL/min corresponding to the desired cross flow velocity of 11 cm/s. The transmembrane pressure was adjusted by using high precision needle valve (Cole Parmer) installed in the retentate side. A digital flow sensor (LS32-1500, Sensirion) was installed in the permeate side to monitor the flux. The system was operated in batch recycle mode by continuously returning permeate and concentrate flows to the feed tank except during sampling. Pressure and temperature were monitored using analog transducers (PX603 and TJ120-CPSS-116G respectively, Omega).

Table IV-3. Characteristics of the NF270 and NF90 membranes [a]

Membrane	Pure water permeability ($L/m^2.h.bar$)	MWCO (Da)	Contact angle (°)	Zeta potential at pH 7 (mV)	RMS roughness (nm)	NaCl rejection[b] (%)	$MgSO_4$ rejection[b] (%)	Ca^{+2} rejection[c] (%)	Na^{+} rejection[c] (%)	Mg^{+2} rejection[c] (%)	SO_4^{-2} rejection[c] (%)
NF270	8.5 – 13.5	300	27 - 55	-19	5 – 9	40	>97	91.8	60.0	94.2	99.6
NF90	5.2 – 8.4	200	54 - 63	-30	70 – 129	85	>97	99.8	97.4	99.9	99.9

[a] from references [167, 209-216], this work, and manufacturer's specification.
[b] NaCl and MgSO4 rejections reported by manufacturer using single salt solutions at 70 psig.
[c] Ca, Na, and SO_4^{-2} rejections measured in this work for natural water sample from Foss Reservoir at an operating flux of 43 L/m^2h.

Membrane coupons were first thoroughly rinsed with nanopure water before placing them in the filtration cell. Next, nanopure water was passed through the system at high cross flow velocity and low pressure for 1 h during which time both the permeate and retentate were disposed to remove any impurities that may be present. Then a Na_2SO_4 solution having a similar salinity to that of Foss Reservoir water (2 g/L) was passed through the system at 11 cm/s cross flow velocity and permeate flux of 48 L/m^2h to set the membrane and achieve a pseudo steady-state flux. Pretreated (i.e. microfiltered) Foss Reservoir water or the model solution was nanofiltered for ~ 1 week duration at the same hydrodynamic conditions, i.e. 43 L/m^2.h initial permeate flux (70 psig for NF270 and 110 psig for NF90) and 11 cm/s cross flow velocity to accurately compare fouling of both membranes.

Spectroscopy

At the conclusion of NF, the membrane was cut into smaller pieces and dried in a vacuum desiccator for 24 h. Coupons were harvested from four to five different locations to obtain representative information on dominant foulants. The infrared spectra was collected using Nicolet iS10 spectrometer equipped with mid infrared Ever-Glo source, DTGS detector, KBr beam splitter and Omnic 9.0 Software. A diamond iTX accessory was also installed to allow sampling in ATR mode. A background spectrum was also collected on a clean ATR window prior to each analysis. Approximately 0.5 cm^2 membrane samples were then placed on the window and IR spectrum was obtained by averaging 128 scans collected at 4 cm^{-1} resolution over 650 – 4000 cm^{-1}.

Detailed information on the elemental composition and functionalities of the surfaces of virgin and fouled membranes was also obtained with a PHI 5700 X-ray photoelectron spectrometer equipped with a monochromatic Al Kα X-ray source (hν = 1486.7 eV) incident

at 90° relative to the axis of a hemispherical energy analyzer. A neutralizer was used to reduce charging problems due to the non-conducting nature of polymeric membranes. Survey spectra were obtained over the entire range of binding energies (0-1400 eV) based on which high-resolution elemental spectra were targeted; C 1s and O1s regions for NF270 and C 1s, O 1s, Ca 2p and S 2p for NF90. Electron binding energies were calibrated with respect to the C 1s line at 285 eV corresponding to adventitious carbon. After integrated baseline background subtraction with Shirley routine, peak areas for C 1s, O1s, Ca 2p, and S 2p regions were obtained assuming mixed Gaussian-Lorentzian shapes and correcting for sensitivity factors.

Results and discussion

Differences in NF90 and NF270 fouling

The normalized specific flux for both membranes, accounting for the osmotic pressure (i.e. net driving force) is depicted in Figure IV-1. Two major observations can be made from these fouling profiles: (i) for each feed water NF90 fouled more than NF270 and (ii) microfiltered Foss Reservoir water fouled both membranes to a greater extent than the model solution. Our results are consistent with earlier reports that NF90 is more prone to fouling than NF270 [211, 214].

Figure IV-1 shows that NF90 water permeability declined by 20% over the entire duration (7-days) of model solution filtration suggesting inorganic fouling of the highly salt rejecting membrane. Precipitates resembling gypsum crystals [197, 217, 218] were observed especially around the edges of the membrane and close to the brine exit (top left panel in Figure IV-2). The ATR-FTIR spectrum of these crystals is indicative (top right panel in Figure IV-2) of gypsum [219] including a strong doublet at 600 and 665 cm^{-1} corresponding to asymmetric

bending vibrations of SO_4^{-2}. A weak peak at 1003 cm^{-1} due to symmetric stretching vibrations of sulfates can also be seen. The strong peak at 1105 cm^{-1} with a shoulder (1140 cm^{-1}) is typical of asymmetric sulfate stretching. Water bending vibrations around 1619 cm^{-1} and 1682 cm^{-1} and symmetric and asymmetric stretching (3398 cm^{-1} and 3529 cm^{-1}) of water found in pure gypsum were also observed [220, 221]. Hence, gypsum scaling is the dominant cause of NF90 fouling with the model solution.

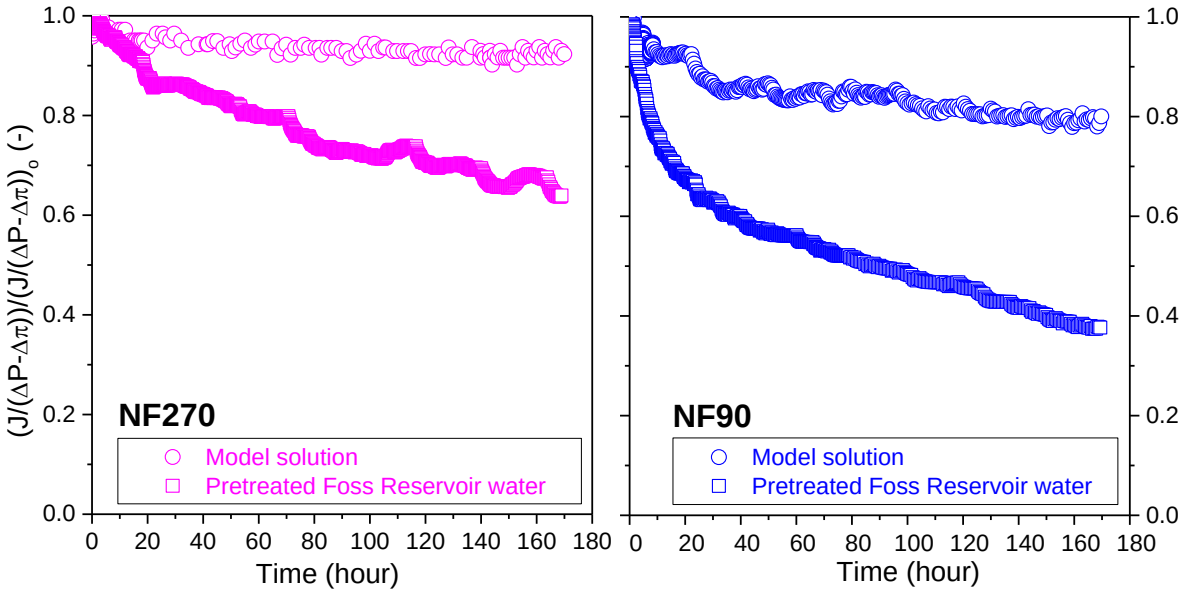

Figure IV-1. Flux decline profiles for NF270 (left) and NF90 (right) for model solution and Foss Reservoir water.

The overall concentration polarization was estimated using film-theory [222] with mass transfer coefficients correlations for a spacer-filled channel [223] which resulted in an average gypsum saturation index below unity for both membranes. However, microenvironments with localized high degrees of supersaturation have been shown to exist in regions of high recirculation [224]. As described in the previous paragraph, gypsum crystals were observed largely near the cell edges and brine exit only of NF90 suggesting a higher driving force for

precipitation attributed to its higher rejection of both mono- and divalent cations (see Table IV-3) [225]. In contrast, NF270 water permeability declined only by 7% over the entire duration of model solution filtration and no precipitates were visually observed, suggesting negligible inorganic fouling over the timeframe of experimentation. Mass transfer calculations coupled with observed rejections revealed a higher ionic strength in the concentration polarization layer of the "tighter" membrane (NF90) compared with the "looser" membrane (NF270).

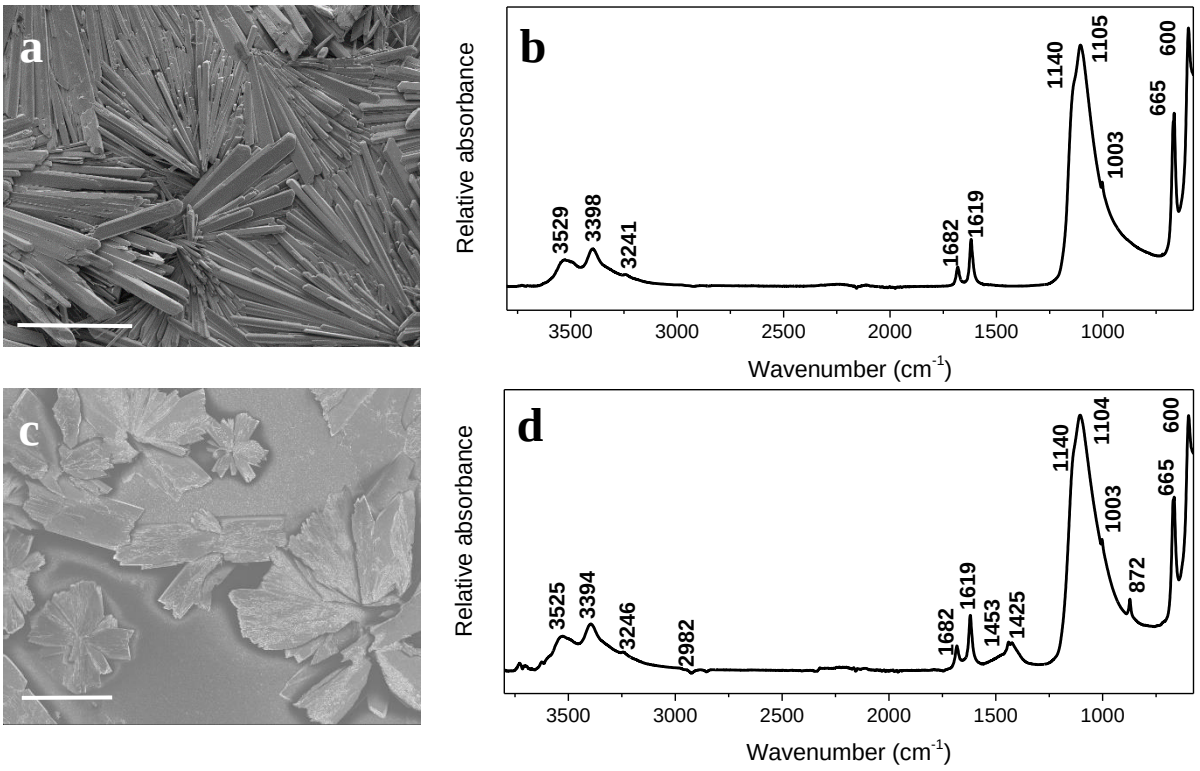

Figure IV-2. Electron micrographs of gypsum precipitated on NF90 membranes during filtration of model solution and pretreated Foss Reservoir water (panels a and c). The scale bars in panels (a) and (c) represent 200 µm. Corresponding ATR-FTIR spectra are shown in panels (c) and (d) for precipitates formed on the NF90 membrane for the model solution and pretreated Foss Reservoir water respectively.

Also, as shown in Figure IV-1, Foss Reservoir water significantly increased fouling

compared with the model ionic solution, reducing the permeability of NF270 by 35% and NF90 by 62% after 7-days. The increased fouling was primarily attributed to NOM (along with any nanocolloids that escaped MF) in pretreated natural water since the ionic composition of both feed waters were matched. For both NF270 and NF90, organic fouling induced by the NOM in Foss Reservoir would have been exacerbated by the high calcium concentrations due to NOM-Ca interactions.

Importantly, Figure IV-1 shows that Foss Reservoir fouled NF90 to a significantly greater extent than NF270. The higher degree of concentration polarization in NF90 discussed earlier increased the local solubility index on the membrane surface leading to gypsum precipitation but not NF270 (bottom left panel of Figure IV-2). Hence, similar to the model solution, inorganic scaling worsened NF90 fouling compared with NF270. The corresponding IR spectrum of the crystals (bottom right panel of Figure IV-2) show all the gypsum signals described earlier for the model solution. In addition, signals corresponding to trace amounts of NOM or carbonates such as peaks at 872 cm^{-1} (δC-H or δC-O), 1425 cm^{-1} (νN-CH3, δC-H), 1453 (νC-O), and 2982 cm^{-1} (νC-H aliphatic) were observed. Simultaneously, the ionic strength near the NF90 membrane surface was higher than NF270, leading to a coiled and compact conformation of NOM in its concentration polarization layer, which has been shown to exacerbate organic fouling [186, 226, 227]. Further, the surface of the virgin NF90 membrane appeared considerably rougher than NF270, which was quantified by atomic force microscopy. The root mean squared surface roughness of virgin NF90 and NF270 were measured to be 71 ± 6 nm and 5 ± 1 nm respectively, which are in the range reported in the literature [214, 216] and confirm that NF270 has a significantly smoother surface. Organic matter and nanocolloids can be expected to preferentially deposit and clog the valleys of the rougher surface of NF90

worsening fouling [210, 228]. As expected from these arguments, a considerably thicker cake was visualized by scanning electron microscopy for NF90 compared with NF270 (Figure IV-3).

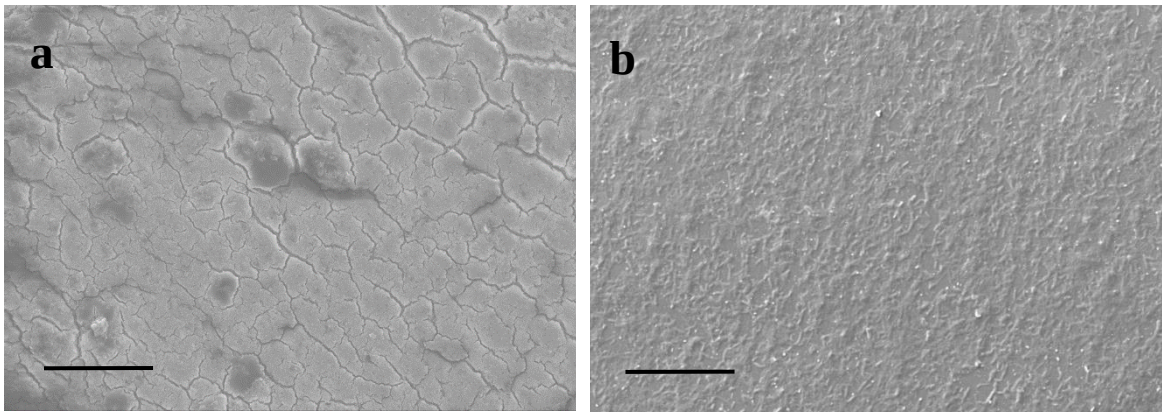

Figure IV-3. Electron micrographs of the fouled NF 90 (panel a) and NF 270 (panel b) membranes after 7-days of filtering pretreated Foss Reservoir water. Scale bars represent 40 µm.

ATR-FTIR spectra of NF90 and NF270 membrane surfaces

Additional information on foulants were obtained by collecting ATR-FTIR spectra of membranes before and after filtration of the model solution and Foss Reservoir water as shown in Figure IV-4.

Virgin membranes

Both virgin membranes exhibited bands typical of the polysulfone support layer in thin film composite (TFC) polyamide membranes [229, 230] such as (i) sharp and prominent peaks at 1151, 1243, and 1323 cm^{-1} corresponding respectively to Ar-SO_2-Ar, Ar-O-Ar, and asymmetric SO_2 stretching vibrations and (ii) C=C aromatic in-plane ring bend stretching vibrations at 1586, 1504, and 1488 cm^{-1}. Even though the active layer of both NF270 and NF90 are based on polyamide chemistry, the different synthesis method employed for their manufacture affects their surface chemistry and separation characteristics. The fully aromatic

polyamide NF90 membrane exhibited three unique peaks at (i) 1663 cm^{-1} corresponding to *v*C=O, *v*C-N, and C-C-N deformation vibration in a secondary amide group (Amide I), (ii) 1609 cm^{-1} attributed to aromatic amide, and (iii) 1542 cm^{-1} assigned to amide II band (δN-H + *v*C-N). In contrast, the amide II band and aromatic amide peaks were absent in the semi-aromatic poly(piperazinamide) NF270 membrane. As reported earlier [231], the amide I band was observed at lower wave number (1626 cm^{-1}) for the semi-aromatic NF 270 membrane compared with the fully aromatic NF 90 membrane (1663 cm^{-1}).

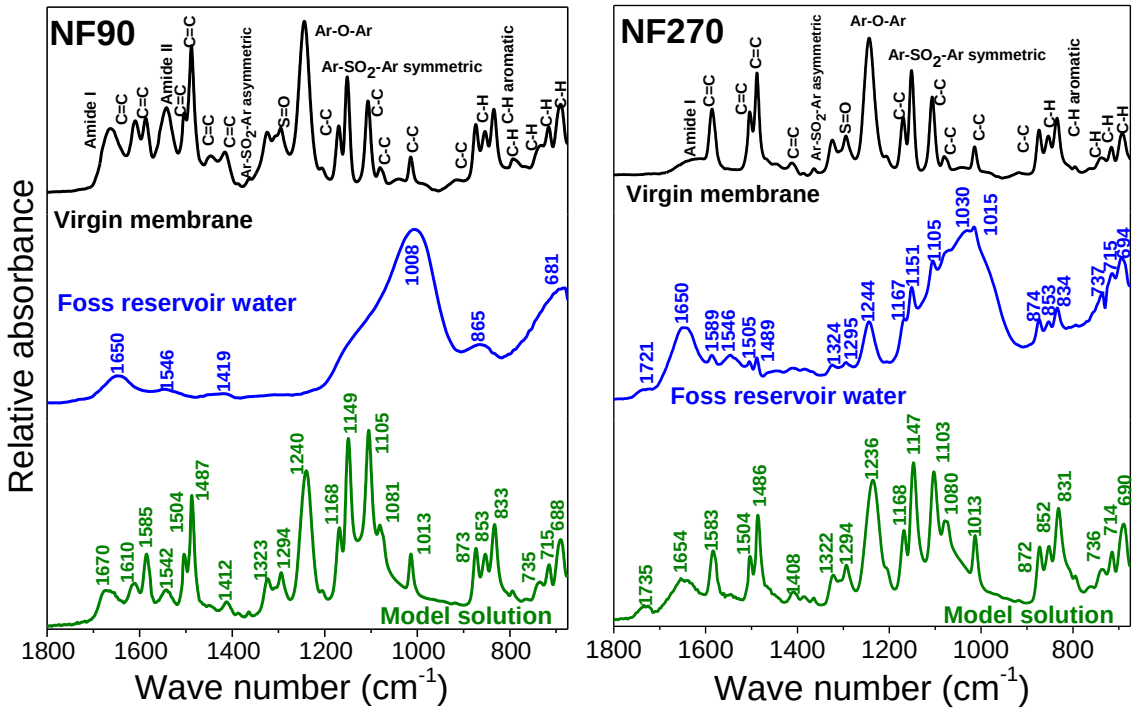

Figure IV-4. ATR-FTIR spectra of virgin and fouled membranes after filtration of model solution and pretreated natural water for 7-days. The panel on the left represents NF90 and the one on the right represents NF270. The top spectrum (shown in black) represents the virgin membrane. The spectrum in the middle (shown in blue) represents the surface of the membrane fouled by Foss reservoir water. The bottom spectrum (shown in green) represents the surface of the membrane fouled by the synthetic water that did not contain NOM.

Membranes after filtering the model solution

Even after 7-days of filtering the model solution, many of the virgin membrane peaks were still clearly visible suggesting that only a thin foulant layer was formed. Since the model solution did not contain nitrogenous compounds, amide peak intensities (1670, 1610, and 1542 cm^{-1}) on NF90 were reduced and the amide II band was still not visible in NF270. The sulfate stretching region around 1100 cm^{-1} in NF90 increased in intensity (although it overlapped with signals corresponding to virgin membrane) and the amide I peak blue-shifted to 1670 cm^{-1} from 1663 cm^{-1} as seen in virgin membrane indicated the presence of gypsum. For NF270, the intensity of the sulfate stretching region did not increase appreciably. Hence, the blue-shift of the amide I peak to from 1626 cm^{-1} to 1650 cm^{-1} and the appearance of a peak at 1735 cm^{-1} is interpreted as the presence of C=O possibly from carbonates. Hence, IR spectra did not provide any evidence of gypsum on the NF270 membrane as expected.

Filtration of pretreated Foss Reservoir water

As expected from the thick foulant layer formed on NF90 (Figure IV-3), all of its characteristic virgin membrane peaks were totally obscured after 7-days of filtering microfiltered natural water. In contrast, several peaks associated with the virgin membrane were still visible for NF270 (e.g. 1151 cm^{-1} and 1243 cm^{-1}) in accordance with its thinner cake layer. Both membranes exhibited signs of fouling by carbohydrate-like and proteinaceous compounds in Figure IV-4. The strong and broad band around 900-1000 cm^{-1} demonstrates νC-O-C and C-O ring vibrations from polysaccharides [176]. The amide I peaks on both membranes (νC=O + δC-N + δN-H) were shifted toward 1650 cm^{-1} (from 1663 and 1626 cm^{-1} for virgin NF90 and NF270 membranes, respectively), suggesting that the proteins present were of bacterial origin [232]. The amide II (δN-H + νC-N) band near 1546 cm^{-1} [166] was

visible in the foulant layer of both membranes even though it was not even present for the virgin NF270 membrane. These signals were more prominent for NF90 compared to NF270 consistent with its thicker cake and greater extent of fouling. Signals corresponding to hydrophobic fraction of NOM such as humic and fulvic acids were negligible consistent with its low concentration in the feed water or due to masking by extracellular materials [17].

Evidence of inorganic fouling can also be seen in Figure IV-4 for both membranes. The broad shoulder around 1100-1145 cm^{-1} [180] depicts the presence of both sulfate and silicon (*v*Si-O; Si-O-Si or Si-O-C) on the surface of the fouled NF90 membrane. A signal corresponding to *v*Si-O could also be seen in the same region although there were interferences from the membrane itself (e.g. at 1167, 1151, and 1105 cm^{-1}). Note that sulfate stretching was not observed on NF270 filtering model solution thereby allowing the assignment of the mentioned region to *v*Si-O for NF270 filtering natural water. Interestingly, a weak shoulder appeared at 1721 cm^{-1} only for NF270 after NF of Foss Reservoir water. Such a peak was also visible after filtering the model solution. This is attributed to O-C=O of carbonates with the membrane masking other accompanying peaks (C-O stretching mode at 1453 cm^{-1} and bending at 873 cm^{-1}). Importantly, carbonates were not seen for NF90 both after filtering the model solution and Foss Reservoir water since gypsum scaling inhibits $CaCO_3$ precipitation [10]. Hence, NF270 fouling can be attributed to NOM fouling with limited contributions from calcium carbonate whereas NF90 fouling is dominated by both gypsum and NOM.

XPS confirms FTIR results

The elemental composition of virgin and fouled membranes were also obtained to better understand fouling mechanisms. Survey scans summarized in Table IV-4 show that C, N, and O were the major constituents of the virgin membranes. Foulant deposition from the model

solution and pretreated Foss Reservoir water was manifested as reductions in relative atomic percentages of C and N with a concomitant increase in O, suggesting presence of inorganic precipitates such as carbonates and sulfates [233]. Changes in the relative C percentage were higher for NF90 compared NF270 consistent with its thicker foulant layer (Figure IV-3).

Table IV-4. Relative atomic percentage of elements of virgin and fouled membrane surfaces.

NF90	C 1s	N 1s	O 1s	Si 2p	S 2p	Ca 2p
Virgin membrane	73.5	11.7	14.7	0.0	0.1	0.0
Foss Reservoir	48.1	5.2	40.3	2.0	1.8	2.6
Model solution	62.3	2.5	30.8	0.0	1.9	2.5
NF270						
Virgin membrane	69.5	11.9	18.5	0.0	0.1	0.0
Foss Reservoir	65.0	5.6	27.9	0.9	0.0	0.6
Model solution	66.8	5.6	26.8	0.0	0.0	0.8

Ca and S were detected on the NF90 surface following filtration of the model solution and pretreated Foss Reservoir water indicating the presence of gypsum. The positions of the binding energies of Ca ($2P_{3/2}$ = 347.9 eV and $2P_{1/2}$ = 351.4 eV) and S 2p (169.3 eV) obtained via high resolution scans confirmed calcium sulfate scaling [234, 235]. In contrast, S was not detected for NF270 although Ca was seen. These are consistent with FTIR evidence of major gypsum presence on NF90 and weak $CaCO_3$ signals from NF270.

High resolution XPS scans of C1s and O1s regions were also obtained to analyze the surface functionalities of virgin and fouled membranes (Figure IV-5 and Figure IV-6). The C 1s peak in the virgin membranes was deconvoluted into three components: (i) one at 284.8 eV from C-(C,H) or C=C, (ii) a second one at 286 eV from C-(O,N, OH), and (iii) a third one at 287.8 eV from C=O, N-C=O, or C=N. The O 1s peak was resolved into two peaks one at 531.2

eV from O=C, O=C-N, C-O and another at 532.6 eV from O-C=O, H··O=C-N. This deconvolution of C 1s and O 1s peaks and their assignments is similar to earlier reports for the virgin NF270 and NF90 membranes [236].

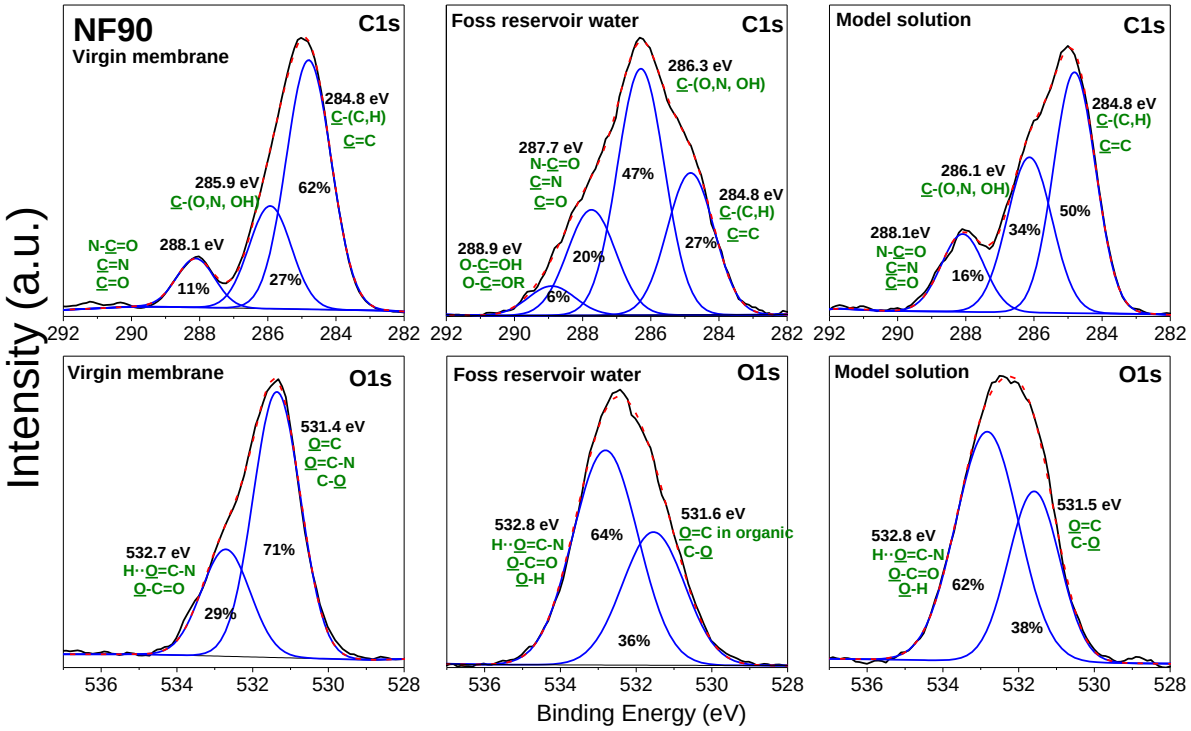

Figure IV-5. XPS High resolution scans of virgin and fouled NF90 membranes.

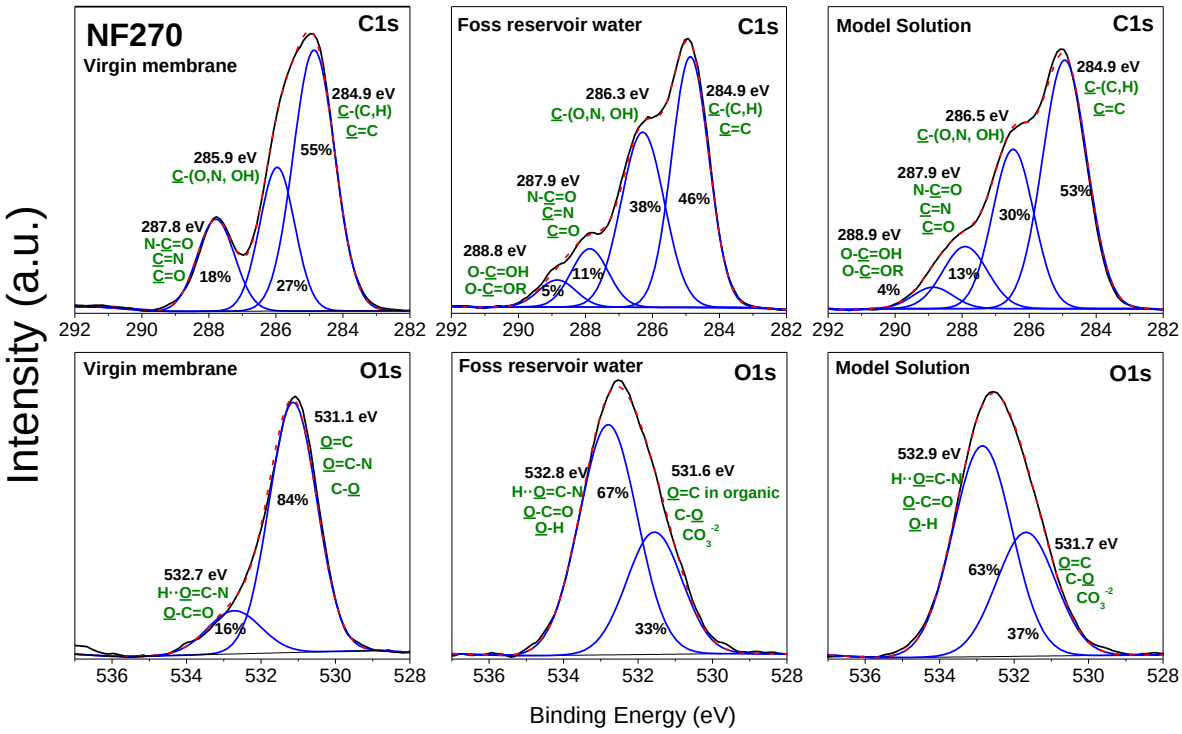

Figure IV-6. XPS High resolution scans of virgin and fouled NF270 membranes.

Similar to FTIR, foulant deposition modified virgin membrane spectral features for both NF270 and NF90. Bigger changes were observed in C 1s features for fouled NF90 compared with NF270 providing further evidence for its thicker foulant layer (see top three panels in Figure IV-5 and Figure IV-6). Fouling by organics (proteins and polysaccharides) and/or inorganics (sulfates and carbonates) for nanofiltration of Foss Reservoir water by both membranes were evidenced by: (i) intensification of the peak around 286 eV, (ii) increase in the peak near 288.1 eV, and (iii) the appearance of small peak near 288.9 eV. For the model solution, the small peak around 288.9 eV appeared only for NF270 confirming carbonate fouling for this membrane. O 1s peaks on fouled membranes changed in accordance with the C 1s peaks. For example, the peaks near 531.3 eV in virgin membranes was shifted to higher binding energy (around 531.6 eV) corresponding to C=O in organics and/or carbonates (CO_3^-

^{2}). Also, the peak near 532.6 eV shifted to slightly higher binding energies (around 532.9 eV) for both membranes along with an increase in their relative area percentages due stronger binding of foulants to the membrane surface.

Conclusions

During nanofiltration of pretreated Foss Reservoir water, a low monovalent ion rejecting membrane (NF270) was fouled predominantly by NOM with limited contributions from $CaCO_3$ whereas both NOM and gypsum contributed to fouling of a membrane that highly rejected both mono- and divalent ions (NF90). Importantly, gypsum was precipitated around the cell edges and brine exit, corresponding to regions of high recirculation, only for NF90. Hence, mineral scales appear to form in localized supersaturation regions for high salt rejecting nanofilters even when the overall solubility product is not exceeded. The prominent band around 900-1000 cm^{-1} (*v*C-O-C and C-O ring vibrations from polysaccharides) and the appearance of amide 1 (1650 cm^{-1}) and amide II (1546 cm^{-1}) bands on both membrane surfaces were evidence that carbohydrate-like and proteinaceous compounds were major foulants during NF of brackish surface water similar to low salinity surface water [5, 17, 53, 212].

The significantly greater flux decline measured for NF90 was attributed to (i) the combined synergistic effects of inorganic and organic foulants [198, 202], (ii) formation of a more compact cake layer resulting from a higher degree of NOM-Ca interactions and the high ionic strength at the membrane-feed water interface [186], and (iii) an increase in "valley clogging" by organic matter and nanocolloids due to its rough surface [210, 228]. Therefore, the relative dominance of NOM and inorganic scaling during inland brackish water desalination is not only closely related to a nanofilter's surface characteristics (e.g. roughness,

hydrophobicity, zeta potential) but also dependent on its ability to reject mono- and divalent ions. Hence, fouling will be mitigated by selecting a more salt permeable membrane (which may also be more water permeable as was in the case of the two membranes selected for this study), which would be the optimal engineering option as long as all water quality requirements are met. An important consideration that was beyond the scope of this investigation is that precipitative fouling of highly salt rejecting nanofilters could be controlled by employing antiscalants if their use is necessitated.

CHAPTER V

ELECTROCOAGULATION PROCESS CONSIDERATIONS DURING ADVANCED PRETREATMENT FOR BRACKISH INLAND SURFACE WATER DESALINATION: NANOFILTER FOULING CONTROL AND PERMEATE WATER QUALITY

Introduction

Desalination is becoming an increasingly discussed alternative in our toolkit of available treatment options to provide drinking water [237] especially in times of drought when water supplies increase in salinity [6]. To this end, a significant body of research has demonstrated the capability of reverse osmosis (RO) to desalinate seawater and brackish groundwater [194]. However, RO requires very high transmembrane pressures making it economically less attractive in many occasions. Importantly, energy costs can be significantly reduced by implementing nanofiltration (NF) [238] especially in cases when divalent ions are the dominant component of salinity as in many lakes and reservoirs in West-Central United States [195, 196]. An important impediment to NF implementation, especially during surface water treatment is fouling [5, 12, 13, 239].

Microfiltration (MF) or ultrafiltration (UF) pretreatment is necessary to mitigate colloidal fouling during surface water desalination [12, 20, 21, 240]. However, low-pressure membrane pretreatment may not be sufficient for waters with severe organic fouling potential, necessitating coagulation as an additional pretreatment step [53, 241, 242] to maintain flux. Electrocoagulation (EC) is an attractive alternative to conventional chemical coagulation especially for smaller plants given its many operational advantages including (1) portability

and modularity, (2) reduced handling of corrosive chemicals, (3) lower alkalinity consumption, and (5) ease of automation [33, 35, 243]. To date, the available investigations on membrane fouling control by EC have focused largely on MF and UF [23, 35, 84, 85, 89, 90] consequently shedding little light on its impacts on NF performance in an integrated dual-membrane system. To our knowledge, only one investigation has coupled both EC and MF as pretreatment for surface water NF [53]. This work demonstrated significantly lower NF fouling with electrochemical pretreatment compared with conventional coagulation for a non-saline "freshwater" supply. Based on this recent finding, we hypothesized that EC would be highly efficient in combating membrane fouling during desalination of high salinity surface water by MF-NF since (i) electrolysis can be performed at very high current density given the high conductivity of the source water thereby substantially reducing electrolysis time (i.e. allowing for very small and portable EC systems), and (ii) generation of a greater number of smaller-sized hydrogen bubbles at high current density [244] will facilitate natural organic matter (NOM) removal by increased hydrophobic interactions thereby reducing organic fouling.

In addition to being capable of high removals of divalent ions, NF provides an excellent barrier against disinfection by-product (DBP) precursors [12], contaminants of emerging concern [7, 8], and many other currently regulated contaminants while providing treated water with sufficiently low dissolved solids concentrations [205]. Of particular interest to this research is strontium, which is a top priority for the United States Environmental Protection Agency and categorized as Group I in its third Contaminant Candidate List (CCL3) for regulatory consideration as a primary drinking water standard [245]. Sr^{+2} occurs widely in public water systems [246] along with other divalent ions such as Ca^{+2} and Mg^{+2} but its removal during drinking water treatment is only beginning to be investigated. For example,

Sr^{+2} was recently shown to be better removed from groundwater by lime softening and NF [247, 248] than from surface water by conventional treatment processes [247]. It has also been artificially spiked to a freshwater source and shown to be very well removed by low-pressure RO [249]. To our knowledge, there are no reports of the removal of naturally occurring Sr^{+2} from saline surface water by NF.

The principal objectives of this research focusing on desalination of brackish water from the Foss Reservoir in West-Central Oklahoma, USA are to: (i) optimize EC operating parameters to maximize NOM removal and (ii) evaluate the effectiveness of coupling EC and MF pretreatment to mitigate NF fouling. We also report data on strontium removal by NF. Transient NF fouling profiles following pretreatment by EC-MF and MF-only were compared with a synthetic feed water, which was formulated to closely mimic the ionic composition of Foss Reservoir water without any added NOM to operationally establish the role of NOM on fouling. All experiments were performed at bench-scale using a commercial NF membrane (NF270, Dow), whose surfaces were characterized in detail by Fourier Transform Infrared (FTIR) Spectroscopy and X-ray Photoelectron Spectroscopy (XPS) after different pretreatments to identify dominant foulants and establish fouling mechanisms.

Materials and methods

Source water

A sample was collected in November 2015 from the Foss Reservoir in Oklahoma, USA serving as a model inland brackish surface water. The source water was slightly alkaline (pH 8.0 ± 0.2), very hard (total hardness 1620.7 ± 10.61 mg/L as $CaCO_3$ and calcium hardness 720.3 ± 3.54 mg/L as $CaCO_3$), and high in buffering capacity (alkalinity 115.8 ± 2.0 mg/L as

$CaCO_3$) and salinity (conductivity 2766 ± 235 µS/cm). Major anions were quantified by ion chromatography (IC) revealing sulfate (1623.5 ± 90 mg/L) as the dominant one with lesser amounts of chloride (174.5 ± 21 mg/L), and bicarbonate (141.2 ± 2.4 mg/L). Calcium (286.9 ± 7.7 mg/L), magnesium (218.1 ± 12.9 mg/L), sodium (199.2 ± 8.2 mg/L) were the major cations measured by inductively coupled plasma–mass spectrometry (ICP-MS) with lower concentrations of potassium (10.5 ± 1.2 mg/L), strontium (8.8 ± 1.0 mg/L) and aluminum (0.5 ± 0.002 mg/L). Silicon was also present (13.8 ± 0.2 mg/L) in the water sample.

The source water also had moderately high natural organic matter (NOM) concentrations, measured as dissolved organic carbon (DOC) and UV_{254} absorbance (9.4 ± 0.5 mg/L and UV_{254} 0.11 ± 0.004 cm^{-1}, respectively), despite being low in turbidity (2.2 ± 0.6 NTU). The low specific UV absorbance value (SUVA, defined as the ratio of UV_{254} in m^{-1} and DOC concentration in mg/L) of 1.19 ± 0.08 m.L/mg indicated that the NOM was predominantly non-humic, highly hydrophilic, and low in molecular weights [133]. Fractionation using Supelite DAX-8 resin (Sigma Aldrich) confirmed that only 24% of NOM was hydrophobic; the remaining 76% comprising hydrophilic/transphilic fractions.

A model solution formulated to have similar ionic concentration and pH as Foss Reservoir water but without added NOM was also employed as a negative control to evaluate organic fouling. It was prepared by dissolving 3.29 mM Na_2SO_4, 8.98 mM $MgSO_4$, 2.52 mM $CaCO_3$, 4.63 mM $CaSO_4$, 2.08 mM NaCl, and 2.84 mM HCl in nanopure water.

NF pretreatment

Two NF pretreatment processes were evaluated; MF-only and EC followed by MF. Dead-end MF was performed at constant pressure (1.38 bar) using a 300-mL stainless steel

stirred cell (SEPA ST, Osmonics) and 0.22 µm modified PVDF membranes (GVWP04700, Millipore).

Batch EC experiments were performed in galvanostatic mode using a 500 mL custom-made Perspex cell fitted with an Al anode (99.9965%, Alfa Aesar) with initial effective area of 16.39 cm^2 and a perforated cylindrical 316-stainless steel cathode. The anode was mechanically scrubbed and thoroughly rinsed prior to electrolysis. Occasionally, the entire cell was rinsed with dilute HNO_3 to remove traces of precipitated coagulant. Operating conditions were optimized by systematically varying the current density (10 or 40 mA/cm^2), pH (5.5 and 6.2) and target aluminum concentrations (0 – 40 mg/L) by adjusting the electrolysis time, cell potential, and adding H_2SO_4 as necessary. After electrolysis, the suspension was flocculated for 30 minutes and allowed to settle for 30 minutes. The total aluminum concentration was measured by ICP-MS after acidification with HNO_3, which agreed to within 5% of the value obtained by simply weighing the anode before and after electrolysis. The zeta potential of suspensions was measured using an electrophoretic light scattering technique (Zetasizer Nano S90, Malvern). Approximately 10 L of Foss Reservoir water was electrocoagulated at optimum operational conditions (10 mA/cm^2, pH 5.5, and 25.6 mg /L aluminum dosage as explained in **Result and discussion**) and then microfiltered for integrated EC-MF pretreatment.

MF surfaces after filtering raw Foss Reservoir water and after EC pretreatment were visualized under an electron microscope (Tescan Vega 3 SEM-EDS). A heterogeneous layer comprising siliceous diatoms and other colloids present in Foss Reservoir were seen in Figure V-1a. Note that silica in the feed water was confirmed by ICP-MS (refer to ***Source water***) and was detected by FTIR and XPS on membrane surfaces (sections 0 and 0). A thick cake layer

of $Al(OH)_3$ flocs that completely enveloped the natural colloids were seen after EC in Figure V-1b.

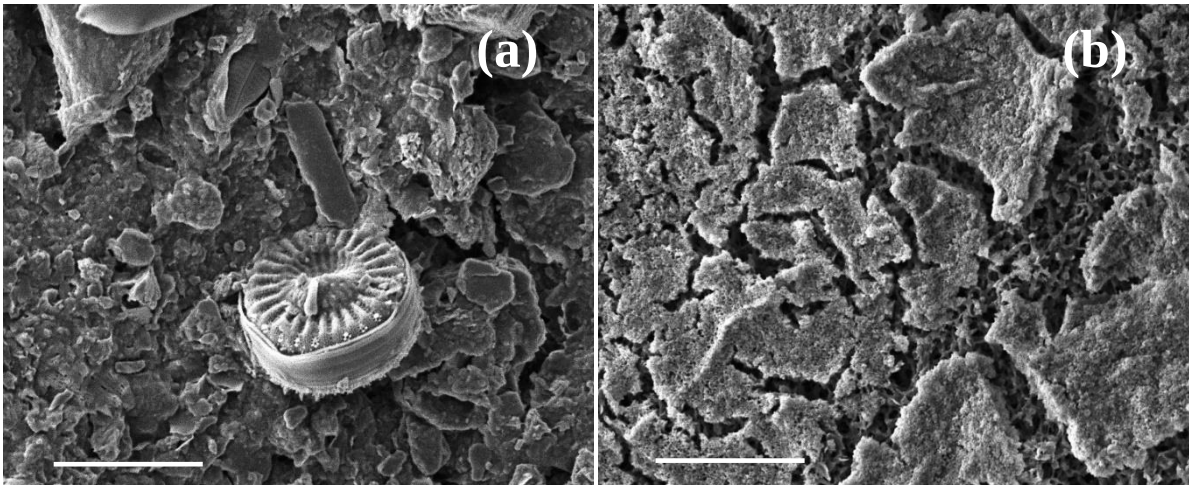

Figure V-1. Scanning electron micrographs of fouled microfilters: (a) after filtering 300 mL of untreated Foss Reservoir water and (b) after filtering 300 mL of electrocoagulated Foss Reservoir water at optimum conditions. The scale bars represent 10µm.

Nanofiltration

Crossflow NF was performed using a stainless-steel plate-and-frame module (SEPA-CF, Osmonics) housing a 139 cm^2 commercially available thin film composite membrane (NF270, Dow) fitted with feed and permeate spacers. The NF270 is a "loose" semi-aromatic poly(piperazinamide) membrane exhibiting relatively high pure water permeability (8.5 – 13.5 L/m^2.h.bar) [54, 210, 213, 250] and low NaCl rejection (40% at 4.82 bar). Its surface has been characterized as being relatively smooth (RMS roughness 5 – 9 nm) [54, 214], hydrophilic (27-55° contact angle) [209, 210, 213], and negatively charged at neutral pH (-10 to -19 mV) [209, 215] with a molecular weight cut-off of 300 Da [211].

Prior to each experiment, the membrane coupon was gently rinsed using nanopure water before placing it in the filtration cell. Nanopure water was then passed through the system at high crossflow velocity and low pressure for 1 h in flow-through mode to remove any

impurities that may be present. Next, the membrane coupon was conditioned by recirculating 2 g/L Na_2SO_4 solution at 11 cm/s cross flow velocity and permeate flux of 48 L/m^2.h until attaining a pseudo steady-state flux. Following membrane setting, the feed water was replaced with the sample water and filtration was started at the initial permeate flux of 43 L/m^2.hr (permeate flow rate of 10 mL/min) and at constant cross flow velocity of 11 cm/s. The system was operated in batch recycle mode by continuously returning permeate and concentrate flows to the feed tank (except during sampling). The transmembrane pressure was kept constant corresponding to the initial flux (ΔP=4.82 bar) for the entire filtration duration (~168 hours). The feed water temperature was maintained at 23 ± 0.3°C by using a chilled water recirculator (RTE-111, Neslab). Pressure and temperature were monitored using analog transducers (PX603 and TJ120 CPSS 116G respectively, Omega). Two digital flow sensors were installed in the system to continuously monitor the permeate flux (LS32-1500, Sensirion) and crossflow velocity (McMillan model 101, Cole Parmer) using a LabVIEW program (National Instruments).

Attenuated total reflectance – Fourier transform infrared spectroscopy (ATR-FTIR)

After NF, membrane coupons were carefully retrieved, cut into smaller pieces, and dried in a vacuum desiccator for 24 hours. The infrared spectra of virgin and fouled membranes in the range 650 – 4000 cm^{-1} were collected using Nicolet iS10 spectrometer (Thermo Scientific). The spectrometer was equipped with a Mid-infrared Ever-Glo source, deuterated-triglycine sulfate (DTGS) detector, KBr beam splitter, Omnic 9.0 Software, and a diamond iTX accessory to allow sampling in ATR mode. A background spectrum was collected on a clean ATR window prior to each analysis. The IR spectrum of each sample presented herein is an average of four separate spectra, each consisting of 128 coadded scans at 4 cm^{-1}

resolution, obtained from different locations to obtain representative information on dominant foulants. A 11 kHz low-pass filter was also used to prevent aliasing along with a zero-filling factor of 2 using a Norton-Beer Strong apodization and Mertz correction.

X-ray photoelectron spectroscopy (XPS)

A spectrometer equipped with a monochromatic Al Kα X-ray source (hν = 1486.7 eV) incident at 90° relative to the axis of a hemispherical energy analyzer (PHI model 5700, Physical Electronics) was used to obtain further information on the elemental composition and functionalities of the surfaces of virgin and fouled membranes. Charging problems arising from the non-conducting nature of polymeric membrane were reduced by using neutralizer. Samples were first scanned at pass energy of 187.85 eV for 5 minutes to obtain wide-scan spectra (0-1400 eV) which showed all elements present on the surface. High resolution (narrow) scans were then obtained for C1s and O1s regions at pass energy of 23.5 eV and 45° take-off angle. Electron binding energies were calibrated with respect to the C1s line at 285 eV corresponding to adventitious carbon. Peak areas for C1s and O1s regions were obtained assuming mixed Gaussian-Lorentzian shapes and correcting for sensitivity factors after integrated baseline background subtraction with Shirley routine.

Results and discussion

Super-faradaic aluminum dissolution during electrocoagulation

Figure V-2a and Figure V-2b show the measured total aluminum concentrations in suspensions after electrolysis as a function of time (left panel) and electrical charge passage and (right panel). As expected from Faraday's law, total aluminum concentrations increased linearly with electrolysis time and increasing current density 4-fold from 10 to 40 mA/cm^2

decreased electrolysis time by a factor of 4 for the same target aluminum dosage (Figure V-2a). Additionally, aluminum dissolution was insensitive to pH in the range 5.5 – 6.2 (at 40 mA/cm^2). Further, as summarized in Figure V-2b, all experimental data coalesced into a single straight line with respect to the total charge passed [41, 243] with a slope of 0.121±0.002 mg/A-s, which was 29% higher than Faraday's law prediction (0.0932 mg/A-s).

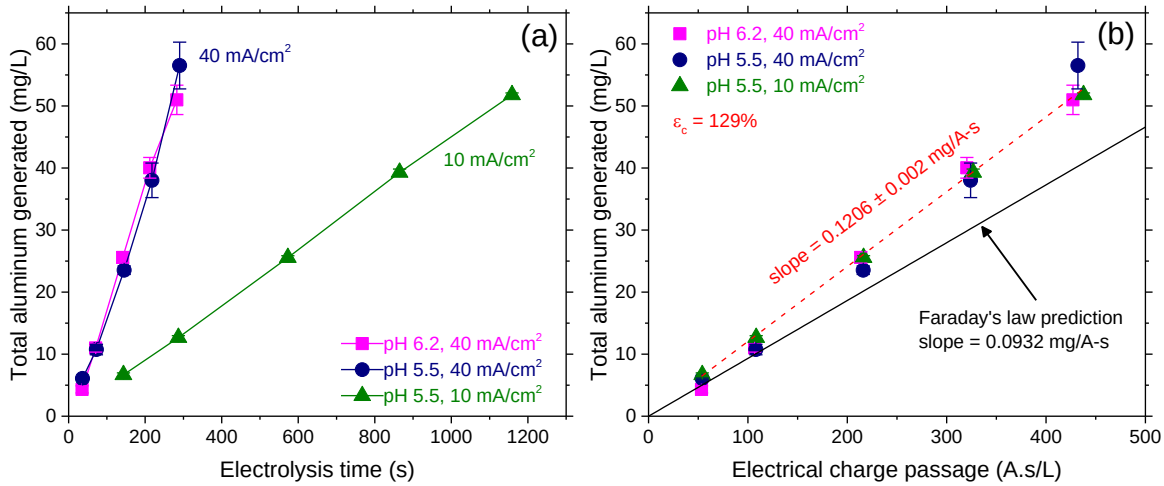

Figure V-2. Total aluminum generated during electrolysis as a function of time (panel a) and electrical charge passage (panel b).

Super-Faradaic aluminum dissolution at 129% current efficiency suggests the combined effect of electrochemical and chemical processes involving chloride-assisted localized dissolution at the (hydr)oxide-aluminum interface leading to pitting corrosion [251, 252]. High concentrations of sulfate ions in Foss Reservoir suggests that pit-growth would have been enhanced thereby accelerating aluminum dissolution contributing to the observed super-Faradaic behavior [253]. Additionally, since NOM in Foss Reservoir is principally hydrophilic (non-humic), organics are not expected to play a significant role in modifying aluminum electrodissolution unlike humic acids [254].

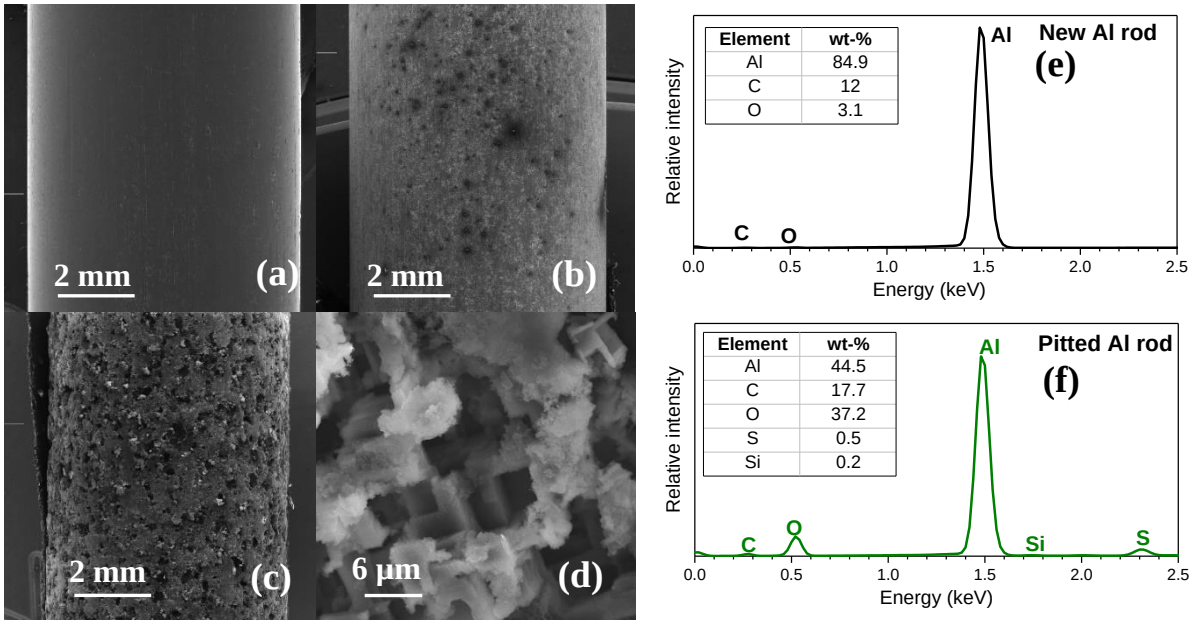

Figure V-3. Electron micrographs of a new aluminum rod (a), after electrcoagulating 450 mL water or 1-cycle (b), after electrocoagulating 15 L water or 33-cycles (c). A pit from (c) under higher magnification is shown in (d). The corresponding EDS spectra of the new aluminum anode (e) and after 33-cycles (f) are also shown.

Electron micrographs of the new anode, after 1-cycle of electrolysis to treat 450 mL, and after 33 electrolysis cycles to coagulate 15 L of Foss Reservoir water are shown in Figure V-3. As seen in Figure V-3a, the surface of the new elemental aluminum rod was smooth. Progressive electrolysis (Figure V-3b and Figure V-3c) induced more and more pitting. A magnified image of the corroded aluminum rod showed the existence of geometric facets (Figure V-3d) suggesting the crystallographic nature of pitting as reported earlier for anodically polarized aluminum [255, 256]. Using a high current density also most likely induced severe corrosion; i.e. more number of large pits [255]. Energy dispersive spectra (EDS) of the new anode (Figure V-3e) primarily detected aluminum, adventitious carbon, and oxygen possibly from the passive oxide layer. After electrolysis (Figure V-3f), weight fractions of carbon and oxygen increased and new peaks for sulfur and silicon appeared consistent with

deposition of NOM, sulfate, and colloidal components present in Foss Reservoir water. Presence of sulfate ions close to the pits provide evidence for enhanced aluminum dissolution since they tend to adsorb and attack the bottom of the preexisting pits [253]. The absence of chloride and presence of sulfur in EDS was attributed to the monovalent chloride ion's affinity to the outer (hydr)oxide film and subsequent release to the bulk solution at the slightly acidic pH of our experiments and to preferential adsorption of sulfate to the passive layer [252, 253].

Electrocoagulation process optimization

NOM removal was used to optimize EC operating conditions (Figure V-4a). In all cases, DOC removal exhibited saturation-type behavior with significant improvements at lower Al dosages before reaching a relatively constant (asymptotic) value beyond 25 mg Al/L. Higher removals were measured at pH 5.5 due to the lower charge density of NOM following greater protonation which rendered it more hydrophobic and adsorbable [134] similar to "enhanced" conventional chemical coagulation using alum [257, 258]. Highest removals were measured at 10 mA/cm^2 current density and pH 5.5. The SUVA slightly decreased with aluminum addition (Figure V-4b) suggesting incrementally better removal of the aromatic and hydrophobic fraction of NOM by EC [259, 260].

Given the high salinity of Foss Reservoir, very high current densities up to 40 mA/cm^2 were feasible. However, NOM removal was lower at 20 and 40 mA/cm^2 (Figure V-4c) for a fixed dosage of 25.6 mg Al/L consistent with earlier observations that higher electrolysise times are necessary to achieve sufficient contact between the coagulant and NOM for effective sorptive removal [131]. Note that electrolysis at higher current density generates a greater number of smaller-sized hydrogen bubbles [244] that rapidly carry a majority of the flocs to the surface (i.e. electroflotation) thereby reducing collision frequency between NOM and the

electrocoagulant [261]. Further, NOM removal was nearly the same for 5 and 10 mA/cm^2 demonstrating that the residence time corresponding to 10 mA/cm^2 was sufficient, similar to earlier reports [131]. Hence, optimal EC conditions corresponded to 25.6 mg/L dosage, 10 mA/cm^2 current density, and pH 5.5, which resulted in 40.4 ± 0.3% and 43.6 ± 0.6% DOC and UV254 removal respectively. These DOC and UV_{254} removal levels are consistent with conventional coagulation of from non-saline natural water predominantly containing low-molecular weight, non-humic, hydrophilic NOM [259, 262].

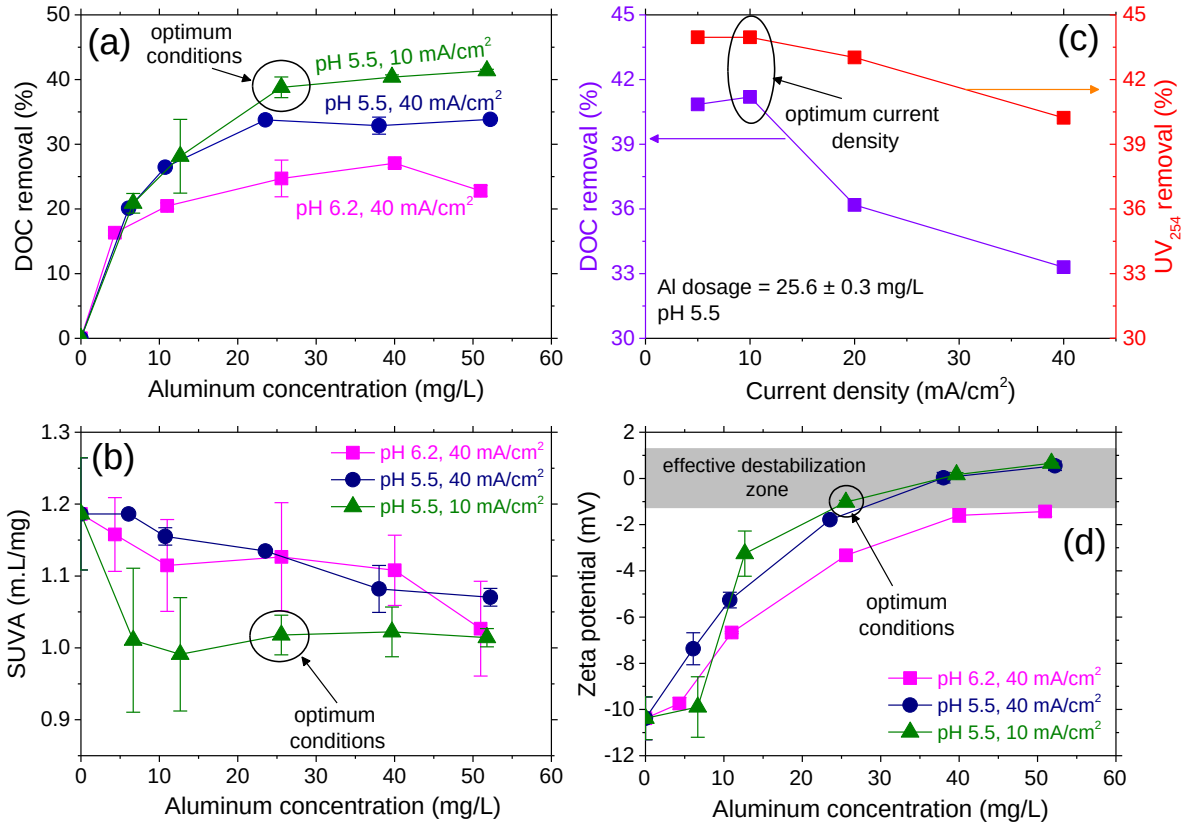

Figure V-4. Electrocoagulation process optimization measured by DOC removal and SUVA as a function of aluminum dosage at two pH values (a) and current density at optimal dosage and pH (c). Decreasing SUVA with aluminum dosage is shown in (b). Progressive charge neutralization with increasing aluminum dosage at all conditions evaluated is also shown in panel (d).

The ζ potential of colloids in untreated Foss Reservoir water was only -10.3 ± 0.9 mV as shown in Figure V-4d, which is attributed to its high ionic strength (~0.1 M) and high concentrations of divalent cations. Also as seen, increasing aluminum dosage monotonically decreased the magnitude of ζ potential demonstrating progressive adsorption and charge neutralization at both pH values and current densities investigated. Higher DOC and UV removal at pH 5.5 indicates more effective destabilization arising from the greater degree of protonation of adsorbed NOM functional groups by $Al(OH)^{2+}$, the dominant dissolved aluminum species, in addition to sweep flocculation by $Al(OH)_{3\ (s)}$. The ζ potential was insensitive to current density at pH 5.5 demonstrating that it did not significantly influence destabilization, rather the longer contact time achieved at lower current densities was necessary for effective NOM sorption as summarized in Figure V-4a. Complete charge neutralization was obtained at the optimum EC conditions (ζ potential ~ 0 mV) resulting in effective destabilization and higher NOM removals.

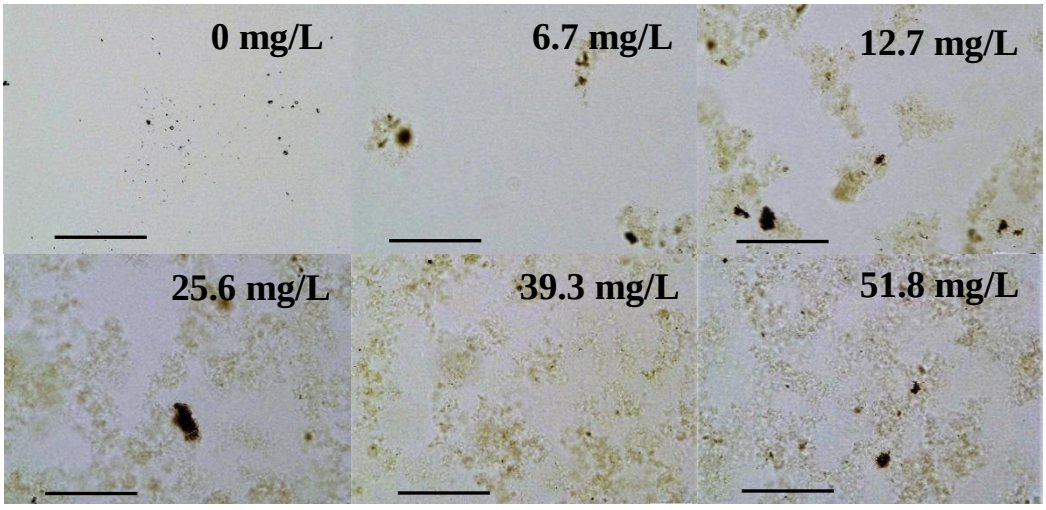

Figure V-5. Optical images of flocs formed by electrocoagulation at different aluminum dosages (at pH 5.5 and current density of 10 mA/cm^2). All images were taken at 10X magnification with scale bars representing 200 µm.

Suspensions electrocoagulated at optimum pH and current density were visualized using an optical microscope (Olympus BX51), which showed that increasing dosage formed more and more aggregates that were also larger in size (Figure V-5). As reported earlier for conventional aluminum coagulation, electrocoagulated flocs also appeared to be porous, elongated, and slender especially at higher dosages (≥ 13 mg/L) [24, 263].

Pretreatment effects on nanofilter fouling

NF fouling profiles, accounting for the osmotic pressure ($\Delta\pi$), over a 7-day period with three different feed waters are summarized in Figure V-6. The specific permeate flux declined by 36% following MF-only pretreatment but only by 8% following EC-MF pretreatment. Importantly, the flux after EC-MF pretreatment declined in a similar manner as the model solution operationally demonstrating negligible NF organic fouling by integrating EC pretreatment along with MF.

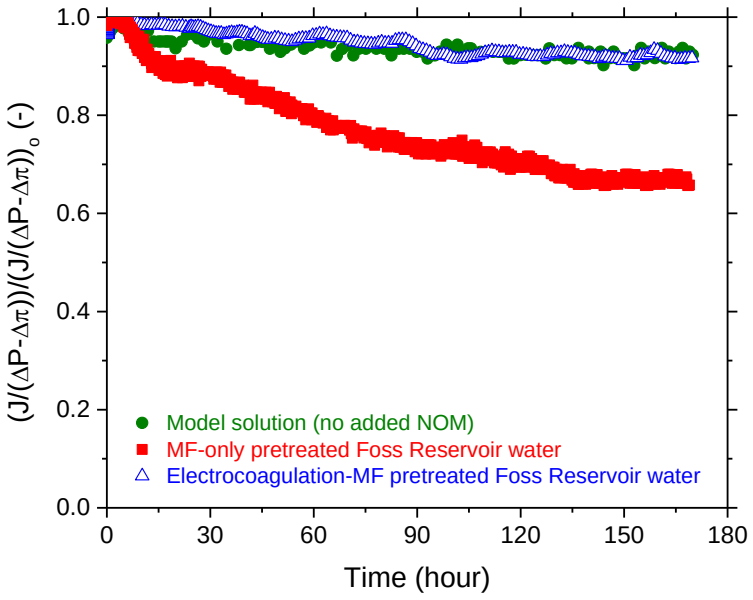

Figure V-6. NF flux profiles following MF-only pretreatment, EC-MF pretreatment, and for the model solution.

Incorporating EC pretreatment to MF preferentially removed hydrophobic and high molecular weight components of NOM as indicated by the lower SUVA values (from 1.18 to 1.02 m-L/mg). Hence, EC-MF pretreatment not only decreased NOM concentration in the NF feed water compared to the MF-only case (from 8.9 mg/L to 5.6 mg/L) but also simultaneously increased the hydrophilic fraction of the remaining NOM.

Identification of dominant surface functionalities on virgin and fouled nanofilters using ATR-FTIR

Virgin membrane

The ATR-FTIR spectrum of the virgin membrane, shown in black color in Figure V-7 exhibited (i) an amide I band at 1629 cm^{-1}, (ii) small peaks corresponding to aromatic *v*C-H vibrations around 3000 – 3100 cm^{-1}, and (iii) symmetric (2854 and 2967 cm^{-1}) and asymmetric (2872 and 2931 cm^{-1}) vibrations of aliphatic *v*C-H arising from its active layer [175]. As is typically the case for semi-aromatic polyamide membranes, aromatic amide (1609 cm^{-1}) and amide II (1542 cm^{-1}) bands were absent due to the aliphatic nature of the piperazine monomers and the absence of N-H bond in the poly(piperazinamide) active layer of NF270 [264]. Peaks at 1151 (*v*Ar-SO_2-Ar), 1243 (*v*Ar-O-Ar), and 1323 cm^{-1} ($\nu_{as}SO_2$), along with C=C aromatic in-plane ring bend stretching vibrations (1586, 1504, and 1488 cm^{-1}) are characteristic of the polysulfone support layer.

MF-only pretreatment

Figure V-7 also shows IR spectra for fouled membranes, which continued to exhibit virgin membrane peaks albeit with reduced intensities. Virgin membrane peaks were attenuated to the greatest extent for the case of MF-only pretreatment (red colored spectrum), consistent with the prominent flux decline seen in Figure V-6. NOM components such as

polysaccharides, proteins, and humic acids were also detected on the nanofilter's surface following MF-only pretreatment. A broad band around 900-1100 cm^{-1} was assigned to *v*C-O-C and C-O dominated by ring vibrations of carbohydrate-like compounds of microbial origin [176], although the peaks overlapped with the characteristic peaks of virgin membrane around this region. The increase in the *v*Si-O peak around ~1100 cm^{-1} is thought to originate from diatoms (see Figure V-1a) and siliceous nanocolloids [180]. A faint peak in this region at 1039 cm^{-1} probably signifies proteins or N-acetyl amino sugars from bacterial cell walls [173]. The presence of proteinaceous compounds manifested as an increase in amide I band intensity (at 1654 cm^{-1}) and an appearance of the amide II band (1546 cm^{-1}). The amide I band also seemed to be blue-shifted to 1654 cm^{-1} compared to virgin membrane (1629 cm^{-1}), indicating the presence of proteins of bacterial origin [232]. The deposition of polysaccharides and amides also manifested as an increase in intensity of *v*C-H (at 2854 and 2927 cm^{-1}) and *v*O-H (at 3284 cm^{-1}) stretching vibrations compared to the virgin membrane [167, 265]. In addition, the appearance of a weak shoulder at 1721 cm^{-1} was attributed to carbonyl groups corresponding to humic acids [176, 266, 267], ester-rich organics [268], and possibly O-C=O of carbonates with the membrane masking other accompanying peaks (*v*C-O at 1453 cm^{-1} and *v*C-O at 873 cm^{-1}).

EC-MF pretreatment

Electrocoagulation-MF pretreatment induced several differences in the IR spectra of fouled NF membrane surfaces (blue colored spectrum in Figure V-7) compared to MF-only pretreatment discussed in the previous paragraph. For example, the broad polysaccharide peak (900-1100 cm^{-1}) disappeared. A slight increase in intensity around 1080-1100 cm^{-1} might be due to *v*Si-O of silica nanocolloids. Proteinaceous compounds were still visible and manifested

as a slight increase in intensity and continued presence of the amide I and amide II bands (at 1654 cm^{-1} and 1546 cm^{-1}). Peaks corresponding to *v*C-H (at 2857 and 2931 cm^{-1}) and *v*O-H (at 3288 cm^{-1}) from polysaccharides and amides were weakened, consistent with partial removal of these constituents by EC-MF discussed previously. These results demonstrate that reducing EC pH to a more acidic value compared to the pH of minimum aluminum solubility (i.e. 5.5 versus 6.2) improves removal of hydrophilic NOM moieties such as carbohydrate-like and proteinaceous compounds in addition to hydrophobic, large molecular weight components as reported in previous section and earlier research [53, 260]. It is emphasized that a fraction of the proteinaceous compounds was not removed by EC-MF pretreatment and consequently was present in the NF feed water.

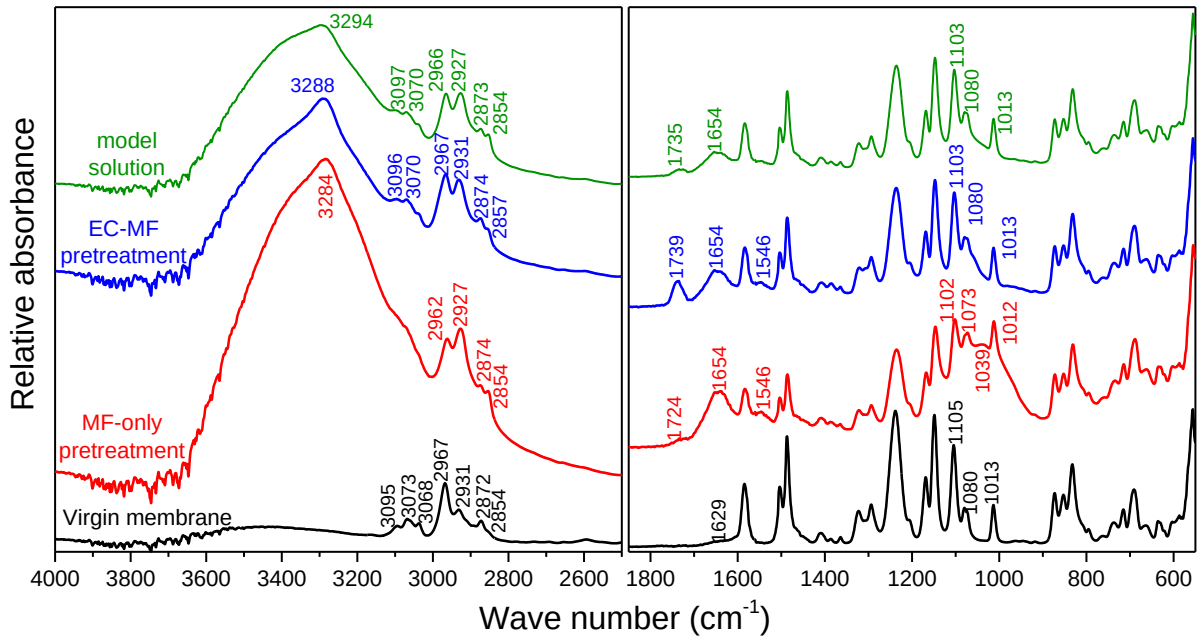

Figure V-7. ATR-FTIR spectra of virgin and fouled membranes (MF-only pretreatment, EC-MF pretreatment and model solution).

A carboxyl peak appeared following NF of EC-MF pretreated water at 1739 cm^{-1} compared to 1721 cm^{-1} for MF-only pretreatment. This peak position is close to what was observed for the case of the model solution (at 1735 cm^{-1}) and arises from carbonate in $CaCO_3$ [54]. Since the model solution did not contain any organics, signals corresponding to carbohydrate-like (~ 900-1100 cm^{-1}) and protein-like compounds (1542 cm^{-1}) were absent in the corresponding spectrum shown in green color in Figure V-7. These results suggest that $CaCO_3$ scaling prevailed when NOM did not contribute significantly to fouling (i.e. for the model solution and EC-MF pretreatment). As reported earlier [269], coagulation would have reduced NOM-calcium complexation in the feed water leading to $CaCO_3$ precipitation due to high affinity of the free calcium ion to the negatively charged membrane surface. SEM provided additional evidence for inorganic fouling (Figure V-8), which shows $CaCO_3$ crystal fragments after NF of EC-MF pretreated Foss Reservoir water. Importantly, $CaCO_3$ scaling in these cases only reduced NF permeability by ~8% (see Figure V-6).

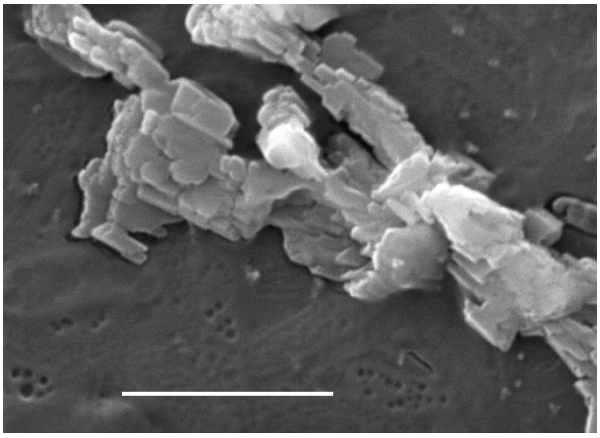

Figure V-8. Fragments of $CaCO_3$ crystals visible after nanofiltration of EC-MF pretreated Foss Reservoir water. The scale bar represents 4 µm.

Evidence of NOM fouling by XPS

XPS was performed to validate IR findings of dominant foulants. Major elements on the surface of the virgin and fouled membranes and their relative atomic concentrations were first identified by XPS wide scans. As summarized in Table V-1, the relative concentrations of carbon in fouled NF270 membranes were only slightly lower than the virgin membrane. Hence, fouling was not as catastrophic as reported for a "tighter" NF membrane operating on the same source water [54]. The relative oxygen content in the foulant layer increased after nanofiltration for all three feed waters (reaching approximately the same level of 27%). This suggests the presence of oxygen-containing foulants including NOM, Si-O, and carbonates for MF-only and EC-MF pretreatments. Since the model solution did not contain colloids and organics, the oxygen increase in its case was solely attributed to the presence of carbonates. Calcium was consistently detected on all fouled membranes confirming its role in flux decline. Silicon was detected on surfaces of both membranes filtering natural water demonstrating that nanocolloidal silicon penetrates coagulation and membrane pretreatments [270]. Importantly, silicon was better removed by EC-MF as evidenced by its lower atomic percentage (0.3%) compared to MF-only pretreatment (1.6%). Importantly, Al wasn't detected either in the EC-MF pretreated water by ICP-MS (< 0.61 µg/L) or on the NF surface by XPS demonstrating no coagulant carryover to NF system [43, 55]. More evidence for NOM and $CaCO_3$ deposition via narrow scan XPS is shown next.

Table V-1. Average elemental composition of virgin and fouled NF membrane surfaces from XPS survey scans.

	C1s	N1s	O1s	Si2p	S2p	Ca2p
Virgin membrane	69.2	11.9	18.5	0.0	0.4	0.0
MF-only	65.7	5.1	27.0	1.6	0.0	0.6
Electrocoagulation-MF	67.7	5.0	26.9	0.3	0.0	0.5
Model solution	67.1	5.6	26.4	0	0	0.9

C1s and O1s component peaks from high resolution XPS of surfaces of virgin and fouled NF membranes were also deconvoluted using our recently published procedure [54] and are shown in Figure V-9. The relative area percentage of the C-(O, N, OH) peak in the virgin membrane was 27%, which increased to ~36% for the fouled nanofilters. This provides additional evidence for carbonate-deposition for the case of model solution, and fouling by carbonates (with limited contributions from proteinaceous compounds) following EC-MF pretreatment as discussed in previous section and from XPS survey scans. However, for the case of MF-only pretreatment, the increase in the C-(O, N, OH) relative peak area is the result of an increase in the number of corresponding bonds arising from natural water components such as polysaccharides, amides, and carbonates also as seen in IR spectra. For example, carbonyl groups from the polyamide backbone appeared as a peak at ~ 288 eV for the virgin nanofilter, whose intensity was reduced after fouling. Further, evidence of O=C-OH or O=C-OR deposition from pretreated Foss Reservoir water, manifested as an additional peak at ~288.9 eV. O1s peaks around 532.8 eV also increased in relative area percentage consistent with C1s spectra, also demonstrating an increase in the number of bonds associated with foulants such as O=C-O from NOM and/or carbonates, H··O=C-N from proteinaceous compounds, O-H from polysaccharides and/or carbonates, and Si-O from silica.

Importantly, narrow scan XPS peaks corresponding to C-(O, N, OH) were shifted to higher binding energies at ~286.4 eV compared to the virgin membrane (285.9 eV). The O=C, O=C-N, and C-O peak at 531.1 eV for virgin membrane was also shifted to higher binding energy for both fouled membranes (~531.7 eV), providing evidence for specific interactions of foulants with the nanofilter surface (e.g. complexation).

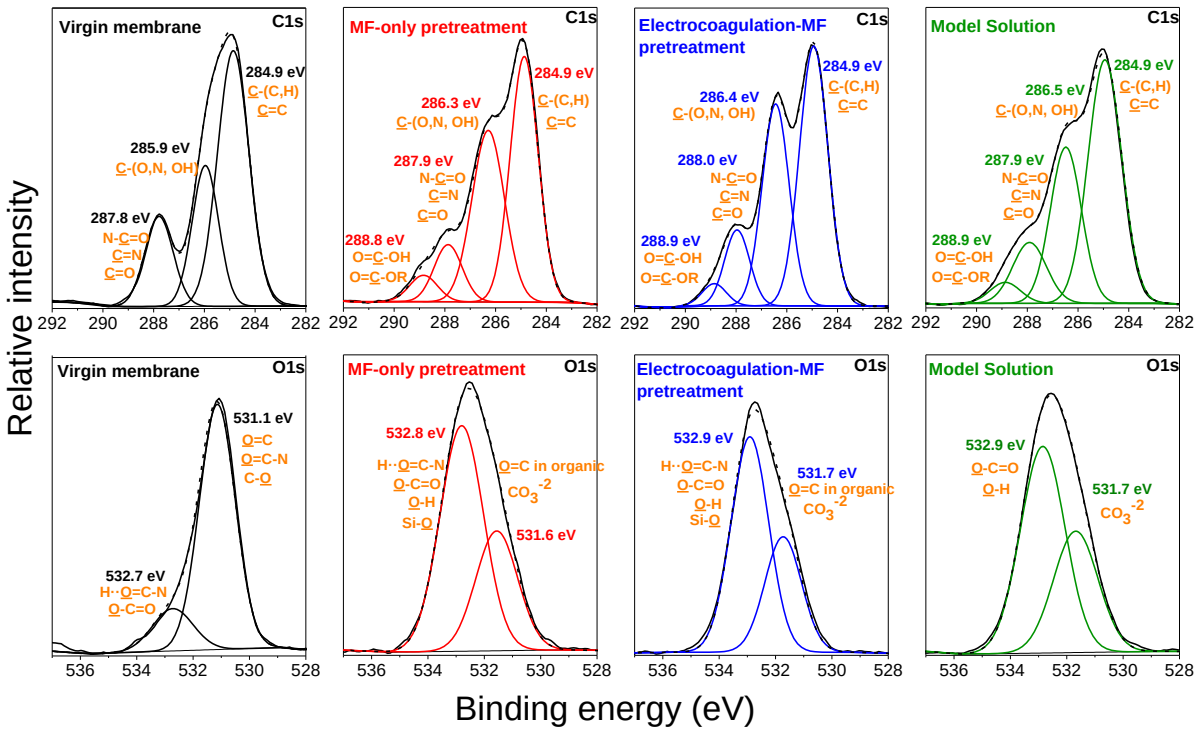

Figure V-9. High resolution scans of C 1s and O 1s regions for virgin and fouled membrane.

NF permeate water quality considerations

The observed rejection ($R_{obs} = 1 - C_p/C_f$, where C_p and C_f are the permeate and feed concentrations respectively) of several ions, DOC, and UV_{254} absorbing substances are summarized in Figure V-10, which depicts very similar ionic rejection from natural water after both pretreatments and from the model solution. Excellent sulfate removal (≥ 99.5%) was assigned to anion repulsion [230, 271] given that the NF270 membrane is negatively charged at the operating pH of 7.8 (~ -15 mV) [209]. High rejection of divalent cations (≥ 90%) can be explained by their large hydrated size and stability constants for the corresponding sulfate ion pairs [272]. Magnesium, calcium, and strontium were all rejected to the same extent [248, 273, 274] demonstrating small differences in hydrated radii do not impact rejection by NF. To our knowledge, this is one of the first measurements demonstrating excellent strontium removal

from surface water by NF, which is similar to ground water NF [248] but unlike conventional treatment [247]. Rejection of other ions is consistent with coupled transport to preserve electroneutrality, which is characteristic of natural waters [207, 275] resulting in only 44% sodium rejection. Interestingly, negative rejection of the chloride ion was observed, as reported earlier for multi-component solutions comprising electrolytes of different valency [276-278]. Under these conditions, a strong Donnan potential is generated due to very high divalent ion rejection enhancing the permeation of monovalent ions to preserve electroneutrality [279]. This is manifested as negative chloride rejection in our experiments because of the low Cl^-/SO_4^{-2} concentration ratio in Foss Reservoir (0.11), which is below the reported threshold value of 0.4 [280].

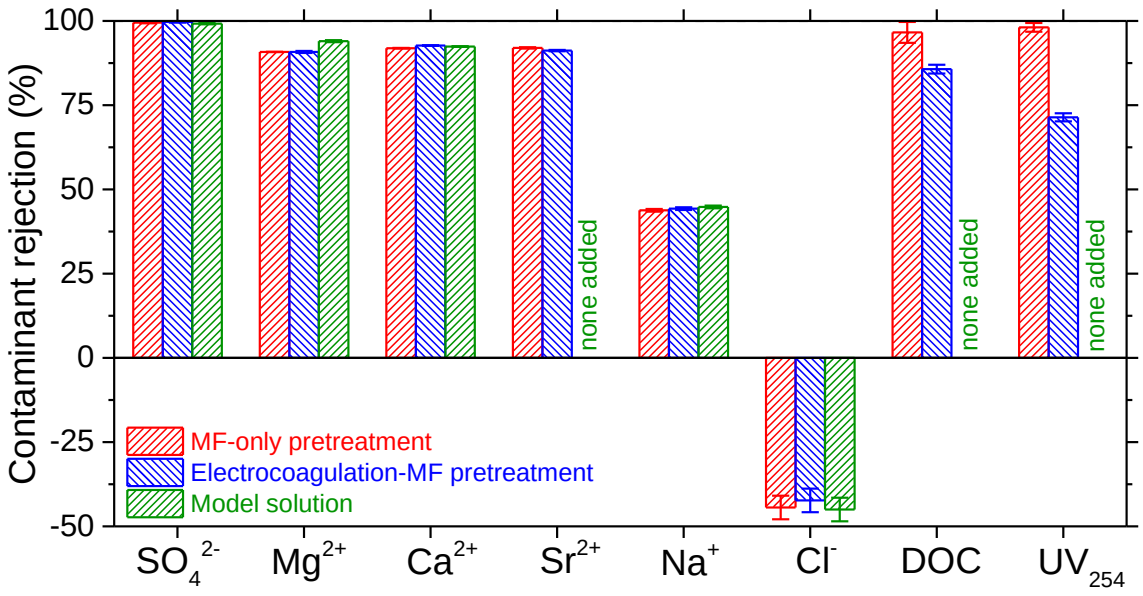

Figure V-10. Observed rejection of major ions by nanofiltration of Foss Reservoir water with MF-only and EC-MF pretreatment. Data from experiments with the model solution are also shown for comparison.

Unlike ionic rejections, Figure V-10 shows pretreatment effects on NOM removal from

Foss Reservoir with DOC and UV_{254} rejection decreasing following EC-MF pretreatment compared with MF-only pretreatment. A relatively thick foulant layer was formed on the NF membrane after MF-only pretreatment (Figure V-11c and 11d) than for the case of EC-MF pretreatment (Figure V-11e and 11f) as seen by electron microscopy. IR spectra also corroborated the formation of a thicker foulant layer with MF-only pretreatment since virgin NF270 peaks were attenuated to a greater extent in its case. Micrographs of the virgin nanofilter (Figure V-11a and 11b) and after NF of the model solution (Figure V-11g and 11h) are also shown for comparison. Small particles visible in case of EC-MF pretreatment and model solution (Figure V-11f and 11h) are most likely fragmented $CaCO_3$ crystals and/or mixed precipitates [281]. Higher DOC and UV_{254} removal for the case of MF-only pretreatment is attributed to the additional hindrance offered by the cake layer to NOM transport [167, 214]. An additional consideration is that EC preferentially removes hydrophobic and high molecular weight NOM components [259, 260] along with a smaller amount of carbohydrate-like and protein-like compounds [90]. For example, as seen by ATR-FTIR, humic acids were seen only on the nanofilter surface following MF-only pretreatment and several peaks corresponding to hydrophilic NOM moieties were more prominent (i.e. these components were well-removed by EC and consequently not found on the nanofilter surface). Hence, EC "fractionated" NOM by not capturing its non-ionic and low molecular weight fractions, whose passage across the NF270 membrane would have been facilitated due to reduced electrosteric interactions thereby reducing DOC and UV_{254} rejection [167].

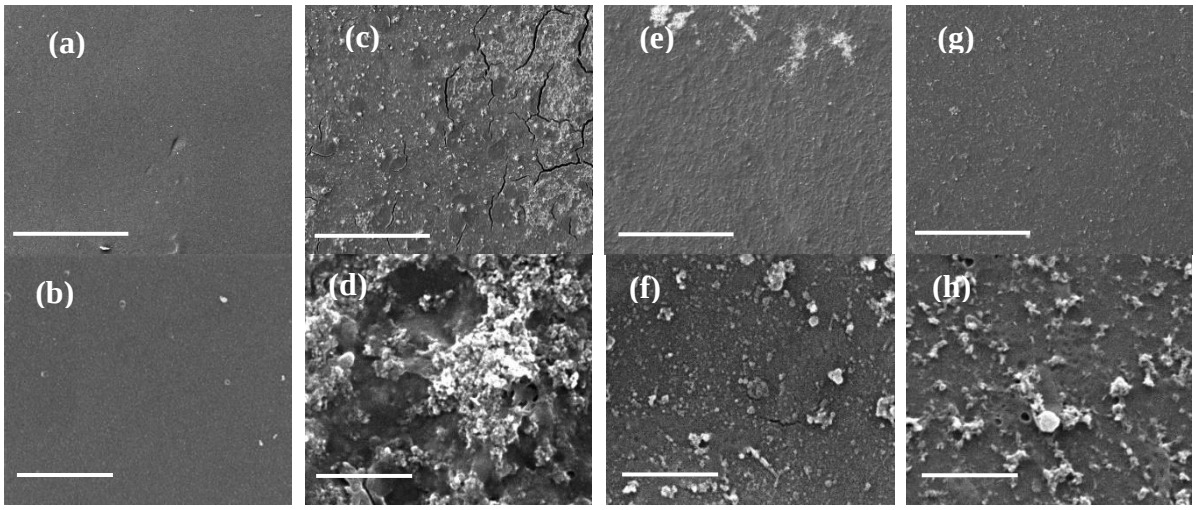

Figure V-11. Electron micrographs of the virgin nanofilter (a-b), after fouling by MF-only pretreatment of Foss Reservoir water (c-d), after fouling by EC-MF pretreated Foss Reservoir water (e-f), and model solution (g-h). The images in the top row were obtained at a magnification of 1000x where the scale bars represent 100 µm. Higher magnification (18000x) images are shown in the bottom row where the scale bars represent 4 µm.

Conclusions

DOC removal was enhanced by performing EC at a slightly lower pH than that of minimum Al solubility (i.e. 5.5 versus 6.2), which removed a portion of the hydrophilic fraction in addition to the typical hydrophobic and higher molecular weight NOM fractions [35] similar to enhanced conventional chemical coagulation [134]. Hence, in addition to better controlling nanofilter fouling this would also reduce disinfection by-product formation since hydrophilic NOM components also serve as trihalomethane and haloacetic acid precursors [206]. An additional consideration is that although it is possible to design smaller, low-residence time EC units by employing high current densities for brackish waters, this will correspondingly reduce NOM-hydrogen bubble collision frequency and NOM removal leading to non-optimal implementation. A highest current density of 10 mA/cm^2 is recommended for aluminum similar to iron [131] to maximize NOM control while minimizing electrolysis time.

Polysaccharides and proteins IR peaks on NF surfaces (~1000 cm^{-1}, 1546 cm^{-1}, and 1654 cm^{-1}) were strongly attenuated following integrated EC-MF pretreatment (compared with MF-only pretreatment) providing direct evidence for excellent hydrophilic NOM removal by EC. However, NOM removal by EC reduced the NOM-Ca interactions causing higher affinity of calcium towards negatively charged nanofilter leading to $CaCO_3$ precipitation, which was also observed for the model solution containing no organics. Importantly, this did not significantly reduce flux under conditions of our experiments. Therefore, both operational data and surface spectra demonstrate that higher NF fluxes were obtained following EC-MF pretreatment because it controlled organic fouling. On the other hand, the relative concentration of small, non-ionic NOM moieties preferentially passed through the nanofilter because of the relatively thin cake layer formed by enhanced pretreatment.

The Donnan effect arising from the very high rejection of divalent ions substantially decreased monovalent ion removal, even leading to negative observed rejection of chloride. Hence, concentrations of individual electrolytes in the NF permeate will differ significantly from that of the feed water, which should be considered while formulating post-treatment corrosion control strategies when the Cl^-/SO_4^{-2} concentration ratio is low (< 0.4). All Group II cations were removed to a very high degree and approximately the same extent demonstrating that they all behave similarly in natural waters. This suggests that strontium removal by NF can be estimated simply using the more commonly measured values for calcium and magnesium. Additionally, since strontium also complexes with NOM [282] it can be expected to exacerbate fouling in an analogous manner to calcium [186]. Finally, results presented in this manuscript demonstrate the feasibility of nanofiltration to desalinate brackish surface water when sulfate and other divalent ions are dominant contributors of salinity and that

advanced pretreatment can significantly control organic and colloidal fouling during such applications.

CHAPTER VI

REVERSE OSMOSIS FOULING DURING PILOT-SCALE MUNICIPAL WATER REUSE: EVIDENCE FOR ALUMINUM COAGULANT CARRYOVER *

Introduction

Factors such as population growth, climate change, and drought have reduced the availability of high quality water sources sometimes necessitating wastewater reclamation to meet our growing demands for drinking water. Purifying municipal wastewater to drinking water standards requires a series of advanced technologies serving as multiple, redundant barriers against myriad contaminants (i.e. the multiple-barrier approach) [283]. Reverse osmosis (RO) is almost universally employed during water reuse as the final filtration step to remove numerous trace organic compounds including contaminants of emerging concern, disinfection by-products and their precursors, etc. [284, 285]. However, like in all other RO applications, colloids, organic matter, precipitated salts, and microorganisms tend to accumulate on, in, or near the membrane surface reducing the overall water permeability; i.e. cause fouling [165, 286].

To reclaim/reuse wastewater effluent, our current practice is often to simply append all necessary advanced technologies, including RO to existing unit processes without any changes to the treatment plant. However, much of our current civil engineering infrastructure is ageing and outdated [287]. Hence, even if the secondary-treated effluent meets all regulatory permits (mainly biochemical oxygen demand and total suspended solids), it could still contain

* Reprinted with permission from "Reverse osmosis fouling during pilot-scale municipal water reuse: Evidence for aluminum coagulant carryover", M.A. Sari and S. Chellam, 2016, Journal of Membrane Science, 520, 231-239, Copyright 2017 by Elsevier.

substantial amounts of non-biodegradable organics, inorganics, and submicron colloids, since they aren't covered by federal or state water quality standards. Hence, to reduce the migration of these possible foulants to the RO system, existing wastewater treatment unit operations need to be tightly controlled and possibly even upgraded for the successful operation of the retrofitted water reuse treatment train. However, this issue is often not considered during the design and implementation of advanced water reclamation technologies.

RO fouling during water reuse is commonly reduced by treating the secondary effluent using microfiltration (MF) or ultrafiltration (UF) [283, 288-291]. However, MF/UF only remove colloidal foulants such as turbidity, bacteria, and high molecular weight organic matter and therefore only partially control RO fouling [240, 289]. Additional MF/UF/RO fouling control can be achieved by dosing coagulants to enhance the removal of colloidal, dissolved, and macromolecular foulants [25, 53]. In some cases, coagulation may already be employed to enhance liquid-solid separation in the secondary clarifier [292], capable of enhancing the flux of any downstream membranes employed for water reclamation [293]. However, as described above, the coagulation conditions may not be properly controlled resulting in overdosing, since aluminum or iron are not included in effluent permits. But, improper coagulant control can exacerbate fouling, which has been demonstrated during surface water treatment and desalination [25, 43, 294] but not for water reclamation.

Foulants can be identified by sacrificing the RO module and examining the membrane surface spectroscopically and microscopically at the conclusion of testing, i.e. performing an "autopsy" [295]. Autopsies have revealed that organics of microbial origin (i.e. proteins and polysaccharides), humic-like compounds, as well as calcium, sulfur, silicon, and phosphorous are major RO foulants during wastewater reclamation [165, 285, 286, 288, 296]. Also,

bioorganic fouling typically dominates lead elements while inorganic fouling contributes more for tail elements [286]. Autopsies on RO membranes following conventional (i.e. coagulation, flocculation, sedimentation, and media filtration) pretreatment during brackish water desalination have shown that any residual coagulant can also cause fouling [42, 43, 294]. These investigations focused more on bulk water chemistry and operational data to infer that aluminosilicates and aluminum hydroxides were possible foulants. Detailed surface characterization and specific coagulant-membrane interactions were not pursued.

The primary objective of this research is to perform autopsy of RO membranes used to reclaim wastewater which underwent secondary treatment including alum coagulation to determine relative contributions of organic and inorganic fouling. Fouled RO elements obtained from a pilot-scale study conducted in support of full-scale plant design were extensively characterized using Scanning Electron Microscopy – Energy Dispersive X-ray Spectrometry (SEM-EDS), Fourier Transform Infrared (FTIR) spectroscopy, and X-ray Photoelectron Spectroscopy (XPS) to determine dominant foulants present on membrane surfaces. Based on autopsy results, citric acid at pH 4 and EDTA at pH 11 were selected as simple 1-step cleaning agents. Their regeneration efficacy was assessed by measuring the hydraulic permeability and characterizing the surfaces of cleaned RO membranes.

Experimental work

RO pilot-plant and pretreatment

The municipal wastewater was treated at full-scale with an extended aeration activated sludge process followed by tertiary treatment using single-stage media filtration, ultraviolet disinfection, and post-aeration. Alum (aluminum sulfate) was added to promote colloid

coagulation and sedimentation in the secondary clarifier. The pilot-plant was designed to evaluate the possibility of reclaiming only the secondary effluent water (i.e. after aeration, alum addition, and secondary clarification) by MF and RO as shown in Figure VI-1. In other words, tertiary treatment unit processes were not included for RO pretreatment and wastewater reclamation. A 2 mg/L chloramine residual was maintained in the MF feed water by pre-ammoniation to control biofouling. Over the duration of the study, the average total organic carbon concentration, 5-day biochemical oxygen demand (BOD_5), and chemical oxygen demand (COD) of the RO feed water were 6.3 ± 0.5 mg/L, < 2 mg/L, and 22.3 ± 4 mg/L, respectively. Note that alum also successfully removed phosphorus, which was below detection limits in the microfiltered wastewater. The alkalinity (buffering capacity), total dissolved solids, calcium, sodium, chloride, and sulfate concentrations were 106.8 ± 14.3 mg/L as $CaCO_3$, 1,117.1 ± 35.5 mg/L, 110.0 ± 8.2 mg/L, 222.9 ± 11.1 mg/L, 298.6 ± 10.7 mg/L, and 143.3 ± 23.2, respectively. A proprietary phosphonate-based antiscalant was added before RO. The two-stage RO system was operated at an overall flux of 19 L/m^2-h and 85% recovery with concentrate recirculation in the second stage.

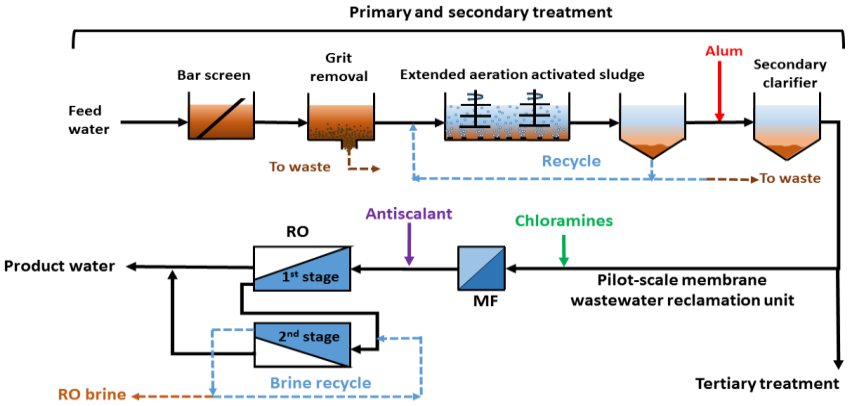

Figure VI-1. Schematic of full-scale wastewater treatment processes and pilot-scale membrane wastewater reclamation unit.

RO membranes

Two fouled 4-inch diameter thin-film composite spiral wound RO elements (KOCH HR-4040), one from each stage of the pilot plant, were brought back to our labs for further analysis. Coupons of the virgin membrane were also purchased from the manufacturer to serve as controls, the contact angle of which was measured to be 35° ± 1.8° similar to previous reports [167, 297] demonstrating its hydrophilic nature. Upon receipt both membrane modules were visually inspected revealing that the fiberglass casings, permeate tubes, and brine seals were all in a good condition showing no signs of physical damage or external contamination. The module was sacrificed and central portion of the membranes were cut into flat sheets, stored in moist sealed plastic bags, and preserved at 4°C in a refrigerator before further analysis. A minimum of three coupons from different locations on the membrane element were characterized by SEM-EDS, XPS, and FTIR.

Scanning electron microscopy and elemental analysis (SEM-EDS)

Prior to analysis, membrane coupons were further cut into smaller pieces and dried in a vacuum desiccator for 24 h. A scanning electron microscope equipped with X-ray microanalysis (SEM-EDS) was also used to obtain preliminary information on the overall surface elemental composition of the virgin and fouled membranes. These measurements were made using a JEOL JSM-6010LA InTouchScope SEM with integrated Energy Dispersive X-ray Spectroscopy (EDS) analyzer at an acceleration voltage of 15 kV, 10 mm working distance, and 250X magnification.

X-ray photoelectron spectroscopy (XPS)

More detailed information on the surface elemental composition of virgin and fouled membranes were obtained with a PHI 5700 X-ray photoelectron spectrometer equipped with a

monochromatic Al Kα X-ray source ($h\nu$ = 1486.7 eV) incident at 90° relative to the axis of a hemispherical energy analyzer. The neutralizer was turned on to reduce charging of the non-conductive polymeric membranes. Survey spectra were obtained over the entire range (0-1400 eV) and high-resolution spectra were obtained for photoelectrons emitted from C 1s, O 1s, and Al 2p regions to verify surface functionalities. Prior to high resolution scans analysis, the electron binding energy was calibrated initially with respect to the adventitious C 1s line at 284.8 eV. Component peaks were deconvoluted using the Shirley routine assuming mixed Gaussian-Lorentzian shapes and correcting for sensitivity factors after integrated baseline background subtraction. Using this procedure, the C 1s peak was resolved into four components: (1) aromatic or aliphatic C-(C,H) at 284.8 eV, (2) a peak at 286.0 eV attributed to C-(O,N, OH), (3) a peak at 287.8 eV from C=O, or N-C=O, and (4) a weak peak at 288.9 eV arising from O=C-OH and O=C-OR. Similarly, O 1s region was decomposed to: (1) a peak at 531.22 eV attributed to O=C, (2) a peak at 532.35 eV possibly from O-(C, H), and (3) a peak at 533.45 eV primarily due to adventitious water and/or esters (shown in Figure VI-4 and Figure VI-6).

Attenuated total reflectance – Fourier transform infrared spectroscopy (ATR-FTIR)

The infrared spectra of virgin and fouled membranes over the range of 650 to 4000 cm^{-1} were collected using a Nicolet iS10 spectrometer equipped with an Ever-Glo MIR source, DTGS detector, KBr beam splitter and Omnic 8.5 Software. Prior to each analysis, the background spectrum was collected on a clean transmissive Ge window. Small membrane samples (approximately 1 cm^2) were then placed on the window and IR spectrum of each membrane was obtained by averaging 512 scans collected at 4 cm^{-1} resolution. A 20 kHz low-pass filter was used to prevent aliasing along with a zero filling factor of 2 using a Blackman

Harris three-term apodization and Mertz phase correction.

Chemical cleaning

Only two cleaning agents were evaluated based on autopsy results since they have been shown to effectively remove aluminum from RO membrane surfaces; citric acid at pH 4 and ethylenediaminetetraacetic acid (EDTA) at high pH [15, 42, 298, 299]. The chelating ability of a 2 mM solution of EDTA was enhanced by completely deprotonating the carboxylic functional groups by adding 1 M NaOH to raise its pH to 11, which has been suggested to remove both organic and inorganic foulants in a single step [15, 298]. Separately, a 2 wt% citric acid solution at pH 4 (adjusted using 5 N NH_4OH) was also evaluated [42, 300]. Three separate coupons were cut from different locations in the membrane element from each stage of the pilot-plant to conduct cleaning experiments. Each membrane coupon (17 cm^2) was cleaned by fully submerging it in 100 mL of the cleaning solution and shaking at 220 rpm for 30 minutes at room temperature. After cleaning, membranes were thoroughly washed with ultrapure water three times, then submerged in 100 mL of ultrapure water and shaken for 30 minutes, before resistance measurement. The efficacy of EDTA and citric acid were assessed by comparing the respective membrane resistances after cleaning and analyzing the residual cleaning solutions for calcium and aluminum. Cleaned membranes were air-dried for 24-hours and their surfaces were characterized using XPS and FTIR to provide direct evidence of foulant removal.

Results and discussion

SEM-EDS suggests the importance of aluminum fouling

As shown in Figure VI-2, electron microscopy revealed a smooth surface for the virgin

membrane. EDS revealed that it consisted mostly of carbon and oxygen with small amounts of sulfur likely arising from the polysulfone support. Patches of an amorphous scaly layer coating were seen on the fouled first stage membrane. Only a very thin and discontinuous foulant layer was observed on the surface of the second stage membrane, whose image was similar to that of the virgin membrane. Importantly, Al and Ca were additionally detected on both fouled membranes as shown in Figure VI-2 and Table VI-1.

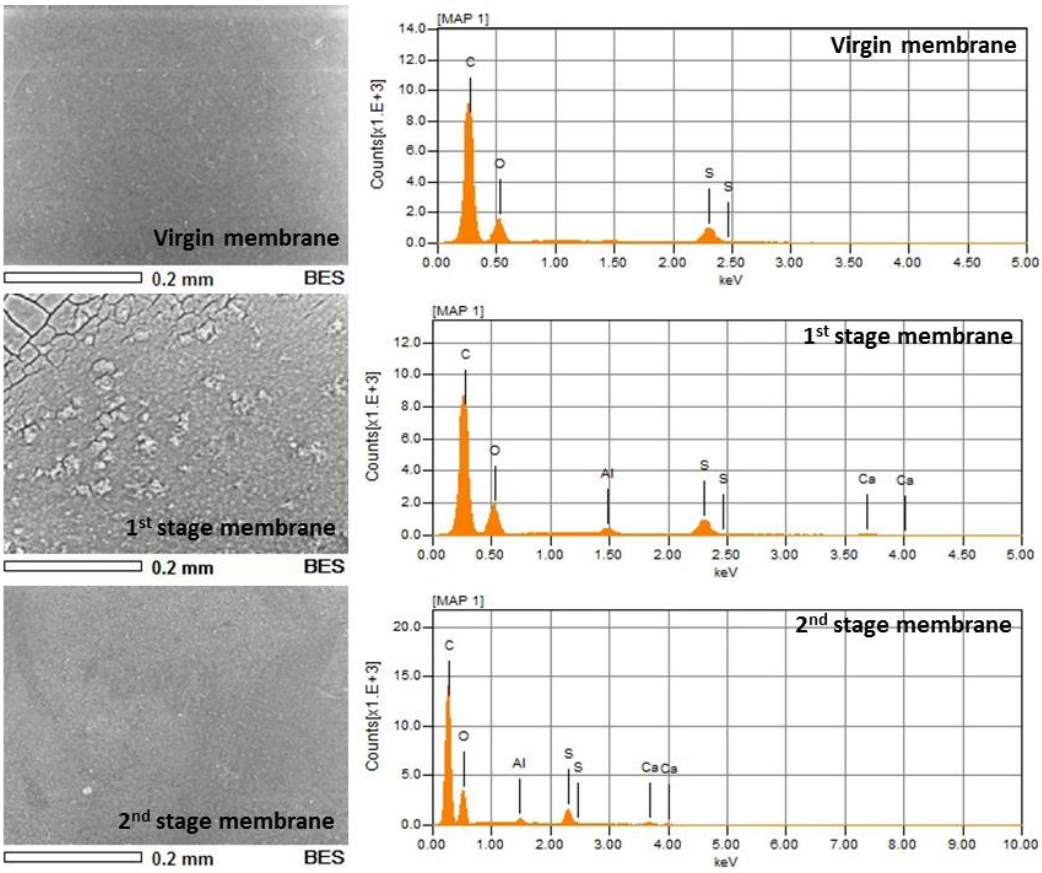

Figure VI-2. Scanning electron micrographs (at 250x magnification) of virgin and fouled membranes along with their respective surface elemental compositions obtained via EDS.

Table VI-1. Relative atomic concentration percentage of virgin and fouled membrane obtained by EDS.

Element	Virgin membrane	1st stage membrane	2nd stage membrane
C	83.69	73.50	80.84
O	13.37	22.84	15.57
S	2.95	2.54	3.17
Al	0.00	0.95	0.33
Ca	0.00	0.18	0.10

The higher relative amount of Al in the first stage membrane (Table VI-1) and the visible cake layer in the corresponding SEM image (Figure VI-2) suggest the carryover of aluminum precipitates from pretreatment. C and O concentrations were very similar in the virgin and second stage membrane, suggesting that the majority of carried over foulants deposited in the first stage itself. However, Al was detected even in the second stage, albeit at a lower concentration, suggesting that it was carried over the entire 2-stage pilot-plant. Si was not detected in any of the samples suggesting the dominance of aluminum (hydr)oxides over aluminosilicates that are present in silicon-laden feed waters [42, 193]. Very small amounts of Ca (< 0.2%) were also measured on both fouled membranes. XPS, a more sensitive technique than EDS was performed to validate these results as discussed next.

XPS survey scans confirm the presence of inorganic foulants

Al, Cl, P, and Ca were detected in survey XPS scans of fouled membranes but were absent in the virgin membrane (Table VI-2) providing further evidence for the presence of inorganic foulants. Atomic compositions of the first stage membrane after EDTA and citric acid cleaning are also shown in Table VI-2, which will be discussed later. Al and Ca were present on membrane surfaces from both stages, with more Al detected in the first-stage, validating SEM-EDS results and providing additional evidence for their role in fouling.

Interestingly, P was detected only in the second stage, which is attributed to the phosphonate based antiscalant [43, 295], as no phosphate was detected in the treated wastewater. This suggests the presence of aluminum phosphate in addition to aluminum hydroxide in the second stage [43]. Note that XPS measured only minimal S in the virgin membrane since it analyzes electrons only from the top ~10 nm. In contrast, EDS measured 3% S (Table VI-1) since its sampling depth is ~1-5 μm, which is sufficient to reach the polysulfone support.

Table VI-2. Percentage atomic concentrations of elements on virgin and fouled membranes obtained by XPS survey scans.

RO Membrane	C 1s	N 1s	O 1s	Al 2p	S 2p	Si 2p	P 2p	Cl 2p	Ca 2p
Virgin	71.7	4.5	23.7	0.0	0.1	0.0	0.0	0.0	0.0
1st stage	60.6	2.1	33.7	1.5	0.4	0.0	0.0	0.2	1.3
2nd stage	60.1	3.9	32.2	0.7	0.0	0.1	1.8	0.1	1.0
1st stage after citric acid cleaning	67.1	2.5	28.7	1.2	0.5	0.0	0.0	0.0	67.1
1st stage after EDTA cleaning	69.8	4.9	23.8	0.0	0.1	0.0	0.0	1.0	0.0

XPS survey scans also detected N in all cases, unlike EDS, given its higher sensitivity. For the virgin membrane, 4.5% N was measured and attributed to the polyamide skin layer. Lesser N percentages in fouled membranes (2.1% and 3.9% for the 1st and 2nd stage respectively) indicate relatively low amounts of proteinaceous foulants in line with visual evidence of low organic fouling. The larger decrease in N in the first stage membrane is probably due to partial masking of the polyamide signal by the thicker fouling layer (see Figure VI-2). In contrast, the very thin foulant layer in the second stage membrane only resulted in a slight reduction in N percentage compared with the virgin membrane. Reduced N coupled with increased Al, P, Ca, and O suggests the importance of inorganic foulants.

ATR-FTIR indicates possible aluminum complexation with membrane surface functionalities

Figure VI-3 shows the IR spectrum of the virgin and both stage membranes in the range 675 – 4000 cm^{-1}. Peak shifts were observed for the amide II and aromatic C=C bands from the virgin to the first stage fouled membrane (1544 to 1552 cm^{-1} and 1586 to 1584 cm^{-1}, respectively) resulting in overlapping and more intense peaks in the fouled membrane. In contrast to the amide II band, the intensity of the amide I band did not increase significantly, but it shifted from 1665 to 1654 cm^{-1}. These shifts and intensity increases could arise from interactions of membrane surface functional groups with residual organics or aluminum. Typically, the presence of proteinaceous compounds of biological origin is indicated by three absorption bands at 3300, 1653, and 1540 cm^{-1} [301] with more prominent amide I band than the amide II band [302]. However, in Figure VI-3 the amide I peak did not intensify significantly compared to the amide II band. Also, carbohydrate-like compounds that usually appear as a broad band in the region of 900-1100 cm^{-1} (bacterial fingerprints region) [176] were also not observed. These results validate visual evidence of negligible amounts of organic matter on membrane surfaces when modules were sacrificed as reported earlier. This was further corroborated by lack of bacteria seen under a fluorescence microscope (Olympus BX51) following LIVE/DEAD BacLight kit (L7007, Invitrogen) staining with SYTO9 and propidium iodide.

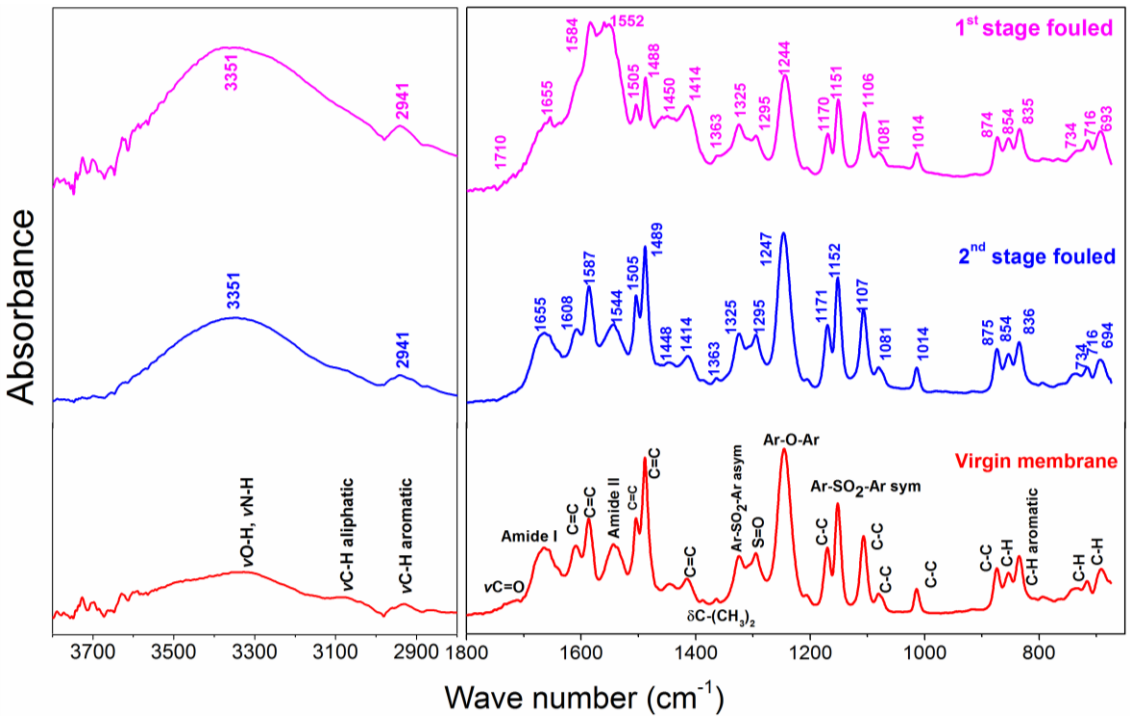

Figure VI-3. FTIR spectra of virgin and fouled membranes.

Additionally, the contact angle measured at various locations of the fouled membranes were statistically unchanged from that of the virgin membrane (33.5 ± 1.9, 32.4 ± 3.6, and 35 ± 1.8 for the first and second stage fouled membranes and the virgin membrane, respectively). Statistically similar contact angles also confirm insignificant surface accumulation of hydrophobic organics. This is consistent with alum preferentially removing hydrophobic organics from feed waters [53, 303]. Lack of significant organic foulants allows the assignment of the 1552 cm^{-1} peak shifted from 1544 cm^{-1} and 1609 cm^{-1} shoulder to asymmetric C-O vibration in bidentate or bridging Al-O-H complexes [304]. Also, the 1654 cm^{-1} peak (shifted from 1665 cm^{-1}) can be attributed to C=O stretching vibrations arising from monodentate complexation with $Al(OH)_3$ [305]. A more prominent *v*O-H band in the 3300 – 3750 cm^{-1} region attributed to Al-O-H was also seen in first stage membrane.

XPS high resolution scans provide additional evidence of specific aluminum interactions with the membrane surface

Figure VI-4 summarizes deconvoluted C 1s, O1s, and Al 2P component peaks with the relative area percentages. Comparison of Figure VI-4a, d, and g shows that interactions of membrane carbonyl functionalities with aluminum were manifested as shifts of the C=O peak from 287.8 eV to 288.1 eV for first stage membrane and to 288.0 eV for second stage membrane. Peak shifts to higher binding energies suggest inner or outer sphere complexation consistent with FTIR spectra [90]. Changes in the chemical states and shifts of Al 2p region (Figure VI-4f and i) could not be rigorously interpreted due to commonly occurring and complicated peak overlaps between oxides and hydroxides of aluminum [306]. Concurrently, the C=O peak relative area percentage increased from 4.7% for the virgin membrane to 17.7% for the first stage membrane and 8.9% for second stage membrane. Correspondingly, as summarized in Figure VI-4b, e, and h, the O=C peak at approx. 531.1 eV in the O1s spectrum increased in relative area from 16.9% for virgin membrane to 35.9% for the first stage membrane and 31.9% for second stage membrane. Significantly higher C=O and O=C peak areas (and stronger Al peak in survey scans) for the first stage is consistent with greater fouling visualized in Figure VI-1.

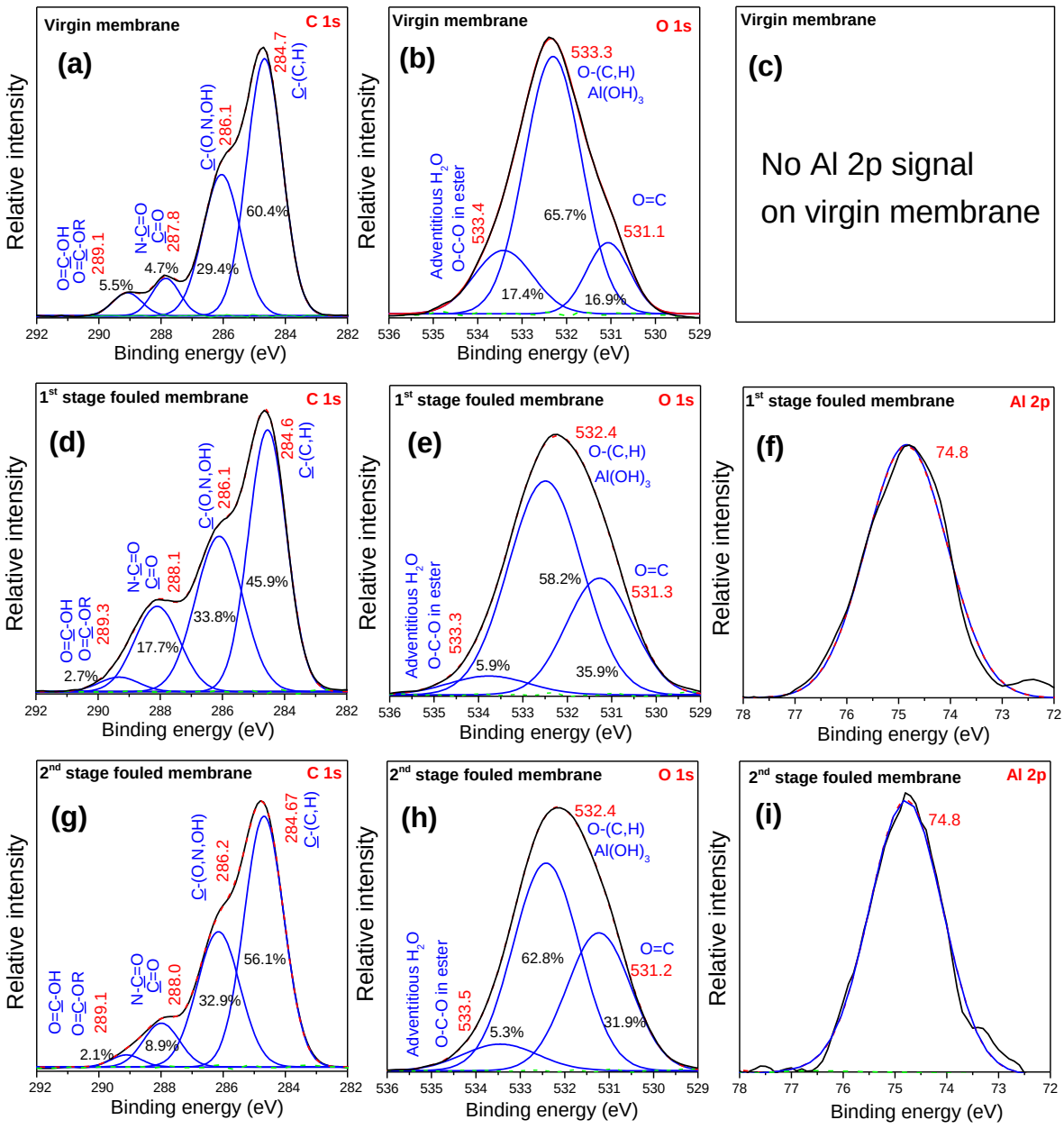

Figure VI-4. High resolution scans of C 1s, O 1s, and Al 2p regions for virgin and first and second stage fouled membranes.

Chemical regeneration of membranes

The Darcy resistance of the virgin membrane was measured to be 1.24 ± 0.01 x 10^{14} m^{-1}, which is within 1% of the manufacturer specified value of 1.23 x 10^{14} m^{-1}. The resistances of the fouled first and second stage membranes were measured to be 1.43 ± 0.02 x 10^{14} and

$1.34 \pm 0.02 \times 10^{14}$ m^{-1}. These correspond to an increase of 15% and 8% from the virgin membrane respectively. EDTA at pH 11 and citric acid at pH 4 were evaluated to detach calcium and aluminum foulants and regenerate the membrane [298-300].

Flux restoration by EDTA and citric acid and removal of Al and Ca

As summarized in Table VI-3, EDTA was better than citric acid in restoring flux in the first stage membrane (98.1 ± 1.0% and 91.0 ± 1.4% respectively). However, both EDTA and citric acid recovered the permeability of the second stage membrane to comparable levels (97.9 ± 0.4% and 98.4 ± 1.0%, respectively).

Table VI-3. Flux restoration and removal of aluminum and calcium by two cleaning agents evaluated.

	EDTA (pH 11)		Citric acid (pH 4)	
	1st stage	**2nd stage**	**1st stage**	**2nd stage**
Aluminum removed (mg/m^2)	16.0 ± 1.9	9.2 ± 2.1	9.8 ± 2.9	5.7 ± 1.8
Calcium removed (mg/m^2)	22.7 ± 3.3	7.1 ± 1.2	25.7 ± 5.4	7.6 ± 2.9
Flux restoration (%)	98.1 ± 1	97.9 ± 0.4	91.0 ± 1.4	98.4 ± 1.0

Spent cleaning solutions after membrane regeneration were analyzed by atomic absorption spectroscopy to quantify the amount of Al and Ca extracted from the membranes. As shown in Table VI-3, Higher Al and Ca concentrations were measured in both the spent cleaning solutions from the first stage consistent with its greater fouling and more intense Al and Ca peaks revealed earlier by SEM-EDS (Table VI-1) and XPS survey spectra (Table VI-2). Also, Al was better removed by EDTA from both membranes whereas Ca was equally well-extracted from both membranes by EDTA and citric acid. Interestingly, even though both cleaning agents were equally effective in removing Ca from the first stage membrane, only

91% of the flux was recovered by citric acid while EDTA restored the flux to essentially that of the virgin membrane. Hence, permeability restoration may be governed in part by aluminum removal. Given the relatively lower amounts of Al and Ca present in the second stage membrane, they were well removed by both cleaning agents consequently equally restoring the flux.

Because the first stage membrane was fouled to a greater extent (15% flux decline), its surface was also examined using XPS and FTIR after chemical cleaning to better assess the efficacy of inorganic foulant removal.

Spectroscopic confirmation of Al and Ca removal from membrane surfaces by chemical cleaning

The relative atomic concentration percentages for cleaned membranes from survey scans have already been summarized in the last two rows of Table VI-2. As observed, the Al signal disappeared after EDTA cleaning but was still present on the membrane after citric acid cleaning. This confirms the efficient Al removal by EDTA and the higher Al concentrations measured in spent EDTA cleaning solutions from both stages (Table VI-3). XPS survey scans did not identify any Ca on cleaned membrane surfaces after regeneration (Table VI-2) consistent with similar concentrations measured in both the spent cleaning solutions (Table VI-3).

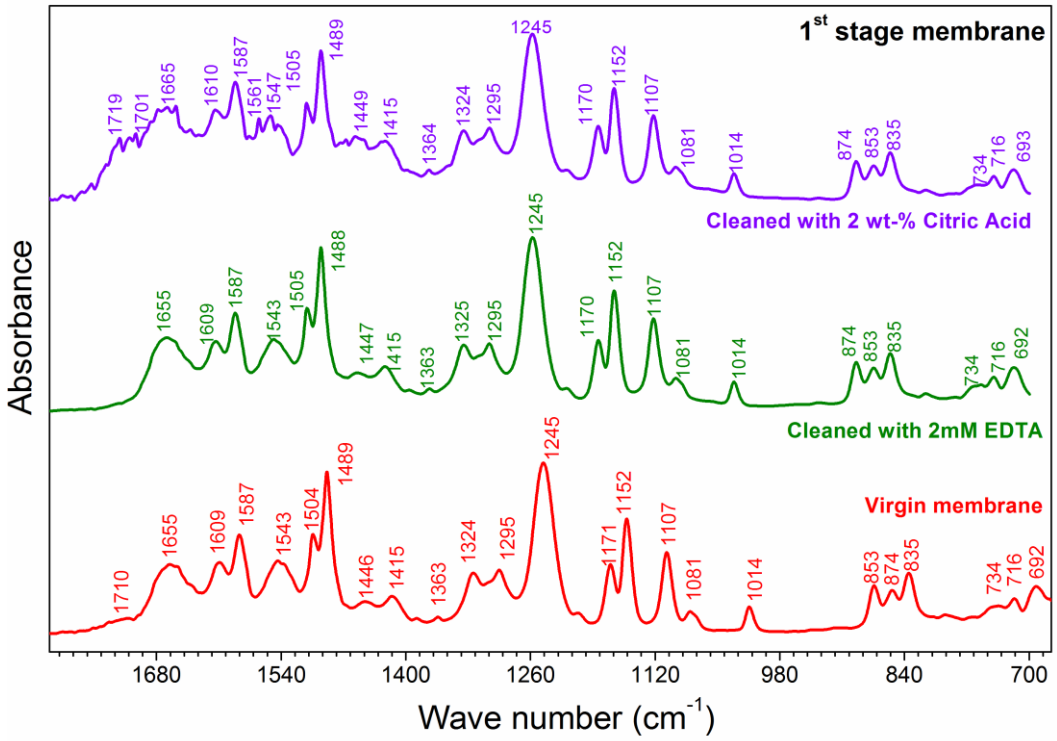

Figure VI-5. Comparison of FTIR spectra of the virgin membrane and after chemical cleaning with EDTA and citric acid.

Evidence for Al removal was also obtained by FTIR spectroscopy. The broad, overlapping, intense peak around 1540 – 1610 cm^{-1} in the spectrum of the first stage fouled membrane corresponding to Al-O-C complexes that was discussed earlier in Figure VI-3 was not observed anymore. EDTA cleaning effectively restored the underlying spectral features of the virgin membrane in this region such as peaks at 1609, 1587, and 1544 cm^{-1} that reappeared in the cleaned membrane (Figure VI-5). The intensity of many peaks (e.g. 1151, 1170, 1245 cm^{-1}, etc.) attributed to the polysulfone support layer of the virgin membrane lost due to fouling was also nearly completely recovered following EDTA cleaning further validating its effectiveness as a cleaning agent. As seen in Figure VI-5, citric acid also restored spectral features of the virgin membrane including peaks corresponding to C=C stretching vibrations,

amide I, and amide II (1540 – 1665 cm^{-1}) and the polysulfone support. However, these peaks were not as prominent compared with EDTA cleaning or the virgin membrane.

Presence of residual chemical regenerants on cleaned membrane surfaces

High resolution XPS of cleaned membrane surfaces shows the incomplete recovery of the C 1s and O 1s regions (Figure VI-6a, b, d, and e) compared with the virgin membrane (Figure VI-4a and b). Figure VI-6a shows a relatively more intense O=C-O-(H, R) peak at 288.9 eV after citric acid cleaning probably due residual –COOH groups from the cleaning solution. This was also consistent with the high resolution scan of O 1s region in which the peak around 533.5 eV corresponding to O-C-O also increased relatively (Figure VI-6b). In addition, the shoulder at 1719 cm^{-1} in IR spectra corresponding to –COOH for the citric acid cleaned membrane (Figure VI-5) was more prominent than even the virgin membrane. These indicate citric acid remnants on the cleaned membrane. Similar observations were also made for membranes cleaned with EDTA. For example, the C-(O, N, OH) peak at 286.3 eV significantly intensified (Figure VI-6d) likely due to amines from residual EDTA. Also, the acid peak at 289.1 eV was negligible (compared with the virgin membrane and citric acid cleaned membrane at 288.9 eV) because of deprotonation of –COOH groups at high pH during EDTA cleaning. Further, this was accompanied by an increase in the 531.4 eV carboxylate peak (Figure VI-6e) in the O 1s region. Hence, even "thorough" rinsing did not completely remove cleaning agents suggesting their strong binding with functionalities on the membrane surface. Therefore, even though residual cleaning agents had negligible impact on flux recovery in the short-term (Table VI-3), their effects over extended periods, i.e. multiple cleaning cycles, need to be evaluated.

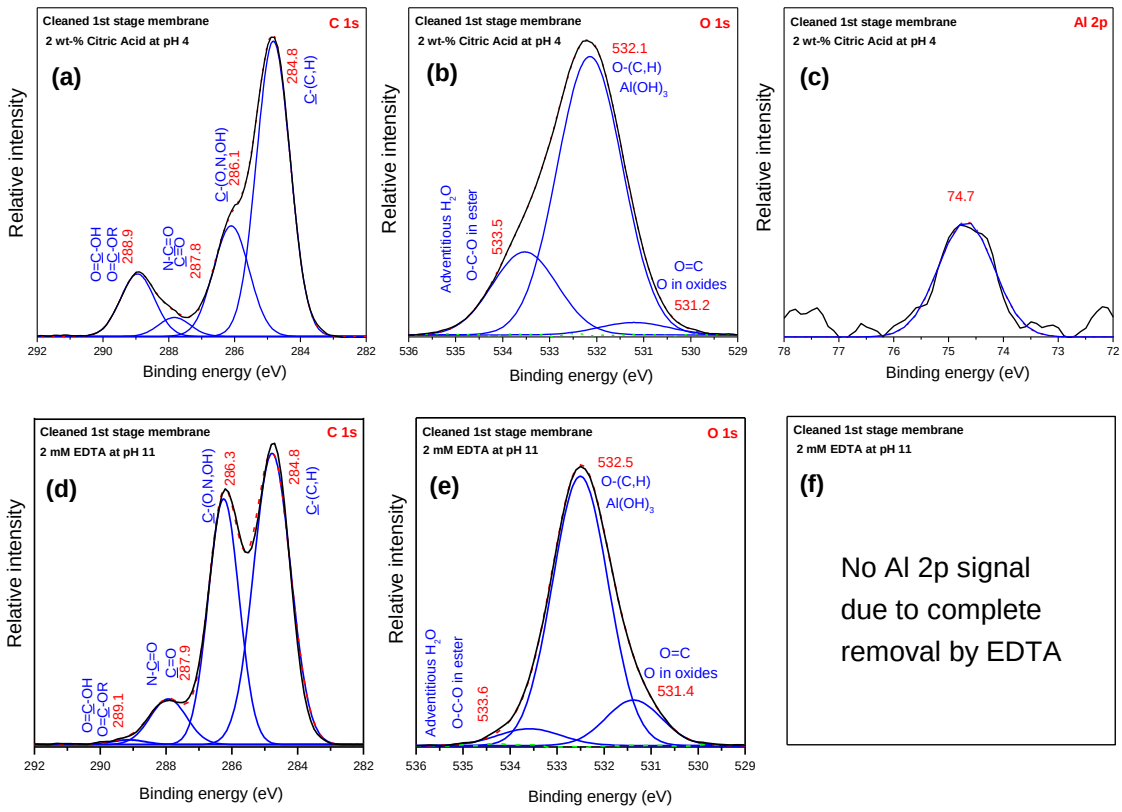

Figure VI-6. High resolution XPS scans of C 1s, O 1s, and Al 2p regions for the cleaned membranes.

Summary and conclusions

Detailed surface analysis of membranes from a real-world two-stage water reuse RO pilot-plant revealed inorganic fouling (Al, Ca, and P) to be the main cause of flux decline. Only weak signals from protein-like and carbohydrate-like substances were observed in FTIR spectra and the contact angle of fouled and virgin membranes were statistically similar suggesting negligible organic fouling and validating EDS and XPS interpretations of inorganic fouling. The first stage membrane exhibited a higher degree of fouling due to deposition of aluminum carried over from coagulation pretreatment. Smaller amounts of aluminum were also detected on the second stage membrane demonstrating extensive carryover throughout the entire pilot system. Hence, proper monitoring and control of coagulation pretreatment is crucial

to successful RO operation. Silicon was not detected in either stage and phosphorous was detected only in the second stage. This suggests deposition of aluminum (hydr)oxide in both stages whereas aluminum phosphate was present only in the second stage. Fouling by aluminosilicate was negligible unlike in silicon-rich waters [42, 193]. Further, polyaluminum chloride may be a better choice than alum [294], since unlike alum it does not complex with phosphonate-based antiscalants thereby leading to fouling [307]. Although Ca was deposited on both the first- and second-stages, it seemed to be less important than Al in causing flux decline, potentially because organic fouling was insignificant [186, 308]. In contrast to Al and Ca, P was detected only in the second stage and attributed to the proprietary antiscalant. To our knowledge, this is one of the first reports of dominant inorganic fouling of RO membranes during wastewater reclamation since most previous investigations have identified organic matter as the major foulant e.g. [165, 285, 286, 296]. Hence, we recommend monitoring any added chemicals such as the coagulant (Al or Fe), antiscalant, or disinfectant in the RO feed water since they may also cause fouling.

EDTA at high pH was more effective than citric acid (pH 4) in removing aluminum and restoring flux. Although citric acid was equally effective as EDTA in removing calcium, it could not completely recover flux from the first stage membrane. Hence, it appears that flux decline may be caused more by aluminum than calcium. Additionally, since EDTA at high pH can also efficiently remove organic foulants [15, 298], a single-step cleaning procedure may be sufficient to regenerate RO membranes employed for water reuse. Nevertheless, we recommend evaluating different chemical formulations at pilot-scale before selecting one for membrane cleaning. Further, high resolution XPS scans detected residues of cleaning agents despite seemingly thorough rinsing by ultrapure water. Although short-term testing did not

show any deleterious effects from such residues, their effects on membrane life and flux deterioration in the long-term need to be evaluated over numerous cleaning cycles. We believe that practicing engineers may be unaware of this issue since commercial autopsies typically rely on EDS and sometimes XPS survey scans that are less sensitive than high resolution XPS and consequently do not detect membrane-bound cleaning agent residues.

CHAPTER VII

MECHANISMS OF BORON REMOVAL FROM HYDRAULIC FRACTURING WASTEWATER BY ALUMINUM ELECTROCOAGULATION *

Introduction

The explosive growth in the exploration and production of oil and gas from unconventional sources is associated with significant water management issues [309]. One increasingly popular well stimulation method is hydraulic fracturing (or fracking) wherein large quantities of water mixed with a proppant and other chemicals is injected into the subsurface at high pressure to unlock hydrocarbons [310]. This environmentally controversial technique produces copious amounts of briny wastewater consisting of a mixture of the injected fluid, local groundwater, and hydrocarbons. Concerns regarding high water consumption, environmental impacts of local wastewater discharge, onsite (waste)water trucking, and the desire to reuse water have resulted in growing regulatory and technological interest in treating flowback and produced water [311, 312].

One of the myriad chemicals used in fracturing fluids is boron, which is used as a cross-linking agent to impart the necessary rheological properties to successfully deliver the proppant to fracture the rock and also to recover the injected fluid after fracking. Although boron is essential for plant growth and is a possible human trace nutrient, chronic exposure even at low doses causes testicular atrophy, decreased survival, and developmental and reproductive toxicity in animals [313]. Some crops such as blackberry are sensitive to even low (< 0.5 mg/L)

* Reprinted with permission from "Mechanisms of boron removal from hydraulic fracturing wastewater by aluminum electrocoagulation", M.A. Sari and S. Chellam, 2015, Journal of Colloid and Interface Science, 458, 103-111, Copyright 2015 by Elsevier.

levels of boron while many other fruits and vegetables experience toxicity at concentrations > 0.5 mg/L [44, 314]. Boron containing viscosity modifiers also need to be removed from the flowback/produced water to make the reused water compatible with "gel-frac" formulations to fracture subsequent wells [309]. Therefore, boron is an element of concern which needs to be removed from hydraulic fracturing wastewater before it can be beneficially reused for crop irrigation, reused to frack additional wells, or discharged into receiving surface waters [44, 315, 316].

Ion exchange, electrocoagulation, adsorption onto clays and double-layered hydroxides have been shown to be effective for boron removal from low-salinity wastewater [44, 317-320]. Low concentrations of boron can also be effectively removed from seawater using reverse osmosis. However, these results do not directly apply to hydraulic fracturing wastewaters which contain high concentrations of boron as well as other inorganic constituents, organic compounds, and microorganisms [318, 321-323]. On the other hand, physicochemical techniques for flowback/ produced water treatment have largely focused on dispersed and soluble oil, organic compounds, naturally occurring radioactive materials, "heavy" metals, and several cations and anions but much less is known about boron treatment from oil-field wastewaters [323]. Electrocoagulation of most hydraulic fracturing wastewaters can be performed at elevated current densities in an energy efficient manner due to their high electrical conductivity [324]. Hence, small and portable electrolysis systems with short residence times can be designed for rapid field deployment making electrocoagulation a potentially promising technology for treatment of flowback/produced water including boron.

To date, boron removal by electrocoagulation has been predominantly evaluated using low salinity synthetic wastewaters to empirically determine the role of operating parameters

[48, 49, 324] although limited data with actual wastewater are becoming available [50-52]. However, the nature of specific interactions leading to a mechanistic understanding of boron uptake during electrochemical treatment of wastewater remains elusive even though bulk measurements suggest that chemisorption of boron to aluminum precipitates is endothermic [51].

The principal objectives of this manuscript are to provide direct evidence of boron adsorption onto electrochemically generated aluminum hydroxide flocs and obtain clues to associated uptake mechanisms. Electro-coagulation experiments were performed using an actual hydraulic fracturing wastewater sample from the Eagle Ford reservoir in Southeast Texas. Floc surfaces were rigorously characterized using Attenuated Total Reflection – Fourier transform infrared (ATR-FTIR) spectroscopy and X-ray photoelectron spectroscopy (XPS) to establish boron coordination. Experiments were designed primarily to investigate boron uptake mechanisms by $Al(OH)_3$ flocs, not simply to parametrically evaluate the role of electrochemical cell operating conditions to maximize its removal.

Experiments

Boron measurement

Boron was quantified by D-mannitol potentiometric titrations (ASTM D-3082-79) [314, 325]. $KMnO_4$ and EDTA were added prior to mannitol addition to break any organo-boron bonds, oxidize boron to borate, and chelate potentially interfering metals ions especially since aluminum was added as the electrocoagulant. Several QA/QC protocols were performed to ensure the integrity of our measurements. First, a 100 mg/L boron spike in 25,000 mg/L NaCl solution was measured by atomic absorption spectroscopy to be 99.6 ± 2.2 mg/L and by

D-mannitol titration to be 98.9 ± 0.1 mg/L. Next, a 25,000 mg/L NaCl solution spiked with 100 mg/L boron was electro-coagulated at 5 different aluminum dosages. For each dose, boron was measured in the feed water, supernatant, and the flocs after dissolving them at low pH using HCl. Boron recovery in these 5 experiments was 96.3 ± 5.6 %. Finally, using the same floc-dissolution procedure, boron was recovered to 96.1% and 100.7% in two separate tests where it was spiked to the actual hydraulic fracturing water sample. These QA/QC tests demonstrate accurate and precise boron measurements allowing comparison of data generated over the entire duration of experimentation.

Sample water

A flowback/produced water sample was obtained from the Eagle Ford formation in Southeast Texas during hydraulic fracturing after water-flooding. This black calcareous shale was chosen because a 50 mile wide and 250 feet thick play at depths between 4000 and 14,000 feet is one of the most heavily drilled enhanced oil/gas recovery targets in the United States [326, 327]. Several physicochemical water quality parameters were measured using reaction cell inductively coupled plasma – mass spectrometry [328] and colorimetry to establish its composition and assist with data interpretation. Selected experiments were also performed with a 25,000 mg/L NaCl solution containing 100 mg/L boron to better understand electrocoagulation mechanisms by reducing interferences from other hydraulic fracturing water components.

Electrocoagulation

Bench scale experiments were conducted in a 500 mL custom-made Perspex cell fitted with an annular electrode geometry comprised of a 15 cm (9 cm submerged, initial effective area of 20.26 cm^2) aluminum anode (99.95% metal basis, Alfa Aesar) and a porous cylindrical

316-stainless steel cathode . Before each experiment, the anode was mechanically cleaned by using fine sand paper, submerged in dilute HNO_3 solution for 1 hour, and thoroughly rinsed with deionized water. Occasionally, the whole unit was cleaned with dilute HNO_3. Electrocoagulation performance is known to be a strong function of reactor design including geometry, number, spacing, and type of electrodes, current density, background water composition, and numerous other operational parameters [32, 33, 89]. Since a variety of bench-scale cell configurations have already been used to empirically determine boron removal, tests were designed to better understand removal mechanisms, not simply to maximize removal. Initial experiments were conducted at pH 6.4 and 8.0, high current densities (20, 50, and 80 mA/cm^2), and aluminum dosages < 1,400 mg/L to evaluate boron removal [49, 51, 314, 329]. High current densities were achieved since the high wastewater salinity substantially lowered the cell internal resistance. Due to the high rate of aluminum dissolution and high electrocoagulant dosages, the anode diameter was measured at the start of each experiment for accurate comparisons with Faraday's law. A 12 mL sample was collected immediately after electrolysis and acidified to pH 2 using HCl to dissolve $Al(OH)_3$ precipitates before measuring total aluminum concentrations using atomic absorption spectroscopy (Flame AA-AAnalyst 300, Perkin-Elmer) [24]. Flocs were harvested at the end of the experiment by centrifugation for 20 minutes at 6000 rpm (*4500g*) for detailed spectroscopic analysis as described next. The pH was continuously monitored and held constant by periodically adding small amounts of HCl because a slight drift towards higher values was observed especially for long electrolysis durations, i.e. high coagulant dosages.

ATR-FTIR spectroscopy and XPS

The moist paste generated after centrifugation described earlier was vacuum-dried and

ground to fine particles using an agate mortar and pestle. Infrared spectra between 4000 – 650 cm^{-1} were collected using a Nicolet iS10 spectrometer equipped with an Ever-Glo MIR source, DTGS detector, KBr beam splitter and Omnic 8.5 Software. Prior to each analysis, the background spectrum was collected on a clean transmissive Ge window. An average of three separate spectra, each consisting of 512 scans collected at 4 cm^{-1} resolution is reported herein. A 20 kHz low-pass filter was used to prevent aliasing along with a zero filling factor of 2 using a Blackman Harris three-term apodization and Mertz phase correction. ATR-FTIR spectra were collected for (1) fresh "pure" $Al(OH)_3$ precipitates formed by electrolyzing 25,000 mg/L NaCl solution without boron, (2) fresh $Al(OH)_3$ precipitates by electrocoagulating 100 mg/L boron in 25,000 mg/L NaCl solution, (3) electrocoagulated flocs of actual hydraulic fracturing wastewater from Eagle Ford, and (4) raw flowback/produced water components after room temperature evaporation.

Detailed information on the surface elemental composition of the solids was also obtained with a PHI 5700 X-ray photoelectron spectrometer equipped with a monochromatic Al Kα source ($h\nu$ = 1486.7 eV) incident at 90° relative to the axis of a hemispherical energy analyzer. Since the material of the solids is non-conducting, the neutralizer was turned on to reduce charging artifacts. Survey spectra were obtained over the entire range (0-1400 eV) and high-resolution spectra were obtained for photoelectrons emitted from B 1s, O 1s, and Al 2p regions to analyze their respective functionalities. Prior to high resolution scanning, electron binding energies were calibrated with respect to adventitious carbon at 285 eV. After integrated baseline background subtraction with Shirley routine, peak areas for B 1s, O 1s, and Al 2p regions were obtained assuming mixed Gaussian-Lorentzian shapes and correcting for sensitivity factors. It is emphasized that the B 1s region is susceptible to interference from the

Cl 2p peak arising from the high chloride concentration. Therefore, only for XPS (not FTIR), the moist centrifuged paste was carefully washed three times with ultrapure water to reduce the chloride concentration while still being able to detect boron. The paste was then vacuum-dried and pressed on 0.25 mm thick indium substrates (99.99% as In, Alfa Aesar) prior to XPS.

X-ray diffractometry

Aluminum polymorphs generated during electrocoagulation were also examined by X-ray diffraction (XRD, Siemens D5000) equipped with a graphite monochromator. The moist centrifuged paste was vacuum-dried at room temperature (to avoid crystallinity development that accompanies high-temperature drying [306, 330]), powdered, and deposited as a thin uniform coat on a zero background sample holder. Diffraction patterns were collected using CuK□ radiation (1.54056 Å) at 40 kV and 30 mA in the 2θ scan range from 10° to 75° with steps of 0.03°2θ/s. The Joint Committee for Powder Diffraction Studies database was used to interpret diffractograms and identify peaks.

Results and discussion

Chemical composition of the hydraulic fracturing wastewater

The collected sample was highly saline with chloride and sodium as its main components and calcium contributing to most of the hardness (Table VII-1). It was also high in turbidity and rich in organic carbon. The high alkalinity, silica, and calcium are consistent with its geologic origins in calcium carbonate rock (predominantly limestone and marlstone) and shale [326, 327]. Phosphate and ammonia were low facilitating boron measurement by D-mannitol potentiometric titration. Aluminum and iron were also low as reported for other produced waters, but boron levels were slightly elevated at ~ 120 mg/L [51, 297, 315, 331,

332].

Table VII-1. Summary of flowback/produced water characteristics.

Parameter	Unit	Concentration or value
pH	-	7.8 ± 0.1
Turbidity	NTU	117 ± 15
Total suspended solids	mg/L	219
Total dissolved solids	mg/L	28,900 ± 200
Dissolved organic carbon	mg/L	1,089 ± 115
UV_{254}	cm^{-1}	2.39 ± 0.1
Total hardness	mg/L as $CaCO_3$	2,920 ± 170
Ca hardness	mg/L as $CaCO_3$	2,620 ± 28
Alkalinity	mg/L as $CaCO_3$	355 ± 9.5
SiO_2	mg/L	185 ± 22
Cl^-	mg/L	20,606 ± 1070
Fe	mg/L	5 ± 0.5
B	mg/L	123 ± 4
Na	mg/L	8,769 ± 675
Al	mg/L	< 0.5
Ba	mg/L	49 ± 5
Ca	mg/L	1,038 ± 14
P	mg/L as PO_4^{-3}	1.19 ± 0.15
Nitrate	mg/L	2.25 ± 0.07
Ammonia	mg/L	0.4 ± 0.01
Sulfate	mg/L	69.95 ± 1.2

30 mL of this sample was evaporated at room temperature to be probed by ATR-FTIR analysis (see red colored spectrum later in Figure VII-8). IR bands primarily corresponded to inorganic constituents including silica (νSi-O-Si 830 cm^{-1}, νSi-O 1100 cm^{-1}), boron compounds (νB-O-B 1340 cm^{-1}, νB-O 1000 cm^{-1}), carbonates (νCO_3^{2-} 1456 cm^{-1}, νC-O 830 cm^{-1}), coordinated carbonates (νCO_3^{2-} 1640-1540 cm^{-1}, νC-O 1340 cm^{-1}, νC-O 960 cm^{-1}), and sulfates (ν_{as} S-O 1064 cm^{-1}). Aliphatic and aromatic stretching vibrations (νC-H aliphatic 2850 cm^{-1}, νC-H aromatic 2950 cm^{-1}) were also observed indicating the presence of oil and grease

[333]. Significant bands at 3700-3000 cm^{-1} (νH-O-H) and 1700-1600 cm^{-1} (δH-O-H) are largely due to residual water with potential contributions from phenol, which is commonly reported as a produced water constituent [321].

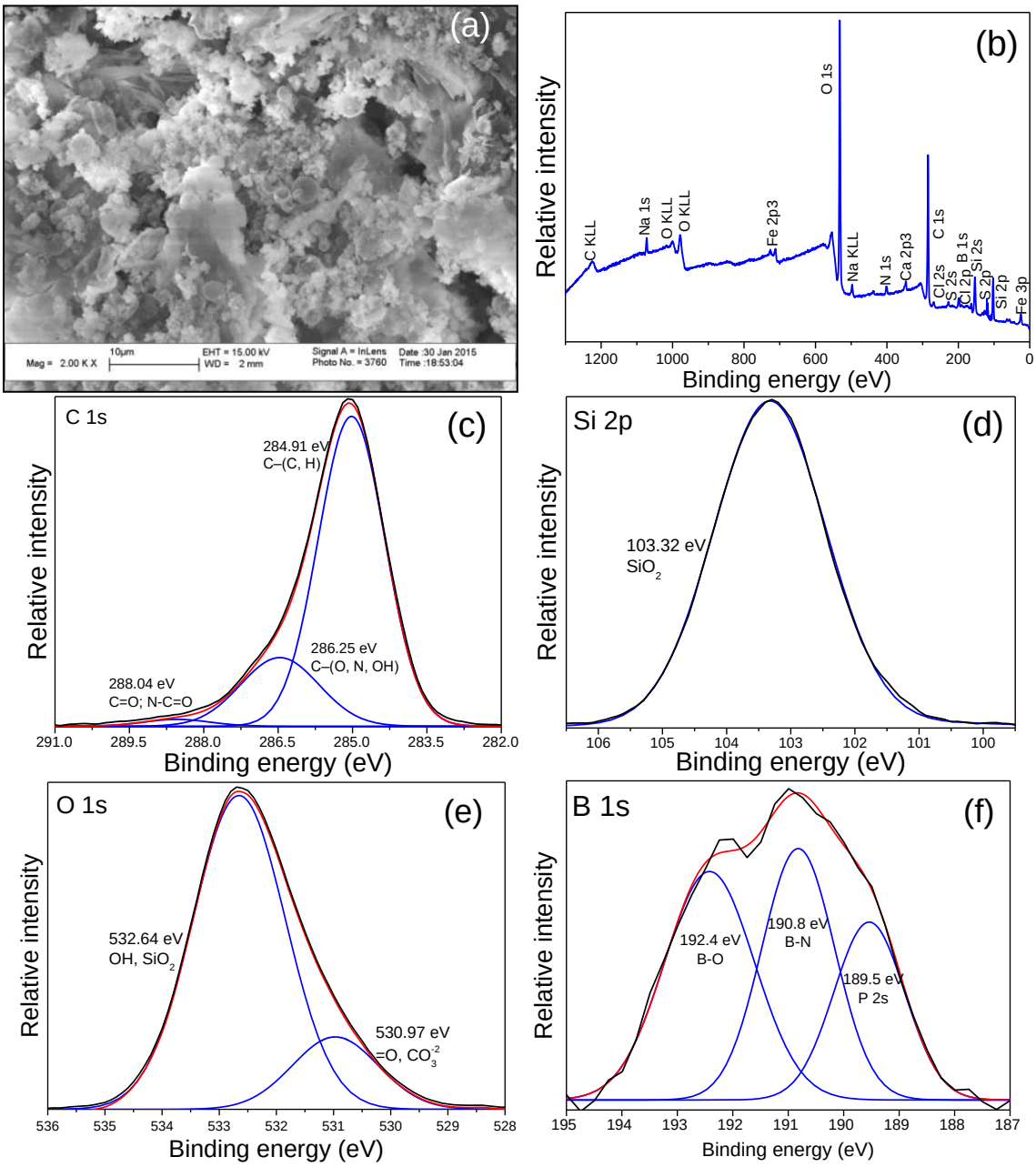

Figure VII-1. Hydraulic fracturing wastewater components captured by a nanofiltration membrane: SEM image (a), XPS survey scan (b), high resolution scans for carbon, silicon, oxygen, and boron (c, d, e, and f respectively).

Additional qualitative compositional information on the air-dried solids was also obtained by XPS. However, the massive excess of chloride masked all other signals, particularly boron (the focus of this study), since their binding energies are very close to each other. Hence, 500 mL of the produced water was nanofiltered in the dead-end mode with vigorous stirring in an effort to selectively remove chloride and obtain a clear XPS boron signal. (Note that the extremely high osmotic pressure and inherently higher rejection of chloride disallowed the use of reverse osmosis.) A thick cake layer was visualized on the nanofiltration membrane surface by scanning electron microscopy suggesting that this procedure successfully captured a substantial fraction of the produced water components and precipitated solids (Figure VII-1a). The cake morphology suggests the dominance of inorganic materials in the hydraulic fracturing wastewater, consistent with water quality data in Table VII-1 as well as FTIR and XPS data described below. Survey scans (Figure VII-1b) revealed C, O, and Si as the major elements with lesser contributions from B, Fe, Ca, N, and S.

Note that weak Cl 2p signals in Figure VII-1b confirm that the nanofilter allowed the relatively free passage of chloride ions but captured other trace constituents allowing detection by XPS. High resolution scans for the major elements in the produced water were also obtained to establish their chemical states. The C 1s peak (Figure VII-1c) was deconvoluted into three components: (i) a C–(C, H) bonding peak at 284.9 eV associated with carbon chains, (ii) a peak at 286.3 eV attributed to C–(O, N, OH) associated with alcohol, ether, or amine, (iii) a C=O or N–C=O peak at 288 eV as in carboxylate, carbonyl, amide, acetal, or hemiacetal. The position of Si 2p peak at 103.3 eV (Figure VII-1d) revealed silica as its principal component. The O 1s peak (Figure VII-1e) was resolved into two peaks at 530.9 eV corresponding to carbonates and 532.6 eV corresponding to oxygen in SiO_2. The B 1s spectrum was

deconvoluted into three peaks (Figure VII-1f), (i) B-N peak at 190.8 eV, (ii) B-O peak at 192.4 eV and (iii) elemental boron, boride, or a shifted P 2s peak at 189.5 eV [334]. The assignment to P is justified by its detection by colorimetry (Table VII-1) and high resolution XPS of P 2p (see, which shows the relative atomic concentrations of the solids deposited on the nanofilter surface calculated from XPS).

Table VII-2. XPS measurements of relative atomic concentrations of produced water constituents concentrated by NF.

Element	C 1s	N 1s	O 1s	Na 1s	Si 2p	S 2p	Cl 2p	Ca 2p	Fe 2p3	B 1s	P 2p
Relative atomic percentage (%)	42.47	2.21	34.4	1.36	13.23	1.07	1.57	0.73	1.41	1.12	0.44

Boron speciation

Figure VII-2 depicts boron speciation using stability constants measured at high ionic strength [335] and boron concentration of 123 mg/L, which closely represents the saline hydraulic fracturing water. The least hydrolyzed form of boron, $B(OH)_3$ is a weak acid and is a trigonal planar molecule. Its hydrolysis to the tetrahedral monoborate ion is rapid and reversible in alkaline pH values [335]: $B(OH)_3 + H_2O \leftrightarrow B(OH)_4^- + H^+$. Polyborates can be formed rapidly and reversibly: $xB(OH)_3 + (y\text{-}z)H_2O \leftrightarrow B_xO_z(OH)_{3x+y-2z}^{\ y-} + yH^+$. However, as seen in the inset of Figure VII-2, polynuclear species are not significant for concentrations typical of flowback/produced waters. $B(OH)_3$ is the dominant species at pH 8 of our experiments with only minor (~10 %) contributions from $B(OH)_4^-$.

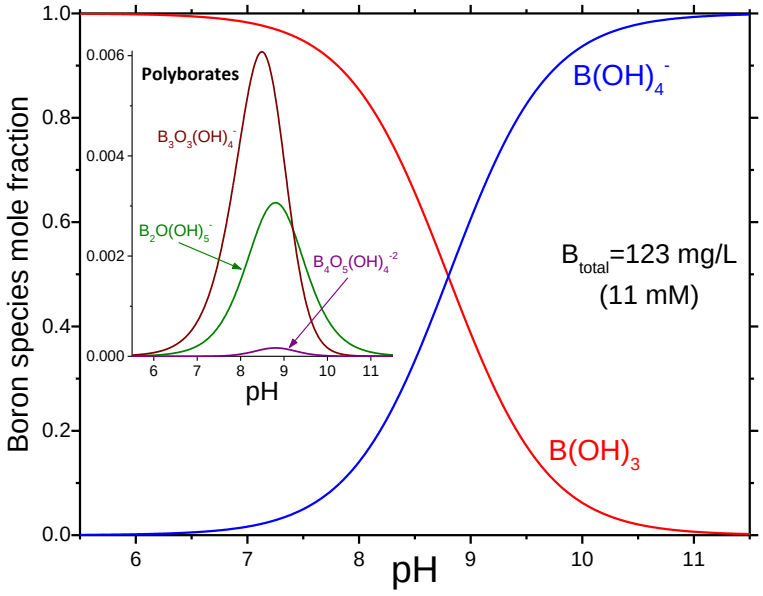

Figure VII-2. Equilibrium boron speciation at high background ionic strength and at 11 mM concentration. Note that polyborates do not represent a significant mole fraction under these conditions (equilibrium constants from [335]).

Aluminum dissolution

As seen in Figure VII-3a, higher aluminum concentrations were measured in suspension for the 25,000 mg/L NaCl solution and actual hydraulic fracturing wastewater compared to strictly electrochemical dissolution. Aluminum increased linearly with electrolysis time with statistically indistinguishable slopes for both feed waters (0.237 ± 0.004 mg/L-s) compared with the theoretically predicted value of 0.181 mg/L-s from Faraday's law. No statistical differences in aluminum dissolution between the NaCl solution devoid of organic matter and the actual wastewater containing over 1,000 mg/L dissolved organic carbon demonstrates that organics did not contribute significantly to passivation under our experimental conditions [254]. Hydrogen bubbles were visibly released at the cathode but did not cause significant flotation suggesting that these organic moieties were less hydrophobic than those in surface water (e.g. humic acids) which facilitate electroflotation [31, 89]. The

consistent super-Faradaic dissolution with 131% efficiency suggests that a portion of aluminum was chemically dissolved from the anode and that there was no competition with oxygen evolution [243]. The (hydr)oxide passivation layer undergoes localized attack in the presence of chloride ions causing super-Faradaic electrocoagulant dissolution [111, 336]. Evidence for pitting corrosion was obtained by examining the anode surface by electron microscopy. The new anode surface was smooth (Figure VII-3b), whereas deep pits were observed after electrolysis (Figure VII-3c and d). Chloride ions can also be incorporated into the anodic (hydr)oxide film to form $Al(OH)_2Cl$, $Al(OH)Cl_2$, and $AlCl_3$ which will be subsequently dissolved into the solution by formation of $AlCl_4^-$ [337, 338].

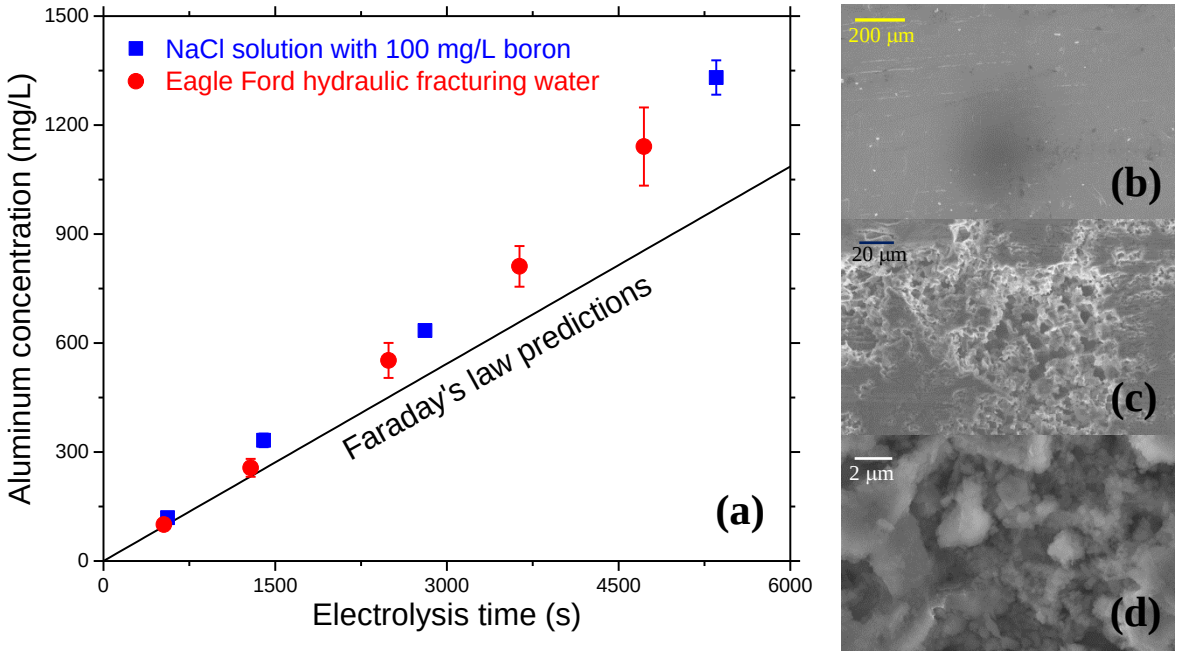

Figure VII-3. Super-Faradaic aluminum dissolution in chloride containing solutions (a). Trends for a 25 g/L NaCl solution (blue squares ■) and the produced water containing organic matter (red circles ●) were statistically indistinguishable. The solid black line depicts purely theoretical predictions of Faraday's law with no fitting parameters. Electron micrographs of a new electrode (b), pitted anode (c), and a high magnification image of a pit (d) are shown. The scale bars are different by a factor of 10 in (b), (c), and (d).

Aluminum precipitation

The O/Al ratio in flocs formed by electrolyzing NaCl solution → 3 suggesting the presence of $Al(OH)_3$. This was confirmed by the position of the Al 2p peak at 74.56 eV reported for pure $Al(OH)_3$ [115]. The O-H bond at 523.3eV contributed to 71% of the deconvoluted O 1s peak resulting in a 1:3 stoichiometric Al:OH ratio proving the dominance of $Al(OH)_3$ rather than oxides or oxyhydroxides (data not shown). The only strong peaks in X-ray diffractograms of harvested electrocoagulated flocs corresponded to halite as summarized in Figure VII-4.

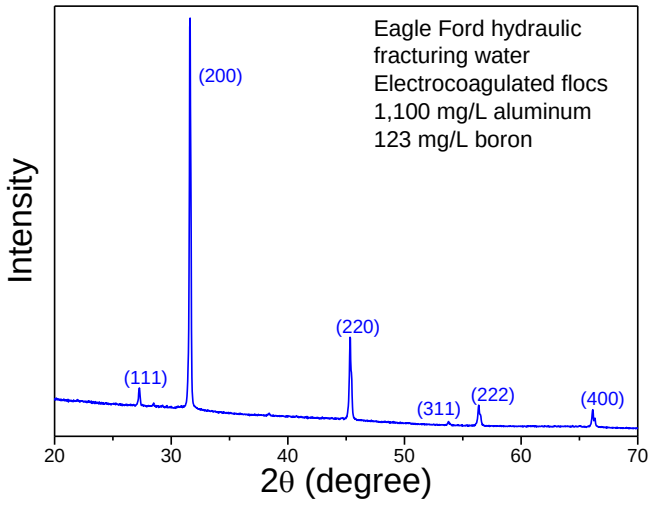

Figure VII-4. X-ray diffractograms of flocs formed after electrocoagulation of produced water showing halite as the only strong signals.

Hence, there was no evidence of crystallinity and electrolysis of the produced water generated only amorphous $Al(OH)_3$ similar to low salinity surface water and alum coagulation of surface water [24, 339]. Boron adsorption would have also inhibited polymerization and prevented the formation of highly ordered structures [340]. The absence of any crystalline phase was also evident in FTIR spectra (Figure VII-8) where only one broad band appeared

around 3400 cm^{-1} in flocs following electrocoagulation of NaCl solutions and the produced water [340]. These observations point to the following aluminum reactions in the electrochemical cell [24, 32, 33, 111, 243]:

$Al^0(s) \rightarrow Al^{3+} + 3e^-$ (anode)

$3H_2O + 3e^- \rightarrow 3OH^- + 1.5H_2(g)$ (cathode)

$Al^{3+} + 6H_2O \rightarrow [Al(H_2O)_6]^{3+}(aq)$ (hydrolysis)

$[Al(H_2O)_6]^{3+}(aq) \rightarrow [AlOH(H_2O)_5]^{2+}(aq) + H^+$(hydrolysis)

$[AlOH(H_2O)_5]^{2+}(aq) \rightarrow [Al(OH)_2(H_2O)_4]^+(aq) + H^+$ (hydrolysis) and many other such reactions

$Al^{3+} + 3OH^- \rightarrow Al(OH)_3(am)$ (precipitation)

$Al^0(s) + 3H_2O \rightarrow Al(OH)_3(s) + 1.5H_2(g)$ (electrodissolution)

$2Al^0(s) + 6H_2O \leftrightarrow 2Al^{3+}(aq) + 3H_2(g) + 6OH^-$ (chemical dissolution)

Chlorine generation during electrocoagulation

Anodic oxidation of chloride ions can yield chlorine gas which disproportionates into HOCl that dissociates to OCl^- at alkaline pH:

$2Cl^- (aq) \leftrightarrow Cl_2 (g) + 2e^-$

$Cl_2 (g) + H_2O \leftrightarrow HOCl (aq) + H^+ + Cl^-$

$HOCl (aq) \leftrightarrow OCl^- + H^+$

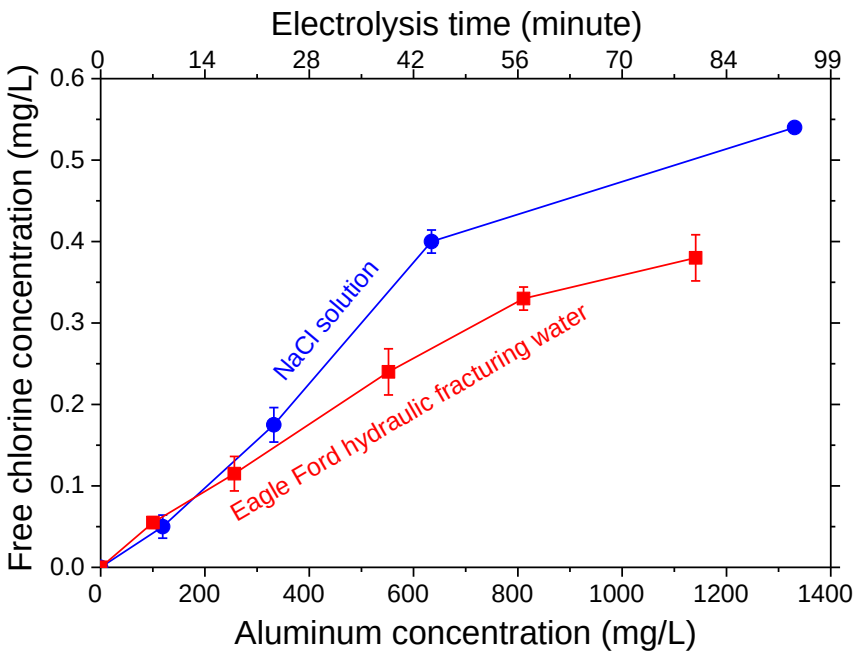

Figure VII-5. Aluminum electrocoagulation of salt solutions and hydraulic fracturing wastewater generates free chlorine.

As predicted, chlorine was measured during electrocoagulation of the NaCl solution and hydraulic fracturing wastewater. Figure VII-5 shows the production of higher concentrations of chlorine when electrolysis duration or electrical charge passage was increased corresponding to the electrooxidation of progressively more chloride ions. Free chlorine generated during electrocoagulation can inactivate bacteria, algae, and viruses [41, 70, 341] in produced waters, which is necessary when it is stored in surface impoundments prior to treatment. This represents an additional advantage over conventional coagulation using alum or iron salts. As shown in Figure VII-5, measured chlorine concentrations were lower during electrocoagulation of actual produced water compared to NaCl solution demonstrating a higher demand arising from reactions with organics and other wastewater components [144].

Electrocoagulation process parameters

Electrocoagulation process parameters that favored boron removal were first

established to select appropriate experimental conditions to generate flocs for detailed surface analysis. As reported by others [47, 324], higher boron removal was observed at pH 8.0 compared with pH 6.4 (Figure VII-6a). Hence, preferential adsorption of boric acid onto $Al(OH)_3$ floc surfaces occurred at a pH just below the value where the negatively charged aluminum species ($Al(OH)_4^-$) became dominant [342, 343]. Boron removal monotonically increased in the range of aluminum dosages employed (Figure VII-6b) but remained relatively constant at current density values $\geq$ 50 mA/cm^2 (Figure VII-6c). Based on these observations, surfaces of flocs generated in experiments performed at 1,100 mg/L aluminum dosage, pH 8, and 50 mA/cm^2 were analyzed in detail. The relatively low (49%) boron removal under these conditions corresponds to an extremely low Al:B mass ratio of only 9. Boron removal can be increased by adding more aluminum electrocoagulant. For example, > 90% of boron was removed by increasing Al:B ratio to near 70 [47, 51, 324]. Note that this translates to an aluminum dosage of > 8,000 mg/L. Such a high dosage was not attempted since our objective was not to simply maximize boron removal instead focusing to elucidate boron uptake mechanisms.

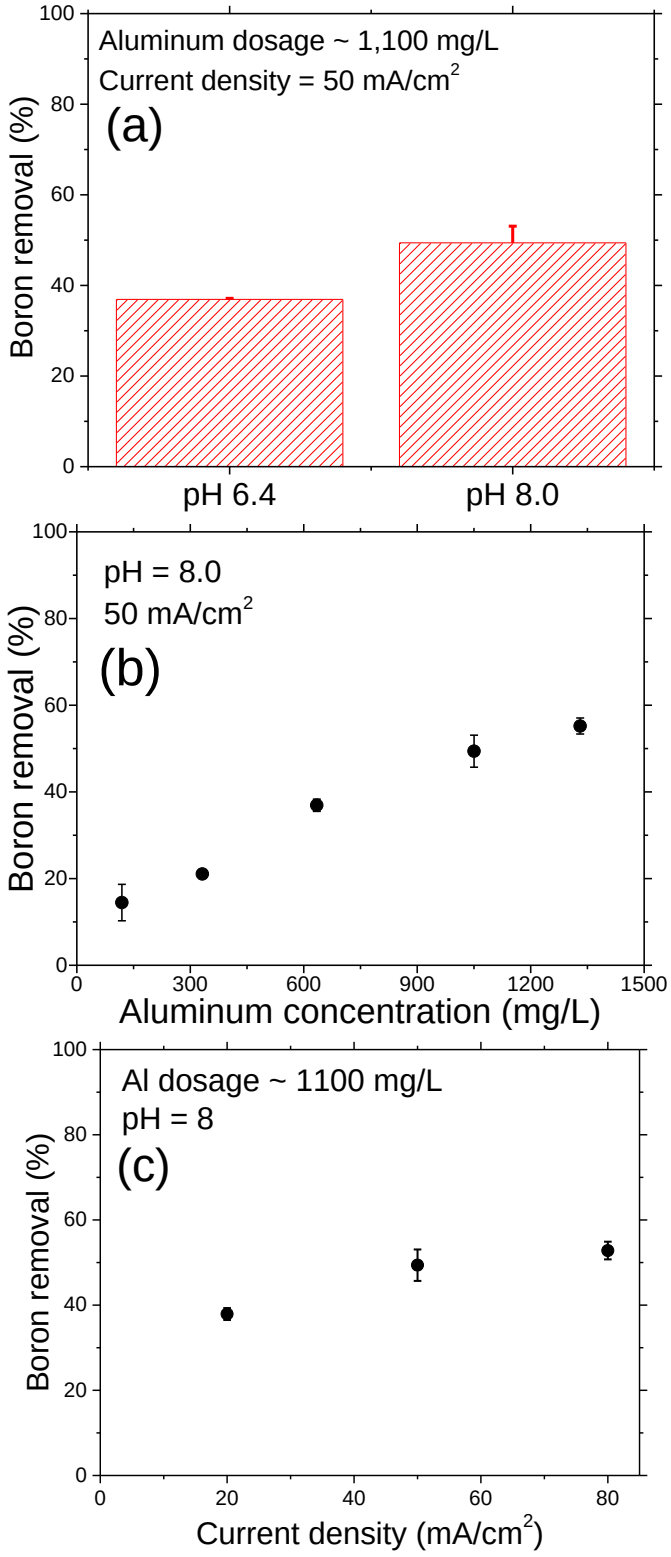

Figure VII-6. Effects of electrocoagulation process conditions on boron removal from actual produced water. Better boron removal was observed at pH 8 (a) and increasing electrocoagulant dosage (b), but remained relatively constant at current densities ≥ 50 mA/cm^2 (c).

Boron coordination with $Al(OH)_3$ in flocs

High resolution B 1s XPS spectra of actual hydraulic fracturing wastewater and the solution containing 25,000 mg/L NaCl + 100 mg/L boron after electrocoagulation are shown in Figure VII-7a and b respectively. Note that deconvolution of the broad boron band in the raw hydraulic fracturing water has already been discussed previously. Unlike the three component peaks necessary to interpret boron bonding in the raw flowback/produced water (Figure VII-1f), boron in flocs could be fully explained with only the B-O peak at ~ 192 eV in both cases. Importantly, electrocoagulation shifted the B-O bond to slightly lower binding energies (192.4 → 192.0 eV) suggesting inner-sphere complexation of boron to $Al(OH)_3$ [344]. Additionally, Al 2p peaks shifted by 0.2 – 0.3 eV towards lower binding energies in flocs formed in boron containing waters compared with "pure" $Al(OH)_3$ coagulant generated by electrolyzing NaCl solutions in the absence of boron (data not shown). Finally, no peak at 188 eV corresponding to direct Al-B bonding was observed. Hence, boron uptake appears to be mainly via complexation rather than co-precipitation, consistent with a ligand exchange mechanism [343, 345].

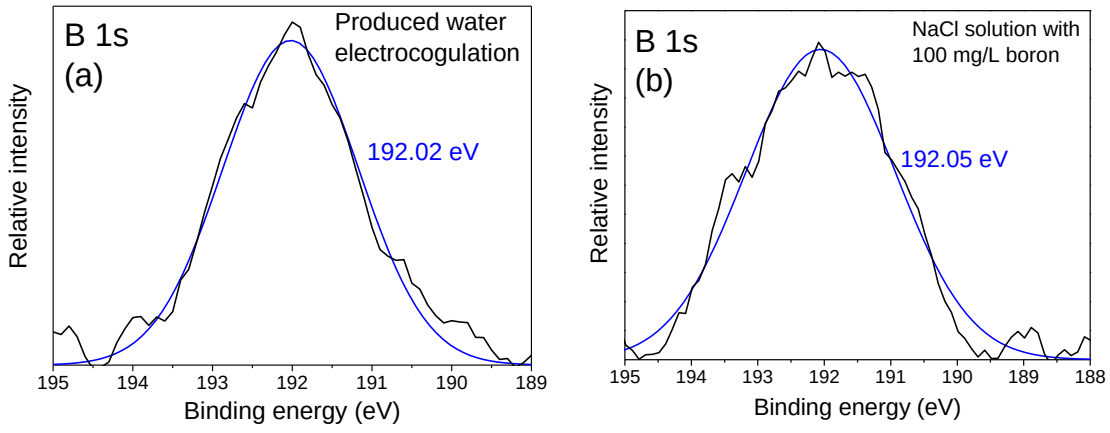

Figure VII-7. High resolution XPS B 1s spectra for electrocoagulated suspensions of the actual produced water (a) and synthetic wastewater (b).

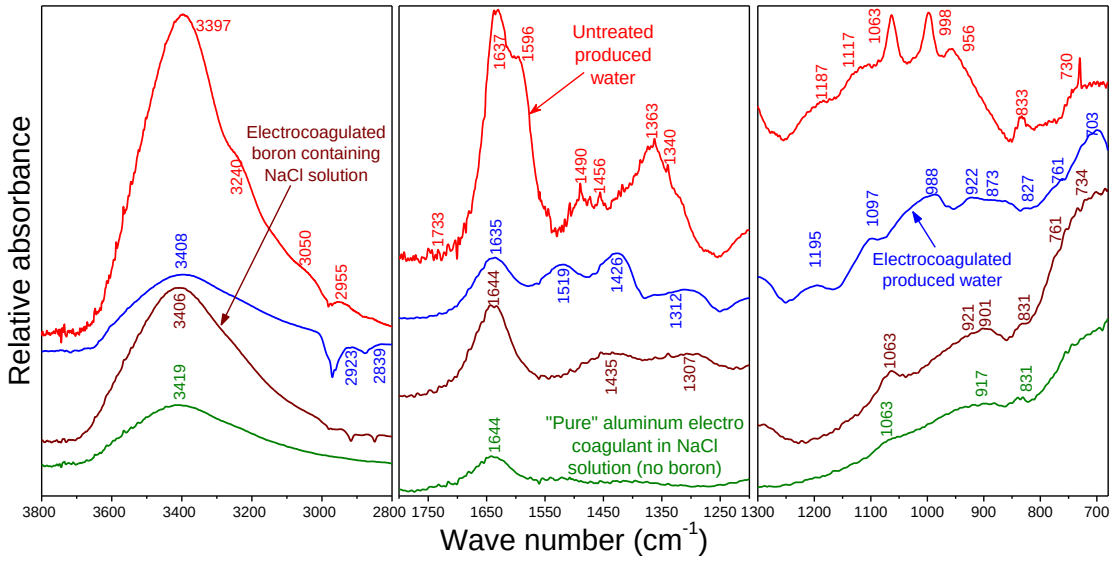

Figure VII-8. Comparison of ATR-FTIR spectra of (a) $Al(OH)_3$ precipitates generated by electrocoagulation of NaCl solution without boron ("pure" coagulant), (b) $Al(OH)_3$ precipitates generated by electrocoagulation of 100 ppm boron dissolved in NaCl solution, (c) flocs produced during produced water electrocoagulation, and (d) raw produced water constituents without electrocoagulation.

Additional evidence for boron complexation with the surface functional groups (e.g. –Al-O-H) was obtained by ATR-FTIR (Figure VII-8). First, only a single broad peak was observed at 3400 cm^{-1} in the spectrum of freshly precipitated $Al(OH)_3$ in NaCl solution without boron or any other contaminants (bottom most curve in green color) confirming their amorphous nature that was discussed earlier and Figure VII-4 [340]. Next, spectra of electrocoagulated NaCl solution containing 100 mg/L boron only (with no other contaminants) and the actual produced water are shown in brown color and blue color respectively. Two new peaks appeared in the region 1300-1400 cm^{-1} for both these cases (1435 and 1307 cm^{-1} for NaCl solution and 1426 and 1312 cm^{-1} for actual produced water) indicating complexation of boron on $Al(OH)_3$ surfaces. These peaks correspond to blue shifted B-O asymmetric stretching and B-OH in-plane bending of trigonal boron respectively, arising from strengthening of these bonds in the surface complex [340, 343]. The measured peaks were at slightly higher wavenumbers than reported values probably due to presence of carbonates [346]. These spectra

also showed a weak peak around 900-920 cm^{-1} probably from tetrahedral boron ($B(OH)_4^-$), but is subject to severe Al-O interferences [340, 343]. More prominent peaks measured around 1430 and 1310 cm^{-1} demonstrates that trigonal $B(OH)_3$ is the predominant species on floc surfaces at pH 8 of our experiments as expected from Figure VII-2. The trigonal boron peak around 1430 cm^{-1} suggests electrostatic interactions with boron serving as a Lewis acid that accepts electrons from oxygen present on the surface to form outer-sphere complexes [342, 347]. The 1310 cm^{-1} peak suggests that this is followed by ligand exchange to form strong inner-sphere trigonal boron complexes [342, 346, 347]. Severe Al-O interferences arising from aluminum addition during electrocoagulation disallowed direct interpretation of the formation of tetrahedral inner-sphere boron complexes in our experiments. Note that the red colored untreated hydraulic fracturing water spectrum has already been discussed.

Sorption of other produced water components onto $Al(OH)_3$ flocs

The "pure" coagulant spectrum in Figure VII-8 only exhibited bands of $Al(OH)_3$ solids consisting of O-H (3700-2800 cm^{-1}), Al-O-Al (1100-950 cm^{-1}), and Al-O (850-680 cm^{-1}) stretching vibrations. In contrast, electrocoagulation of the hydraulic fracturing wastewater generated flocs that additionally showed broad and intense bands in the 1200-900 cm^{-1} and 1700-1300 cm^{-1} regions, arising from uptake of a number of constituents present in the raw hydraulic fracturing wastewater that exhibited stretching and deformation vibrations. Additionally, XPS showed sorption of Si, Ca, and organic matter by $Al(OH)_3$(am) due to their increasing relative atomic percentages compared with the "pure" coagulant. Independently, dissolved organic carbon removal was measured to be 51±4 % at 1,100 mg/L aluminum dosage at pH 8 confirming spectroscopic results. These data demonstrate that a wide range of

contaminants present in flowback/produced water can be removed after sorption onto electrochemically-generated $Al(OH)_3$ flocs.

Conclusions

Electrocoagulation of the hydraulic fracturing wastewater could be performed at high current densities ($\geq$ 20 mA/cm^2) due to its high salinity at which point, boron removal progressively increased with aluminum dosage and was higher at pH 8 compared with 6.4. Amorphous $Al(OH)_3$ precipitates were generated *in situ* by aluminum electrocoagulation along with free chlorine. Visual evidence for pitting of the elemental aluminum anode surface leading to super-Faradaic dissolution was presented via SEM imaging. ATR-FTIR suggested outer-sphere and inner-sphere complexation of trigonal boron with $Al(OH)_3$, which was confirmed by the B-O bond shifting towards lower binding energies in XPS. Boron could also be tetrahedrally coordinated, which could not be probed by FTIR since electrocoagulation overwhelmed the suspension with Al-O bonds necessitating techniques such as nuclear magnetic resonance spectroscopy [346]. It is emphasized that relatively low Al/B ratios (< 10) were employed in this study since our main objective was to investigate boron uptake mechanisms during electrocoagulation not to simply maximize its removal. However, effective (> 90%) boron removal can be achieved at high Al/B ratios of > 70 [51, 324].

Our results add to the growing body of literature showing that electrocoagulation can effectively remove a range of contaminants including organic matter [24, 89, 98], microorganisms [41], boron and other inorganic constituents [50]. Moreover since elevated current densities (and concomitantly short residence times) are possible, compact and portable units can be fabricated for easy field-deployment suggesting that electrocoagulation may be a

facile choice for flowback/produced water treatment. However, it is emphasized that long-term data need to be generated on-site to evaluate potential electrode passivation in order to appropriately scale-up these bench-scale results before it can be implemented for full-scale treatment.

CHAPTER VIII

CONCLUSIONS AND RECOMMENDATIONS FOR FUTURE WORK

Conclusions

Electrocoagulation can be integrated ahead of MF to effectively control turbidity, microorganisms, and DBPs and simultaneously maintain a high MF specific flux during surface water treatment. Electrolysis efficiently removes hydrophobic NOM, viruses, and siliceous foulants. Additional contaminant removal is also possible during MF due to formation thick cake layer of $Al(OH)_3$ flocs that acts like a dynamic membrane. Hence, an integrated EC-MF system can be an attractive option for small-scale decentralized facilities due to its portability and ease of automation while providing multiple barriers against myriad contaminants.

Coupling of electroflotation and MF processes as pretreatment is also shown to be effective in controlling fouling during NF of non-saline surface water. These results were benchmarked with EC-MF (no flotation), conventional chemical coagulation-MF, and MF-only pretreatments. Attenuated total reflection-Fourier transform infrared spectroscopy and X-ray photoelectron spectroscopy revealed hydrophilic components of NOM (polysaccharides and proteins) as major NF foulants. This was also corroborated by negligible change in contact angle for virgin and fouled nanofilters and presence of acidic polysaccharides as evidenced by Alcian Blue staining. Importantly, weaker FTIR signals emanating from these foulants suggest their effective removal by EF-MF pretreatment leading to improved NF flux.

In contrast to non-saline surface water NF where mineral scaling is not dominant, careful considerations must be made when implementing NF for treating brackish surface water. Relative importance of organic fouling versus mineral scaling was shown to be strongly

membrane-dependent as determined by ion rejection characteristics of individual nanofilters. High salt rejection will lead to high product quality, but at the cost of higher tendency for precipitative and organic membrane fouling. Hence, the optimal membrane selection needs to balance total dissolved solids concentration of the product water with the need to minimize fouling. In other words, low salt rejecting nanofilter may be the appropriate selection for surface water desalination due to its higher water permeability and lower mineral scaling tendency as long as wall water quality requirements are met.

Further, organic fouling during brackish surface water NF can also be controlled by implementing EC-MF as pretreatment. NOM removal by EC was enhanced by (i) maintaining a slightly acidic pH compared with that of minimum aluminum solubility, (ii) operating at an intermediate current density of 10 mA/cm^2 (no floc-flotation), and (iii) increasing aluminum dosage. This was attributed to the greater degree of NOM protonation, provision of sufficient contact time during electrolysis and flocculation, and a combination of charge neutralization and sweep coagulation, respectively. Similar to non-saline surface water NF, EC-MF pretreatment removed both hydrophobic and hydrophilic fraction of NOM in brackish surface water as evidenced by ATR-FTIR, leading to NF flux enhancement. These results suggest that the performance of electrochemical coagulation is strongly affected by the source water chemistry; therefore, optimization of the operating conditions is imperative to achieve target water quality. It is emphasized that long-term data need to be generated on-site to appropriately scale-up these bench-scale results before full-scale EC implementation.

Although adding coagulants, antiscalants, and disinfectants typically help in improving performance of NF/RO, it is possible that these added chemicals can also have detrimental effects. This issue becomes more important for large-scale systems especially when NF/RO is

simply retrofitted to the existing water/wastewater treatment plants that utilize coagulation pretreatment. In some instances, these plants are not tightly controlled or optimized for subsequent advanced treatment such as NF/RO. Forensic post-analysis (by ATR-FTIR, XPS, and SEM-EDS) of RO membranes obtained from a real-world water reuse pilot plant with coagulation pretreatment showed significant aluminum fouling even though MF was implemented prior to RO. Calcium and phosphorous (from added antiscalant) were also detected along with only weak signals from organic matter suggesting the dominance of inorganic fouling. These results demonstrate that chemicals added during wastewater reclamation can foul downstream membranes necessitating careful monitoring of existing wastewater treatment unit operations and RO pretreatment processes.

Lastly, EC can also be a feasible approach to remove boron from flowback/produced water. Boron removal by EC was achieved via ligand exchange and complexation with surface hydroxyl groups of freshly precipitated amorphous $Al(OH)_3$ precipitates. Direct measurements of boron uptake along with its chemical state and coordination were made using ATR-FTIR and XPS. ATR-FTIR suggested outer-sphere and inner-sphere complexation of trigonal $B(OH)_3$ with $Al(OH)_3$, which was confirmed by the B-O bond shifting towards lower binding energies in XPS. Severe Al-O interferences precluded evidence for tetrahedral $B(OH)_4^-$ complexation. No evidence for co-precipitation was obtained. Importantly, the capability of EC to remove boron makes it an attractive option as RO pretreatment. To date, multiple stage RO is needed to effectively remove boron [44-46]; therefore, appending EC as pretreatment may reduce the number of stages needed for RO.

Recommendations for future work

Based on this research, the following ideas can be used as directions for future work:

Temperature effects

The effects of seasonal temperature variation on integrated electrocoagulation-membrane processes needs to be addressed. The preliminary hypotheses for this research are: (a) temperature will reduce the kinetics of aluminum dissolution and frequency of particle collisions during electrocoagulation, (b) lower reduction of organics will be observed during electrocoagulation possibly due to passivation of anode at low temperature and decrease mixing efficiency during flocculation due to increase in water viscosity, and (c) more occurrence of salt precipitation on the membrane surface at low temperature.

To date, the effect of temperature during electrocoagulation process has not been thoroughly investigated. Although limited number of studies have reported the effect of temperature on contaminant removal during EC [348, 349], the inherent mechanisms remain elusive. In addition, no investigation has been made on the behavior of anode pitting corrosion as affected by temperature during EC.

In-line EC-MF/UF-NF/RO

All EC experiments in this study were conducted in batch-mode. Although in-line EC-UF processes have been reported earlier [84, 85], the continuation of this treatment train to NF/RO has not been evaluated yet. In addition, the current available in-line system involving EC and NF/RO omitted the use of MF/UF while relying on sedimentation post coagulation [269, 350]. Sedimentation alone may not be enough to prevent colloids, residual coagulant, and microorganisms to get carried over to NF/RO and induce fouling. Moreover, the use of MF/UF provides another barrier in case there is an upset in downstream coagulation process.

REFERENCES

1. United-Nations. *Water scarcity*. 2014 [cited 2015 April 22]; Available from: http://www.un.org/waterforlifedecade/scarcity.shtml.

2. UN-Water. *Coping with water scarcity: A strategic issue and priority for system-wide action*. UN-Water Thematic Initiatives 2006 [cited 2016 04/18/2016]; Available from: http://www.un.org/waterforlifedecade/pdf/2006_unwater_coping_with_water_scarcity_eng.pdf.

3. Gabrysch, R.K., *Ground-water withdrawals and land-surface subsidence in the Houston-Galveston region, Texas, 1906 - 80*. 1984, Texas Department of Water Resources and U.S. Geological Survey: Austin.

4. Galloway, D.L., D.R. Jones, and S.E. Ingebritsen, *Land subsidence in the United States*, in *Circular 1182*. 1999, U.S. Geological Survey: Reston.

5. Speth, T.F., R.S. Summers, and A.M. Gusses, *Nanofiltration foulants from a treated surface water*. Environmental Science & Technology, 1998. **32**(22): p. 3612-3617.

6. Kaushal, S.S., et al., *Increased salinization of fresh water in the northeastern United States.* Proceedings of the National Academy of Sciences of the United States of America, 2005. **102**(38): p. 13517-13520.

7. Snyder, S.A., et al., *Role of membranes and activated carbon in the removal of endocrine disruptors and pharmaceuticals.* Desalination, 2007. **202**(1): p. 156-181.

8. Yangali-Quintanilla, V., et al., *Rejection of pharmaceutically active compounds and endocrine disrupting compounds by clean and fouled nanofiltration membranes.* Water Research, 2009. **43**(9): p. 2349-2362.

9. Allgeier, S.C. and R.S. Summers, *Evaluating NF for DBP control with the RBSMT*. Journal-American Water Works Association, 1995. **87**(3): p. 87-99.

10. Rahardianto, A., B.C. McCool, and Y. Cohen, *Reverse osmosis desalting of inland brackish water of high gypsum scaling propensity: kinetics and mitigation of membrane mineral scaling.* Environmental Science & Technology, 2008. **42**(12): p. 4292-4297.

11. Van der Bruggen, B. and C. Vandecasteele, *Removal of pollutants from surface water and groundwater by nanofiltration: overview of possible applications in the drinking water industry.* Environmental Pollution, 2003. **122**(3): p. 435-445.

12. Chellam, S., et al., *Effect of pretreatment on surface water nanofiltration.* Journal-American Water Works Association, 1997. **89**(10): p. 77-89.

13. van Paassen, J.A.M., et al., *Integrated multi-objective membrane systems for surface water treatment : Pre-treatment of nanofiltration by riverbank filtration and conventional ground water treatment.* Desalination, 1998. **118**: p. 239-248.

14. Contreras, A.E., A. Kim, and Q. Li, *Combined fouling of nanofiltration membranes: Mechanisms and effect of organic matter.* Journal of Membrane Science, 2009. **327**(1-2): p. 87-95.

15. Li, Q. and M. Elimelech, *Organic fouling and chemical cleaning of nanofiltration membranes: measurements and mechanisms.* Environmental Science & Technology, 2004. **38**(17): p. 4683-4693.

16. Cho, J., G. Amy, and J. Pellegrino, *Membrane filtration of natural organic matter: initial comparison of rejection and flux decline characteristics with ultrafiltration and nanofiltration membranes.* Water Research, 1999. **33**(11): p. 2517-2526.

17. Her, N., et al., *Identification of nanofiltration membrane foulants.* Water Research, 2007. **41**(17): p. 3936-3947.

18. Bond, T., et al., *Disinfection by-product formation of natural organic matter surrogates and treatment by coagulation, MIEX and nanofiltration.* Water Research, 2010. **44**(5): p. 1645-1653.

19. Chellam, S., *Effects of nanofiltration on trihalomethane and haloacetic acid precursor removal and speciation in waters containing low concentrations of bromide ion.* Environmental Science & Technology, 2000. **34**(9): p. 1813-1820.

20. Nederlof, M.M., et al., *Comparison of NF/RO membrane performance in integrated membrane systems.* Desalination, 2000. **131**(1–3): p. 257-269.

21. Van der Bruggen, B., et al., *How a microfiltration pretreatment affects the performance in nanofiltration.* Separation Science and Technology, 2005. **39**(7): p. 1443-1459.

22. Lee, N., et al., *Morphological analyses of natural organic matter (NOM) fouling of low-pressure membranes (MF/UF).* Journal of Membrane Science, 2005. **261**(1-2): p. 7-16.

23. Bagga, A., S. Chellam, and D.A. Clifford, *Evaluation of iron chemical coagulation and electrocoagulation pretreatment for surface water microfiltration.* Journal of Membrane Science, 2008. **309**(1-2): p. 82-93.

24. Gamage, N.P. and S. Chellam, *Aluminum electrocoagulation pretreatment reduces fouling during surface water microfiltration.* Journal of Membrane Science, 2011. **379**(1-2): p. 97-105.

25. Howe, K.J. and M.M. Clark, *Effect of coagulation pretreatment on membrane filtration performance.* Journal-American Water Works Association, 2006. **98**(4): p. 133-146.

26. Lahoussine-Turcaud, V., et al., *Coagulation-flocculation with aluminium salts: Influence on the filtration efficacy with microporous membranes.* Water Research, 1992. **26**(5): p. 695-702.

27. Lahoussine-Turcaud, V., et al., *Coagulation pretreatment for ultrafiltration of a surface water.* Journal-American Water Works Association, 1990. **82**(12): p. 76-81.

28. Kimura, M., et al., *Hydraulically irreversible membrane fouling during coagulation–microfiltration and its control by using high-basicity polyaluminum chloride.* Journal of Membrane Science, 2015. **477**(0): p. 115-122.

29. Chen, G., *Electrochemical technologies in wastewater treatment.* Separation and Purification Technology, 2004. **38**(1): p. 11-41.

30. Chen, X., G. Chen, and P.L. Yue, *Novel electrode system for electroflotation of wastewater.* Environmental Science & Technology, 2002. **36**(4): p. 778-783.

31. Gamage, N.P., J.D. Rimer, and S. Chellam, *Improvements in permeate flux by aluminum electroflotation pretreatment during microfiltration of surface water.* Journal of Membrane Science, 2012. **411-412**: p. 45-53.

32. Cañizares, P., et al., *Study of the electrocoagulation process using aluminum and iron electrodes.* Industrial & Engineering Chemistry Research, 2007. **46**(19): p. 6189-6195.

33. Mollah, M.Y.A., et al., *Fundamentals, present and future perspectives of electrocoagulation.* Journal of Hazardous Materials, 2004. **114**(1–3): p. 199-210.

34. Moreno C., H.A., et al., *Electrochemical reactions for electrocoagulation using iron electrodes.* Industrial & Engineering Chemistry Research, 2009. **48**(4): p. 2275-2282.

35. Chellam, S. and M.A. Sari, *Aluminum electrocoagulation as pretreatment during microfiltration of surface water containing NOM: A review of fouling, NOM, DBP, and virus control.* Journal of Hazardous Materials, 2016. **304**: p. 490-501.

36. Tanneru, C.T. and S. Chellam, *Mechanisms of virus control during iron electrocoagulation – Microfiltration of surface water.* Water Research, 2012. **46**(7): p. 2111-2120.

37. Zhu, B., D.A. Clifford, and S. Chellam, *Comparison of electrocoagulation and chemical coagulation pretreatment for enhanced virus removal using microfiltration membranes.* Water Research, 2005. **39**(13): p. 3098-3108.

38. Alizadeh Tabatabai, S.A., J.C. Schippers, and M.D. Kennedy, *Effect of coagulation on fouling potential and removal of algal organic matter in ultrafiltration pretreatment to seawater reverse osmosis.* Water Research, 2014. **59**(0): p. 283-294.

39. Chon, K., et al., *The role of a combined coagulation and disk filtration process as a pre-treatment to microfiltration and reverse osmosis membranes in a municipal wastewater pilot plant.* Chemosphere, 2014. **117**: p. 20-26.

40. Ho, J.S., et al., *Inline coagulation–ultrafiltration as the pretreatment for reverse osmosis brine treatment and recovery.* Desalination, 2015. **365**(0): p. 242-249.

41. Tanneru, C.T., et al., *Relative insignificance of virus inactivation during aluminum electrocoagulation of saline waters.* Environmental Science & Technology, 2014. **48**(24): p. 14590-14598.

42. Gabelich, C.J., et al., *The role of dissolved aluminum in silica chemistry for membrane processes.* Desalination, 2005. **180**(1-3): p. 307-319.

43. Gabelich, C.J., et al., *Effects of aluminum sulfate and ferric chloride coagulant residuals on polyamide membrane performance.* Desalination, 2002. **150**(1): p. 15-30.

44. Xu, Y. and J.-Q. Jiang, *Technologies for boron removal.* Industrial & Engineering Chemistry Research, 2008. **47**(1): p. 16-24.

45. Dydo, P., et al., *Boron removal from landfill leachate by means of nanofiltration and reverse osmosis.* Desalination, 2005. **185**(1–3): p. 131-137.

46. Öztürk, N., D. Kavak, and T.E. Köse, *Boron removal from aqueous solution by reverse osmosis.* Desalination, 2008. **223**(1–3): p. 1-9.

47. Yilmaz, A.E., R. Boncukcuoğlu, and M.M. Kocakerim, *A quantitative comparison between electrocoagulation and chemical coagulation for boron removal from boron-containing solution.* Journal Of Hazardous Materials, 2007. **149**(2): p. 475-81.

48. Jiang, J.-Q., et al., *Mechanisms of boron removal with electrocoagulation.* Environmental Chemistry, 2006. **3**(5): p. 350-354.

49. Sayiner, G., F. Kandemirli, and a. Dimoglo, *Evaluation of boron removal by electrocoagulation using iron and aluminum electrodes.* Desalination, 2008. **230**(1-3): p. 205-212.

50. Esmaeilirad, N., K. Carlson, and P. Omur Ozbek, *Influence of softening sequencing on electrocoagulation treatment of produced water.* Journal of Hazardous Materials, 2015. **283**: p. 721-729.

51. Isa, M.H., et al., *Boron removal by electrocoagulation and recovery.* Water Research, 2013. **51C**(0): p. 113-123.

52. Yılmaz, a.E., et al., *An empirical model for kinetics of boron removal from boroncontaining wastewaters by the electrocoagulation method in a batch reactor.* Desalination, 2008. **230**(1-3): p. 288-297.

53. Sari, M.A. and S. Chellam, *Surface water nanofiltration incorporating (electro) coagulation–microfiltration pretreatment: Fouling control and membrane characterization.* Journal of Membrane Science, 2013. **437**: p. 249-256.

54. Sari, M.A. and S. Chellam, *Relative contributions of organic and inorganic fouling during nanofiltration of inland brackish surface water.* Journal of Membrane Science, 2017. **523**: p. 68-76.

55. Sari, M.A. and S. Chellam, *Reverse osmosis fouling during pilot-scale municipal water reuse: Evidence for aluminum coagulant carryover.* Journal of Membrane Science, 2016. **520**: p. 231-239.

56. Sari, M.A. and S. Chellam, *Mechanisms of boron removal from hydraulic fracturing wastewater by aluminum electrocoagulation.* Journal of Colloid and Interface Science, 2015. **458**: p. 103-111.

57. Coplin, L.S. and D. Galloway, *Chapter 7. Houston-Galveston, Texas: Managing coastal subsidence*, in *Land subsidence in the united states*, D. Galloway, D.R. Jones, and S.E. Ingebritsen, Editors. 1999, U.S. Department of the Interior and U.S. Geological Survey: Reston, VA. p. 35-48.

58. Letterman, R.D., ed. *Water quality and treatment: A handbook of community water supplies*. 5th ed. 1999, McGraw Hill, Inc.: New York.

59. Hoek, E.M.V. and V.V. Tarabara, eds. *Encyclopedia of membrane science and technology*. 2013, John Wiley & Sons, Inc. : New York, N.Y.

60. Xagoraraki, I., Z.Q. Yin, and Z. Svambayev, *Fate of viruses in water systems.* Journal of Environmental Engineering, 2014. **140**(7): p. Article number 04014020.

61. Antony, A., J. Blackbeard, and G. Leslie, *Removal efficiency and integrity monitoring techniques for virus removal by membrane processes.* Critical Reviews in Environmental Science and Technology, 2012. **42**(9): p. 891-933.

62. Zhu, B.T., D.A. Clifford, and S. Chellam, *Virus removal by iron coagulation-microfiltration.* Water Research, 2005. **39**(20): p. 5153-5161.

63. Meyn, T., T.O. Leiknes, and A. Konig, *MS2 removal from high NOM content surface water by coagulation - ceramic microfiltration for potable water production.* AIChE Journal, 2012. **58**(7): p. 2270-2281.

64. Shirasaki, N., et al., *Comparison of removal performance of two surrogates for pathogenic waterborne viruses, bacteriophage Qβ and MS2, in a coagulation-ceramic microfiltration system.* Journal of Membrane Science, 2009. **326**(2): p. 564-571.

65. Chellam, S. and J.G. Jacangelo, *Existence of critical recovery and impacts of operational mode on potable water microfiltration.* Journal of Environmental Engineering, 1998. **124**(12): p. 1211-1219.

66. Kimura, K., K. Tanaka, and Y. Watanabe, *Microfiltration of different surface waters with/without coagulation: Clear correlations between membrane fouling and hydrophilic biopolymers.* Water Research, 2014. **49**: p. 434-443.

67. Molgora, C.C., et al., *Removal of arsenic from drinking water: A comparative study between electrocoagulation-microfiltration and chemical coagulation-microfiltration processes.* Separation and Purification Technology, 2013. **118**: p. 645-651.

68. Wiesner, M.R. and J.-M. Laine, *Coagulation and membrane separation*, in *Water treatment membrane processes*, J. Mallevialle, P.E. Odendaal, and M.R. Wiesner, Editors. 1996, McGraw Hill: New York, N.Y. p. 16.1-16.12.

69. Jimenez, C., et al., *Electrochemical dosing of iron and aluminum in continuous processes: A key step to explain electro-coagulation processes.* Separation and Purification Technology, 2012. **98**: p. 102-108.

70. Gao, S., et al., *Effects of chloride ions on electro-coagulation-flotation process with aluminum electrodes for algae removal.* Journal of Hazardous Materials, 2010. **182**(1-3): p. 827-834.

71. Matis, K.A. and E.N. Peleka, *Alternative flotation techniques for wastewater treatment: Focus on electroflotation.* Separation Science and Technology, 2010. **45**(16): p. 2465-2474.

72. Harif, T., M. Khai, and A. Adin, *Electrocoagulation versus chemical coagulation: Coagulation/flocculation mechanisms and resulting floc characteristics.* Water Research, 2012. **46**(10): p. 3177-3188.

73. Wan, W., et al., *Effects of water chemistry on arsenic removal from drinking water by electrocoagulation.* Water Research, 2011. **45**(1): p. 384-392.

74. Mohora, E., et al., *Removal of natural organic matter and arsenic from water by electrocoagulation/flotation continuous flow reactor.* Journal of Hazardous Materials, 2012. **235–236**(0): p. 257-264.

75. Yıldız, Y.Ş., A.S. Koparal, and B. Keskinler, *Effect of initial pH and supporting electrolyte on the treatment of water containing high concentration of humic substances by electrocoagulation.* Chemical Engineering Journal, 2008. **138**(1–3): p. 63-72.

76. Vepsäläinen, M., M. Pulliainen, and M. Sillanpää, *Effect of electrochemical cell structure on natural organic matter (NOM) removal from surface water through electrocoagulation (EC).* Separation and Purification Technology, 2012. **99**(0): p. 20-27.

77. Vasudevan, S., J. Lakshmi, and G. Sozhan, *Effects of alternating and direct current in electrocoagulation process on the removal of cadmium from water.* Journal of Hazardous Materials, 2011. **192**(1): p. 26-34.

78. Hanay, O. and H. Hasar, *Effect of anions on removing Cu^{2+}, Mn^{2+} and Zn^{2+} in electrocoagulation process using aluminum electrodes.* Journal of Hazardous Materials, 2011. **189**(1-2): p. 572-576.

79. Khatibikamal, V., et al., *Fluoride removal from industrial wastewater using electrocoagulation and its adsorption kinetics.* Journal of Hazardous Materials, 2010. **179**(1-3): p. 276-280.

80. Kilic, M.G. and C. Hosten, *A comparative study of electrocoagulation and coagulation of aqueous suspensions of kaolinite powders.* Journal of Hazardous Materials, 2010. **176**(1-3): p. 735-740.

81. Lee, S.Y. and G.A. Gagnon, *Review of the factors relevant to the design and operation of an electrocoagulation system for wastewater treatment.* Environmental Reviews, 2014. **22**(4): p. 421-429.

82. Barrera-Diaz, C., et al., *Physicochemical aspects of electrocoagulation.* Separation and Purification Reviews, 2011. **40**(1): p. 1-24.

83. Balasubramanian, N., et al., *Removal of arsenic from aqueous solution using electrocoagulation.* Journal of Hazardous Materials, 2009. **167**(1-3): p. 966-969.

84. Timmes, T.C., H.-C. Kim, and B.A. Dempsey, *Electrocoagulation pretreatment of seawater prior to ultrafiltration: Pilot-scale applications for military water purification systems.* Desalination, 2010. **250**(1): p. 6-13.

85. Timmes, T.C., H.-C. Kim, and B.A. Dempsey, *Electrocoagulation pretreatment of seawater prior to ultrafiltration: Bench-scale applications for military water purification systems.* Desalination, 2009. **249**(3): p. 895-901.

86. Ben-Sasson, M. and A. Adin, *Fouling mechanisms and energy appraisal in microfiltration pretreated by aluminum-based electroflocculation.* Journal of Membrane Science, 2010. **352**(1-2): p. 86-94.

87. Ben-Sasson, M. and A. Adin, *Fouling mitigation by iron-based electroflocculation in microfiltration: Mechanisms and energy minimization.* Water Research, 2011. **44**(13): p. 3973-3981.

88. Ben-Sasson, M., Y.M. Lin, and A. Adin, *Electrocoagulation-membrane filtration hybrid system for colloidal fouling mitigation of secondary-effluent.* Separation and Purification Technology, 2011. **82**: p. 63-70.

89. Ben-Sasson, M., et al., *Enhanced removal of natural organic matter by hybrid process of electrocoagulation and dead-end microfiltration.* Chemical Engineering Journal, 2013. **232**: p. 338-345.

90. Gamage, N.P. and S. Chellam, *Mechanisms of physically irreversible fouling during surface water microfiltration and mitigation by aluminum electroflotation pretreatment.* Environmental Science & Technology, 2014. **48**(2): p. 1148-1157.

91. Lakshmanan, D., D.A. Clifford, and G. Samanta, *Ferrous and ferric ion generation during iron electrocoagulation.* Environmental Science & Technology, 2009. **43**(10): p. 3853-3859.

92. Li, L., et al., *Modeling As(III) oxidation and removal with iron electrocoagulation in groundwater.* Environmental Science & Technology, 2012. **46**(21): p. 12038-12045.

93. Gamage, N.P., *Electrocoagulation pretreatment for microfiltration of surface water: Mechanisms of fouling and its control*, in *Civil and Environmental Engineering*. 2014, University of Houston: Houston, TX.

94. Tanneru, C.T., J.D. Rimer, and S. Chellam, *Sweep Flocculation and Adsorption of Viruses on Aluminum Flocs during Electrochemical Treatment Prior to Surface Water Microfiltration.* Environmental Science & Technology, 2013. **47**(9): p. 4612-4618.

95. Chellam, S. and N.G. Cogan, *Colloidal and bacterial fouling during constant flux microfiltration: Comparison of classical blocking laws with a unified model combining pore blocking and EPS secretion.* Journal of Membrane Science, 2011. **382**(1-2): p. 148-157.

96. Xu, W.D. and S. Chellam, *Initial stages of bacterial fouling during dead-end microfiltration.* Environmental Science & Technology, 2005. **39**(17): p. 6470-6476.

97. Bowen, W.R., J.I. Calvo, and A. Hernandez, *Steps of Membrane Blocking in Flux Decline during Protein Microfiltration.* Journal of Membrane Science, 1995. **101**(1-2): p. 153-165.

98. Dubrawski, K.L. and M. Mohseni, *In-situ identification of iron electrocoagulation speciation and application for natural organic matter (NOM) removal.* Water Research, 2013. **47**(14): p. 5371-5380.

99. Ben-Sasson, M., W. Calmano, and A. Adin, *Iron-oxidation processes in an electroflocculation (electrocoagulation) cell.* Journal of Hazardous Materials, 2009. **171**(1-3): p. 704-709.

100. Mechelhoff, M., G.H. Kelsall, and N.J.D. Graham, *Electrochemical behaviour of aluminium in electrocoagulation processes.* Chemical Engineering Science, 2013. **95**: p. 301-312.

101. Ghernaout, D., *Advanced oxidation phenomena in electrocoagulation process: a myth or a reality?* Desalination and Water Treatment, 2013. **51**(40-42): p. 7536-7554.

102. Cañizares, P., et al., *Comparison of the aluminum speciation in chemical and electrochemical dosing processes.* Industrial & Engineering Chemistry Research, 2006. **45**(26): p. 8749-8756.

103. Davis, C.C. and M. Edwards, *Coagulation with hydrolyzing metal salts: Mechanisms and water quality impacts.* Critical Reviews in Environmental Science and Technology, 2014. **44**(4): p. 303-347.

104. Gomes, J.A.G., et al., *Arsenic removal by electrocoagulation using combined Al-Fe electrode system and characterization of products.* Journal of Hazardous Materials, 2007. **139**(2): p. 220-231.

105. Dubrawski, K.L., M. Fauvel, and M. Mohseni, *Metal type and natural organic matter source for direct filtration electrocoagulation of drinking water.* Journal of Hazardous Materials, 2013. **244**: p. 135-141.

106. Stumm, W. and J.J. Morgan, *Aquatic chemistry: Chemical equilibria and rates in natural waters.* 2nd ed. 1996, New York: Wiley.

107. Gu, Z., et al., *Estimating dosing rates and energy consumption for electrocoagulation using iron and aluminum electrodes.* Industrial & Engineering Chemistry Research, 2009. **48**(6): p. 3112-3117.

108. Amrose, S., et al., *Arsenic removal from groundwater using iron electrocoagulation: Effect of charge dosage rate.* Journal of Environmental Science and Health Part a-Toxic/Hazardous Substances & Environmental Engineering, 2013. **48**(9): p. 1019-1030.

109. Dubrawski, K.L., et al., *Production and transformation of mixed-valent nanoparticles generated by Fe(0) electrocoagulation.* Environmental Science & Technology, 2015. **49**(4): p. 2171-2179.

110. Theis, T.L. and P.C. Singer, *Complexation of iron(II) by organic matter and its effect on iron(II) oxygenation.* Environmental Science & Technology, 1974. **8**(6): p. 569-573.

111. Mouedhen, G., et al., *Behavior of aluminum electrodes in electrocoagulation process.* Journal of Hazardous Materials, 2008. **150**(1): p. 124-135.

112. Gao, S., et al., *Electro-coagulation-flotation process for algae removal.* Journal of Hazardous Materials, 2010. **177**(1-3): p. 336-343.

113. Ricordel, C., A. Darchen, and D. Hadjiev, *Electrocoagulation-electroflotation as a surface water treatment for industrial uses.* Separation and Purification Technology, 2010. **74**(3): p. 342-347.

114. van Genuchten, C.M., et al., *Removing arsenic from synthetic groundwater with iron electrocoagulation: An Fe and As K-Edge EXAFS study.* Environmental Science & Technology, 2012. **46**(2): p. 986-994.

115. Crist, V.B., *Handbook of monochromatic XPS spectra*. Vol. 2. 2005, California: XPS International LLC.

116. Masion, A., et al., *Chemistry and structure of Al(OH)/organics precipitates. A small-angle x-ray scattering study. 2. Speciation and structure of the aggregates.* Langmuir, 1994. **10**(11): p. 4349-4352.

117. Howe, K.J., et al., *Effect of coagulation on the size of MF and UF membrane foulants.* Environmental Science & Technology, 2006. **40**(24): p. 7908-7913.

118. Wang, J., et al., *Effect of aggregate characteristics under different coagulation mechanisms on microfiltration membrane fouling.* Desalination, 2010. **258**(1-3): p. 19-27.

119. Chellam, S. and W. Xu, *Blocking laws analysis of dead-end constant flux microfiltration of compressible cakes.* Journal of Colloid and Interface Science, 2006. **301**(1): p. 248-257.

120. Belfort, G., R.H. Davis, and A.L. Zydney, *The behavior of suspensions and macromolecular solutions in crossflow microfiltration.* Journal of Membrane Science, 1994. **96**(1–2): p. 1-58.

121. Lee, D.J., et al., *Filtration of highly compactible filter cake: Variable internal flow rate.* AIChE Journal, 2000. **46**(1): p. 110-118.

122. Tiller, F.M. and J.H. Kwon, *Role of porosity in filtration: XIII. Behavior of highly compactible cakes.* AIChE Journal, 1998. **44**(10): p. 2159-2167.

123. Harif, T. and A. Adin, *Size and structure evolution of kaolin-Al(OH)$_3$ flocs in the electroflocculation process: A study using static light scattering.* Water Research, 2011. **45**(18): p. 6195-6206.

124. Lee, S.A., A.G. Fane, and T.D. Waite, *Impact of natural organic matter on floc size and structure effects in membrane filtration.* Environmental Science & Technology, 2005. **39**(17): p. 6477-6486.

125. Yamamura, H., K. Kimura, and Y. Watanabe, *Mechanism involved in the evolution of physically irreversible fouling in microfiltration and ultrafiltration membranes used for drinking water treatment.* Environmental Science & Technology, 2007. **41**(19): p. 6789-6794.

126. Tian, J.-y., et al., *Correlations of relevant membrane foulants with UF membrane fouling in different waters.* Water Research, 2013. **47**(3): p. 1218-1228.

127. Echlin, P., *Analysis of organic and biological surfaces.* Chemical Analysis, ed. P.J. Elving, J.D. Winefordner, and I.M. Kolthoff. 1984, New York: Wiley.

128. Naumkin, A.V., et al., *NIST X-ray photoelectron spectroscopy database* 2012, National Institute of Standards and Technology (NIST).

129. Watts, J.F. and J. Wolstenholme, *An introduction to surface analysis by XPS and AES*. 2003, Chichester, West Sussex, England: J. Wiley.

130. Jacangelo, J.G., S.S. Adham, and J.M. Laine, *Mechanism of Cryptosporidium, Giardia, and MS2 virus removal by MF and UF.* Journal-American Water Works Association, 1995. **87**(9): p. 107-121.

131. Dubrawski, K.L. and M. Mohseni, *Standardizing electrocoagulation reactor design: Iron electrodes for NOM removal.* Chemosphere, 2013. **91**(1): p. 55-60.

132. Ulu, F., et al., *An evaluation on different origins of natural organic matters using various anodes by electrocoagulation.* Chemosphere, 2015. **125**: p. 108-114.

133. Weishaar, J.L., et al., *Evaluation of specific ultraviolet absorbance as an indicator of the chemical composition and reactivity of dissolved organic carbon.* Environmental Science & Technology, 2003. **37**(20): p. 4702-4708.

134. Krasner, S.W. and G. Amy, *Jar-test evaluations of enhanced coagulation.* Journal-American Water Works Association, 1995. **87**(10): p. 93-107.

135. Cañizares, P., et al., *The pH as a key parameter in the choice between coagulation and electrocoagulation for the treatment of wastewaters.* Journal of Hazardous Materials, 2009. **163**(1): p. 158-164.

136. Singer, P.C., *Control of disinfection by-products in drinking water.* Journal of Environmental Engineering-ASCE, 1994. **120**(4): p. 727-744.

137. Reckhow, D.A. and P.C. Singer, *The removal of organic halide precursors by preozonation and alum coagulation.* Journal-American Water Works Association, 1984. **76**(4): p. 151-157.

138. Sillanpaa, M., et al., *NOM removal by electrochemical methods*. Natural organic matter in water: Characterization and treatment methods. 2015. 81-111.

139. Chellam, S. and S.W. Krasner, *Disinfection byproduct relationships and speciation in chlorinated nanofiltered waters.* Environmental Science & Technology, 2001. **35**(19): p. 3988-3999.

140. Martinez-Huitle, C.A. and E. Brillas, *Electrochemical alternatives for drinking water disinfection.* Angewandte Chemie-International Edition, 2008. **47**(11): p. 1998-2005.

141. Jeong, J., C. Kim, and J. Yoon, *The effect of electrode material on the generation of oxidants and microbial inactivation in the electrochemical disinfection processes.* Water Research, 2009. **43**(4): p. 895-901.

142. Delaire, C., et al., *Escherichia coli attenuation by Fe electrocoagulation in synthetic Bengal groundwater: Effect of pH and natural organic matter.* Environmental Science & Technology, 2015. **49**(16): p. 9945-9953.

143. Ghernaout, D., et al., *Application of electrocoagulation in Escherichia coli culture and two surface waters.* Desalination, 2008. **219**(1–3): p. 118-125.

144. Ghernaout, D., M.W. Naceur, and A. Aouabed, *On the dependence of chlorine by-products generated species formation of the electrode material and applied charge during electrochemical water treatment.* Desalination, 2011. **270**(1-3): p. 9-22.

145. Noubactep, C., A. Schoner, and P. Woafo, *Metallic iron filters for universal access to safe drinking water.* Clean-Soil Air Water, 2009. **37**(12): p. 930-937.

146. Jacangelo, J.G., et al., *Low-pressure membrane filtration for removing Giardia and microbial indicators.* Journal-American Water Works Association, 1991. **83**(9): p. 97-106.

147. Noubactep, C., *On the mechanism of microbe inactivation by metallic iron.* Journal of Hazardous Materials, 2011. **198**: p. 383-386.

148. Kim, J.Y., et al., *Inactivation of MS2 coliphage by ferrous ion and zero-valent iron nanoparticles.* Environmental Science & Technology, 2011. **45**(16): p. 6978-6984.

149. Matsushita, T., et al., *Virus inactivation during coagulation with aluminum coagulants.* Chemosphere, 2011. **85**(4): p. 571-576.

150. Kreissel, K., et al., *Inactivation of F-specific bacteriophages during flocculation with polyaluminum chloride - A mechanistic study.* Water Research, 2014. **51**: p. 144-151.

151. Gutierrez, L. and T.H. Nguyen, *Interactions between rotavirus and suwannee river organic matter: Aggregation, deposition, and adhesion force measurement.* Environmental Science & Technology, 2012. **46**(16): p. 8705-8713.

152. Matsushita, T., et al., *Investigating norovirus removal by microfiltration, ultrafiltration, and precoagulation-microfiltration processes using recombinant norovirus virus-like particles and real-time immuno-PCR.* Water Research, 2013. **47**(15): p. 5819-5827.

153. Shirasaki, N., et al., *Feasibility of in-line coagulation as a pretreatment for ceramic microfiltration to remove viruses.* Journal of Water Supply Research and Technology-Aqua, 2010. **59**(8): p. 501-511.

154. Chellam, S., M.R. Wiesner, and C. Dawson, *Slip at a uniformly porous boundary: Effect on fluid flow and mass transfer.* Journal of Engineering Mathematics, 1992. **26**(4): p. 481-492.

155. Shirasaki, N., et al., *Effects of reversible and irreversible membrane fouling on virus removal by a coagulation-microfiltration system.* Journal of Water Supply Research and Technology-Aqua, 2008. **57**(7): p. 501-506.

156. Cañizares, P., et al., *Coagulation and electrocoagulation of wastes polluted with dyes.* Environmental Science & Technology, 2006. **40**(20): p. 6418-6424.

157. Holt, P.K., G.W. Barton, and C.A. Mitchell, *The future for electrocoagulation as a localised water treatment technology.* Chemosphere, 2005. **59**(3): p. 355-367.

158. Lakshmanan, D., *A systematic study of arsenic removal from drinking water using coagulation-filtration and electrocoagulation-filtration*, in *Civil and Environmental Engineering*. 2007, University of Houston: Houston, TX.

159. van Genuchten, C.M., A.J. Gadgil, and J. Pena, *Fe(III) nucleation in the presence of bivalent cations and oxyanions leads to subnanoscale 7 angstrom polymers.* Environmental Science & Technology, 2014. **48**(20): p. 11828-11836.

160. van Genuchten, C.M., et al., *Structure of Fe(III) precipitates generated by the electrolytic dissolution of Fe(0) in the presence of groundwater ions.* Geochimica et Cosmochimica Acta, 2014. **127**: p. 285-304.

161. Van der Bruggen, B., et al., *Application of nanofiltration for removal of pesticides, nitrate and hardness from ground water: rejection properties and economic evaluation.* Journal of Membrane Science, 2001. **193**(2): p. 239-248.

162. Semião, A.J.C. and A.I. Schäfer, *Xenobiotics removal by membrane technology: An overview*, in *Xenobiotics in the urban water cycle: Mass flows, environmental processes and mitigation strategies*, K. Bester, K. Kümmerer, and D. Fatta-Kassinos, Editors. 2012, Springer: Berlin, Germany.

163. Yangali-Quintanilla, V., et al., *Proposing nanofiltration as acceptable barrier for organic contaminants in water reuse.* Journal of Membrane Science, 2012. **362**(1-2): p. 334-345.

164. Mansouri, K., et al., *Anodic dissolution of pure aluminum during electrocoagulation process: Influence of supporting electrolyte, initial ph, and current density.* Industrial & Engineering Chemistry Research, 2011. **50**(23): p. 13362-13372.

165. Xu, P., C. Bellona, and J.E. Drewes, *Fouling of nanofiltration and reverse osmosis membranes during municipal wastewater reclamation: Membrane autopsy results from pilot-scale investigations.* Journal of Membrane Science, 2010. **353**(1-2): p. 111-121.

166. Park, N., et al., *Characterizations of the colloidal and microbial organic matters with respect to membrane foulants.* Journal of Membrane Science, 2006. **275**(1-2): p. 29-36.

167. Xu, P., et al., *Effect of membrane fouling on transport of organic contaminants in NF/RO membrane applications.* Journal of Membrane Science, 2006. **279**(1-2): p. 165-175.

168. Chang, E.E., et al., *Reduction of natural organic matter by nanofiltration process.* Chemosphere, 2009. **76**(9): p. 1265-72.

169. Sharma, R.R., R. Agrawal, and S. Chellam, *Temperature effects on sieving characteristics of thin-film composite nanofiltration membranes: Pore size distributions and transport parameters.* Journal of Membrane Science, 2003. **223**: p. 69-87.

170. DiGiano, F.A., S. Arweiler, and J.A. Riddick, Jr., *Alternative tests for evaluating NF fouling.* Journal-American Water Works Association, 2000. **92**(2): p. 103-115.

171. Badireddy, A.R., et al., *Spectroscopic characterization of extracellular polymeric substances from Escherichia coli and Serratia marcescens: suppression using sub-inhibitory concentrations of bismuth thiols.* Biomacromolecules, 2008. **9**(11): p. 3079-89.

172. Lee, S., et al., *Characterizations of NOM included in NF and UF membrane permeates.* Desalination, 2005. **173**(2): p. 131-142.

173. Shon, H.K., et al., *Fouling of ultrafiltration membrane by effluent organic matter: A detailed characterization using different organic fractions in wastewater.* Journal of Membrane Science, 2006. **278**(1-2): p. 232-238.

174. Song, W., et al., *Nanofiltration of natural organic matter with H_2O_2/UV pretreatment: fouling mitigation and membrane surface characterization.* Journal of Membrane Science, 2004. **241**(1): p. 143-160.

175. Tang, C.Y., Y.-N. Kwon, and J.O. Leckie, *Effect of membrane chemistry and coating layer on physiochemical properties of thin film composite polyamide RO and NF membranes.* Desalination, 2009. **242**(1-3): p. 149-167.

176. Mantsch, H.H. and D. Chapman, *Infrared spectroscopy of biomolecules*. 1996, New York: John Wiley & Sons, Inc. p. 2-3, 262-263, 283-285.

177. Cho, J., et al., *Characterization of clean and natural organic matter (NOM) fouled NF and UF membranes, and foulants characterization.* Desalination, 1998. **118**(1-3): p. 101-108.

178. Kong, J. and S. Yu, *Fourier transform infrared spectroscopic analysis of protein secondary structures.* Acta Biochimica et Biophysica Sinica, 2007. **39**(8): p. 549-559.

179. Pihlajamaki, A., P. Vaisanen, and M. Nystro, *Characterization of clean and fouled polymeric ultrafiltration membranes by Fourier transform IR spectroscopy -*

attenuated total reflection. Colloids and Surfaces A: Physicochemical and Engineering Aspects, 1998. **138**(2-3): p. 323-333.

180. Stuart, B.H., *Infrared spectroscopy: Fundamentals and applications*. 2004, Chichester, West Sussex: John Wiley & Sons Ltd. p. 144.

181. Zhang, L. and J. Hermans, *Helix versus α-helix: A molecular dynamics study of conformational preferences of aib and alanine.* Journal of the American Chemical Society, 1994. **116**(14): p. 11915-11921.

182. Villacorte, L.O., et al., *The fate of transparent exopolymer particles (TEP) in integrated membrane systems: removal through pre-treatment processes and deposition on reverse osmosis membranes.* Water Research, 2009. **43**(20): p. 5039-52.

183. Van Nevel, S., et al., *Transparent exopolymer particle removal in different drinking water production centers.* Water Research, 2012. **46**(11): p. 3603-11.

184. Boussu, K., et al., *Influence of membrane and colloid characteristics on fouling of nanofiltration membranes.* Journal of Membrane Science, 2007. **289**(1-2): p. 220-230.

185. Comerton, A.M., R.C. Andrews, and D.M. Bagley, *The influence of natural organic matter and cations on fouled nanofiltration membrane effective molecular weight cut-off.* Journal of Membrane Science, 2009. **327**(1-2): p. 155-163.

186. Hong, S. and M. Elimelech, *Chemical and physical aspects of natural organic matter (NOM) fouling of nanofiltration membranes.* Journal of Membrane Science, 1997. **132**(2): p. 159-181.

187. Li, Q. and M. Elimelech, *Synergistic effects in combined fouling of a loose nanofiltration membrane by colloidal materials and natural organic matter.* Journal of Membrane Science, 2006. **278**(1-2): p. 72-82.

188. Kwon, B., et al., *Organic nanocolloid fouling in UF membranes.* Journal of Membrane Science, 2006. **279**(1-2): p. 209-219.

189. Fergason, K.C., M.L. Rucker, and B.B. Panda, *Methods for monitoring land subsidence and earth fissures in the Western USA.* Proceedings of the International Association of Hydrological Sciences (PIAHS), 2015. **372**: p. 361-366.

190. Lins, H.F., R.M. Hirsch, and J. Kiang, *Water - The nation's fundamental climate issue: A white paper on the U.S. Geological survey role and capabilities*, in *Circular 1347*. 2010, U.S. Geological Survey.

191. Nicot, J.-P., et al., *A desalination database for texas.* Bureau of Economic Geology 2006.

192. Schneider, R.P., et al., *Analysis of foulant layer in all elements of an RO train.* Journal of Membrane Science, 2005. **261**(1–2): p. 152-162.

193. Tran, T., et al., *An autopsy study of a fouled reverse osmosis membrane element used in a brackish water treatment plant.* Water Research, 2007. **41**(17): p. 3915-3923.

194. Greenlee, L.F., et al., *Reverse osmosis desalination: Water sources, technology, and today's challenges.* Water Research, 2009. **43**(9): p. 2317-2348.

195. Iowa Department of Natural Resources, *Water quality standards review: Chloride, sulfate and total dissolved solids.* 2009.

196. Nance, H.S., *Tracking salinity sources to Texas streams: Examples from West Texas and the Texas gulf coastal plain* 2006, The Gulf Coast Association of Geological Societies. p. 675-693.

197. Rahardianto, A., et al., *Diagnostic characterization of gypsum scale formation and control in RO membrane desalination of brackish water.* Journal of Membrane Science, 2006. **279**(1-2): p. 655-668.

198. Wang, J., et al., *Enhanced gypsum scaling by organic fouling layer on nanofiltration membrane: Characteristics and mechanisms.* Water Research, 2016. **91**: p. 203-213.

199. Mattaraj, S., et al., *A combined pore blockage, osmotic pressure, and cake filtration model for crossflow nanofiltration of natural organic matter and inorganic salts.* Desalination, 2011. **274**(1–3): p. 182-191.

200. Radu, A.I., et al., *Combined biofouling and scaling in membrane feed channels: a new modeling approach.* Biofouling, 2015. **31**(1): p. 83-100.

201. Thompson, J., et al., *RO membrane mineral scaling in the presence of a biofilm.* Journal of Membrane Science, 2012. **415–416**: p. 181-191.

202. Liu, Y. and B. Mi, *Combined fouling of forward osmosis membranes: Synergistic foulant interaction and direct observation of fouling layer formation.* Journal of Membrane Science, 2012. **407–408**: p. 136-144.

203. Fritzmann, C., et al., *State-of-the-art of reverse osmosis desalination.* Desalination, 2007. **216**(1): p. 1-76.

204. Hilal, N., et al., *A comprehensive review of nanofiltration membranes:Treatment, pretreatment, modelling, and atomic force microscopy.* Desalination, 2004. **170**(3): p. 281-308.

205. Van der Bruggen, B., *Nanofiltration*, in *Encyclopedia of membrane science and technology*, E.M.V. Hoek and V.V. Tarabara, Editors. 2013, John Wiley & Sons, Inc.

206. Hua, G. and D.A. Reckhow, *Characterization of disinfection byproduct precursors based on hydrophobicity and molecular size.* Environmental Science & Technology, 2007. **41**(9): p. 3309-3315.

207. Chellam, S. and J.S. Taylor, *Simplified analysis of contaminant rejection during ground- and surface water nanofiltration under the information collection rule.* Water Research, 2001. **35**(10): p. 2460-2474.

208. Sharma, R.R. and S. Chellam, *Temperature and concentration effects on electrolyte transport across porous thin-film composite nanofiltration membranes: Pore transport mechanisms and energetics of permeation.* Journal of Colloid And Interface Science, 2006. **298**(1): p. 327-340.

209. Bellona, C., M. Marts, and J.E. Drewes, *The effect of organic membrane fouling on the properties and rejection characteristics of nanofiltration membranes.* Separation and Purification Technology, 2010. **74**(1): p. 44-54.

210. Boussu, K., et al., *Characterization of polymeric nanofiltration membranes for systematic analysis of membrane performance.* Journal of Membrane Science, 2006. **278**(1–2): p. 418-427.

211. Dixon, M.B., et al., *Removal of cyanobacterial metabolites by nanofiltration from two treated waters.* Journal of Hazardous Materials, 2011. **188**(1-3): p. 288-95.

212. Park, N., et al., *Foulants analyses for NF membranes with different feed waters: coagulation/sedimentation and sand filtration treated waters.* Desalination, 2007. **202**(1-3): p. 231-238.

213. Simon, A., W.E. Price, and L.D. Nghiem, *Influence of formulated chemical cleaning reagents on the surface properties and separation efficiency of nanofiltrationmembranes.* Journal of Membrane Science, 2013. **432**: p. 73-82.

214. Tang, C.Y., Y.-N. Kwon, and J.O. Leckie, *Fouling of reverse osmosis and nanofiltration membranes by humic acid: Effects of solution composition and hydrodynamic conditions.* Journal of Membrane Science, 2007. **290**(1-2): p. 86-94.

215. Xu, B., et al., *Measurements of dissolved organic nitrogen (DON) in water samples with nanofiltration pretreatment.* Water research, 2010. **44**(18): p. 5376-84.

216. Nghiem, L.D., D. Vogel, and S. Khan, *Characterising humic acid fouling of nanofiltration membranes using bisphenol A as a molecular indicator.* Water research, 2008. **42**(15): p. 4049-4058.

217. Shih, W.-Y., et al., *Morphometric characterization of calcium sulfate dihydrate (gypsum) scale on reverse osmosis membranes.* Journal of Membrane Science, 2005. **252**(1–2): p. 253-263.

218. Xie, M. and S.R. Gray, *Gypsum scaling in forward osmosis: Role of membrane surface chemistry.* Journal of Membrane Science, 2016. **513**: p. 250-259.

219. Böke, H., et al., *Quantification of $CaCO_3$–$CaSO_3{\cdot}0.5H_2O$–$CaSO_4{\cdot}2H_2O$ mixtures by FTIR analysis and its ANN model.* Materials Letters, 2004. **58**(5): p. 723-726.

220. Anbalagan, G., et al., *Infrared, optical absorption, and EPR spectroscopic studies on natural gypsum.* Vibrational Spectroscopy, 2009. **50**(2): p. 226-230.

221. Rosi, F., et al., *On the use of overtone and combination bands for the analysis of the $CaSO_4$-H_2O system by mid-infrared reflection spectroscopy.* Applied Spectroscopy, 2010. **64**(8): p. 956-963.

222. Zydney, A.L., *Stagnant film model for concentration polarization in membrane systems.* Journal of Membrane Science, 1997. **130**(1–2): p. 275-281.

223. Mariñas, B. and R. Urama, *Modeling concentration-polarization in reverse osmosis spiral-wound elements.* Journal of Environmental Engineering, 1996. **122**(4): p. 292-298.

224. Lyster, E., et al., *Coupled 3-D hydrodynamics and mass transfer analysis of mineral scaling-induced flux decline in a laboratory plate-and-frame reverse osmosis membrane module.* Journal of Membrane Science, 2009. **339**(1–2): p. 39-48.

225. Uchymiak, M., et al., *Kinetics of gypsum crystal growth on a reverse osmosis membrane.* Journal of Membrane Science, 2008. **314**(1–2): p. 163-172.

226. Braghetta, A. and F.A. DiGiano, *Nanofiltration of natural organic matter: pH and ionic strength effects.* Journal of Environmental Engineering, 1997. **123**(7): p. 628.

227. Jucker, C. and M.M. Clark, *Adsorption of aquatic humic substances on hydrophobic ultrafiltration membranes.* Journal of Membrane Science, 1994. **97**: p. 37-52.

228. Vrijenhoek, E.M., S. Hong, and M. Elimelech, *Influence of membrane surface properties on initial rate of colloidal fouling of reverse osmosis and nanofiltration membranes.* Journal of Membrane Science, 2001. **188**(1): p. 115-128.

229. Kwon, Y. and J. Leckie, *Hypochlorite degradation of crosslinked polyamide membranes II. Changes in hydrogen bonding behavior and performance.* Journal of Membrane Science, 2006. **282**(1-2): p. 456-464.

230. Petersen, R.J., *Composite reverse osmosis and nanofiltration membranes.* Journal of Membrane Science, 1993. **83**(1): p. 81-150.

231. Tang, C.Y., Y.-N. Kwon, and J.O. Leckie, *The role of foulant-foulant electrostatic interaction on limiting flux for RO and NF membranes during humic acid fouling-Theoretical basis, experimental evidence, and AFM interaction force measurement.* Journal of Membrane Science, 2009. **326**(2): p. 526-532.

232. Jarusutthirak, C., G. Amy, and J.-P. Croué, *Fouling characteristics of wastewater effluent organic matter (EfOM) isolates on NF and UF membranes.* Desalination, 2002. **145**: p. 247-255.

233. Gorzalski, A.S. and O. Coronell, *Fouling of nanofiltration membranes in full- and bench-scale systems treating groundwater containing silica.* Journal of Membrane Science, 2014. **468**: p. 349-359.

234. Christie, A.B., et al., *An XPS study of ion-induced compositional changes with group II and group IV compounds.* Applications of Surface Science, 1983. **15**(1–4): p. 224-237.

235. Siriwardane, R.V. and J.M. Cook, *Interactions of SO_2 with sodium deposited on CaO.* Journal of Colloid And Interface Science, 1986. **114**(2): p. 525-535.

236. Do, V.T., et al., *Degradation of polyamide nanofiltration and reverse osmosis membranes by hypochlorite.* Environmental Science & Technology, 2012. **46**(2): p. 852-859.

237. Ang, W.L., et al., *A review on the applicability of integrated/hybrid membrane processes in water treatment and desalination plants.* Desalination, 2015. **363**: p. 2-18.

238. Mohammad, A.W., et al., *Nanofiltration membranes review: Recent advances and future prospects.* Desalination, 2015. **356**: p. 226-254.

239. Schäfer, A.I., A.G. Fane, and T.D. Waite, *Fouling effects on rejection in the membrane filtration of natural waters.* Desalination, 2000. **131**(1): p. 215-224.

240. Gao, L.X., et al., *Novel design and operational control of integrated ultrafiltration — Reverse osmosis system with RO concentrate backwash.* Desalination, 2016. **382**: p. 43-52.

241. Reiss, R.C., J.S. Taylor, and C. Robert, *Surface water treatment using nanofiltration—pilot testing results and design considerations.* Desalination, 1999. **125**(1): p. 97-112.

242. Huang, H., K. Schwab, and J.G. Jacangelo, *Pretreatment for low pressure membranes in water treatment: A review.* Environmental Science & Technology, 2009. **43**(9): p. 3011-3019.

243. Cañizares, P., et al., *Electrodissolution of Aluminum Electrodes in Electrocoagulation Processes.* Industrial & Engineering Chemistry Research, 2005. **44**(12): p. 4178-4185.

244. Sarkar, M.S.K.A., G.M. Evans, and S.W. Donne, *Bubble size measurement in electroflotation.* Minerals Engineering, 2010. **23**(11–13): p. 1058-1065.

245. Roberson, J.A., et al., *Development of recommendations for the fourth contaminant candidate list.* Journal-American Water Works Association, 2015. **107**(10): p. E509-E522.

246. USEPA, *The third unregulated contaminant monitoring rule (UCMR 3): Data summary, July 2016*, USEPA, Editor. 2016.

247. O'Donnell, A.J., et al., *Removal of strontium from drinking water by conventional treatment and lime softening in bench-scale studies.* Water Research, 2016. **103**: p. 319-333.

248. Richards, L.A., B.S. Richards, and A.I. Schäfer, *Renewable energy powered membrane technology: Salt and inorganic contaminant removal by nanofiltration/reverse osmosis.* Journal of Membrane Science, 2011. **369**(1–2): p. 188-195.

249. Ding, S., et al., *The effects of organic fouling on the removal of radionuclides by reverse osmosis membranes.* Water Research, 2016. **95**: p. 174-184.

250. Nghiem, L.D. and S. Hawkes, *Effects of membrane fouling on the nanofiltration of trace organic contaminants.* Desalination, 2009. **236**(1): p. 273-281.

251. McCafferty, E., *The electrode kinetics of pit initiation on aluminum.* Corrosion Science, 1995. **37**(3): p. 481-492.

252. Tomcsányi, L., et al., *Electrochemical study of the pitting corrosion of aluminium and its alloys—II. Study of the interaction of chloride ions with a passive film on aluminium and initiation of pitting corrosion.* Electrochimica Acta, 1989. **34**(6): p. 855-859.

253. Lee, W.-J. and S.-I. Pyun, *Effects of sulphate ion additives on the pitting corrosion of pure aluminium in 0.01 M NaCl solution.* Electrochimica Acta, 2000. **45**(12): p. 1901-1910.

254. Mechelhoff, M., G.H. Kelsall, and N.J.D. Graham, *Super-faradaic charge yields for aluminium dissolution in neutral aqueous solutions.* Chemical Engineering Science, 2013. **95**: p. 353-359.

255. Aballe, A., et al., *Localized alkaline corrosion of alloy AA5083 in neutral 3.5% NaCl solution.* Corrosion Science, 2001. **43**(9): p. 1657-1674.

256. Zaid, B., et al., *Effects of pH and chloride concentration on pitting corrosion of AA6061 aluminum alloy.* Corrosion Science, 2008. **50**(7): p. 1841-1847.

257. Iriarte-Velasco, U., J.I. Álvarez-Uriarte, and J.R. González-Velasco, *Enhanced coagulation under changing alkalinity-hardness conditions and its implications on trihalomethane precursors removal and relationship with UV absorbance.* Separation and Purification Technology, 2007. **55**(3): p. 368-380.

258. Matilainen, A., M. Vepsäläinen, and M. Sillanpää, *Natural organic matter removal by coagulation during drinking water treatment: A review.* Advances in Colloid and Interface Science, 2010. **159**(2): p. 189-197.

259. Bose, P. and D.A. Reckhow, *The effect of ozonation on natural organic matter removal by alum coagulation.* Water Research, 2007. **41**(7): p. 1516-1524.

260. Singer, P.C., *Formation and control of disinfection by-products in drinking water*. 1999, Denver, CO: American Water Works Association.

261. Holt, P.K., et al., *A quantitative comparison between chemical dosing and electrocoagulation.* Colloids and Surfaces A: Physicochemical and Engineering Aspects, 2002. **211**(2–3): p. 233-248.

262. Kim, H.-C. and M.-J. Yu, *Characterization of natural organic matter in conventional water treatment processes for selection of treatment processes focused on DBPs control.* Water Research, 2005. **39**(19): p. 4779-4789.

263. Chakraborti, R.K., J.F. Atkinson, and J.E. Van Benschoten, *Characterization of alum floc by image analysis.* Environmental Science & Technology, 2000. **34**(18): p. 3969-3976.

264. Tang, C.Y., Y.-N. Kwon, and J.O. Leckie, *Probing the nano- and micro-scales of reverse osmosis membranes—A comprehensive characterization of physiochemical properties of uncoated and coated membranes by XPS, TEM, ATR-FTIR, and streaming potential measurements.* Journal of Membrane Science, 2007. **287**(1): p. 146-156.

265. Jeong, S., et al., *Foulant analysis of a reverse osmosis membrane used pretreated seawater.* Journal of Membrane Science, 2013. **428**: p. 434-444.

266. Leenheer, J.A., *Systematic approaches to comprehensive analyses of natural organic matter.* Annals of Environmental Science, 2009. **3**: p. 1-130.

267. Marley, N.A., et al., *Chemical characterization of size-fractionated humic and fulvic materials in aqueous samples.* Science of The Total Environment, 1992. **113**(1): p. 159-177.

268. Maurice, P.A., et al., *A comparison of surface water natural organic matter in raw filtered water samples, XAD, and reverse osmosis isolates.* Water Research, 2002. **36**(9): p. 2357-2371.

269. Ang, W.L., et al., *Hybrid coagulation–NF membrane processes for brackish water treatment: Effect of pH and salt/calcium concentration.* Desalination, 2016. **390**: p. 25-32.

270. Chon, K., et al., *Combined coagulation-disk filtration process as a pretreatment of ultrafiltration and reverse osmosis membrane for wastewater reclamation: An autopsy study of a pilot plant.* Water Research, 2012. **46**(6): p. 1803-1816.

271. Schäfer, A.I., A.G. Fane, and T.D. Waite, *Nanofiltration : Principles and applications*, ed. A.I. Schäfer, A.G. Fane, and T.D. Waite. 2005: Oxford ; New York : Elsevier Advanced Technology.

272. Martell, A.E. and R.J. Motekaitis, *Determination and use of stability constants*. 2nd ed, ed. A.E. Martell and R.J. Motekaitis. 1992, New York: VCH Publishers.

273. Sharma, R.R. and S. Chellam, *Concentration effects on electrolyte transport across porous thin-film composite nanofiltration membranes: Pore transport mechanisms and energetics of permeation.* Journal of Colloid and Interface Science, 2006. **298**(1): p. 327-340.

274. Wang, J., et al., *Effects of water chemistry on structure and performance of polyamide composite membranes.* Journal of Membrane Science, 2014. **452**: p. 415-425.

275. Schaep, J., et al., *Retention mechanisms in nanofiltration*, in *Chemistry for the protection of the environment*, L. Pawłowski, et al., Editors. 1998, Springer US: New York. p. 117-125.

276. Gilron, J., N. Gara, and O. Kedem, *Experimental analysis of negative salt rejection in nanofiltration membranes.* Journal of Membrane Science, 2001. **185**(2): p. 223-236.

277. Levenstein, R., D. Hasson, and R. Semiat, *Utilization of the Donnan effect for improving electrolyte separation with nanofiltration membranes.* Journal of Membrane Science, 1996. **116**(1): p. 77-92.

278. Rautenbach, R. and A. Gröschl, *Separation potential of nanofiltration membranes.* Desalination, 1990. **77**: p. 73-84.

279. Yaroshchuk, A.E., *Negative rejection of ions in pressure-driven membrane processes.* Advances in Colloid and Interface Science, 2008. **139**(1–2): p. 150-173.

280. Krieg, H.M., et al., *Salt rejection in nanofiltration for single and binary salt mixtures in view of sulphate removal.* Desalination, 2005. **171**(2): p. 205-215.

281. Rahardianto, A., et al., *High recovery membrane desalting of low-salinity brackish water: Integration of accelerated precipitation softening with membrane RO.* Journal of Membrane Science, 2007. **289**(1-2): p. 123-137.

282. Ding, S., et al., *Effects of feed solution chemistry on low pressure reverse osmosis filtration of cesium and strontium.* Journal of Hazardous Materials, 2015. **294**: p. 27-34.

283. National Research Council, *Water reuse: Potential for expanding the nation's water supply through reuse of municipal wastewater*. 2012, Washington, D.C.: The National Academies Press.

284. Wachinski, A.M., *Membrane processes for water reuse*. 2013: McGraw-Hill.

285. Tang, F., et al., *Fouling of reverse osmosis membrane for municipal wastewater reclamation: Autopsy results from a full-scale plant.* Desalination, 2014. **349**: p. 73-79.

286. Khan, M.T., et al., *How different is the composition of the fouling layer of wastewater reuse and seawater desalination RO membranes?*. Water Research, 2014. **59**: p. 271-282.

287. ASCE. *2013 Report card for America's infrastructure: Wastewater*. 2013 [cited 2016, May 26]; Available from: http://www.infrastructurereportcard.org/a/#p/wastewater/overview.

288. Kim, J., F.A. DiGiano, and R.D. Reardon, *Autopsy of high-pressure membranes to compare effectiveness of MF and UF pretreatment in water reclamation.* Water Research, 2008. **42**(3): p. 697-706.

289. Durham, B., M.M. Bourbigot, and T. Pankratz, *Membranes as pretreatment to desalination in wastewater reuse: operating experience in the municipal and industrial sectors.* Desalination, 2001. **138**(1–3): p. 83-90.

290. Farias, E.L., K.J. Howe, and B.M. Thomson, *Spatial and temporal evolution of organic foulant layers on reverse osmosis membranes in wastewater reuse applications.* Water Research, 2014. **58**: p. 102-110.

291. Tang, F., et al., *Fouling characteristics of reverse osmosis membranes at different positions of a full-scale plant for municipal wastewater reclamation.* Water Research, 2016. **90**: p. 329-336.

292. Metcalf & Eddy and AECOM, *Wastewater engineering: Treatment and resource recovery*. 5 ed. 2014, New York: McGraw-Hill Education.

293. Shon, H.K., et al., *Influence of flocculation and adsorption as pretreatment on the fouling of ultrafiltration and nanofiltration membranes: Application with biologically treated sewage effluent.* Environmental Science & Technology, 2005. **39**(10): p. 3864-3871.

294. Gabelich, C.J., et al., *Control of residual aluminum from conventional treatment to improve reverse osmosis performance.* Desalination, 2006. **190**(1-3): p. 147-160.

295. Pontie, M., et al., *Tools for membrane autopsies and antifouling strategies in seawater feeds: a review.* Desalination, 2005. **181**(1-3): p. 75-90.

296. Chon, K., et al., *Advanced characterization of organic foulants of ultrafiltration and reverse osmosis from water reclamation.* Desalination, 2012. **301**: p. 59-66.

297. Xu, P. and J.E. Drewes, *Viability of nanofiltration and ultra-low pressure reverse osmosis membranes for multi-beneficial use of methane produced water.* Separation and Purification Technology, 2006. **52**(1): p. 67-76.

298. Ang, W.S., et al., *Fouling and cleaning of RO membranes fouled by mixtures of organic foulants simulating wastewater effluent.* Journal of Membrane Science, 2011. **376**(1-2): p. 196-206.

299. Al-Amoudi, A. and R.W. Lovitt, *Fouling strategies and the cleaning system of NF membranes and factors affecting cleaning efficiency.* Journal of Membrane Science, 2007. **303**(1-2): p. 4-28.

300. Hydranautics, *Foulants and cleaning procedures for composite polyamide RO membrane elements (ESPA, ESNA, CPA, LFC, and SWC)*. 2003, Technical service bulletin: Oceanside. p. 1-14.

301. Oldani, M. and G. Schock, *Characterization of ultrafiltration membranes by infrared spectroscopy, ESCA, and contact angle measurements.* Journal of Membrane Science, 1989. **43**(2-3): p. 243-258.

302. Belfer, S., et al., *Surface characterization by FTIR-ATR spectroscopy of polyethersulfone membranes-unmodified , modified and protein fouled.* Journal of Membrane Science, 2000. **172**(1-2): p. 113-124.

303. White, M.C., et al., *Evaluating criteria for enhanced coagulation compliance.* Journal-American Water Works Association, 1997. **89**(5): p. 64-77.

304. Guan, X.-h., G.-h. Chen, and C. Shang, *ATR-FTIR and XPS study on the structure of complexes formed upon the adsorption of simple organic acids on aluminum hydroxide.* Journal of Environmental Sciences (China), 2007. **19**(4): p. 438-43.

305. Socrates, G., *Infrared and Raman characteristic group frequencies: Tables and charts*. 3 ed. 2000, Chichester, New York: Wiley.

306. Kloprogge, J.T., et al., *XPS study of the major minerals in bauxite: Gibbsite, bayerite and (pseudo-)boehmite.* Journal of Colloid and Interface Science, 2006. **296**(2): p. 572-576.

307. Shih, W.-Y., et al., *Ranking of antiscalant performance for gypsum scale suppression in the presence of residual aluminum.* Desalination, 2006. **196**(1-3): p. 280-292.

308. Clark, M.M. and P. Lucas, *Diffusion and partitioning of humic acid in a porous ultrafiltration membrane.* Journal of Membrane Science, 1998. **143**(1–2): p. 13-25.

309. Gregory, K.B., R.D. Vidic, and D.A. Dzombak, *Water management challenges associated with the production of shale gas by hydraulic fracturing.* Elements, 2011. **7**(3): p. 181-186.

310. Scanlon, B.R., R.C. Reedy, and J.P. Nicot, *Comparison of water use for hydraulic fracturing for unconventional oil and gas versus conventional oil.* Environmental Science & Technology, 2014. **48**(20): p. 12386-12393.

311. Vengosh, A., et al., *A critical review of the risks to water resources from unconventional shale gas development and hydraulic fracturing in the united states.* Environmental Science & Technology, 2014. **48**(15): p. 8334-8348.

312. Mauter, M.S., et al., *Regional variation in water-related impacts of shale gas development and implications for emerging international plays.* Environmental Science & Technology, 2014. **48**(15): p. 8298-8306.

313. U.S. Environmental Protection Agency, *Health effects support document for boron* 2008, Office of Water (4304T), Health and Ecological Criteria Division: Washington, DC.

314. Yilmaz, A.E., et al., *Boron removal from geothermal waters by electrocoagulation.* Journal of Hazardous Materials, 2008. **153**(1-2): p. 146-151.

315. Xu, P., J.E. Drewes, and D. Heil, *Beneficial use of co-produced water through membrane treatment: technical-economic assessment.* Desalination, 2008. **225**(1-3): p. 139-155.

316. Mauter, M.S. and V.R. Palmer, *Expert elicitation of trends in Marcellus oil and gas wastewater management.* Journal of Environmental Engineering, 2014. **140**(5): p. B4014004.

317. Theiss, F.L., G.A. Ayoko, and R.L. Frost, *Removal of boron species by layered double hydroxides: a review.* Journal of Colloid And Interface Science, 2013. **402**: p. 114-121.

318. Wang, B., X. Guo, and P. Bai, *Removal technology of boron dissolved in aqueous solutions – A review.* Colloids and Surfaces A: Physicochemical and Engineering Aspects, 2014. **444**: p. 338-344.

319. Wolska, J. and M. Bryjak, *Methods for boron removal from aqueous solutions — A review.* Desalination, 2013. **310**: p. 18-24.

320. Karahan, S., et al., *Removal of boron from aqueous solution by clays and modified clays.* Journal of Colloid and Interface Science, 2006. **293**(1): p. 36-42.

321. Benko, K.L. and J.E. Drewes, *Produced water in the Western United States: Geographical distribution, occurrence, and composition.* Environmental Engineering Science, 2008. **25**(2): p. 239-246.

322. Shaffer, D.L., et al., *Desalination and reuse of high-salinity shale gas produced water: Drivers, technologies, and future directions.* Environmental Science & Technology, 2013. **47**(17): p. 9569-9583.

323. Ahmadun, F.R., et al., *Review of technologies for oil and gas produced water treatment.* Journal of Hazardous Materials, 2009. **170**(2-3): p. 530-551.

324. Yilmaz, A.E., R. Boncukcuoğlu, and M.M. Kocakerim, *An empirical model for parameters affecting energy consumption in boron removal from boron-containing wastewaters by electrocoagulation.* Journal of Hazardous Materials, 2007. **144**(1-2): p. 101-107.

325. ASTM, *Standard test methods for boron in water* in *Annual book of ASTM standards section 11*. 1985, ASTM International: Philadelphia. p. 353-359.

326. Denne, R.A., et al., *The Cenomanian-Turonian Eagle Ford Group of South Texas: Insights on timing and paleoceanographic conditions from geochemistry and micropaleontologic analyses.* Palaeogeography Palaeoclimatology Palaeoecology, 2014. **413**: p. 2-28.

327. Wang, L., J.D. Fortner, and D.E. Giammar, *Impact of water chemistry on element mobilization from Eagle Ford shale.* Environmental Engineering Science, 2015. **32**(4): p. 310-320.

328. Danadurai, K.S.K., et al., *Trace elemental analysis of airborne particulate matter using dynamic reaction cell inductively coupled plasma - mass spectrometry: Application to monitoring episodic industrial emission events.* Analytica Chimica Acta, 2011. **686**(1-2): p. 40-49.

329. Yilmaz, A.E., et al., *The investigation of parameters affecting boron removal by electrocoagulation method.* Journal of Hazardous Materials, 2005. **125**(1-3): p. 160-165.

330. Zhang, J., M. Klasky, and B.C. Letellier, *The aluminum chemistry and corrosion in alkaline solutions.* Journal of Nuclear Materials, 2009. **384**(2): p. 175-189.

331. Guerra, K., K. Dahm, and S. Dundorf, *Oil and gas produced water management and beneficial use in the western united states*. 2011, United States Bureau of Reclamation, Science and Technology Program: Denver.

332. Wandera, D., et al., *Modification of ultrafiltration membranes with block copolymer nanolayers for produced water treatment: The roles of polymer chain density and polymerization time on performance.* Journal of Membrane Science, 2012. **403-404**: p. 250-260.

333. Dahm, K.G., et al., *Composite geochemical database for coalbed methane produced water quality in the rocky mountain region.* Environmental Science & Technology, 2011. **45**(18): p. 7655-7663.

334. Eyhusen, S., C. Ronning, and H. Hofsass, *Phase formation of boron nitride thin films under the influence of impurity atoms.* Diamond and Related Materials, 2003. **12**(3-7): p. 1173-1177.

335. Baes, C.F. and R.E. Mesmer, *The hydrolysis of cations*. 1976, New York: Wiley.

336. Silva, J.W.J., et al., *Morphological analysis of pits formed on Al 2024-T3 in chloride aqueous solution.* Applied Surface Science, 2004. **236**(1-4): p. 356-365.

337. Hu, C.Y., S.L. Lo, and W.H. Kuan, *Effects of co-existing anions on fluoride removal in electrocoagulation (EC) process using aluminum electrodes.* Water Research, 2003. **37**(18): p. 4513-4523.

338. Lee, W.-j. and S.-i. Pyun, *Effects of hydroxide ion addition on anodic dissolution of pure aluminium in chloride ion-containing solution.* Electrochimica Acta, 1999. **44**: p. 4041-4049.

339. Berkowitz, J., M.A. Anderson, and R.C. Graham, *Laboratory investigation of aluminum solubility and solid-phase properties following alum treatment of lake waters.* Water Research, 2005. **39**(16): p. 3918-3928.

340. Beyrouty, C.A., G.E. Van Scoyoc, and J.R. Feldkamp, *Evidence supporting specific adsorption of boron on synthetic aluminum hydroxides.* Soil Science Society of America Journal, 1984. **48**(2): p. 284-287.

341. Cotillas, S., et al., *Coupling UV irradiation and electrocoagulation for reclamation of urban wastewater.* Electrochimica Acta, 2014. **140**: p. 396-403.

342. Goldberg, S., *Inconsistency in the triple layer model description of ionic strength dependent boron adsorption.* Journal of Colloid and Interface Science, 2005. **285**(2): p. 509-517.

343. Su, C. and D.L. Suarez, *Coordination of adsorbed boron: A ftir spectroscopic study.* Environmental Science & Technology, 1995. **29**(2): p. 302-311.

344. Xu, D. and D. Peak, *Adsorption of boric acid on pure and humic acid coated am-Al $(OH)_3$: A boron K-edge XANES study.* Environmental Science & Technology, 2007. **41**(3): p. 903-908.

345. Khare, N., D. Hesterberg, and J.D. Martin, *XANES investigation of phosphate sorption in single and binary systems of iron and aluminum oxide minerals.* Environmental Science & Technology, 2005. **39**(7): p. 2152-60.

346. Kim, Y. and R.J. Kirkpatrick, *^{11}B NMR investigation of boron interaction with mineral surfaces: Results for boehmite, silica gel and illite.* Geochimica et Cosmochimica Acta, 2006. **70**(13): p. 3231-3238.

347. Peak, D., G.W. Luther, and D.L. Sparks, *ATR-FTIR spectroscopic studies of boric acid adsorption on hydrous ferric oxide.* Geochimica et Cosmochimica Acta, 2003. **67**(14): p. 2551-2560.

348. Uduman, N., et al., *A parametric study of electrocoagulation as a recovery process of marine microalgae for biodiesel production.* Chemical Engineering Journal, 2011. **174**(1): p. 249-257.

349. Vepsäläinen, M., et al., *Investigations of the effects of temperature and initial sample pH on natural organic matter (NOM) removal with electrocoagulation using response*

surface method (RSM). Separation and Purification Technology, 2009. **69**(3): p. 255-261.

350. Listiarini, K., et al., *Hybrid coagulation–nanofiltration membrane for removal of bromate and humic acid in water*. Journal of Membrane Science, 2010. **365**(1–2): p. 154-159.

351. Da Costa, A.R., A.G. Fane, and D.E. Wiley, *Spacer characterization and pressure drop modelling in spacer-filled channels for ultrafiltration.* Journal of Membrane Science, 1994. **87**(1-2): p. 79-98.

APPENDICES

Supporting information for chapter III

Lake Houston water quality

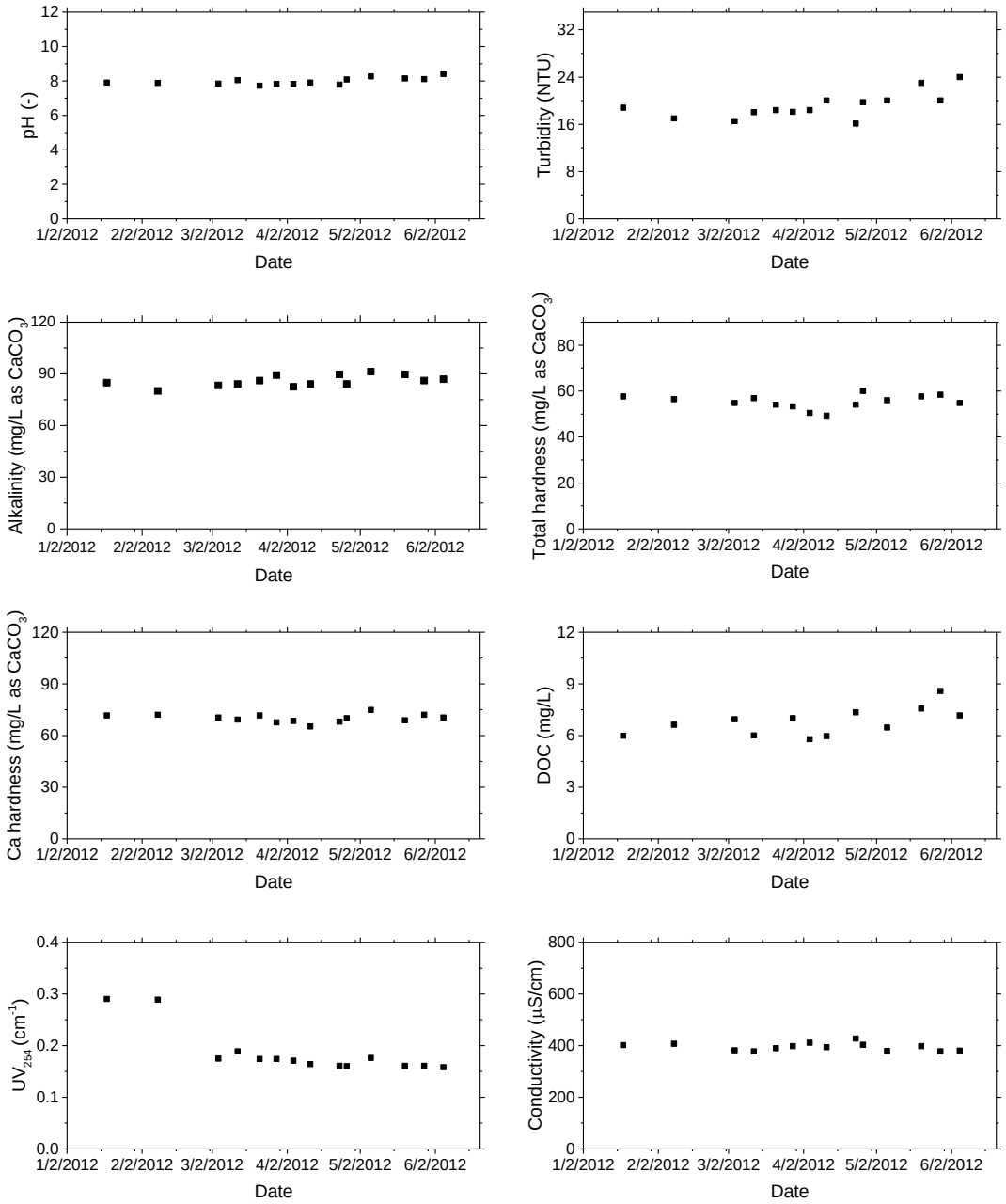

Figure A-1. Summary of Lake Houston water quality for the sample collected on December 2012.

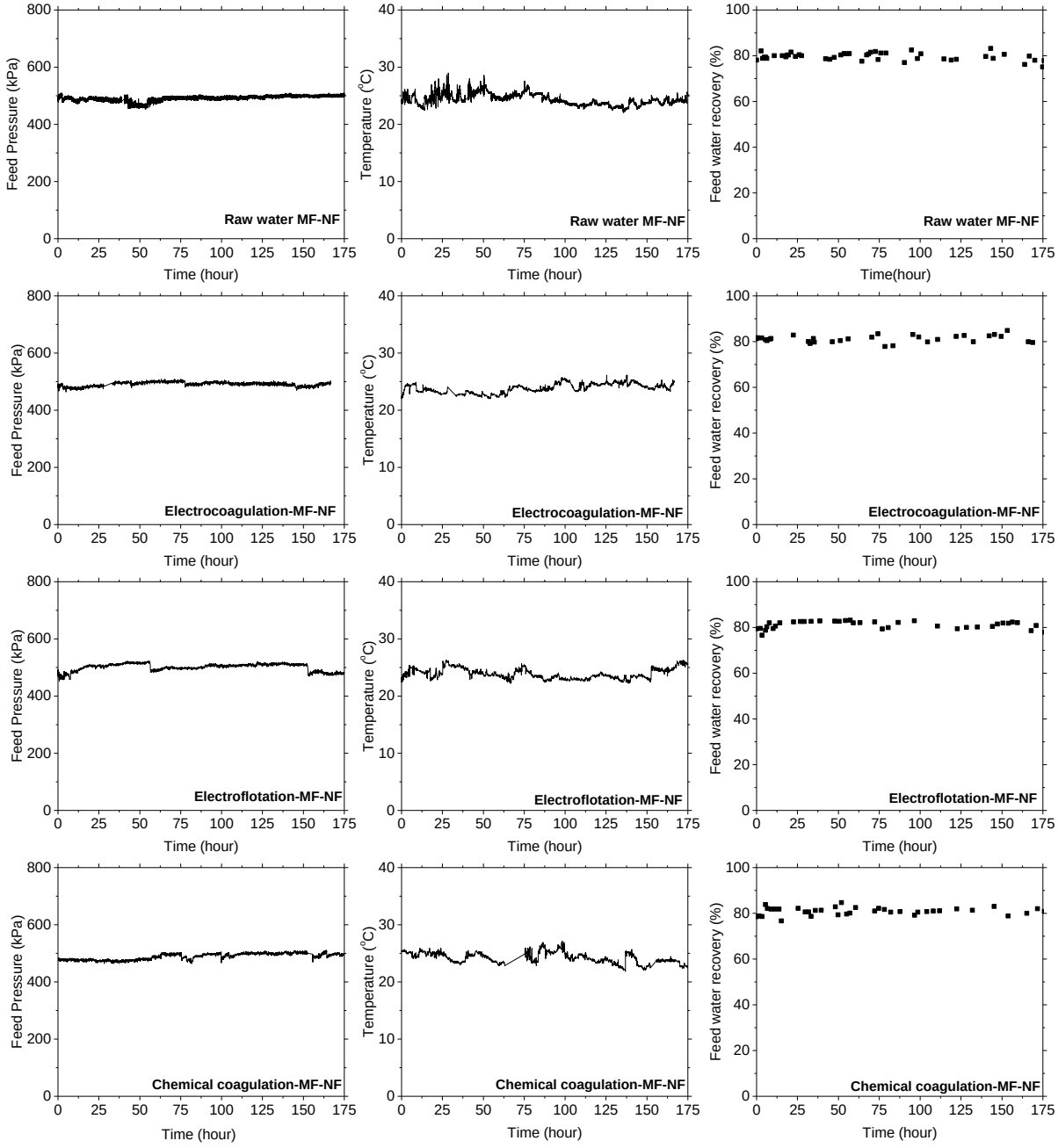

Figure A-2. Continuous monitoring of permeate recovery, transmembrane pressure and temperature of the feed water throughout the NF fouling test.

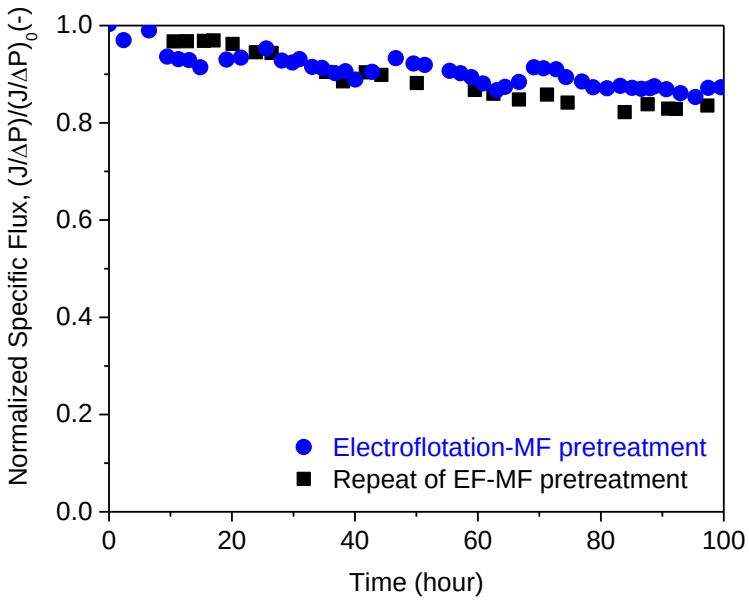

Figure A-3. Repeat of electrofloation-MF-NF to ensure the reproducibility of fouling test.

Figure A-2 depicts the constant operating conditions during the entire nanofiltration experiment for at least 170 hrs. The transmembrane pressure was kept at 470 kPa (70 psi), recovery of 80%, and temperature of 24±1 °C. Constant operating conditions for each nanofiltration experiment were necessary to have a quantitative comparison of the results obtained over the entire duration of the experiments. Additionally, to ensure that the fouling test conducted was reproducible, a repeat of nanofiltration experiment with electroflotation-MF pretreatment was performed. As can be seen in the Figure A-3 above, the flux decline profiles for both experiments were similar (16% flux decline over 100 hr period), which represented the reproducibility of the fouling test conducted in this study.

Sessile-drop technique for contact angle measurement

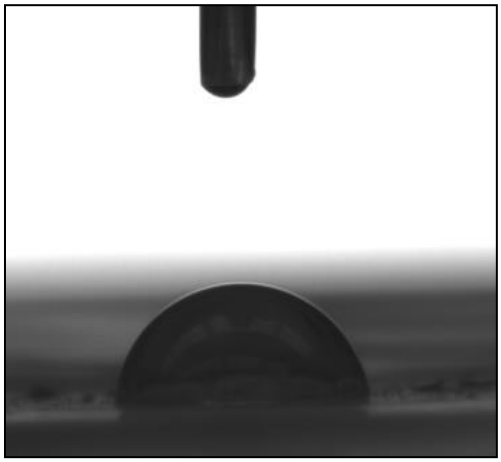

Figure A-4. Contact angle measurement using sessile-drop technique.

Further evidence of hydrophilic NOM removal by EC/EF pretreatment

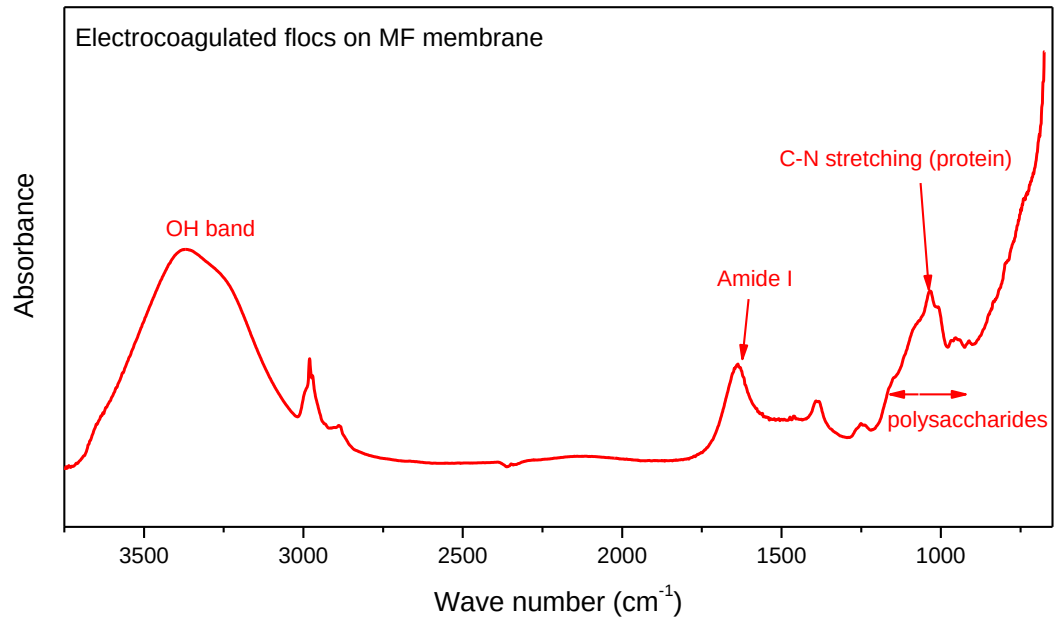

Figure A-5. ATR-FTIR of electrocoagulated flocs on MF membrane.

As seen in Figure IV-4 in chapter III, the intensity of peaks corresponding to hydrophilic fraction of NOM (i.e. polysaccharides and amides) was greatly reduced for membrane fouled with electroflotation-MF pre-treatment. This result suggested that electroflotation-MF pre-treatment transformed the highly fouling potential organics (polysaccharides) into relatively lower fouling potential organics. This argument is supported by further analysis of electrocoagulated flocs on MF membrane by ATR-FTIR as depicted in Figure A-5. The presence of polysaccharides band around 900-1200 cm^{-1} on the microfilter indicates partial removal of these compounds by EC/EF-MF. The presence of Amide I, II, and III bands on the microfilter also indicates the presence of proteins in the foulant layers. The presence of protein on the fouled membranes indicated that the source water may contain biomolecules which can come from plant, bacteria, or animal.

Characterization of protein foulants following MF-only, EC-MF, and EF-MF pretreatment

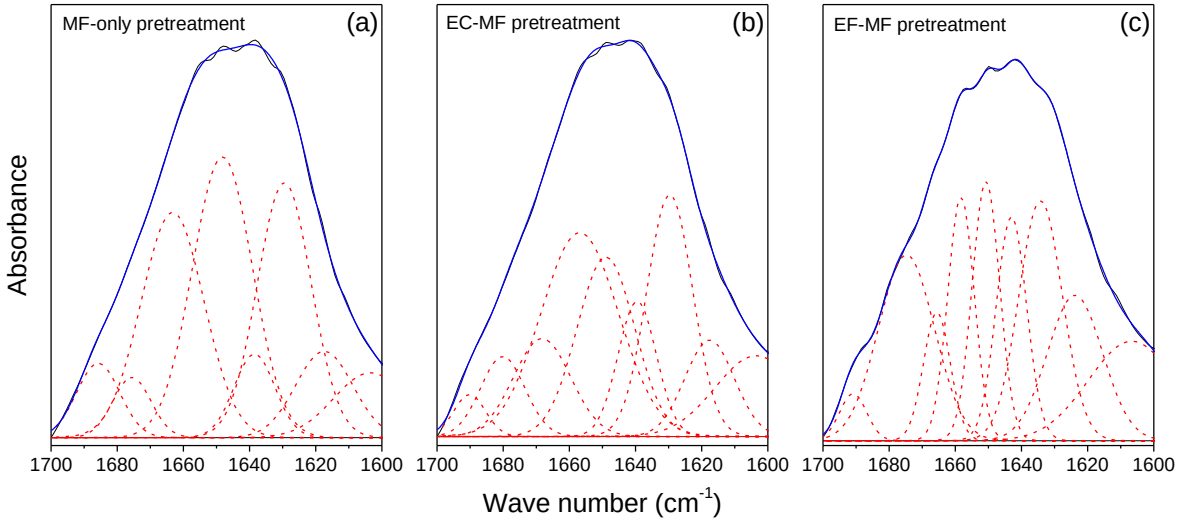

Figure A-6. Second derivative spectrum of the NF membrane surface with: (a) MF-only pretreatment, (b) EC-MF pretreatment, and (c) EF-MF pretreatment.

Disinfection byproduct precursor analysis

Chlorination experiments

Chlorine demand test was performed first to ensure that the chlorine dose given to the samples generated free chlorine residual of 1.0 ± 0.4 mg/L after 24 hour incubation in headspace-free containers at room temperature in the dark as described by Summers et al (1996). Chlorination was performed in 250 mL amber bottles which were previously soaked in diluted chlorine solution and dried in the oven overnight to ensure that the bottles were chlorine demand free. The samples were buffered to pH 8.0 by borate buffer and sufficient amount of sodium hypochlorite was added to ensure that the samples will generate free chlorine residual between 0.71 to 1.71 mg/L after 24 hour incubation. The free chlorine residual was measured by conducting a Hach DPD free chlorine test kit (Hach Company, Loveland, CO). A DPD free chlorine reagent was added to sample in 10 mL vial and the absorbance of the resulting complex was measured by a spectrophotometer (DR/4000 Spectrophotometer, Hach Company, Loveland, CO). The chlorine demand was calculated as the difference between the initial chlorine dose and the free chlorine residual.

DBP formations

The samples were collected in 40 mL vial head-space free after incubation and then quenched with ammonium sulfate for THM and sodium thiosulfate for HAA. All samples were then stored at 4°C prior to analysis. Furthermore, for THM samples, the pH of the samples were reduced to 2 by using hydrogen sulfate. Individual THM species were identified and quantified using a gas chromatography system equipped with mass spectrophotometer and purge and trap concentrator. Whereas, individual HAA species were identified by using a capillary column gas chromatograph fitted with an electron capture detector (5890 GC, Agilent

Technologies, Foster City, CA). The chlorination experiments were conducted in University of Houston, whereas the analysis using GC/MS and GC/ECD was performed in City of Houston's East and South East Water Purification Plants, Houston, TX.

DBP precursors removal by coagulation followed by nanofiltration

Four THMs and six HAAs were quantified to investigate the removal of these compounds by a hybrid system of coagulation coupled with dual membrane system of MF-NF. Figure A-7 depicts the removal of DBP precursors (THM and HAA) by nanofiltration. However, THM and HAA formation for all nanofiltered waters was shifted towards the brominated species (see Figure A-8) This was attributed to high NOM removal (~80%) combined with poor bromide ion removal by NF(>2%).

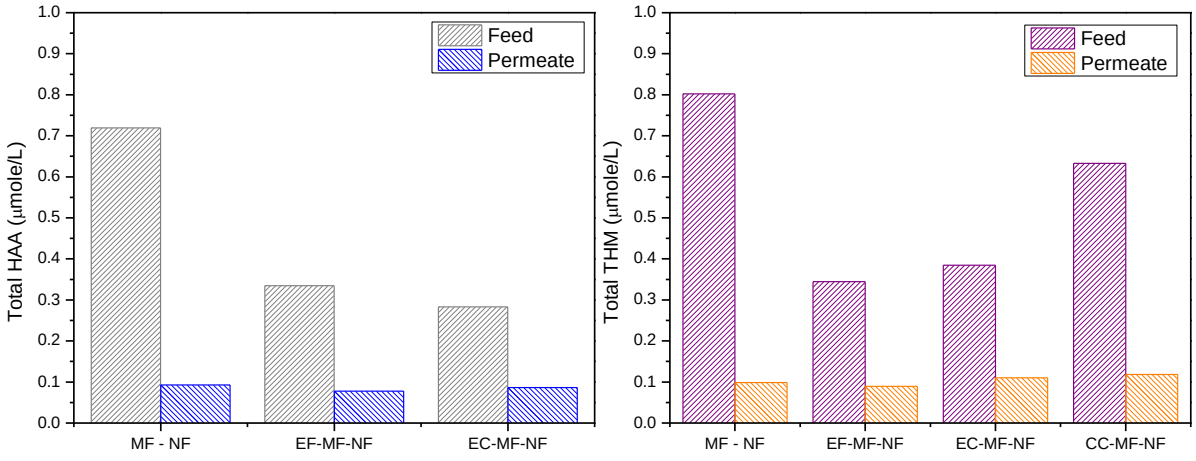

Figure A-7. Total HAA (left) and total THM (right) of feed and permeate by different pretreatments.

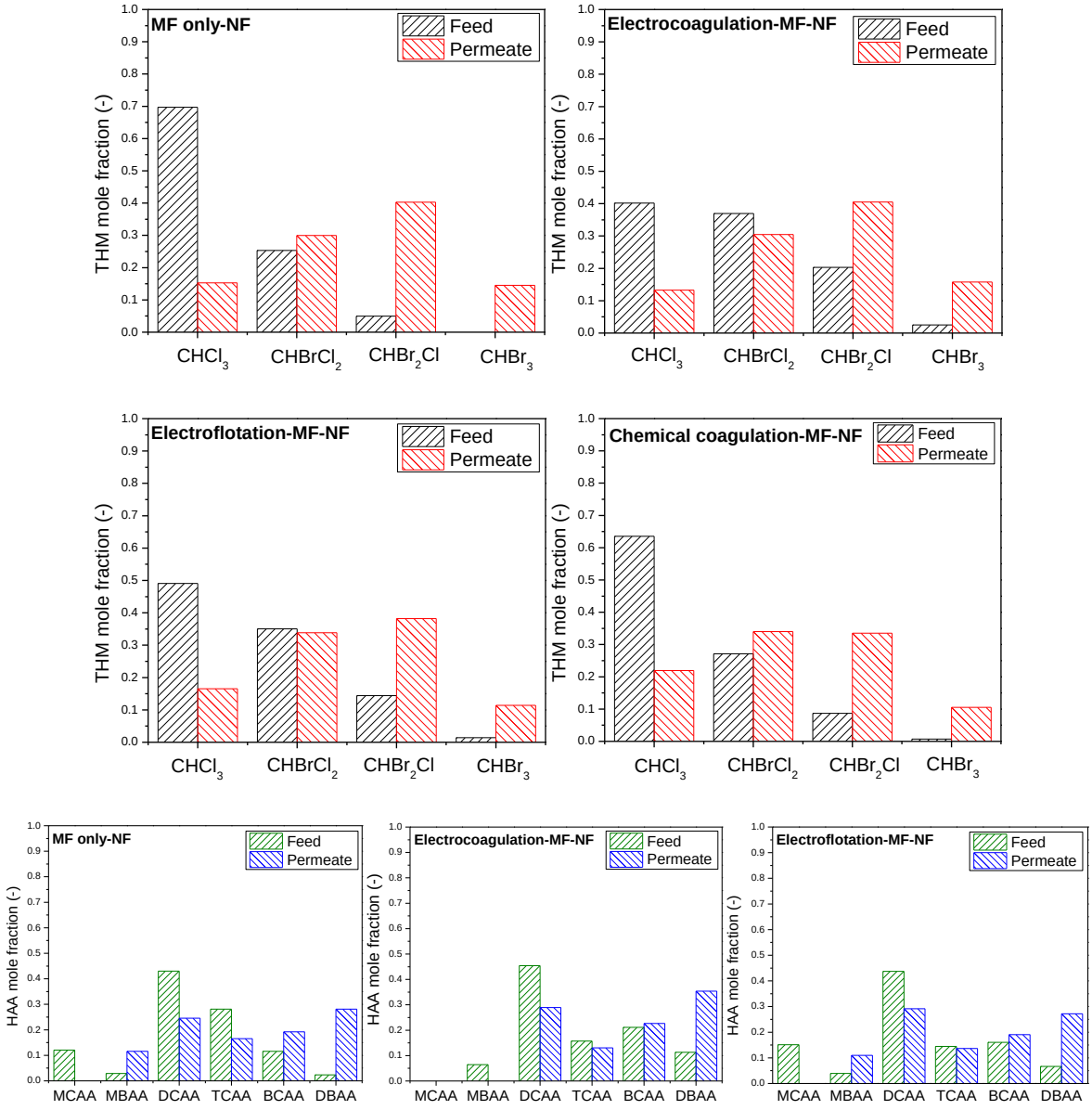

Figure A-8. The shift toward brominated species is observed for THM and HAA analysis of each pretreated water.

Supporting information for chapter IV and chapter V

Foss Reservoir water quality

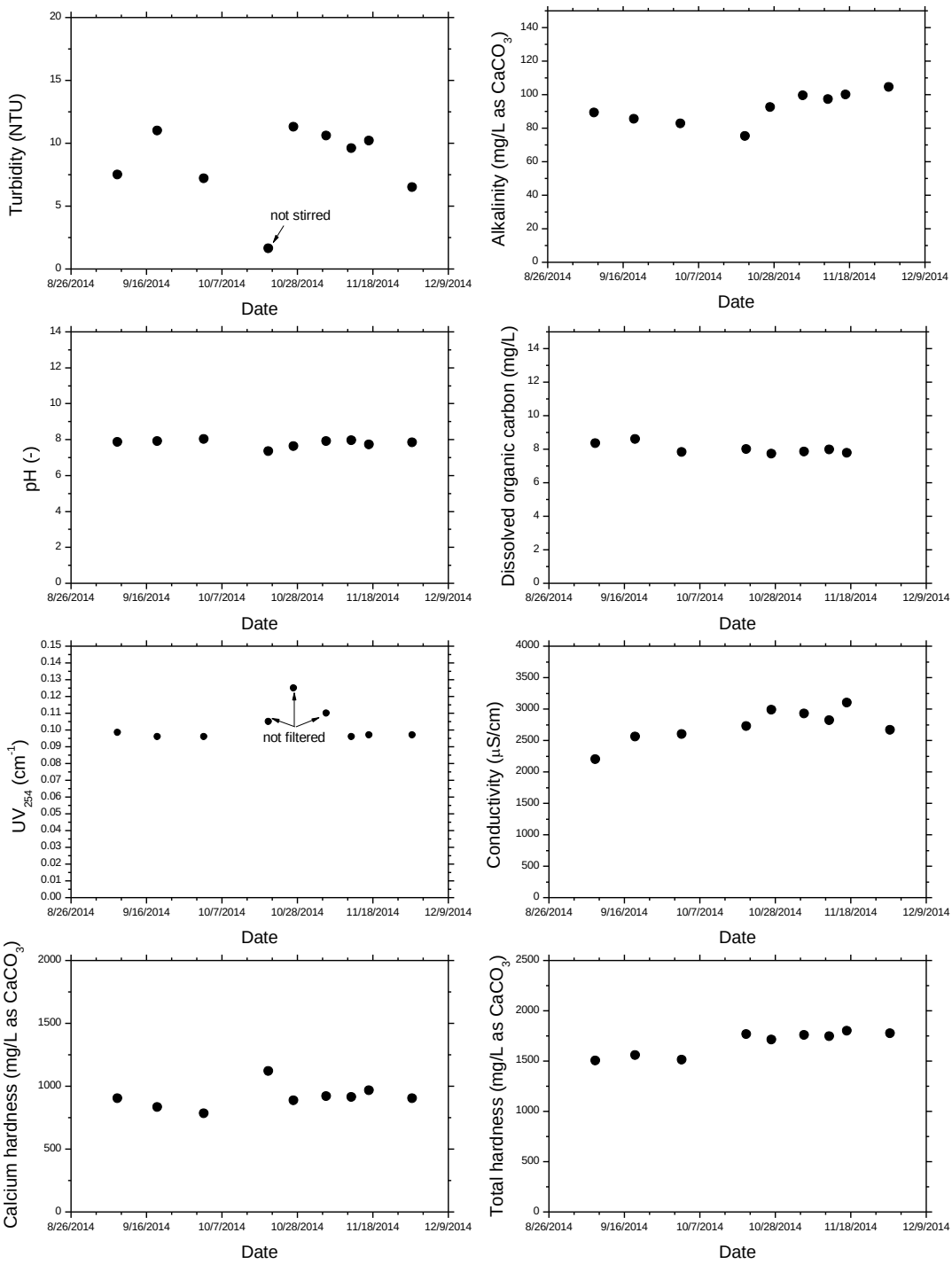

Figure A-9. Summary of Foss Reservoir water quality parameters for sample obtained in 2014

As seen in Figure A-9, many of the water quality parameters remained relatively constant leading to correspondingly low standard deviation values in Table IV-1. The coefficient of variation associated with pH, conductivity, alkalinity, calcium hardness, total hardness, DOC, and UV_{254} was less than 8% demonstrating that the water quality of this sample did not vary appreciably during this time period.

Bench-scale EC/EF setup

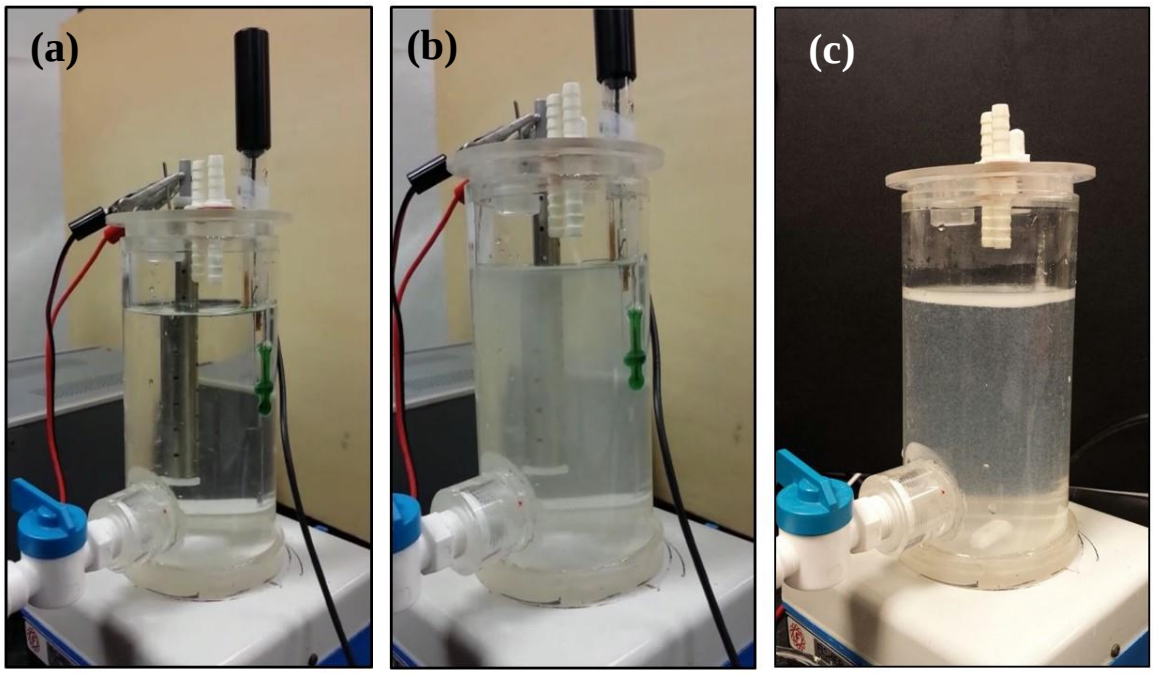

Figure A-10. Electrocoagulation experiment at the initial point (a), during electrolysis and rapid mixing, (c) after flocculation (c). Some of the floated flocs can also be seen at the end of the experiment.

Bench-scale MF setup

Figure A-11. Bench-scale MF apparatus

A photograph of the microfiltration apparatus is given in Figure A-11. The following steps were employed for microfiltration experiments:

1. Pass 300 mL of nanopure water through the virgin membrane to calculate its permeability and flux.

2. Filter approximately 1.5 L of the untreated water and monitor the cumulative permeate volute to quantify fouling rate. This step was done to collect sufficient material on the cake layer for detailed spectroscopic analysis.

3. Stop filtration and carefully remove the membrane. Put the membrane with the cake layer inside a Petri dish and vacuum-dry for 48 hour for spectroscopic analysis.

4. Put a new membrane in the cell and pass about 300 mL of nanopure water to again calculate permeability and flux.

5. Filter approximately 500 mL of untreated Foss Reservoir water. Then, physically regenerate the membrane by gently scraping the thin cake/gel layer using either a flat head forceps or a plastic scraper. Rinse the membrane with a jet of nanopure water to dislodge any remaining deposits until the membrane looks visually clean. This entire filtration and regeneration procedure constitutes one cycle.

6. Repeat the procedure three times (basically to the point that the membrane becomes severely clogged and cannot be effectively regenerated) to generate approximately 1.5 L of filtered water.

7. Repeat steps 4-6 with a new membrane 6 times to generate approximately 9 L of microfiltered water. This represents the nanofiltration feed water.

8. Store the microfiltered water at 4 °C prior to starting nanofiltration experiments.

Bench-scale NF setup

A photograph of the entire bench-scale apparatus is given in Figure A-12, which includes the data acquisition system (left side), the nanofiltration cell (middle), and the cooling water recirculator connected to the feed tank (right side). The pump, transducers, and tubing can also be seen in the middle portion of the photograph. A close-up image of the plate-and frame NF module is also shown in Figure A-13.

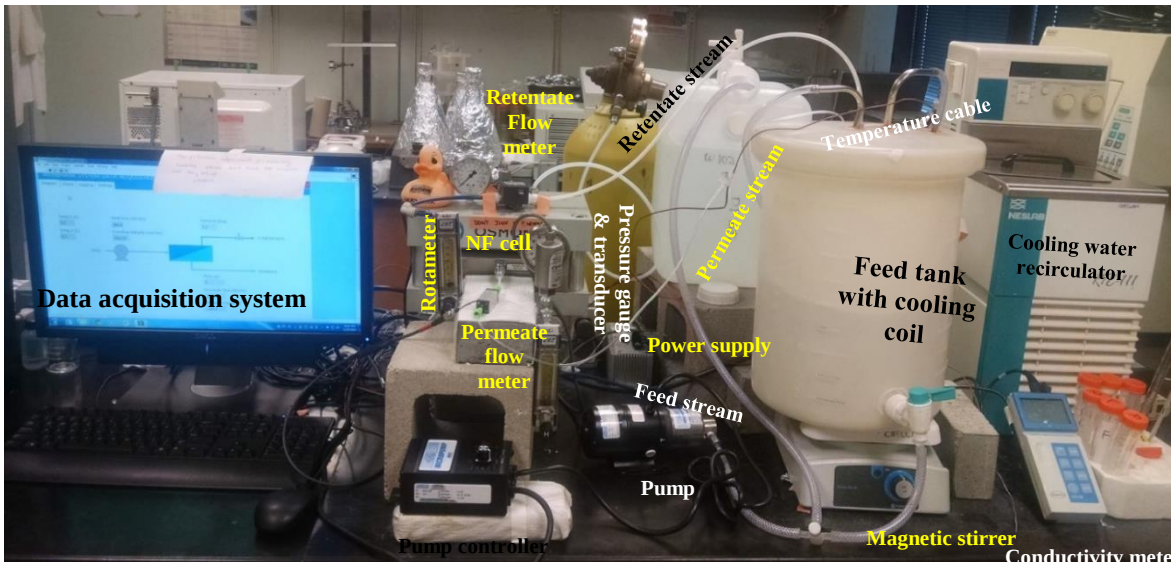

Figure A-12. Bench-scale NF setup.

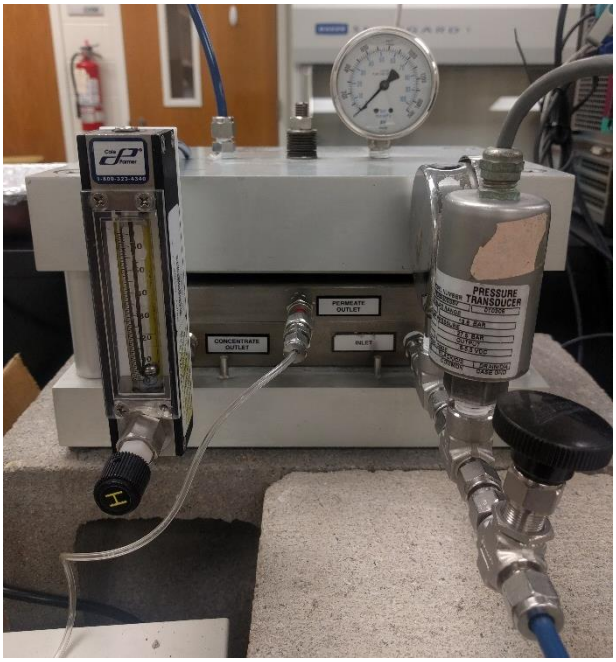

Figure A-13. Stainless-steel plate-and-frame NF/RO cell

Feed spacer geometry

The feed spacer geometry, especially the voidage, was characterized as it directly affects the crossflow velocity which subsequently affects the concentration polarization on the membrane surface. Using correlation derived from the literature [351], the void fraction for rhombus mesh spacer is calculated as:

$$\varepsilon = 1 - \frac{\pi \times d_f}{2 \times l_m \times h_{sp} \times \sin\theta} \quad \textbf{(1)}$$

where $d_{f1}=d_{f2}=$ 0.0432 cm and $l_{m1}=l_{m2}=$0.3 cm in our case and h_{sp} is the height of spacer filled channel or the thickness of the spacer (0.07874 cm). The definitions of d_{f1}, d_{f2}, l_{m1}, and l_{m2} are depicted in Figure A-14. The angle θ was measured to be 90°. The calculated voidage of the feed spacer used in this experiment is found to be 0.876.

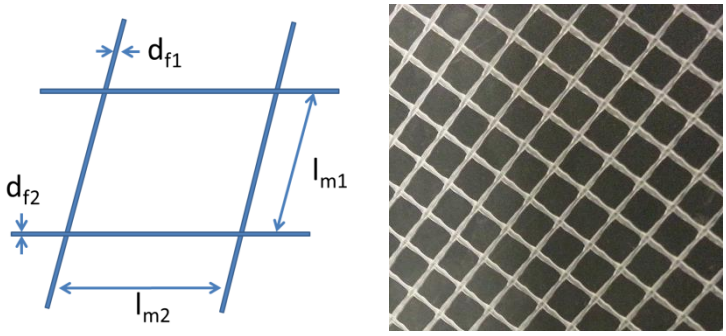

Figure A-14. Feed spacer geometry and photograph of the actual spacer employed in the experiments.

NF quality control and assurance

Several quality control assessments were employed during nanofiltration experiments to ensure the accuracy of experimental protocols. Mass balances were conducted for UV_{254} and conductivity for steady state conditions during the entire duration of nanofiltration (~7

days). Typical comparisons of experimentally observed and theoretically predicted retentate stream concentrations of conductivity and UV_{25} are shown in Figure A-15. As can be seen, the calculated and measured conductivity and UV_{254} values lie very close to the line of equality with less than 5% error. These mass balances showed that our experimental protocols were acceptable and the water quality analysis and flow monitoring were accurate.

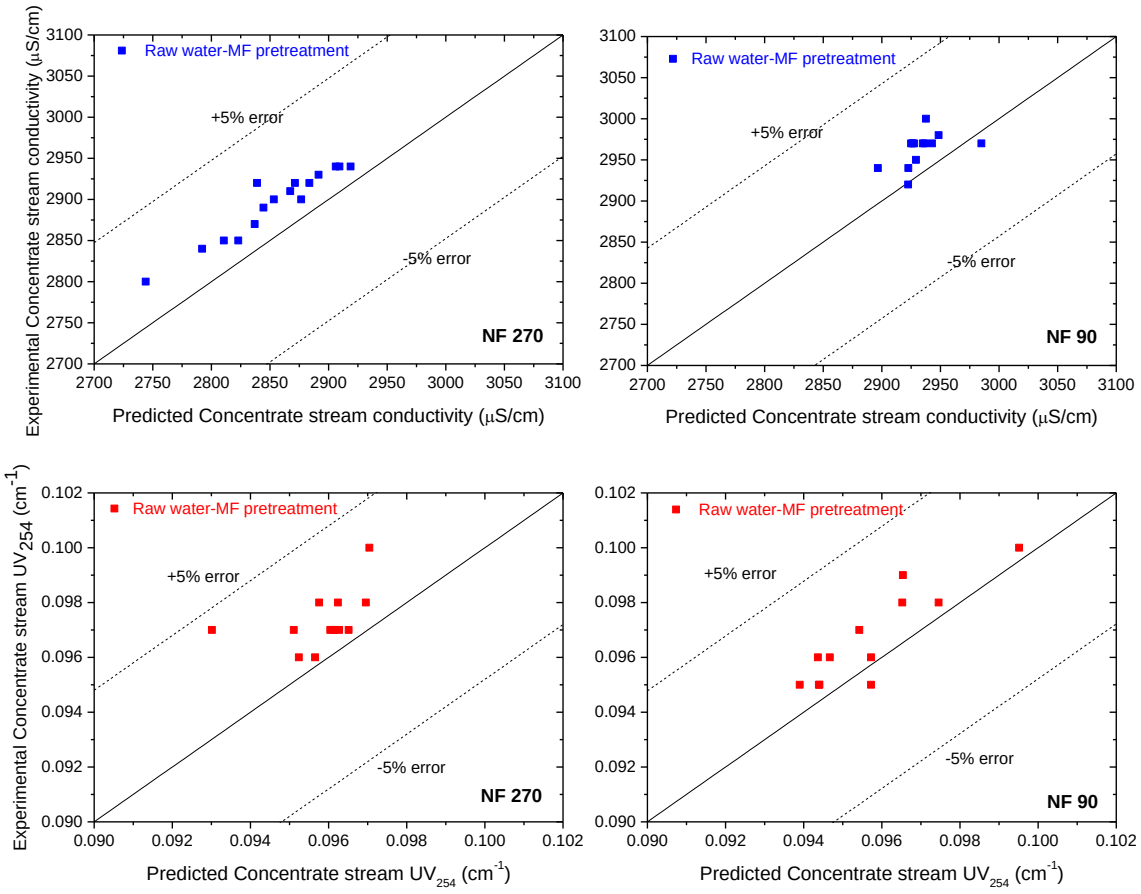

Figure A-15. Steady state mass balances for conductivity and UV_{254} for the retentate stream for experiments with pretreated Foss reservoir water.

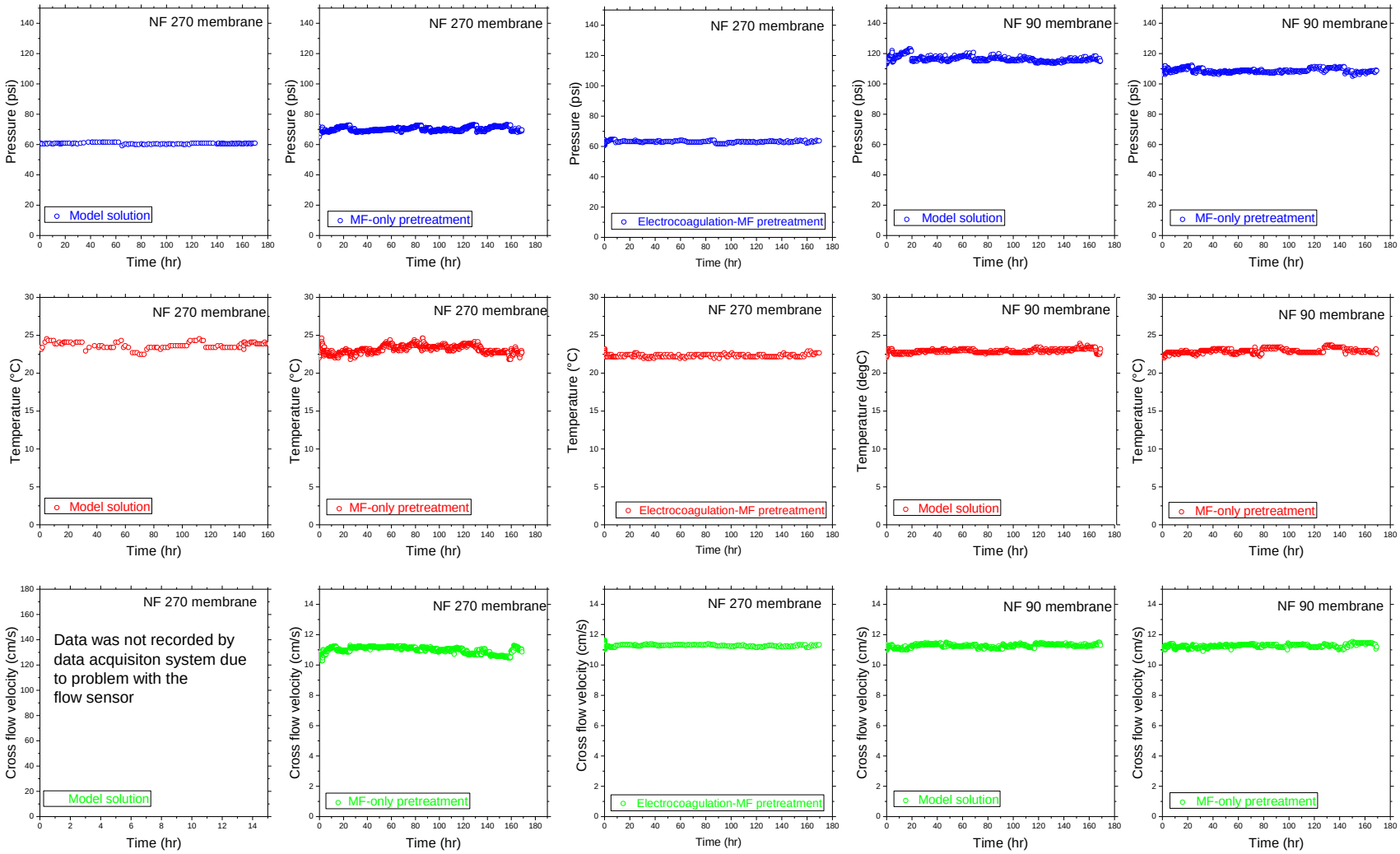

Figure A-16. Continuous monitoring of transmembrane pressure, temperature, and cross flow velocity throughout the duration of NF fouling testing.

Figure A-16 depicts constant operating conditions during the entire duration of each nanofiltration experiment for at least 168 hours (~7 days). This was necessary to be able to quantitatively compare results obtained for multiple experiments performed over the first quarter of research. Note that the flow meter failed during one of the early experiments (model solution with NF 270). Hence, the cross flow velocity profile was not recorded by the data acquisition system (missing graph in the bottom left corner of Figure A-16). However, the cross flow velocity was kept constant during this experiment manually using a calibrated rotameter that was installed in the retentate stream.

Pure water permeability

Pure water permeabilities of NF 270 and NF 90 were measured in the pressure range 30-100 psi as depicted in Figure A-17. The pure water permeability of the NF 270 and NF 90 membranes were 18.3 L/m^2.h.bar and 6.9 L/m^2.h.bar respectively. Hence, NF 270 exhibited nearly 2x higher water flux compared with NF 90.

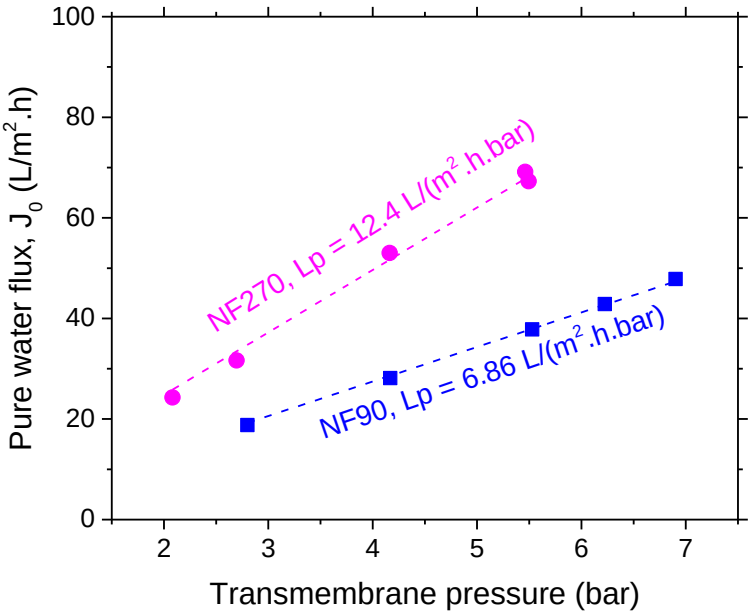

Figure A-17. Pure water permeabilities of NF270 and NF90 membranes.